



**TECHNICAL REPORT 0-7012-1**  
TxDOT PROJECT NUMBER 0-7012

# Proposed Design of Internally Redundant Steel Box Straddle Caps

Todd Helwig  
Esteban Zecchin  
Emma Williams  
Chen Liang  
Michael Engelhardt  
Matthew Hebdon  
Eric Williamson

May 2023

Published January 2025

<https://library.ctr.utexas.edu/ctr-publications/0-7012-1.pdf>



Technical Report Documentation Page

1. Report No. FHWA/TX-24/0-7012-1		2. Government Accession No.		3. Recipient's Catalog No.	
4. Title and Subtitle Proposed Design of Internally Redundant Steel Box Straddle Caps				5. Report Date Submitted: May 31, 2023	
				6. Performing Organization Code	
7. Author(s) Esteban Zecchin. <a href="https://orcid.org/0000-0001-7032-8587">https://orcid.org/0000-0001-7032-8587</a> Emma Williams Chen Liang Todd Helwig, Ph.D. <a href="https://orcid.org/0009-0005-6469-8756">https://orcid.org/0009-0005-6469-8756</a> Michael Engelhardt, Ph.D. <a href="https://orcid.org/0000-0001-5868-196X">https://orcid.org/0000-0001-5868-196X</a> Eric Williamson, Ph.D. Matthew Hebdon, Ph.D. <a href="https://orcid.org/0000-0002-9115-0279">https://orcid.org/0000-0002-9115-0279</a>				8. Performing Organization Report No. 0-7012-1	
9. Performing Organization Name and Address Center for Transportation Research The University of Texas at Austin 3925 W. Braker Lane, 4 <sup>th</sup> Floor Austin, TX 78759				10. Work Unit No. (TRAIS)	
				11. Contract or Grant No. 0-7012	
12. Sponsoring Agency Name and Address Texas Department of Transportation Research and Technology Implementation Division 125 E. 11 <sup>th</sup> Street Austin, TX 78701				13. Type of Report and Period Covered Technical Report August 2019 - May 2023	
				14. Sponsoring Agency Code	
15. Supplementary Notes Project performed in cooperation with the Texas Department of Transportation and the Federal Highway Administration.					
16. Abstract Steel box straddle caps are classified as Fracture Critical Members, requiring stringent design, fabrication, and in-service inspections to comply with the provisions of the Fracture Control Plan. Providing internal redundancy to steel box straddle caps to remove the Fracture Critical inspection requirements is highly desirable.  The research conducted explores two possible approaches to provide internal redundancy to steel box straddle caps by (i) adding high-strength bars as a secondary tensile element and (ii) providing cross-boundary fracture resistance between the components in tension. A full-scale experimental program was conducted and complemented with finite element modeling. The results of these studies are discussed, and design recommendations and examples are provided.					
17. Key Words Internal redundancy, fracture critical, straddle caps, steel, fracture			18. Distribution Statement No restrictions. This document is available to the public through the National Technical Information Service, Alexandria, Virginia 22312; <a href="http://www.ntis.gov">www.ntis.gov</a> .		
19. Security Classif. (of report) Unclassified	20. Security Classif. (of this page) Unclassified	21. No. of pages TBD [Total count excl. cover]		22. Price	



**THE UNIVERSITY OF TEXAS AT AUSTIN  
CENTER FOR TRANSPORTATION RESEARCH**

## **Proposed Design of Internally Redundant Steel Box Straddle Caps**

Esteban Zecchin  
Emma Williams  
Chen Liang  
Todd Helwig, Ph.D.  
Michael Engelhardt, Ph.D.  
Eric Williamson, Ph.D.  
Matthew Hebdon, Ph.D.

---

CTR Technical Report:	0-7012-1
Report Date:	Submitted: May 2023
Project:	0-7012
Project Title:	Proposed Design of Internally Redundant Steel Box Straddle Caps
Sponsoring Agency:	Texas Department of Transportation
Performing Agency:	Center for Transportation Research at The University of Texas at Austin

Project performed in cooperation with the Texas Department of Transportation and the Federal Highway Administration.

Center for Transportation Research  
The University of Texas at Austin  
3925 W. Braker Lane, 4<sup>th</sup> floor  
Austin, TX 78759

<http://ctr.utexas.edu/>

## Disclaimers

---

**Author's Disclaimer:** The contents of this report reflect the views of the authors, who are responsible for the facts and the accuracy of the data presented herein. The contents do not necessarily reflect the official view or policies of the Federal Highway Administration or the Texas Department of Transportation (TxDOT). This report does not constitute a standard, specification, or regulation.

**Patent Disclaimer:** There was no invention or discovery conceived or first actually reduced to practice in the course of or under this contract, including any art, method, process, machine manufacture, design or composition of matter, or any new useful improvement thereof, or any variety of plant, which is or may be patentable under the patent laws of the United States of America or any foreign country.

## Engineering Disclaimer

---

NOT INTENDED FOR CONSTRUCTION, BIDDING, OR PERMIT PURPOSES.

Project Engineer: Todd A. Helwig  
Professional Engineer License State and Number: Texas No. 94280  
P.E. Designation: Research Supervisor



## Acknowledgments

---

The authors would like to acknowledge the Texas Department of Transportation for funding this research project. Particularly, the researchers would like to thank the members of the Project Monitoring Committee for their continued participation and contributions to this project: Jamie Farris, PE (Bridge Division); Tom Fan, PhD, PE (Houston district); David Fish, PE (Bridge Division); Wanching Huang, PE (Houston district); Moheb Labib, PE (Dallas district); Yongqian Lin, PE (Houston district); and Paul Rollins, PE (Bridge Division). In addition, Martin Dassi from TxDOT-RTI assisted the research team a great deal in the administration of the contract, and his efforts are very much appreciated.

Furthermore, the research team would like to express their gratitude to the members of the Industry Advisory Group, whose generous contributions through the different stages of this project were instrumental to the completion of this research study: Dr. Karl Frank; Dr. Jason Lloyd (Nucor, formerly at NSBA/AISC); Dennis Noernberg (WW AFco); Ronnie Medlock (High Steel); and Randy Rogers (Williams Brothers).

## Table of Contents

---

Chapter 1. Introduction .....	1
1.1. Overview .....	1
1.2. Research Objectives and Report Outline .....	4
Chapter 2. Background .....	5
2.1. Historical Development of the Fracture Control Plan .....	5
2.2. Structural Redundancy .....	9
2.2.1. Redundancy Considerations for Steel Box Straddle Caps .....	10
2.3. Previous Research on Fracture Critical Members .....	11
2.4. Applicable Design Provisions .....	12
2.4.1. AASHTO LRFD Bridge Design Specifications, 9 Ed. (2020) .....	12
2.4.2. AASHTO/AWS Bridge Welding Code, Clause 12 (AASHTO/AWS 2015) .	13
2.4.3. National Bridge Inspection Standards – Code of Federal Regulations (23 C.F.R. §§ 650.301-317, 2021) .....	13
2.4.4. TxDOT Bridge Design Manual LRFD (2020) .....	13
2.4.5. AASHTO Guide Specifications for Analysis and Identification of Fracture Critical Members and System Redundant Members (2018) .....	13
2.4.6. AASHTO Guide Specifications for Internal Redundancy of Mechanically- Fastened Built-up Steel Members (2018-1) .....	14
2.5. Summary .....	14
Chapter 3. Preliminary studies .....	16
3.1. Bridge Survey and Industry Advisory Group .....	16
3.1.1. Steel Box Straddle Cap Types .....	16
3.1.2. Geometry and Proportions .....	21
3.1.3. Fabrication and Welding .....	22
3.1.4. Target Load for Redundancy Evaluation .....	23
3.2. Design Approaches for Internal Redundancy .....	23
3.2.1. Design Concept A .....	24
3.2.2. Design Concept B .....	25
3.3. Summary .....	27
Chapter 4. Experimental Program .....	28
4.1. Design and Fabrication of Test Specimens .....	28

4.1.1. Design of Specimens.....	28
4.1.2. Specimen Fabrication and Assembly.....	38
4.1.3. Material Characterization.....	42
4.2. Preliminary Analysis of Selected Design Concepts.....	45
4.2.1. Results of Preliminary Analyses.....	50
4.3. Testing Protocol.....	53
4.3.1. Fracture Test.....	53
4.3.2. Ultimate Strength Test.....	58
4.4. Test Setup.....	59
4.4.1. Hydraulic Actuators Operation for Cyclic Loading and Fracture Test.....	62
4.4.2. Hydraulic Actuators Operation for Ultimate Strength Test.....	64
4.5. Instrumentation.....	64
4.6. Summary.....	69
Chapter 5. Experimental Results and Observations.....	71
5.1. Fracture Test of Baseline Specimen.....	71
5.1.1. Observations.....	80
5.2. Experimental Testing of Specimen A.....	81
5.2.1. Fracture Test of Specimen A.....	82
5.2.2. Ultimate Strength Test of Specimen A.....	91
5.2.3. Observations.....	94
5.3. Experimental Testing of Specimen B1.....	96
5.3.1. Fracture Test of Specimen B1.....	96
5.3.2. Ultimate Strength Test of Specimen B1.....	102
5.3.3. Observations.....	104
5.4. Experimental Testing of Specimen B2.....	105
5.4.1. Fracture Test of Specimen B2.....	105
5.4.2. Ultimate Strength Test of Specimen B2.....	110
5.4.3. Observations.....	111
5.5. Results Comparison.....	111
5.6. Summary.....	114
Chapter 6. Computational Studies.....	116
6.1. Box girder modeling.....	116

6.1.1. FE Model for Design Concept A .....	119
6.1.2. Modeling of Design Concept B .....	120
6.1.3. Boundary Conditions and Applied Loads.....	121
6.1.4. Crack Modeling .....	124
6.1.5. Material Model.....	125
6.1.6. Analysis Procedure .....	126
6.1.7. Finite Element Models Validation .....	126
6.2. Finite Element Modeling of Design Concept A .....	127
6.2.1. Validation of FE models for Specimen A.....	127
6.2.2. FE Studies for Design Concept A.....	129
6.3. Finite Element Modeling of Design Concept B.....	132
6.3.1. Validation of FE models for Specimen B1 and B2.....	132
6.3.2. Parametric Studies for Design Concept B .....	135
6.4. Summary .....	167
Chapter 7. Recommendations And Design Example.....	168
7.1. Considerations on Implementation .....	168
7.2. Design Example .....	170
Chapter 8. Summary and Conclusions.....	177
8.1. Summary .....	177
8.2. Conclusions.....	178
References.....	179
Appendix A. Test Specimens Shop Drawings.....	181
Appendix B. Pilot Specimens Tests.....	185
Appendix C. Design Example Calculations.....	230
D. Value of Research Overview .....	250
D.1 Qualitative Value .....	250
D.2 Economic Value .....	251

## List of Tables

---

Table 4.1: Sectional capacity of Specimen A (undamaged/intact and faulted conditions)	32
Table 4.2: Sectional capacity of Specimen B1 (undamaged/intact and faulted conditions)	33
Table 4.3: Sectional capacity of Specimen B2 (undamaged/intact and faulted conditions)	35
Table 4.4: Ratios of tension components area to total tension area for Specimens B1 and B2	36
Table 4.5: Material properties of test specimens	43
Table 4.6: Overview of the investigated FE models	46
Table 6.1: Parameters considered for the evaluation of the St. Venant torsional constant	140
Table 6.2: Sample calculation of Flexural Strength (Undamaged/intact Condition)	152
Table 6.3: Sample calculation of Flexural Strength (Fractured Bottom Flange)	154
Table 6.4: Sample calculation of Flexural Strength (Fractured Web)	157
Table 6.5: Sample calculation of Maximum Load	160
Table 6.6: Comparison between maximum loads from FE analyses and calculated strengths per AASHTO (2020)	162
Table 7.1: Load Factors and Load Combinations	171
Table 7.2: Cross-section dimensions for Design Example	172
Table 7.3: Summary of sectional capacities	174

## List of Figures

---

Figure 1.1: Steel box straddle cap supporting twin tub girders. Source: Google Maps.	1
Figure 2.1: Point Pleasant Bridge (Silver Bridge) after completion in 1928. Source: US Department of Transportation.	6
Figure 2.2: Collapse of Point Pleasant Bridge (Silver Bridge) in 1967: (A) General view of the collapsed bridge, (B) typical eyebar from the suspension chain (Source: The Herald-Dispatch), and (C) fractured eye bar retrieved from the site and on display in the NIST museum (Source: NIST Museum).	7

Figure 2.3:	Collapse of the hanger span of the Mianus River bridge in Connecticut. Source: Hartford-Courant. ....	8
Figure 3.1:	Straddle bent span length ranges and static configurations identified in the bridge survey .....	17
Figure 3.2:	Non-integral steel box straddle caps supporting longitudinal prestressed concrete girders on South MoPac Expressway and West Cesar Chavez Street, Austin, TX. Source: Google Maps.....	18
Figure 3.3:	Integral Straddle Caps for (A) steel tub girders and (B) I-girders (adapted from TxDOT drawings) .....	19
Figure 3.4:	Non-integral steel box straddle caps: (A) Tub girders on bearings on the top flange; (B) Multiple I-girders supported by corbels; (C) Corbel detail. Adapted from TxDOT drawings. ....	20
Figure 3.5:	Typical support details for the steel box caps (adapted from TxDOT typical details, not to scale).....	21
Figure 3.6:	Typical cross-section dimensions for steel box straddle caps based on the bridge survey .....	22
Figure 3.7:	Typical box corner welds. Adapted from AASHTO/NSBA (2020).....	23
Figure 3.8:	Design Concept A: steel box straddle cap reinforced with PT bars .....	24
Figure 3.9:	Design Concept B: bolted connections between the tension elements..	25
Figure 3.10:	Design Concept B: steel box straddle cap with cross-boundary separation limits the extension of the cracks only to the bottom flange plate.....	26
Figure 4.1:	Full-scale test specimen (not to scale) .....	29
Figure 4.2:	Specimen A details .....	30
Figure 4.3:	Specimen A: possible arrangements of the PT bars .....	30
Figure 4.4:	Specimen A: sectional analysis of undamaged/intact and faulted sections .....	32
Figure 4.5:	Specimen B1: sectional analysis of undamaged/intact and faulted sections .....	34
Figure 4.6:	Specimen B1 details.....	34
Figure 4.7:	Specimen B2 details.....	35
Figure 4.8:	Specimen B2: sectional analysis of undamaged/intact and faulted sections .....	36
Figure 4.9:	Specimen A: testing sequence for Baseline Specimen .....	38
Figure 4.10:	Fabrication of test segments at W&W AFCO Steel, San Angelo. Photos courtesy of Daniel Liendo.....	39

Figure 4.11:	Delivery of test segments at FSEL: (A) and (B) unloading from the truck bed, and (C) and (D) parking of the test segments. ....	40
Figure 4.12:	Test specimen assembly sequence: (A) fitting of the North end segment to the test segment; (B) tightening of bolted splices; and (C) lifting of the assembled test specimen. ....	41
Figure 4.13:	Assembled test specimen placed in the test setup.....	42
Figure 4.14:	Specimen A: CVN test results .....	43
Figure 4.15:	Specimen B1: CVN test results .....	44
Figure 4.16:	Specimen B2: CVN test results .....	44
Figure 4.17:	CVN specimens tested at -120 °F (bottom flange plate) .....	45
Figure 4.18:	Specimen A and Baseline Specimen: crack lengths considered.....	46
Figure 4.19:	Specimen B1: crack sizes considered .....	46
Figure 4.20:	Baseline Specimen FE model: loads and boundary conditions .....	47
Figure 4.21:	Test segment in FE models.....	48
Figure 4.22:	Specimen A: FE models with continuous PT bars .....	49
Figure 4.23:	Specimen A: FE models with staggered PT bars.....	49
Figure 4.24:	Specimen B1 FE model .....	50
Figure 4.25:	Specimen B1 FE model: parts created for the test segment (a) Upper cross-section; (b) bottom flange; and (c) diaphragm. ....	50
Figure 4.26:	Load versus deflection curve for models with cracks that extend through half of the width of the bottom flange for all models and 10 in. in the web in the Baseline and Specimen A models.....	51
Figure 4.27:	Load versus deflection curve for models with cracks that extend through the entire width of the bottom flange and 20 in. on the web in the Baseline and Specimen A models. ....	52
Figure 4.28:	Location of the notched section for the Baseline Specimen.....	54
Figure 4.29:	Initial notches: (A) Baseline Specimen, and (B) Specimen B1 .....	55
Figure 4.30:	Equivalent fatigue crack length, per Novak and Barsom (1976).....	56
Figure 4.31:	Fatigue crack emanating from the initial notch .....	56
Figure 4.32:	Baseline Specimen: cooling equipment inside the box section .....	57
Figure 4.33:	Full-scale test setup: schematic view (strong floor not shown for clarity) .....	59
Figure 4.34:	Test Setup: elevation and plan views.....	60

Figure 4.35:	Test Setup components: (A) North support elastomeric bearings and lateral stops; (B) pair of load cells on top of the spreader beam; (C) hydraulic actuator; and (D) spreader beam, load cells, and actuators. ....	61
Figure 4.36:	Closed-loop system operation process chart.....	62
Figure 4.37:	Closed-loop system components: (A) servo valve; (B) hydraulic service manifold (HSM); (C) computer and MTS controller; and (D) bladder accumulator .....	63
Figure 4.38:	DAQ system: (A) NI chassis and desktop computer, and (B) wiring from chassis to connection board and sensors.....	65
Figure 4.39:	Instrumentation: location of linear potentiometers and load cells.....	65
Figure 4.40:	Instrumentation: linear potentiometers attached to the underside of the bottom flange .....	66
Figure 4.41:	Instrumentation for temperature monitoring: (A) TC wires welded to the bottom flange of specimen B2; (B) TC wire tip insulated with foam; (C) Omega DRSL TC ISO Signal conditioner; and (D) stack of signal conditioners wired to the power supply and DAQ. ....	67
Figure 4.42:	Instrumentation: typical locations of strain gauges and linear potentiometers for all test specimens.....	68
Figure 4.43:	Specimen A: instrumentation of PT bars: (A) Strain gauges; (B) load cells; and (C) insulation. ....	69
Figure 5.1:	Baseline Specimen: location of the notched section.....	72
Figure 5.2:	Baseline Specimen: initial notches made (A) on the lower portion of the webs and (B) bottom flange edge .....	73
Figure 5.3:	Baseline Specimen: dumbbell-shaped crack arrester and vertical groove. ....	73
Figure 5.4:	Baseline Specimen: fatigue cracks emanating from notches: (A) West flange and (B) West web.....	74
Figure 5.5:	Baseline Specimen: temperature distribution at the notched section (°F). ....	75
Figure 5.6:	Baseline Specimen Fracture Test: applied bending moment versus deflection at the cracked section .....	77
Figure 5.7:	Baseline Specimen: cracks after completion of Fracture Test.....	79
Figure 5.8:	Specimen A: testing sequence .....	81
Figure 5.9:	Repair process for Specimen A following Baseline Test .....	82
Figure 5.10:	Specimen A: propagation of fatigue crack on the East edge of the bottom flange during the cooling down under self-weight only .....	83



Figure 5.11:	Specimen A: spliced section after fracture due to uneven distribution of liquid Nitrogen (photo taken inside the specimen) .....	83
Figure 5.12:	Specimen A: location of the notched section.....	84
Figure 5.13:	Specimen A: fatigue cracks emanating from the initial notches: (A) East flange, and (B) West web.....	85
Figure 5.14:	Specimen A: temperature distribution at the notched section (°F).....	85
Figure 5.15:	Specimen A: loading history during the fracture test: total applied load (top) and axial force developed in the PT bars (bottom). ....	86
Figure 5.16:	Specimen A: loading history (first 10 seconds) during the fracture test: total applied load (top) and axial force developed in the PT bars (bottom). ....	87
Figure 5.17:	Specimen A Fracture Test: bending moment versus deflection at the crack location .....	88
Figure 5.18:	Specimen A: cracks after completion of Fracture Test.....	90
Figure 5.19:	Specimen A Ultimate Strength Test: applied bending moment versus deflection at the cracked section .....	92
Figure 5.20:	Specimen A Ultimate Strength Test: Loading sequence; total applied load (top) and axial force developed in the PT bars (bottom) .....	93
Figure 5.21:	Specimen A: cracks observed on the webs through the different test stages: (A) East web; and (B) West web. ....	94
Figure 5.22:	Specimen B1: initial notches .....	96
Figure 5.23:	Specimen B1: location of the notched section.....	97
Figure 5.24:	Specimen B1: initial notches on the East bottom flange edge.....	97
Figure 5.25:	Specimen B1: fatigue crack emanating from the notch on the bottom flange .....	98
Figure 5.26:	Specimen B1: temperature distribution at the notched section (°F). Readings from thermocouples affected by eddy currents at the tips of the wires. ....	99
Figure 5.27:	Specimen B1 Fracture Test: bending moment versus deflection at the cracked section .....	100
Figure 5.28:	Specimen B1: cracks after completion of Fracture Test.....	101
Figure 5.29:	Specimen B1 Ultimate Strength Test: bending moment versus deflection at the cracked section .....	103
Figure 5.30:	Specimen B1 Ultimate Strength Test: bottom flange crack after reaching the calculated plastic moment of the faulted section and unloading the specimen .....	103

Figure 5.31:	Specimen B1 Ultimate Strength Test: (A) Buckled top flange and cover plate, and (B) bottom flange crack and flange connection plates (bolts removed) after final loading.	104
Figure 5.32:	Specimen B2: location of the notched section	105
Figure 5.33:	Specimen B2: initial notch on the West bottom flange plate	106
Figure 5.34:	Specimen B2: fatigue cracks emanating from the notch on the East flange edge	106
Figure 5.35:	Specimen B2: temperature distribution at the notched section (F)	107
Figure 5.36:	Specimen B2 Fracture Test: bending moment versus deflection at the cracked section	108
Figure 5.37:	Specimen B2: fractured bottom flange plate after Fracture Test	109
Figure 5.38:	Specimen B2 Ultimate Strength Test: bending moment versus deflection at the cracked section	111
Figure 5.39:	Ultimate Strength Tests: comparison of results	113
Figure 5.40:	Ultimate Strength Tests: comparison of results (close-up view at the origin)	113
Figure 6.1:	Abaqus FE model for Specimen B2 (shell thickness rendered)	116
Figure 6.2:	Longitudinal cut view of Abaqus/CAE model for Specimen B2	117
Figure 6.3:	Specimen B2 FE Model: tie Constraint between the end segment and test segment (shell thickness not rendered)	118
Figure 6.4:	Specimen B1 FE model: meshed assembly and detail around bolt holes.	119
Figure 6.5:	PT bars (truss elements) anchored at intermediate diaphragms (shell elements). Front web elements were removed from view for clarity.	120
Figure 6.6:	Specimen B2 FE model: MPC connectors between the bottom flange and the flange connection plate	121
Figure 6.7:	Typical support details for the steel box caps	122
Figure 6.8:	Boundary conditions for end supports (pin support depicted)	123
Figure 6.9:	Seam crack on a planar shell part. Adapted from Abaqus Reference Manual (Dassault Systèmes, 2022).	124
Figure 6.10:	Specimen B2 FE model: seam cracks defined on (A) bottom flange plate, and (B) flange connection plate and web plate	125
Figure 6.11:	Specimen A FE model: seam crack defined on (A) bottom flange and half of the depth of both webs and (B) bottom flange and entire depth of both webs	125
Figure 6.12:	Stress-strain model for parametric FE models (not to scale)	126

Figure 6.13:	Specimen A: experimental test and FEA results .....	128
Figure 6.14:	Design Concept A: loading conditions and PT arrangements considered. .....	129
Figure 6.15:	Base cross-section for Design Concept A FEA studies .....	130
Figure 6.16:	Design Concept A: comparison of results from parametric FE studies	131
Figure 6.17:	Specimen B1: experimental test and FEA results.....	133
Figure 6.18:	Specimen B2: experimental test and FEA model results.....	134
Figure 6.19:	Specimen B1: screenshot of the FE model showing equivalent Von Mises stress contours around the fractured section at the maximum load (deformation scale factor of 3) .....	135
Figure 6.20:	Normalized nominal capacity and unbraced length for surveyed box straddle caps .....	138
Figure 6.21:	Torsional constant for undamaged/intact and assumed fractured sections .....	139
Figure 6.22:	Design Concept B parametric FE study: assumed fractured sections .	140
Figure 6.23:	Design Concept B parametric FE study: cross-sectional dimensions considered .....	141
Figure 6.24:	FE model of box member subject to pure-torsion demands .....	142
Figure 6.25:	Design Concept B Parametric Studies: influence of a fractured section on the torsional stiffness .....	144
Figure 6.26:	Design Concept B: influence of the spacing of internal diaphragms ..	145
Figure 6.27:	Design Concept B: torsional constant normalized by span length versus web shear stress due to torsion.....	146
Figure 6.28:	Design Concept B: normalized torsional constant versus web shear stress due to torsion .....	147
Figure 6.29:	Application of four factored HS-20 trucks for a 60-ft long box cap ...	148
Figure 6.30:	Design Concept B parametric FE study: loading conditions and crack locations .....	149
Figure 6.31:	Design Concept B parametric FE study: load versus displacement at the fractured section.....	150
Figure 6.32:	Comparison between FEA results and strength calculations per AASHTO (2020) .....	162
Figure 6.33:	Parametric study: comparison of FE models and AASHTO design equations for models with different assumed cracks .....	163

Figure 6.34: Parametric study: comparison of FE models and AASHTO design equations for all models .....	165
Figure 6.35: Parametric study: comparison of FE models and AASHTO design equations with 0.90 resistance factor .....	166
Figure 7.1: Bridge layout for design example. Adapted from TxDOT drawings. .	170
Figure 7.2: Steel box straddle cap geometry .....	172
Figure 7.3: Internally redundant steel box straddle cap typical cross-section.....	173
Figure 7.4: Flexural demands and capacity in the undamaged/intact condition ....	175
Figure 7.5: Shear demands and capacity in the undamaged/intact condition .....	175
Figure 7.6: Flexural demands and capacity in the faulted condition.....	176
Figure 7.7: Shear demands and capacity in the faulted condition.....	176
Table B.1: Pilot Specimen Section Dimensions and Mechanical Properties.....	186
Table B.2: Mechanical Properties for 1"-thick plates (Chicago Spectro LLC) .....	187
Table B.3: Mechanical Properties for 3/8"-thick plates (Chicago Spectro LLC).....	188
Table B.4: Charpy V-Notch impact tests results (Chicago Spectro LLC).....	189
Table B.4: Charpy V-Notch impact tests results (Chicago Spectro LLC) (Cont.) .....	190
Table B.5: Notch sizes for PS1 .....	204
Table B.6: Final crack lengths (initial notch + fatigue crack) and Novak & Barsom Ratio for PS1 .....	207
Table B.7: Temperatures recorded at the cross-section when fracture loading protocol started.....	209
Table B.8: Notch sizes for PS2A .....	211
Table B.9: Final crack lengths (initial notch + fatigue crack) and Novak & Barsom ratio for PS2A.....	214
Table B.10: Temperatures recorded at the cross-section when fracture loading protocol started.....	216
Table B.11: Notch sizes for PS2B .....	220
Table B.12: Final crack lengths (initial notch + fatigue crack) and Novak & Barsom ratio for PS2B.....	222
Table B.13: Temperatures recorded at the cross-section when fracture loading protocol started.....	225
Table C.1: Cross-section dimensions of the intact section .....	230

Table C.2: Effective Cross-sectional Properties .....	231
Table C.3: Cross-section dimensions of the faulted section (bottom flange fractured)..	236
Table C.4: Effective Cross-sectional Properties .....	237
Table C.5: Cross-section dimensions of the faulted section (web and flange connection plate fractured) .....	243
Table C.6: Effective Cross-sectional Properties .....	244

# Chapter 1. Introduction

## 1.1. Overview

Straddle bents are commonly utilized in bridges located in congested urban environments when using conventional piers is not possible due to the presence of intersecting roadways or railroads beneath the bridge. An example is illustrated in Figure 1.1, which shows the direct connector flyover ramp between the North Interstate Highway 35 to the US Route 290 and the North Interstate Highway 35 Frontage Road in Austin, Texas.



Figure 1.1: Steel box straddle cap supporting twin tub girders. Source: Google Maps.

The high strength-to-weight ratio of steel makes the steel straddle caps efficient from a construction perspective. The selection of steel significantly reduces the weight of the cap relative to a comparable concrete cap, allowing for an easier and faster erection process that reduces the duration of necessary lane closures as well as the required crane capacity. Steel straddle caps are typically a box cross-section due to their high torsional stiffness compared to an I-shaped section. The high torsional stiffness of the box is advantageous for increasing the lateral torsional buckling resistance of the straddle cap since providing lateral bracing is not normally possible. The box section also tends to have improved aesthetics with fewer shadows than a cap comprised of multiple I-shaped sections.

However, the current design provisions of the American Association of State Highway and Transportation Officials (AASHTO) categorize steel straddle caps as Fracture Critical Members (AASHTO 2020), meaning that a fracture of the section may result in either a partial or total collapse of the bridge. The Fracture Critical classification imposes more stringent design and fabrication requirements (AASHTO/AWS 2015) and biennial in-service hands-on inspections (23 C.F.R. §§ 650.301-317, 2021). As a result, the long-term costs of the caps add a significant burden to the owner's inspection budget.

It should be noted that this report makes use of the term “Fracture Critical” (and its variations) which was the denomination utilized when the research project proposal was approved. At the time of the publication of this report, a change of nomenclature from Fracture Critical Members (FCM) to Nonredundant Steel Tension Members (NSTM) was adopted. Since these terms are interchangeable, the results and recommendations presented in this report for FCMs are valid for NSTMs.

In recent years, several studies on structural redundancy and fracture critical members have been conducted (Barnard et al. (2010), Diggleman et al. (2012), and Hebdon et al. (2015)), demonstrating the capacity of steel bridges to perform their functions in a damaged state because of possessing system or member-level redundancy. In 2012, the Federal Highway Administration (FHWA) published a memorandum (FHWA 2012) in which system redundancy was recognized as a valid mechanism to eliminate the fracture critical inspection requirements. Later, in 2019, the FHWA issued a draft memorandum (FHWA 2019) recognizing internal redundancy as an acceptable approach to avoid the fracture critical classification for inspection purposes if demonstrated by approved calculations, analysis, and experimental verification. In 2022, a memorandum published by the FHWA (FHWA 2022) stated that, for bridges without load path redundancy, agencies may choose to demonstrate that a member possesses internal redundancy such that is not considered a nonredundant steel tension member and avoid the requirement for hands-on inspections.

Traffic disruptions and lane closures required for inspections can be significantly reduced or even eliminated if the components of a steel box straddle cap are classified as internally redundant. Monetarily, waving the hands-on inspections will result in significant savings for bridge owners.

The research documented in this report corresponds to a study sponsored by the Texas Department of Transportation (TxDOT) titled: “Development of Non-Fracture Critical Steel Box Staddle Caps” and designated as TxDOT Research Project 0-7012. The goal of TxDOT Project 0-7012 was to develop details to allow steel box straddle caps to be classified as internally redundant, removing the Fracture Critical designation. The study

focused on new construction, although methods for retrofitting existing caps to add internal redundancy were also considered. The main approaches investigated included using high-strength bars as secondary tension elements and bolted connections between the tension components (instead of welds) to introduce cross-boundary fracture resistance.



## 1.2. Research Objectives and Report Outline

---

This project aimed to produce design recommendations and examples for steel box straddle caps that can be classified as non-Fracture Critical. In line with the guidelines provided in the FHWA memorandum (2022), the non-Fracture Critical classification refers to the removal of the biennial hands-on inspection requirements, while the fracture critical requirements related to material properties and fabrication practices would remain in place. The research was conducted at the Ferguson Structural Engineering Laboratory at The University of Texas at Austin and consisted of full-scale laboratory experiments and parametric finite element (FE) analyses.

This report is organized into eight chapters. Following this introductory chapter, the remainder of the document consists of the following:

- A literature review was conducted on fatigue and fracture of steel structures, fracture critical structures and members, and structural redundancy. This information is presented in Chapter 2.
- Working in conjunction with the TxDOT Project Monitoring Committee and a group of industry professionals, several design concepts for internally redundant steel straddle caps were developed. This information is presented in Chapter 3.
- Chapter 4 describes the full-scale test specimens, test setup, and testing protocol. This chapter also explains the instrumentation utilized for the test specimens.
- The results of the fracture and ultimate strength tests in the faulted state of the proposed design concepts are presented in Chapter 5.
- A summary of the analytical work performed using parametric finite element (FE) studies is given in Chapter 6. These parametric studies investigated a wider range of loading configurations, geometries, and initial crack locations than were considered in the experimental program.
- Based on the experimental program and parametric FE studies, design recommendations and examples are presented in Chapter 7.
- Finally, Chapter 8 presents the conclusions and recommendations of this research study

## Chapter 2. Background

This chapter provides relevant background information pertaining to brittle fracture, fracture critical members, and structural redundancy. Additionally, a summary of previous research and the design provisions applicable to steel box straddle caps is presented.

### 2.1. Historical Development of the Fracture Control Plan

---

Fatigue cracks can initiate and grow in steel structures as a result of the repeated application of tensile stresses. The magnitude of the stress levels leading to fatigue crack growth is generally significantly less than the corresponding levels associated with other limit states, such as yielding or buckling. If undetected, fatigue cracks can propagate and produce the rupture of a component due to the loss of cross-section, or they can propagate in an unstable mode if they reach a critical size and the fracture toughness of the material is exceeded, the latter phenomenon known as a brittle fracture. The distinctive characteristic of brittle fracture is that it occurs at stress levels below general yielding, without plastic deformation, and at extremely high speeds (Barsom and Rolfe 1999).

Despite being relatively rare, the consequences of a brittle fracture can be catastrophic in terms of human life and property damage. Therefore, structural engineers attempt to minimize the probability of occurrence with improved fabrication practices, careful design and detailing, and thorough arms-length in-service inspections of welds and other critical details.

In the context of bridge engineering in the United States, the concerns regarding brittle fracture and its devastating consequences started with the collapse of the Point Pleasant Bridge in West Virginia (also known as Silver Bridge, depicted in Figure 2.1). The 1760-foot-long eyebar suspension bridge opened to traffic in 1928 and collapsed in 1967 (shown in Figure 2.2-A) due to the fracture of the lower limb of the eye of an eye bar of the North suspension chain (Figure 2.2-B and C). The National Transportation Safety Board investigated the failure and determined the collapse was caused by the combination of corrosion-induced stresses and fatigue, which ultimately led to the development of a fatigue crack that reached the critical size, leading to a fracture that severed the lower half of the eye (National Transportation Safety Board (1968), West Virginia Department of Transportation (2019)).



*Figure 2.1: Point Pleasant Bridge (Silver Bridge) after completion in 1928. Source: US Department of Transportation.*

The collapse of the Silver Bridge was the catalyst for the creation of the first national bridge inspection program by the Federal-Aid Highway Act (1968). The inspection program required that all bridges constructed with federal funding or that carried a federally-funded road must be inspected according to the safety standards determined by the governing Department of Transportation (DOT). The first version of the National Bridge Inspection Standards (NBIS) was published in 1971. It established a national policy regarding inspection procedures, frequency of inspections, personnel qualifications, inspection reports, and maintenance of the state bridge inventory.

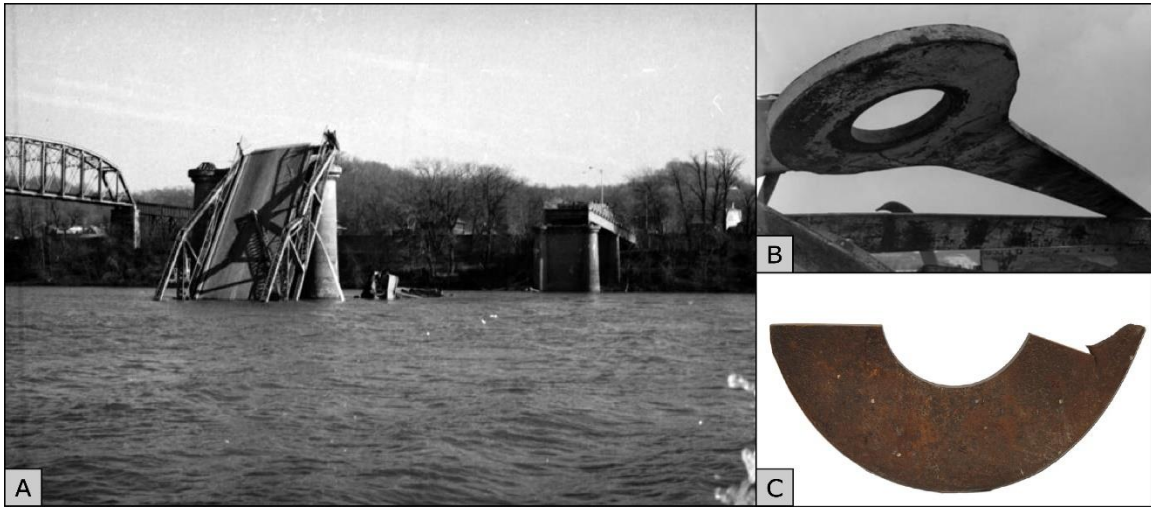


Figure 2.2: Collapse of Point Pleasant Bridge (Silver Bridge) in 1967: (A) General view of the collapsed bridge, (B) typical eyebar from the suspension chain (Source: *The Herald-Dispatch*), and (C) fractured eye bar retrieved from the site and on display in the NIST museum (Source: NIST Museum).

In 1978, the first Fracture Control Plan (FCP) was published by AASHTO, introducing the term Fracture Critical Member. More stringent Charpy V-Notch (CVN) requirements, fabrication procedures, and restrictions to fatigue demands were imposed for these members (AASHTO 1978).

In June of 1983, a 100-ft hanger span of the Mianus River bridge in Connecticut collapsed, killing three motorists (Figure 2.3). This event triggered nationwide emphasis on fatigue and fracture critical bridges, and led to the modification of the NBIS, requiring states to identify bridges with fracture critical details and establish special biennial hands-on inspections. However, the language of these regulations led to different interpretations by the states, resulting in disagreements on what constitutes a fracture critical inspection and its required frequency.

To address these discrepancies, in 2005, the Federal Highway Administration (FHWA) released a memorandum specifically stating that fracture critical inspections must be performed at an interval not to exceed 24 months. These changes were introduced in the NBIS and constitute the current inspection requirements for fracture critical members (23 C.F.R. §§ 650.301-317, 2021).



Figure 2.3: Collapse of the hanger span of the Mianus River bridge in Connecticut. Source: Hartford-Courant.

The current version of the Fracture Control Plan is sometimes described as a three-legged stool (Connor, et al. 2015), which integrates fabrication and shop inspection, material quality and design, and field inspection. ASSHTO and the American Welding Society (AWS) integrate these aspects of the FCP in Clause 12 of the AASHTO/AWS D1.5 Bridge Welding Code (AASHTO/AWS 2015), the AASHTO Load and Resistance Factor Design (LRFD) Bridge Design Specifications (AASHTO 2020), and the National Bridge Inspection Standards (23 C.F.R. §§ 650.301-317, 2021), respectively.

In 2012, the FHWA published another memorandum (FHWA 2012) that clarifies the policy regarding the classification of fracture critical members, mainly due to some language discrepancies between the NBIS, the AASHTO Manual for Bridge Evaluation (2011), and the AASHTO LRFD Specifications (AASHTO 2012). Additionally, this document introduced the term “System Redundant Member” as an acceptable method of reclassifying applicable members as non-fracture critical for inspection purposes. However, the memorandum did not recognize internal redundancy to affect the classification of a fracture

critical member because discovering a partially-damaged section is unlikely without an arms-length inspection.

More recently, in 2022, following the results of several investigations that led to a deeper understanding of system and internal redundancy, the Federal Highway Administration published a draft memorandum (FHWA 2022) in which all three types of redundancy (load-path, system, and internal) were officially acknowledged, as long as supporting analyses and experimental verification are provided.

## 2.2. Structural Redundancy

---

According to the AASHTO LRFD Specifications (2020), redundancy is “the quality of a bridge that enables it to perform its design function in a damaged state,” and a Fracture Critical Member is “a steel primary member or portion thereof subject to tension whose failure would probably cause a portion of or the entire bridge to collapse.” In this context, “performing its function in the damaged state” refers to the ability of the bridge to safely carry a certain level of traffic in the damaged condition (FHWA 2012). From these definitions, it can be understood that if a structural member of a bridge possesses redundancy, its failure will not produce a partial or total collapse and will not be classified as a Fracture Critical Member.

Redundancy can be provided to a bridge in a number of ways, which fall into the following three categories (FHWA 2022):

### ***1. Load-Path Redundancy***

Load-path redundancy is typically determined based on the number of primary load-carrying members with similar stiffness and sufficient strength to support the additional load transferred to them if one of the other members fails. Generally, a bridge with three or more longitudinal girders is considered load-path redundant, and consequently, the longitudinal girders are classified as non-Fracture Critical.

### ***2. System Redundancy***

System redundancy exists in a bridge system without load path redundancy. A bridge possesses system redundancy if the fracture of the cross-section at one location of a primary tension member will not cause a portion of or the entire bridge to collapse. This type of redundancy is typically due to continuity conditions or three-dimensional mechanisms that allow the redistribution of forces. In some cases, the system redundancy of a bridge can be determined by simple engineering judgment, such as a continuous girder with sufficient

capacity in the positive moment region to survive a fracture at an intermediate support. In other cases, identifying the system redundancy requires a refined analysis where several primary members are assumed to be fractured. These analyses of bridges have enabled identifying non-apparent secondary load paths and reclassifying the bridges as non-fracture critical.

### **3. *Internal Redundancy***

Internal redundancy exists within a primary member cross-section without load path redundancy such that the fracture of one component will not propagate through the entire member, is discoverable by the applicable inspection procedures, and will not cause a partial or total collapse of the bridge. The remaining structural section of the member must continue to safely carry a certain level of dead and live load until the fracture is detected. Bolted and riveted girders and axial members are examples of potentially internally redundant members.

#### **2.2.1. Redundancy Considerations for Steel Box Straddle Caps**

Examples of straddle caps were provided in the introductory chapter. The function of a steel straddle cap is to provide support to the adjacent spans of the bridge and is an essential element to the load path of the bridge. As such, steel straddle caps are classified as Fracture Critical Members and are subject to the design, fabrication, and in-service inspection requirements of the Fracture Control Plan. Some of these requirements include minimum Charpy V-Notch requirements for the material, careful inspection of welds or other critical details during fabrication, and designing for infinite fatigue life.

During the design process of a steel box straddle cap, the tension flanges are always designated as Fracture Critical. In the case of the webs, the preferred practice is to only designate the portion below the neutral axis as Fracture Critical so that the welds to the compression flange are not subject to unnecessarily stringent requirements.

There is great interest in the bridge industry in developing design approaches that allow reclassifying steel box straddle caps as internally redundant. This reclassification aims to relax the in-service inspection requirements but maintain the design and fabrication criteria for Fracture Critical Members since that minimizes the probability of a brittle fracture.

The publication of the AASHTO Guide Specifications for Internal Redundancy of Mechanically Fastened Built-Up Steel Members (AASHTO 2018-1) provides engineers with the necessary guidelines for designing non-Fracture Critical box straddle caps. The premise of this guide is to provide cross-boundary fracture resistance (i.e., to separate the



tension components) by mechanically connecting the tension elements and thus preventing the propagation of cracks from one component to another. Therefore, the remaining cross-section is designed to carry the load level defined by the Redundancy Load Combinations defined in the AASHTO Guide Specifications for Analysis and Identification of Fracture Critical Members and System Redundant Members (AASHTO 2018).

### **2.3. Previous Research on Fracture Critical Members**

---

Several studies have been developed on fracture critical members and bridges in recent years. This section cites some of the studies that provided a framework for the research reported in this project.

A study on the redundancy of twin tub girders (Barnard, et al. 2010) conducted at The University of Texas at Austin showed that these systems possess a significant level of redundancy despite consisting of only two longitudinal load-carrying members. The system was evaluated in the faulted condition by fully fracturing one of the girders using explosive charges, and it sustained multiple times its designed load before collapsing. Computational studies complemented the experimental tests, providing a deeper understanding of the load redistribution mechanism in the faulted condition, and demonstrated the existence of system redundancy.

A few years later, researchers from Purdue University conducted a field study on the collapse performance of the Milton-Madison truss bridge (Diggleman, Connor and Sherman 2012). The system-level redundancy of the truss was studied by simulating the fracture of the bottom cord with explosive charges, demonstrating a substantial degree of redundancy which was later confirmed through numerical studies.

Fasl et. al (2016) studied the performance of a three-span twin I-girder bridge. The flanges of the I-girders were made from angles riveted on either side of the web. After eight decades in service, several cracks were discovered throughout the girders. The girders were instrumented by a research team from the University of Texas at Austin to monitor the evolution of the cracks. The alarming growth rate of the cracks prompted the development of a retrofit solution. During the repair works, it was discovered that the cracks had not propagated from the flange angles to the webs due to the cross-boundary separation provided by the riveted connection. Therefore, it was determined that the built-up girder possessed internal redundancy.

Another major research project was conducted at Purdue University to study the internal redundancy of riveted and bolted built-up flexural members (Hebdon, et al. 2015). Several



full-scale tests and subsequent finite element analyses were performed to demonstrate the inherent internal redundancy of these girders. The researchers at Purdue developed a testing protocol to simulate the fracture of the specimens that included: (i) initiating a crack at a critical region by creating a notch, (ii) subjecting the specimen to fatigue loading to produce sharp fatigue crack tips, (iii) cooling the specimen with liquid nitrogen to reduce its fracture toughness, and (iv) loading the specimen at a high load rate.

This work led to the development of two AASHTO-approved Guide Specifications: (i) the Guide Specifications for Internal Redundancy of Mechanically-Fastened Built-Up Steel Members (AASHTO 2018-1) and (ii) the Guide Specifications for Analysis and Identification of Fracture Critical Members and System Redundant Members (AASHTO 2018). The former guide provides a methodology for classifying members as internally redundant. The latter addresses the requirements for demonstrating through analysis that a member possesses sufficient capacity to provide system redundancy to the bridge.

## **2.4. Applicable Design Provisions**

---

Several standards are applicable for the design, fabrication, and inspection of steel box straddle caps. The following list, which by no means is comprehensive, includes some of the most significant code provisions relevant to steel box straddle caps and the development of internally redundant design approaches.

### **2.4.1. AASHTO LRFD Bridge Design Specifications, 9 Ed. (2020)**

Before this edition of the AASHTO LRFD Specifications, the provisions for the flexural design of noncomposite steel box sections were largely inconsistent and scattered throughout Section 6 (Steel Structures). These issues were addressed in the current edition by incorporating the Proposed LRFD Specifications for Noncomposite Steel Box-Section Members (FHWA 2019) into Article 6.12.2.2.2.

This article provides cross-section proportion limits and a thorough methodology to determine the flexural resistance of box sections considering yielding, local buckling, and lateral torsional buckling. The latter, however, rarely controls the capacity of a steel box straddle cap due to its large torsional stiffness and the section proportions typically used for steel box straddle caps. For other limit states, such as fatigue, fracture, and shear, the applicable articles of Section 6 are utilized.

#### **2.4.2. AASHTO/AWS Bridge Welding Code, Clause 12 (AASHTO/AWS 2015)**

Clause 12 of the American Welding Society (AWS) Bridge Welding Code contains the provisions of the Fracture Control Plan for nonredundant members. The provisions in this section aim to minimize the introduction of flaws during the welding process of fracture critical members. It includes material and consumable requirements, procedures, certification and qualification of the personnel, and weld inspection requirements.

#### **2.4.3. National Bridge Inspection Standards – Code of Federal Regulations (23 C.F.R. §§ 650.301-317, 2021).**

This regulation refers to fracture critical members as Nonredundant Steel Tension Members (NSTM). The NBIS establishes the minimum standards for the inspection and evaluation of highway bridges, including the bridge inspection organization and the qualifications of the personnel. Moreover, the inspection intervals and procedures are defined for different types of bridges.

#### **2.4.4. TxDOT Bridge Design Manual LRFD (2020)**

This document aims to assist the bridge designers in applying the AASHTO LRFD Bridge Design Specifications. Of particular interest to this research, Chapter 2 includes the Extreme Event III Load Combination related to a structural member or component failure. In addition, supplemental load and dynamic amplification factors to be used with the HL-93 design live load are provided. These recommendations originated from a study on system redundancy of twin tub girder bridges (Barnard, et al. 2010).

#### **2.4.5. AASHTO Guide Specifications for Analysis and Identification of Fracture Critical Members and System Redundant Members (2018)**

The AASHTO Guide Specifications for Analysis and Identification of Fracture Critical Members and System Redundant Members (referred to as AASHTO Guide for SRMs hereafter) provides guidelines and minimum analysis requirements for evaluating the capacity of a steel bridge with an assumed failed primary tension member.

The Guide also quantifies the demands the bridge must sustain to demonstrate its redundancy at a system level. Although the bridge must survive the failure event, it is accepted that the target reliability in the faulted condition (chosen as 1.5) can be lower than in the undamaged/intact condition.

To that effect, two load combinations were developed: Redundancy I, which represents the demands on the bridge during the fracture event, and Redundancy II, which relates to the normal vehicular use of the bridge after the fracture has occurred but the crack is yet to be detected. As such, the positioning of the live load is specified for each load combination: only the striped or normal lanes are considered for Redundancy I, while the design lanes specified in Article 3.6.1.1.1 of the AASHTO LRFD Specifications (2020) should be considered for Redundancy II. Finally, the Guide provides strength and serviceability acceptance criteria in the faulted condition.

#### **2.4.6. AASHTO Guide Specifications for Internal Redundancy of Mechanically-Fastened Built-up Steel Members (2018-1)**

The AASHTO Guide Specifications for Internal Redundancy of Mechanically-Fastened Built-up Steel Members (referred to as the AASHTO Guide for IRM hereafter) describes procedures for evaluating the internal redundancy of tension components of built-up flexural and tension members.

Requirements for existing and newly-designed members are provided along with criteria to assess the performance of the members in the faulted condition. Stress amplification factors are provided for axial and flexural demands on the members, and strength and fatigue design criteria in the faulted condition are provided. Lastly, guidance is provided to calculate the maximum interval between special inspections.

### **2.5. Summary**

---

The chapter began with an overview of the history of fracture critical members. Some of the most noteworthy structural failures that shaped the current standards were described, along with a recount of the most notable changes to the provisions made by the different governing bodies.

Next, a description of structural redundancy and the different ways in which it can be provided to steel bridges is given. Load path redundancy, system redundancy, and internal redundancy are explained, and a possible approach for designing an internally redundant steel box straddle cap is described.

Additionally, some research studies conducted in the past 20 years that were of major importance for this investigation are acknowledged.

Lastly, a summary of the current specifications applicable to the design, fabrication, and inspection of steel box straddle caps is given. These provisions set a framework for

developing the proposed approaches for internally redundant steel box straddle caps that will be presented in Chapter 3, and the design of the test specimens will be detailed in Chapter 4. Additionally, Chapter 3 will include a summary of key characteristics of steel box straddle caps developed by reviewing design documents.

## **Chapter 3. Preliminary studies**

This chapter describes typical details used for steel box straddle caps in Texas (Section 3.1) and design concepts to introduce internal redundancy (Section 3.2). The information in this chapter was used to develop the full-scale tests covered in Chapter 4.

### **3.1. Bridge Survey and Industry Advisory Group**

---

A survey of steel box straddle bents used in Texas was conducted to identify typical characteristics, such as commonly used types, geometry, and fabrication practices. The survey was based on the documentation of eight bridges and 19 steel box straddle bents provided by TxDOT, which were deemed representative of the different structural configurations of steel box caps used in Texas.

Additionally, several bridge professionals (designers, inspectors, construction contractors, and fabricators) constituted an Industry Advisory Group (IAG) for this research project. Information was obtained pertaining to preferred design and fabrication practices for steel box straddle caps and likely details to improve redundancy through several meetings with the IAG and members of the TxDOT Project Monitoring Committee.

#### **3.1.1. Steel Box Straddle Cap Types**

Most steel box straddle caps consist of simple-span girders supported on reinforced concrete columns. However, cantilevers at one or both ends and two-span continuous bents are also used for relatively wide bridge decks. The span length ranges for the three configurations mentioned are depicted in Figure 3.1. The width of the supported roadway and the conditions below it (i.e., foundation conditions, presence of utilities, and right-of-way limitations) usually drive the choice between these configurations.

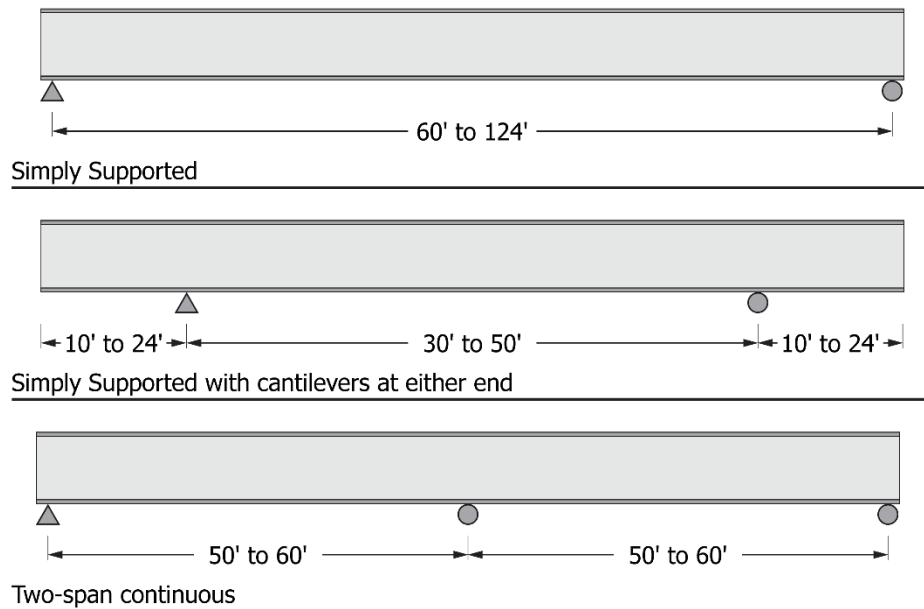


*Figure 3.1: Straddle bent span length ranges and static configurations identified in the bridge survey*

These conditions dictate the length of the straddle cap, which, based on the survey, ranges between 60 and 124 ft. In some cases, there is often a long distance between the outer columns of the bent and edges of the supported deck, as shown in Figure 3.2. A similar geometry was shown previously in Figure 1.1.



*Figure 3.2: Non-integral steel box straddle caps supporting longitudinal prestressed concrete girders on South MoPac Expressway and West Cesar Chavez Street, Austin, TX. Source: Google Maps.*

Longitudinal girders can be integral or non-integral with the steel straddle cap. In the integral configuration, the longitudinal girders frame into the outer faces of the box webs with a full-moment connection. Although this option offers more vertical clearance below the structure, it creates torsional demands on the straddle cap due to the unbalanced dead and live load effects. No internal diaphragms are required in the straddle cap for this configuration because the webs of the longitudinal girders are continuous through the box straddle cap. Examples of integral straddle caps are illustrated in Figure 3.3 for tubs and I-girders.

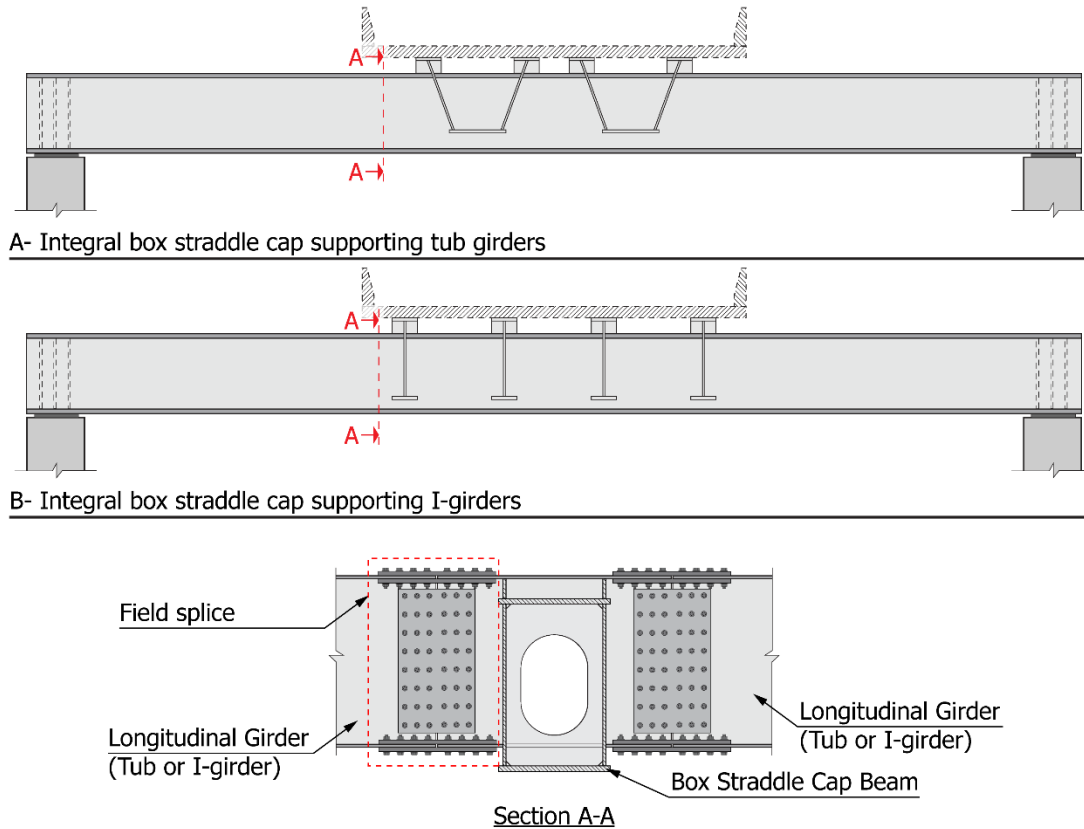


Figure 3.3: Integral Straddle Caps for (A) steel tub girders and (B) I-girders (adapted from TxDOT drawings)

The non-integral configuration, in which the longitudinal girders do not rigidly connect to the straddle cap, can be accomplished in the following ways:

- Stacked system: the longitudinal girders are placed on bearings resting on the top flange of the box cap, as illustrated in Figure 1.1 and Figure 3.4-A. The girders can have a single bearing line for continuous longitudinal girders or two bearing lines for discontinuous longitudinal girders. Internal diaphragms are required in the box section at the locations of the bearings to prevent localized distortion of the box section.

This configuration minimizes the torsional demands on the cap because the vertical loads are approximately centered with the centroid of the box beam. This option is the most straightforward and geometrically flexible but requires more vertical clearance than the other arrangements. It is suitable for almost all types of longitudinal girders: steel tub girders, steel I-girders, or prestressed concrete U- or I-girders.



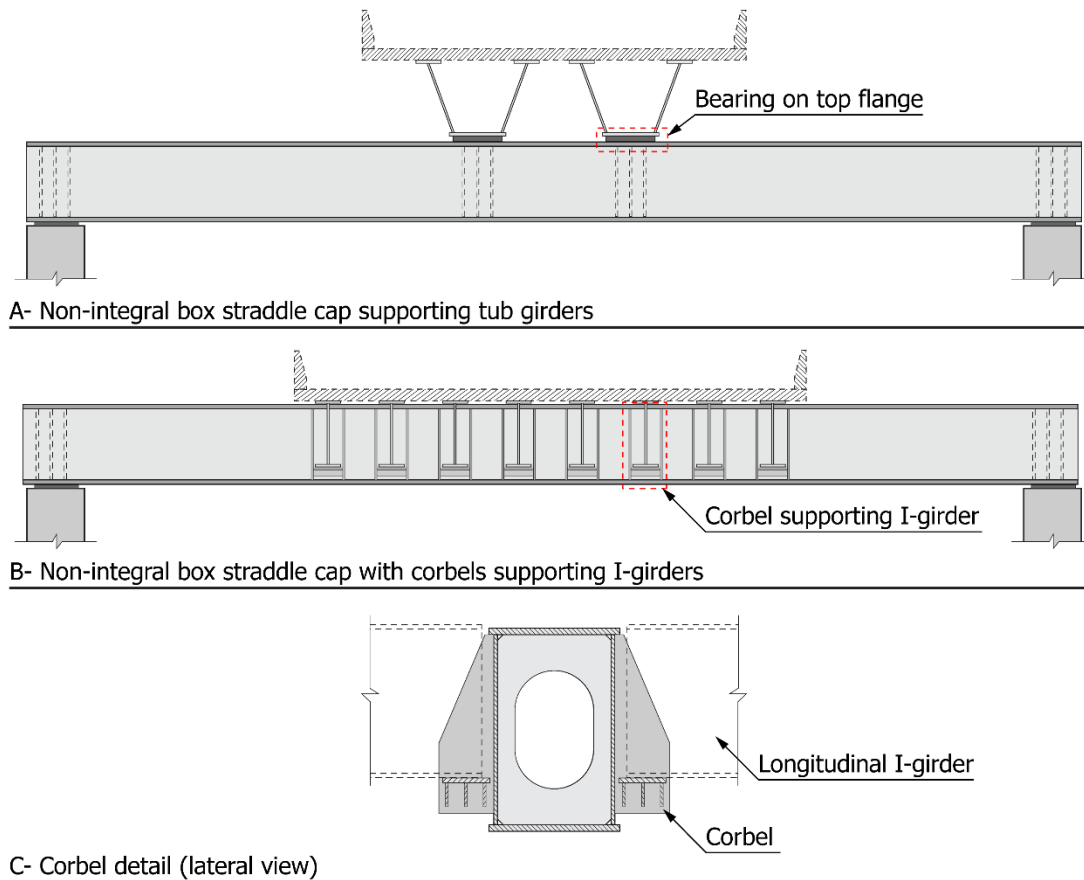


Figure 3.4: Non-integral steel box straddle caps; (A) Tub girders on bearings on the top flange; (B) Multiple I-girders supported by corbels; (C) Corbel detail. Adapted from TxDOT drawings.

- Corbel beam framing: a steel corbel (a triangular-shaped bracket welded to the box webs) supports each longitudinal girder -typically steel or prestressed concrete I-girders- as shown in Figure 3.4-B, Figure 3.4-C, and Figure 3.2. Internal diaphragms are required at the locations of the vertical plates of the corbels.

This configuration increases the torsional demands imparted to the box beam but offers more vertical clearance for the road underneath the bent. It is simpler than the integral system, but the fatigue resistance of the steel box cap at the welded corbels must be carefully considered due to the introduction of vertical welds on the flanges and in the vicinity of the tension flange.

At the supports, steel box caps sit on steel laminated or high-load multi-rotational bearings anchored to reinforced concrete columns, as illustrated in Figure 3.5. This connection restricts displacement in all directions (vertical, longitudinal, and transverse) and provides

torsional restraint to the straddle cap. Internal diaphragms, like those utilized at the supports of the longitudinal girders, are also used at the steel box supports at the columns.

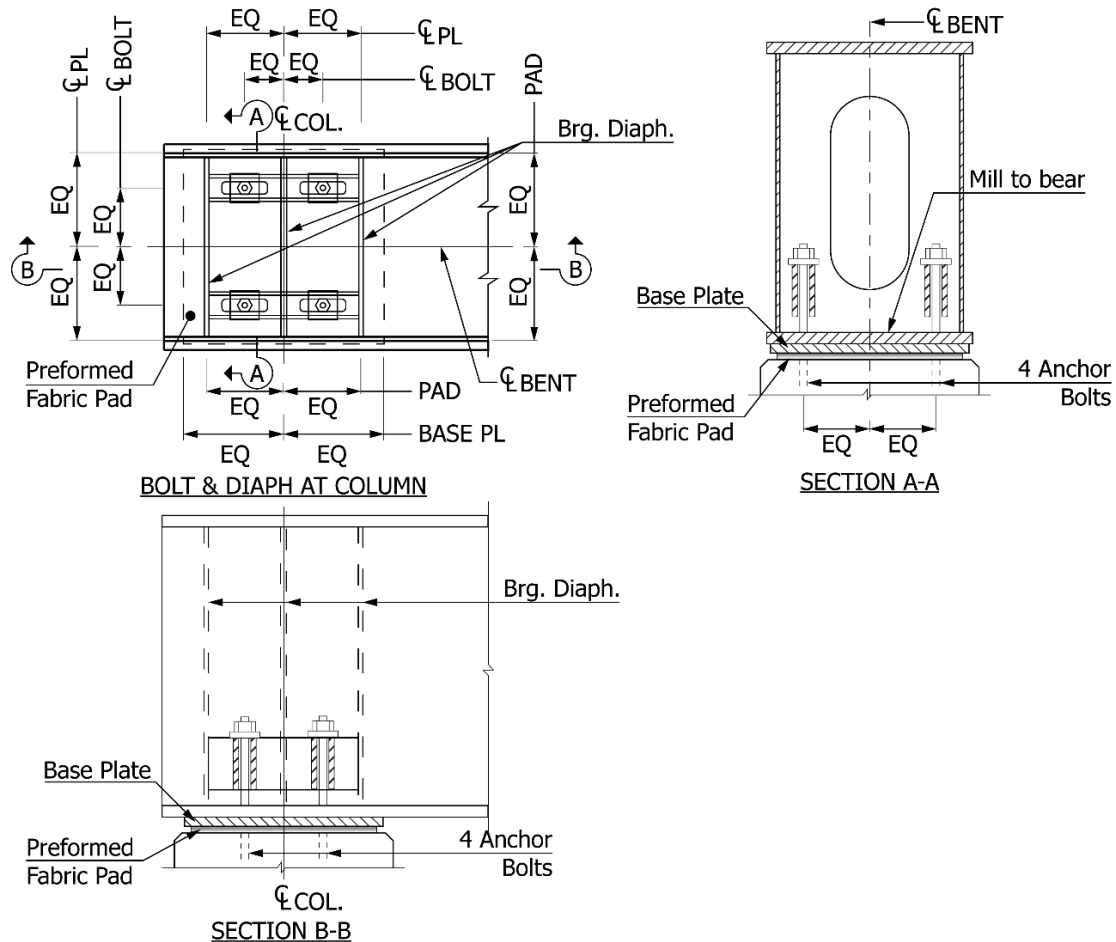


Figure 3.5: Typical support details for the steel box caps (adapted from TxDOT typical details, not to scale)

### 3.1.2. Geometry and Proportions

Based on the straddle cap designs examined in the bridge survey, a span-to-depth ratio,  $L/D$ , of approximately 12 is generally used, although more slender caps with span-to-depth ratios of up to 16 were identified. Regarding cross-section proportions, the depth-to-width ratio,  $D/W$ , normally ranges between 1.0 and 1.9. Values of the plate thicknesses vary from 1/2 in. to 7/8 in. for the web plates and from 3/4 in. to 3 in. for the flanges. Web slenderness values usually range between approximately 108 and 130, while the flange slenderness values range between approximately 24 and 48. For straddle caps fabricated with Grade 50 Steel, these typical webs would be classified as slender, and compression

flanges would be non-compact or slender (AASHTO 2020). These typical dimensions are illustrated in Figure 3.6. The web thickness and depth are generally kept constant along the entire length of the box beam, whereas the flange thicknesses are varied to accommodate the flexural demands.

All interior diaphragms have access holes for inspection and maintenance purposes with minimum dimensions of 18 in. wide by 36 in. tall (Figure 3.6). A common practice is to make the top and bottom of the diaphragms with a 24-in. diameter circular contour.

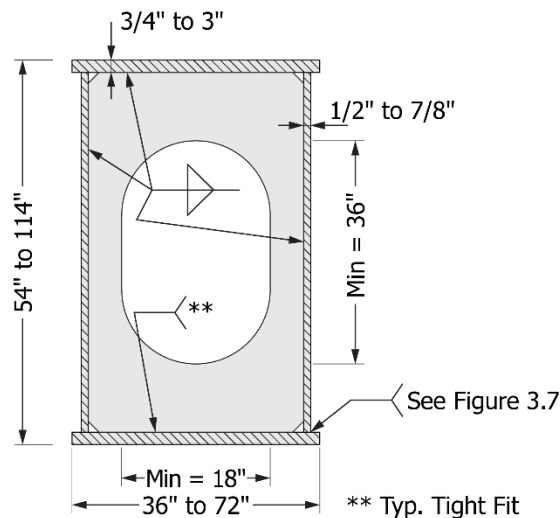


Figure 3.6: Typical cross-section dimensions for steel box straddle caps based on the bridge survey

### 3.1.3. Fabrication and Welding

The typical fabrication sequence of box beams is to attach internal diaphragms to the compression flange, followed by the attachment of the webs to that flange. Finally, the tension flange is welded to the box girder. In general, interior diaphragms are only welded on three sides with a tight-fit condition to the tension flange.

The preferred practice for welding the box corners (AASHTO/NSBA 2020) is to use double fillet welds for one flange and partial joint penetration (PJP) or complete joint penetration (CJP) welds with backing bars for the second flange, as shown in Figure 3.7-A and B. Double or single fillet welds at each of the four corners are also accepted (Figure 3.7-C and D).

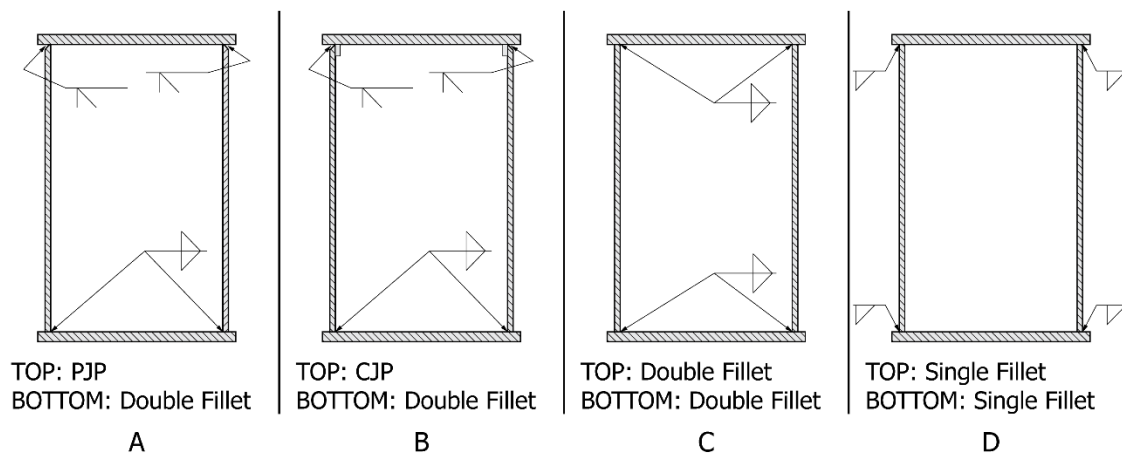


Figure 3.7: Typical box corner welds. Adapted from AASHTO/NSBA (2020).

### 3.1.4. Target Load for Redundancy Evaluation

The Texas bridges reviewed from the bridge survey were analyzed using commercial bridge engineering software to determine the demands on the box straddle caps for the load combinations specified in the AASHTO LRFD Design Specifications (2020). Moreover, the Redundancy load combinations presented in the AASHTO Guide for SRMs (2018) and the Extreme Event III load combination specified in the TxDOT Bridge Design Manual LRFD (2020) were also considered.

This task aimed at determining the demands a steel box straddle cap is likely to sustain in the faulted state to be classified as non-Fracture Critical as a proportion of the maximum demands that typically govern the design. Although this ratio tends to vary case-by-case, it provided a basis for sizing the test specimens for the faulted condition, as described in Chapter 4.

Based on this study, it was found that the demands in the faulted condition generally correspond to approximately 70% of the nominal capacity of the undamaged/intact straddle cap. This 70% proportion was initially considered as the target capacity in the faulted state for all specimens tested, as described in Chapter 5.

## 3.2. Design Approaches for Internal Redundancy

Work was conducted in collaboration with the TxDOT Project Monitoring Committee (PMC) and the Industry Advisory Group (IAG) to develop two design concepts that provide internal redundancy to steel box straddle caps. The two concepts were designated Design Concepts A and B and are described in the following subsections.

### 3.2.1. Design Concept A

In Design Concept A, illustrated in Figure 3.8, internal redundancy is achieved by adding high-strength bars near the bottom flange as a secondary tension element that is engaged if a crack propagates through the bottom flange and the tension portion of the webs. The bars are anchored at several points along the box girder at points corresponding with the internal diaphragms to transfer the loads back to the undamaged/intact cross-section components and allow the cap to perform its function in a faulted state. Furthermore, the added high-strength bars are intended to arrest the crack as it propagates, limiting the damage to the section so that a larger portion of the webs remains undamaged/intact.

These high-strength bars are typically used in post-tensioning applications and are referred to as PT bars herein. However, while most slack would be removed, the bars are not intended to be tensioned to a level that results in the bar sharing in live load-induced stresses. Providing significant tension is likely to create fatigue concerns in the bars and anchorages from live-load-induced forces.

This design concept is primarily intended for retrofitting existing steel box straddle caps, but the potential implementation for new construction was also considered. The test specimen used to study this design concept was designated as Specimen A, and its details and dimensions are outlined in Section 4.1.

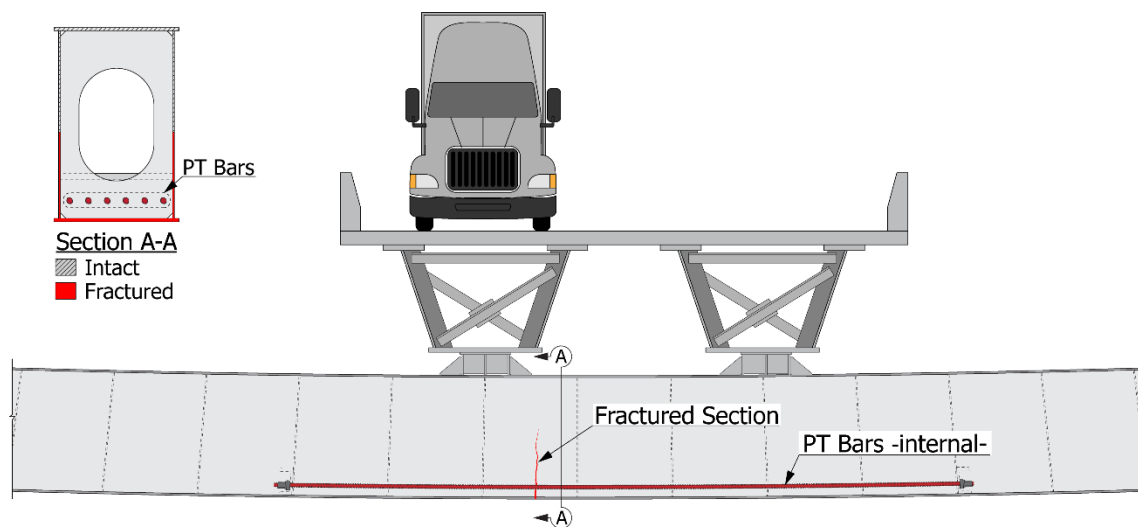


Figure 3.8: Design Concept A: steel box straddle cap reinforced with PT bars

### 3.2.2. Design Concept B

Bolted connections provide internal redundancy for Design Concept B by introducing cross-boundary fracture separation between the components in tension. Although a fully-bolted design was initially considered, the aesthetics and practicality of such a design were deemed inadequate. However, by only bolting the bottom flange, the fabrication process of the box did not differ significantly from a fully-welded box and was favored by the Industry Advisory Group and TxDOT Project Monitoring Committee.

In this design approach, a flange connection plate is welded perpendicular to the bottom edge of each web and then bolted to the bottom flange plate, as shown in Figure 3.9. Besides acting as the connecting element between the bottom flange plate and the webs, the flange connection plates provide additional flexural strength if the bottom flange is fractured, acting as a pair of tension flanges of reduced dimensions. The connections between the top flange, the webs, and the internal diaphragms remain welded as in conventional all-welded box beams.

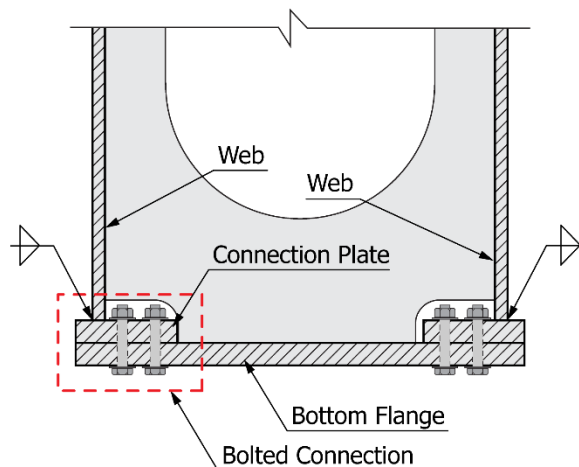


Figure 3.9: Design Concept B: bolted connections between the tension elements

With this design philosophy, a crack can initiate and propagate in any component but can not propagate to an adjacent plate element. For example, a fatigue crack that initiates in the bottom flange can only propagate and fracture that plate, leaving the remaining components undamaged/intact. This situation is illustrated in Figure 3.10. The cross-boundary fracture separation between the tension components leaves the top flange, webs, and connection plates undamaged/intact. These remaining undamaged/intact components can be designed to provide the load capacity required in the faulted state.

Conversely, fatigue cracks that initiate in the webs, typically from lateral brackets welded to them to support the longitudinal girders, will not propagate to the bottom flange or the other web. That same web crack is not likely to propagate across the top flange since that plate is entirely in compression. Therefore, the remaining undamaged/intact components can be designed to provide the load capacity required in the faulted state.

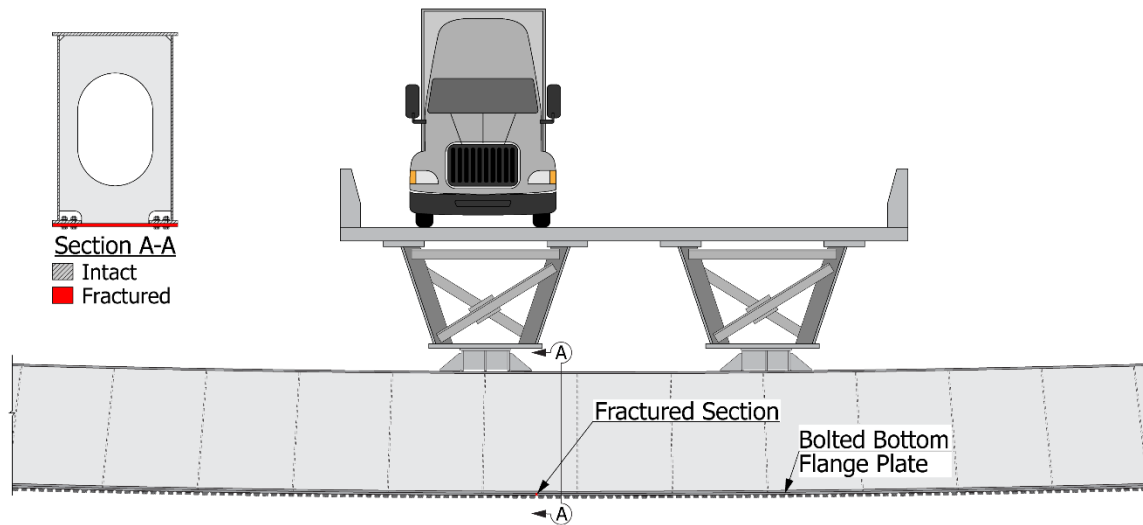


Figure 3.10: Design Concept B: steel box straddle cap with cross-boundary separation limits the extension of the cracks only to the bottom flange plate

Design Concept B is mainly intended for newly constructed steel box straddle caps. However, test results for these specimens are also expected to provide insights into the behavior that would likely result if a bolted plate was added to the bottom flange of an existing fully welded box section.

### 3.3. Summary

---

This chapter has summarized the key characteristics of steel box straddle caps in Texas. This summary included typical span lengths, support conditions, box dimensions, plate thicknesses, diaphragm details, and welding and fabrication details. This information was developed by reviewing design documents for nineteen existing steel box straddle caps and provided the basis for developing design concepts for internal redundancy and the design of the experimental program for this research. In addition, existing standards and design guides for internal redundancy were also reviewed to develop an estimate of the required load-carrying capacity of a steel box straddle cap in the faulted condition. This review indicated that the required capacity of a steel box straddle cap in the faulted condition is approximately 70 percent of the nominal capacity of the undamaged/intact member. Although the actual required capacity in the faulted state will vary on a case-by-case basis, the 70-percent value provides a reasonable estimate for evaluating steel box straddle cap specimens tested in the faulted condition in this research program.

Working with an Industry Advisory Group and TxDOT design, construction, and inspection personnel, two design concepts were developed to investigate the ability to provide internal redundancy for steel box straddle caps. These are referred to as Design Concepts A and B. Design Concept A involves adding high-strength bars near the bottom flange as a secondary tension element that would be engaged if a crack propagates through the bottom flange and a portion of the webs. Design Concept B involves using a bolted bottom flange detail that introduces cross-boundary fracture separation between the components in tension. Design Concept A is intended primarily for retrofitting existing steel box straddle caps but could potentially also be used for new designs. Similarly, Design Concept B is intended primarily for new construction but could also potentially be used as a retrofit for existing steel box straddle caps.

The next chapter describes the development of an experimental program to evaluate the two design concepts described above, including a detailed description of the test specimens and the test setup.



## Chapter 4. Experimental Program

This chapter describes the experimental program for the testing of full-scale steel box girders conducted at the Ferguson Structural Engineering Laboratory (FSEL) to evaluate the effectiveness of the proposed internally redundant design concepts. First, Section 4.1 outlines the design and fabrication of the test specimens. Then, preliminary analyses of the specimens are presented in Section 4.2. Next, the testing protocol followed is outlined in Section 4.3, while the test setup and instrumentation plan are detailed in Sections 4.4 and 4.5, respectively.

### 4.1. Design and Fabrication of Test Specimens

---

The fatigue and fracture behavior of steel bridges is highly influenced by factors such as fabrication practices, welding quality, plate thicknesses, and residual stresses. The influence of these factors on fatigue and fracture behavior may not be properly represented in reduced-scale test specimens. For that reason, it was decided to use large-scale specimens for the experimental phase of the project.

#### 4.1.1. Design of Specimens

The proportions and dimensions of the specimens were selected to be representative of steel box caps commonly designed in Texas based on the information gathered from the bridge survey (Section 3.1). The global dimensions of the test specimens were determined based on space and the testing equipment available at the Ferguson Structural Engineering Laboratory.

To maximize the number of tested specimens, specimens were constructed in three segments, as shown in Figure 4.1. The central segment was the actual test specimen, which had internal redundancy provided according to the approaches described in Section 3.2. The cracks were initiated and the fracture was produced in this central segment, while the two end segments were reusable and were designed to accommodate the geometry of the different test segments and remain in the elastic range during all the test stages.

The three 19.83-ft-long segments were connected with slip-critical bolted splices using ASTM F3125 Grade A490 1-in. diameter bolts. Once assembled, the total length of a full-scale specimen was 59.5 ft. With these dimensions, the test specimen falls at the lower bound of the typical span length range of steel box straddle caps used in Texas based on the survey described in Section 3.1.2.

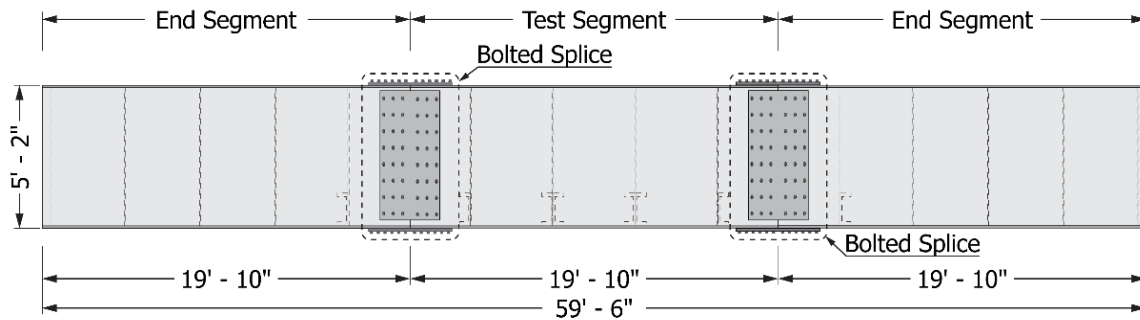


Figure 4.1: Full-scale test specimen (not to scale)

For the sizing of the specimens, a typical span-to-depth ratio,  $L/D$ , of 12 was selected, resulting in a web depth of 60 in. Moreover, a depth-to-width ratio,  $D/W$ , equal to 1.5 was chosen, producing a flange width of 40 in.

Considering the typical plate thicknesses used in practice, material availability, and the capacity of the lifting and testing equipment available at FSEL, the thickness of the webs and the flanges for the test segments were set at 5/8 in. and 1 in., respectively. The web thicknesses were maintained at 5/8 in. for the reusable end segments, but the flange thicknesses were increased to 1-1/4 in. to ensure the elastic behavior of these segments during all test stages. All plates were made of ASTM A572 Grade 50 Steel, with a minimum specified yield stress of 50 ksi. The actual material properties of the plates are presented in Section 4.1.3.

The design of the test specimens was based on the applicable sections of the 8<sup>th</sup> Edition of the AASHTO LRFD Bridge Design Specifications (2018), which was the latest version at the time the specimens were designed. In addition, the Proposed LRFD Specifications for Noncomposite Steel Box-Section Members (FHWA 2019) were followed, which were later incorporated into the 9<sup>th</sup> Edition of the AASHTO LRFD Bridge Design Specifications (2020).

The following subsections describe each test segment designed according to the approaches for internal redundancy explained in Section 3.2. Shop drawings for the test and end segments are provided in Appendix A.

#### 4.1.1.1. Test Specimen A

Test Specimen A is a conventional welded box section that allows the installation of high-strength post-tensioning bars (PT bars) near the tension flange, per Design Concept A (Section 3.2.1). Details and dimensions of this test specimen are shown in Figure 4.2.

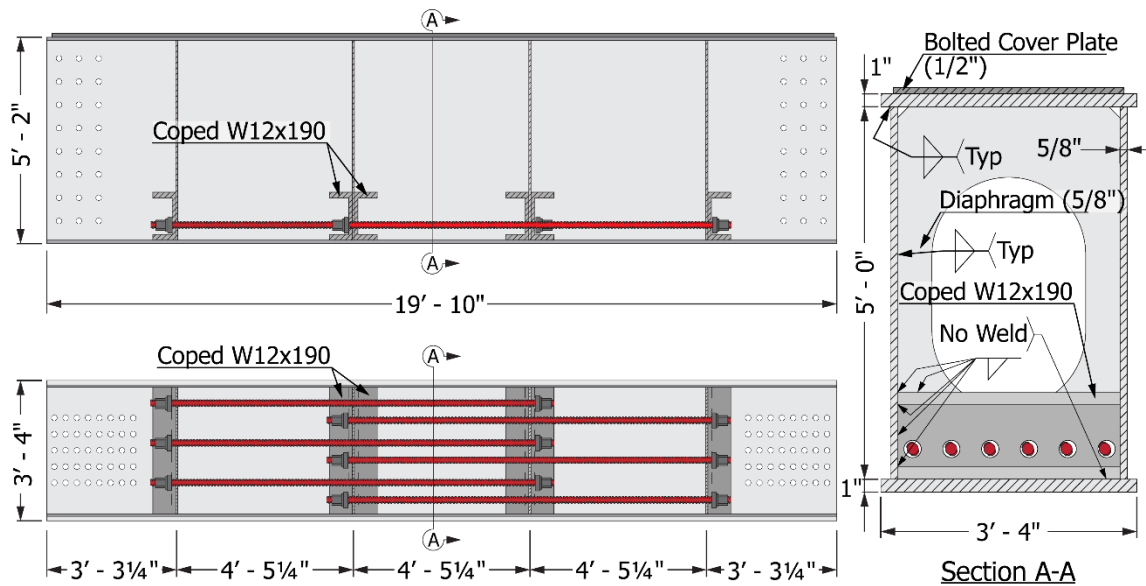


Figure 4.2: Specimen A details

Channel sections fabricated from W12×190 shapes with both flanges coped on one side of the web were welded at each side of the internal diaphragms to anchor the post-tensioning bars in different possible arrangements:

- One possibility, labeled in Figure 4.3-A as “Continuous Arrangement,” consists of installing the bars crossing the entire length of the test specimen and anchoring them at the end segments.
- Another option is to use shorter bars that only span two spaces between intermediate diaphragms, depicted in Figure 4.3-B as “Staggered Arrangement.”

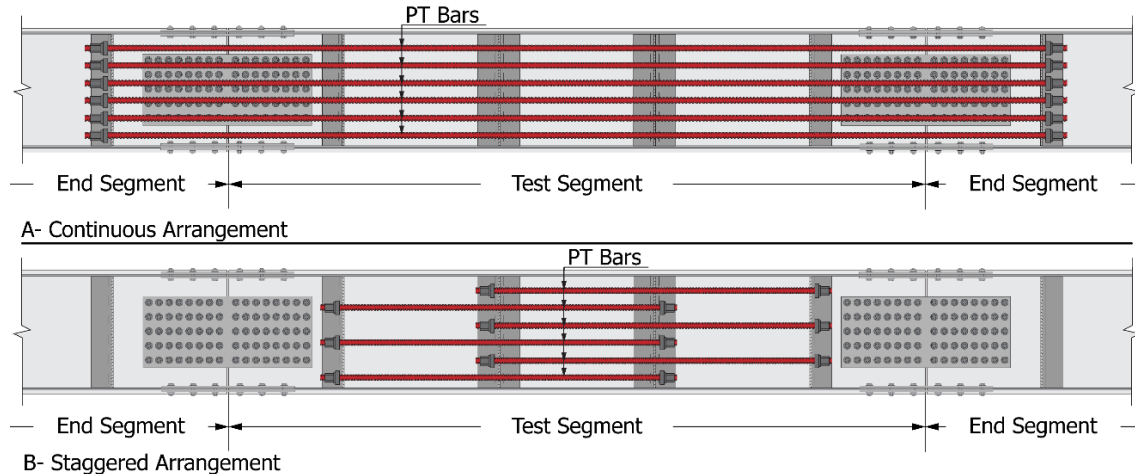


Figure 4.3: Specimen A: possible arrangements of the PT bars

Six 1-1/4-in. diameter ASTM A722 Grade 150 post-tensioning bars were installed in Specimen A. Preliminary finite element analyses (summarized in Section 4.2) showed that the staggered arrangement performed better than the continuous option, as it would provide a higher stiffness following the fracture of the bottom flange plate and was thus the chosen arrangement for the test of Specimen A. Variations in the arrangement of the bars, as well as their diameter, were studied analytically through finite element models. The results of these studies are presented in Chapter 6.

The preliminary analysis of this test specimen also indicated that local buckling of the top flange was possible in the undamaged/intact condition. Hence, Specimen A was retrofitted by bolting a 37 in.  $\times$  1/2 in. cover plate to the top flange of the test segment. With the addition of the cover plate, the top flange became compact, and the section could reach its plastic moment capacity before local buckling occurred.

The sectional capacities of Specimen A in the undamaged/intact and assumed faulted conditions are summarized in Table 4.1. These sectional capacities included the contribution of the cover plate and were computed based on an elastic perfectly plastic material with a yield stress equal to the minimum specified yield stress of 50 ksi. For the undamaged/intact condition, the PT bars were not considered to contribute to the flexural capacity of the section, as shown in Figure 4.4. In the faulted condition, it was assumed that the bottom flange and half of the depth of the webs were fractured, while the PT bars were considered fully effective (Figure 4.4). In this assumed faulted condition, the sectional capacity was limited by the yielding of the lower edges of the webs (i.e., at the crack tips). Beyond this point, the sectional analysis shows that high strains are required at the web edges to satisfy equilibrium, risking the possibility of rupturing them. Hence, although the section could provide more flexural strength, the rupture was deemed undesirable as a limit state, and the capacity was capped at the first yield of the section.

It should be noted that, with the original design (i.e., without the cover plate), the estimated capacity of this specimen in the faulted condition was approximately 70% of the nominal capacity of the undamaged/intact box section, in agreement with the premise described in Section 3.1.4. However, with the addition of the cover plate, the capacity of the undamaged/intact section increased proportionally more than the capacity in the faulted state. Hence, the target ratio is lower than the initial 70-percent estimation, as shown in Table 4.1.

**Table 4.1: Sectional capacity of Specimen A (undamaged/intact and faulted conditions)**

	Condition		$M_{Faulted}/M_{Intact}$ (%)
	Undamaged/ intact	Faulted	
Yield Moment, $M_y$ <sup>1</sup>	13,730 kip·ft	4,903 kip·ft	35.7 %
Plastic Moment, $M_p$ <sup>2</sup>	17,003 kip·ft	7,521 kip·ft	44.2 %
Nominal Moment Capacity, $M_n$ <sup>3</sup>	17,003 kip·ft	7,521 kip·ft	44.2 %

<sup>1</sup> $M_y = S_{min} \cdot F_y$

<sup>2</sup> $M_p = Z \cdot F_y$

<sup>3</sup> $M_n$  = controlling moment capacity of the section considering yielding, local buckling, and LTB.

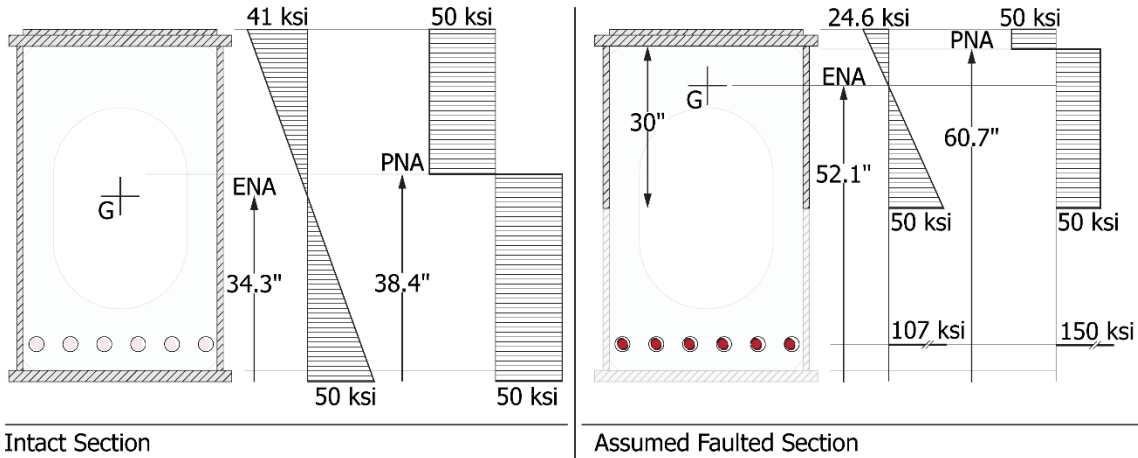


**Figure 4.4: Specimen A: sectional analysis of undamaged/intact and faulted sections**

#### 4.1.1.2. Specimens B1 and B2

In line with the premise of Design Concept B, Specimens B1 and B2 were designed to investigate the effectiveness of the cross-boundary separation as an internal redundancy approach.

The bolted connection between the flange connection plates and the bottom flange plate was sized to provide enough shear capacity to develop the plastic moment of the undamaged/intact cross-section. For this purpose, ASTM F3125 Grade A490 1-in. diameter bolts were used for slip-critical bolted connections with Class B surface conditions. The stitch bolt spacing requirements specified in Articles 6.13.2.6.2 and

6.13.2.6.3 of the AASHTO LRFD Specifications (2022) were also considered in the design of the bolted connection.

The Guide Specifications for IRMs (AASHTO 2018-1) requires that the area of a single tension component flange shall not exceed 60% of the total area of tension components. This limit was derived from the experiments conducted by Hebdon et al. (2015), in which it was found that specimens with a higher ratio experienced a substantial release of energy that may fracture the immediately adjacent tension components.

To assess this limit, the flange connection plates of Specimen B1 were kept at the minimum width required to provide adequate bolt spacing. These dimensions resulted in the bottom flange plate representing 69% of the total area of tension components (see Figure 4.6 for dimensions and details of Specimen B1). The preliminary finite element models also suggested the potential for compression flange buckling in Specimen B1. Hence, as with Specimen A, a cover plate was added to the top flange. With these final dimensions, the theoretical sectional capacity of Specimen B1 in the faulted condition is approximately 70 percent of the undamaged/intact section (Figure 4.5 and Table 4.2).

**Table 4.2: Sectional capacity of Specimen B1 (undamaged/intact and faulted conditions)**

	Condition		$M_{Faulted}/M_{Intact}$ (%)
	Undamaged/ intact	Faulted	
Yield Moment, $M_y$ <sup>1</sup>	17,175 kip·ft	8,730 kip·ft	50.8 %
Plastic Moment, $M_p$ <sup>2</sup>	19,351 kip·ft	12,786 kip·ft	66.1 %
Nominal Moment Capacity, $M_n$ <sup>3</sup>	18,181 kip·ft	12,786 kip·ft	70.3 %

$$^1M_y = S_{min} \cdot F_y$$

$$^2M_p = Z \cdot F_y$$

$$^3M_n = \text{controlling moment capacity of the section considering yielding, local buckling, and LTB.}$$

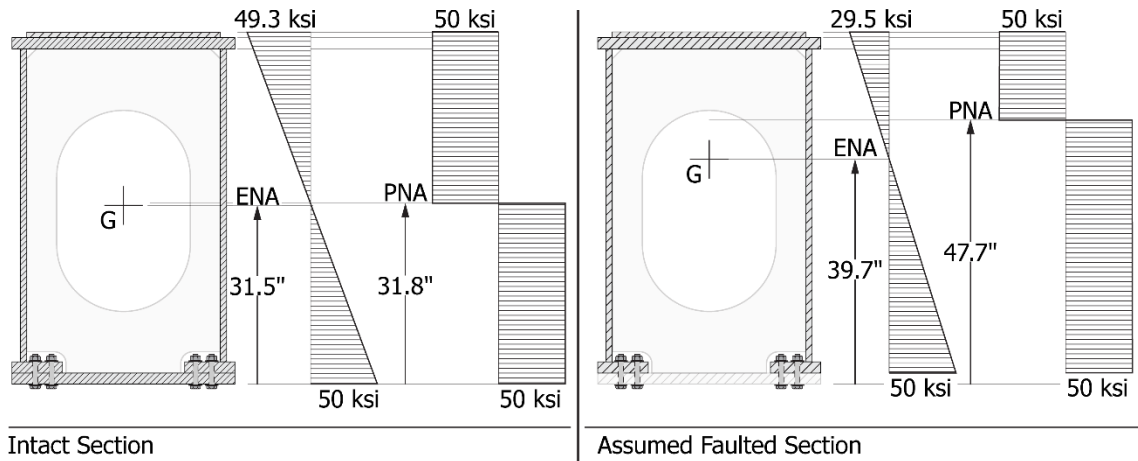


Figure 4.5: Specimen B1: sectional analysis of undamaged/intact and faulted sections

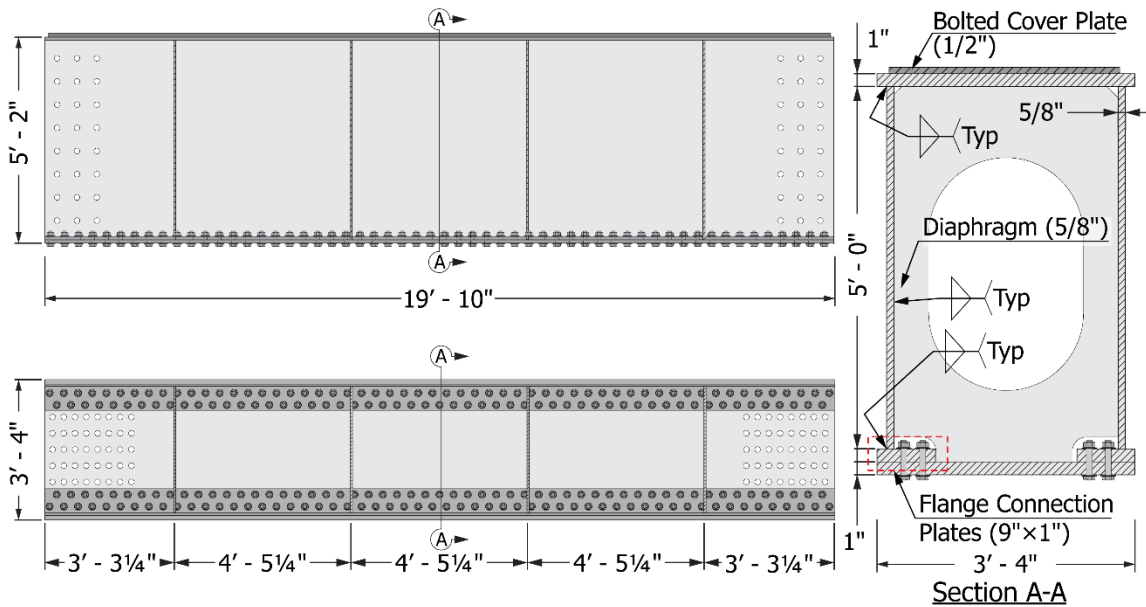


Figure 4.6: Specimen B1 details

For Specimen B2, the flange connection plates were made wider, providing a higher capacity and stiffer response in the faulted condition while meeting the requirements of the Guide Specification for IRMs (AASHTO 2018-1), as shown in Table 4.4. Also, a thicker top flange and thicker web plates were necessary to obtain a compact section in the assumed faulted condition. The details of Specimen B2 are depicted in Figure 4.7, and the sectional capacities of Specimen B2 in the undamaged/intact and assumed faulted conditions are summarized in Table 4.3 and illustrated in Figure 4.8.

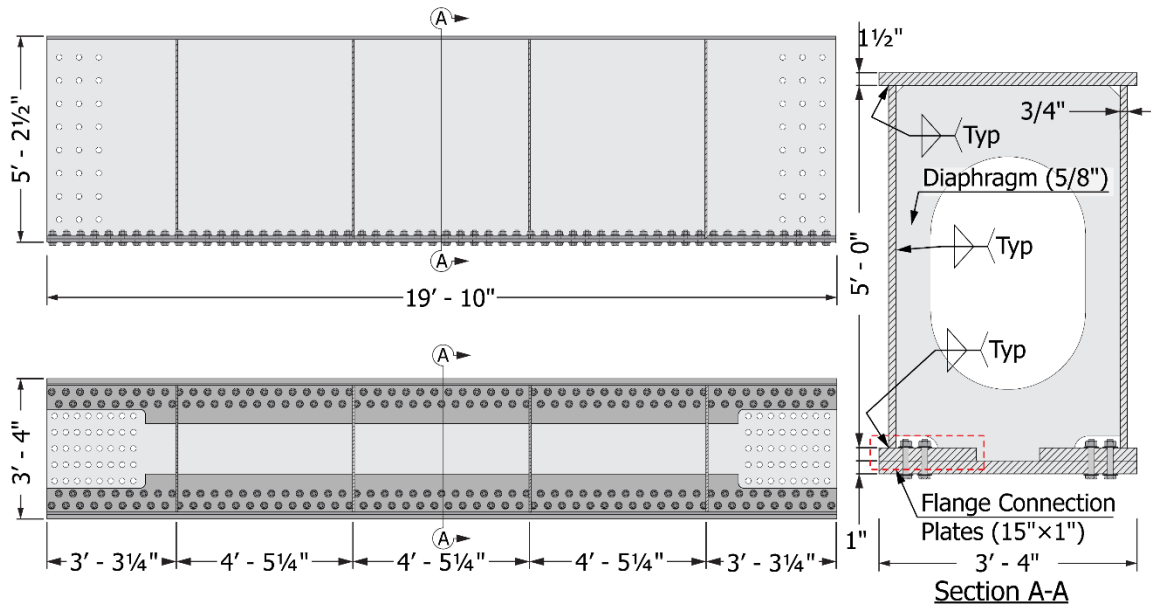


Figure 4.7: Specimen B2 details

Table 4.3: Sectional capacity of Specimen B2 (undamaged/intact and faulted conditions)

	Condition		$M_{Faulted}/M_{Intact}$ (%)
	Undamaged/ intact	Faulted	
Yield Moment, $M_y$ <sup>1</sup>	18,668 kip·ft	12,034 kip·ft	64.4 %
Plastic Moment, $M_p$ <sup>2</sup>	21,849 kip·ft	16,127 kip·ft	73.8 %
Nominal Moment Capacity, $M_n$ <sup>3</sup>	20,787 kip·ft	16,127 kip·ft	77.5 %

<sup>1</sup> $M_y = S_{min} \cdot F_y$

<sup>2</sup> $M_p = Z \cdot F_y$

<sup>3</sup> $M_n$  = controlling moment capacity of the section considering yielding, local buckling, and LTB.



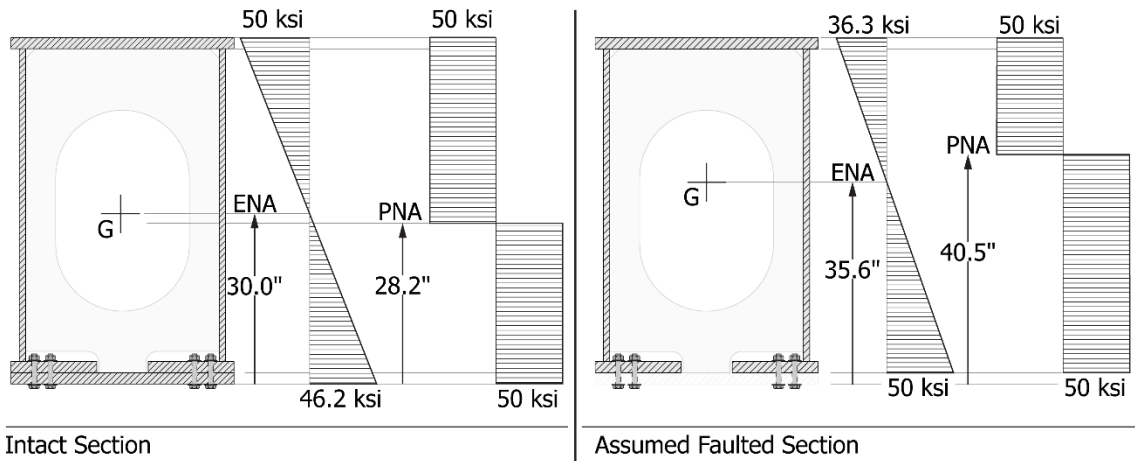


Figure 4.8: Specimen B2: sectional analysis of undamaged/intact and faulted sections

Table 4.4: Ratios of tension components area to total tension area for Specimens B1 and B2

	Specimen B1		Specimen B2	
Bottom Flange	40" × 1"	40 in. <sup>2</sup>	40" × 1"	40 in. <sup>2</sup>
Flange Con Plates (each)	9" × 1"	9 in. <sup>2</sup>	15" × 1"	15 in. <sup>2</sup>
Total Area	58 in. <sup>2</sup>		70 in. <sup>2</sup>	
Bottom Flange Ratio	<b>69.0 %<sup>*1</sup></b>		57.0 %	
Flange Connection Plate	15.5 %		21.5 %	
Ratio (each)				

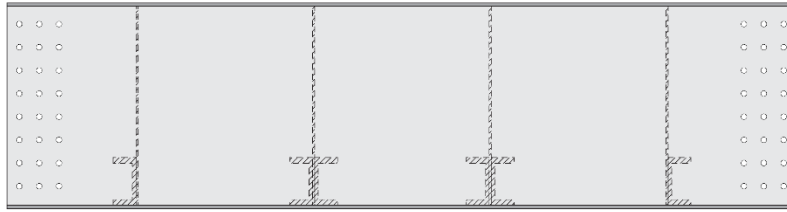
<sup>\*1</sup> Violates AASHTO Guide Specification for IRMs (2018-1)

#### **4.1.1.3. Baseline Specimen**

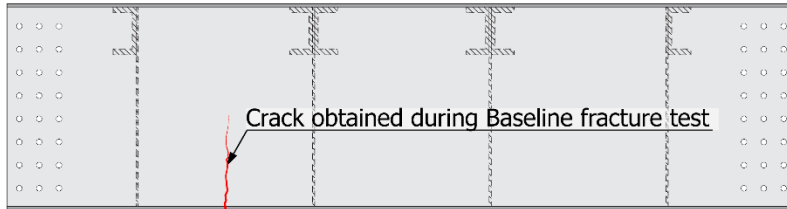
Investigating the fracture response of a conventional all-welded box section (i.e., without internal redundancy) was also of interest. Testing such a specimen was intended to demonstrate the effectiveness of the test protocol in producing a brittle fracture and provide valuable information regarding the crack propagation in a Fracture Critical steel box cap. Furthermore, the response of this specimen would provide a benchmark to which the performance of the proposed internally redundant specimens would be compared.

Instead of having another specimen fabricated, Specimen A was used for this task. Therefore, this specimen was tested in the sequence illustrated in Figure 4.9:

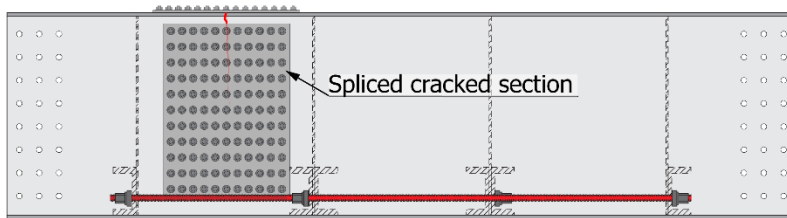
1. Specimen A in its original orientation, with the anchor points for the PT bars at the bottom, before testing.
2. The specimen was flipped upside-down and tested without the PT bars. This test is referred to as the Baseline Specimen test.
3. Once the Baseline test had been completed, the specimen was flipped back to its original orientation. The fractured flange (which in this final orientation was in compression) and the fractured webs were spliced while the tension flange (at the bottom) was undamaged/intact. The PT bars were installed, and the specimen was tested again. This test is referred to as the test of Specimen A.



1. Specimen A, original orientation



2. Specimen A, flipped for Baseline test (shown as fractured)



3. Specimen A flipped back to original orientation after Baseline test (repaired)

Figure 4.9: Specimen A: testing sequence for Baseline Specimen

#### 4.1.2. Specimen Fabrication and Assembly

W&W AFCO Steel fabricated all the test segments in their San Angelo location according to the applicable requirements of the AASHTO/AWS Fracture Control Plan (AASHTO/AWS 2015). Some stages of the fabrication process are shown in Figure 4.10: (A) the welding of the top flange to the webs using the internal diaphragms to maintain the shape of the box; (B) the section flipped on one side to facilitate the welding of the internal diaphragms and stiffeners; (C) the welding of the channel sections on Specimen A to anchor the PT bars; (D) segments ready to weld the bottom flange plates; and (E) bottom flange plate bolted to the flange connection plates for -Specimen B1- ready to be welded to the upper portion of the section.



Figure 4.10: Fabrication of test segments at W&W AFCO Steel, San Angelo. Photos courtesy of Daniel Liendo.

The detail shown in Figure 4.10(E) demonstrates how adding the bolted connection at the bottom flange of a box section can be addressed to maintain the same fabrication sequence as a conventional all-welded box section. Once the bottom flange plate is connected to the flange connection plates, the entire assembly can be welded to the webs.

The segments were delivered to FSEL (Figure 4.11) at the end of the Summer of 2020. The assembly process comprised the following steps:

1. The two end segments and the test segment were placed on timbers and fitted longitudinally (Figure 4.12-A)
2. The splice plates were aligned using drift pins, and the bolts were waxed and installed in a hand-tight condition. Once all bolts were in place, the final alignment of the three segments was made, and the bolts were tightened using impact wrenches and an electronic turn-of-nut wrench to provide the required pretension for the slip-critical condition (Figure 4.12-B).
3. Finally, the assembled specimen was picked up with the cranes (Figure 4.12-C) and placed inside the test setup (Figure 4.13).

The procedure outlined in points 1 through 3 was repeated for each test specimen.



Figure 4.11: Delivery of test segments at FSEL: (A) and (B) unloading from the truck bed, and (C) and (D) parking of the test segments.





Figure 4.12: Test specimen assembly sequence: (A) fitting of the North end segment to the test segment; (B) tightening of bolted splices; and (C) lifting of the assembled test specimen.



*Figure 4.13: Assembled test specimen placed in the test setup*

#### **4.1.3. Material Characterization**

Several material tests were conducted to identify the properties of the components of the specimens. The results of tension tests performed on samples from the different components of the test specimens are presented in Table 4.5. The results obtained from these tests were used to validate the FE models presented in Sections 6.2.1 and 6.3.1

Knowing the fracture properties of the material was essential to determine the target temperature for the fracture tests (described in Section 4.3.1). Therefore, samples were taken from each test specimen from the vicinity of the fractured sections to conduct Charpy V-Notch (CVN) tests and identify the lower-shelf temperature region of the tension components. The results of these tests are shown in Figure 4.18, Figure 4.19, and Figure 4.20.

Despite the differences between the components, particularly at higher temperatures, all the components exhibited average values of absorbed energy below 10 ft·lbs at a temperature of -120 °F, corresponding to a brittle behavior as indicated by the flat cleavage fracture surface shown in Figure 4.17.

**Table 4.5: Material properties of test specimens**

Specimen	Component	Yield Stress @ 0.2% Offset	Tensile Strength	Elongation in 2 in.	Reduction of Area
A/Baseline	Bottom Flange	60.8 ksi	78.7 ksi	33.4%	77.6%
A/Baseline	Top Flange	58.7 ksi	77.4 ksi	34.4%	77.1%
A/Baseline	Web	65.0 ksi	85.3 ksi	32.2%	72.6%
A	PT Bar	142.6 ksi	162.7 ksi	15.2%	44.2%
B1	Bottom Flange	56.4 ksi	83.8 ksi	31.4%	74.3%
B1	Top Flange	55.6 ksi	78.0 ksi	33.1%	77.7%
B1	FCP	60.6 ksi	82.4 ksi	32.6%	70.1%
B1	Web	66.5 ksi	93.0 ksi	28.9%	60.0%
B2	Bottom Flange	55.9 ksi	84.0 ksi	32.3%	68.4%
B2	Top Flange	55.1 ksi	82.4 ksi	31.1%	69.5%
B2	FCP	59.6 ksi	72.4 ksi	31.8%	74.3%
B2	Web	60.7 ksi	86.3 ksi	30.0%	70.4%

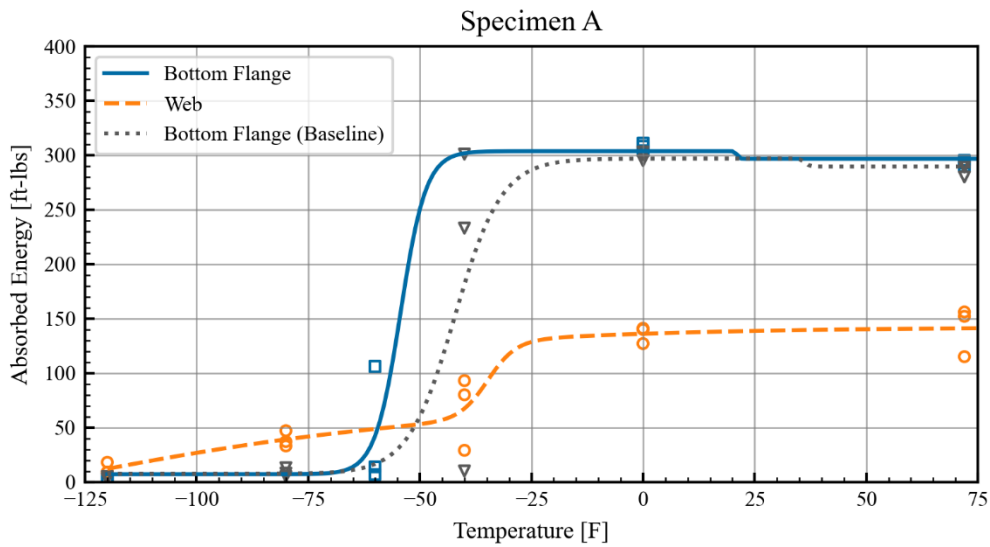


*Figure 4.14: Specimen A: CVN test results*



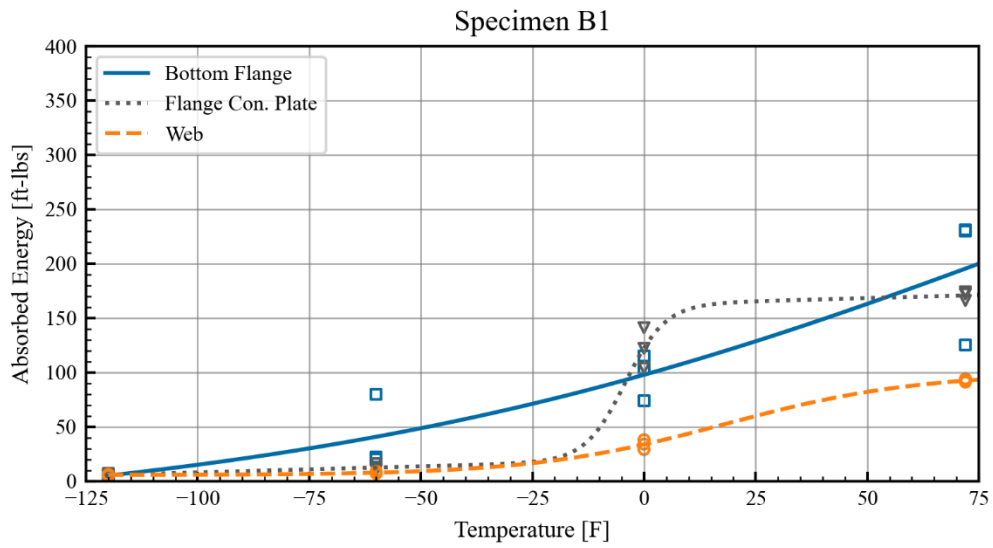


Figure 4.15: Specimen B1: CVN test results

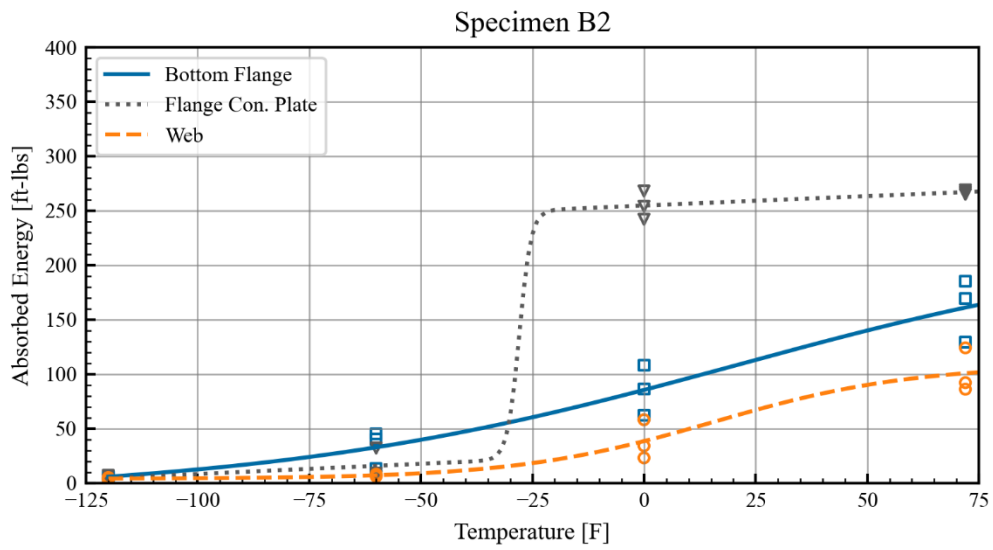


Figure 4.16: Specimen B2: CVN test results



Figure 4.17: CVN specimens tested at -120 °F (bottom flange plate)

## 4.2. Preliminary Analysis of Selected Design Concepts

Twelve finite element models (listed in Table 4.6) were analyzed using Abaqus version 2017 to study Specimen A and B1. The FE models were based on the original geometry of the specimens (i.e., without the cover plate).

One uncracked model and two models with different assumed crack lengths were investigated for each design concept. In each faulted model, the crack was created at the mid-span section by defining a seam crack. More details about using seam cracks in Abaqus are provided in Section 6.1.4.

For the Baseline Specimen and Specimen A, fixed crack lengths on the flange and the webs were specified (Figure 4.18). Previous research on bolted flexural members (Hebdon, et al. 2015) showed that a crack does not propagate between bolted plates. Therefore, for Design Concept B, the crack was assumed to arrest at the interface between the top face of the bottom flange and the bottom face of the flange connection plates (webs were considered undamaged/intact in all three models), as illustrated in Figure 4.19.

Table 4.6: Overview of the investigated FE models

ID	Design Concept	Redundancy Detail	Fixed crack length (in.)	
			Bottom Flange	Web (one side)
Base-f0w0	Baseline	None	0	0
Base-f20w10			20	10
Base-f40w20			40	20
Ar-f0w0	A	Continuous PT-bars	0	0
Ar-f20w10			20	10
Ar-f40w20			40	20
As-f0w0	A	Staggered PT-bars	0	0
As-f20w10			20	10
As-f40w20			40	20
B-f0w0	B1	Bolted plate	0	0
B-f20w0			20	0
B-f40w0			40	0

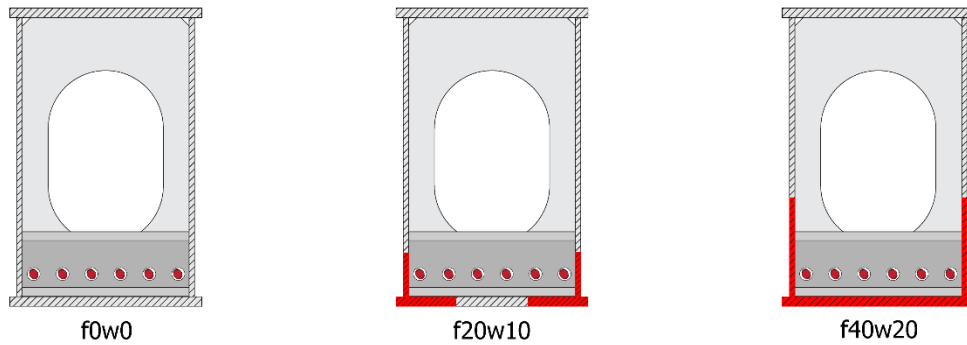


Figure 4.18: Specimen A and Baseline Specimen: crack lengths considered

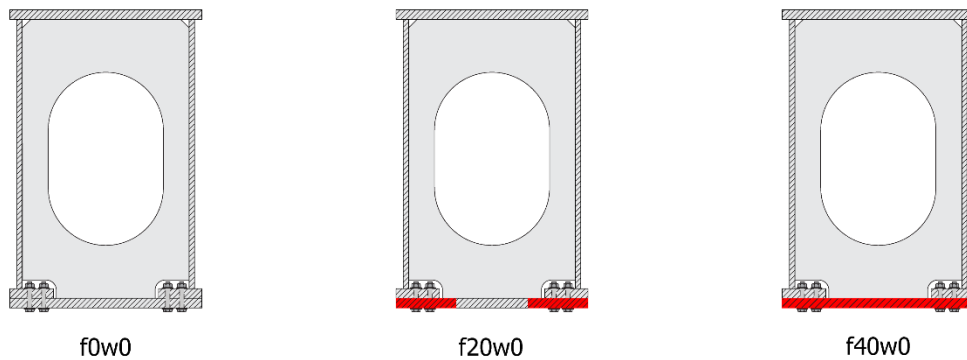


Figure 4.19: Specimen B1: crack sizes considered

Due to the large deformations expected during the analyses, nonlinear static analyses were performed using the Riks (arc-length) solution procedure. All models had identical end segments, boundary conditions, and applied loads, as shown in Figure 4.20. Half-symmetry was considered in the models to reduce the analysis time. Symmetry boundary conditions about the X-Y plane were defined at the surfaces highlighted in Figure 4.20. Independent parts were created for each segment and connected with tie constraints. The test segment of the Baseline specimen is depicted in Figure 4.21.

A mesh sensitivity analysis showed that meshing the central and end segments with 2-in. and 5-in. element sizes, respectively, provided satisfactory results and a high-quality mesh. The mesh was refined to prevent element distortion at particular locations, such as curved edges of the diaphragms. All the parts were meshed with hexahedral solid C3D8R elements. Four elements were used through the thickness of all plate elements to avoid unrealistic deformations and hourglassing (Dassault Systèmes Simulia Corp 2016).

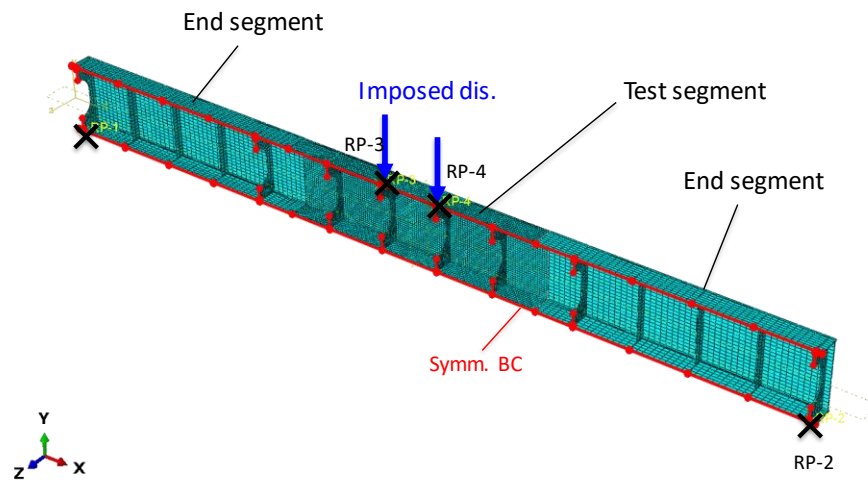


Figure 4.20: Baseline Specimen FE model: loads and boundary conditions

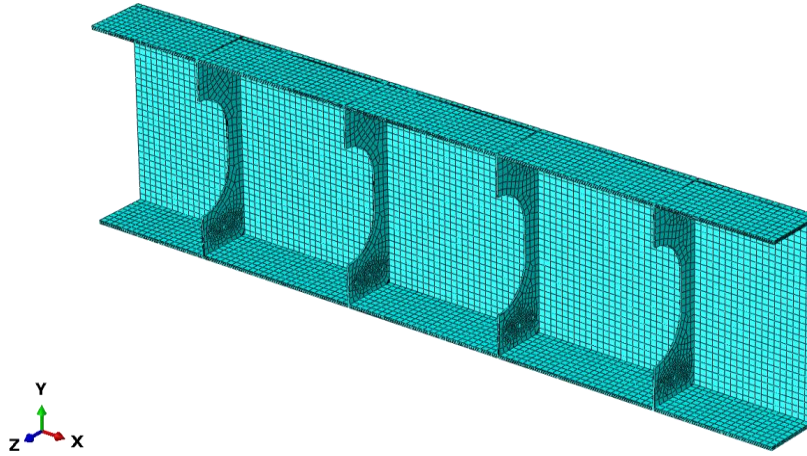


Figure 4.21: Test segment in FE models

All models were supported at two reference points at the ends, designated as RP-1 and RP-2. The nodes under the end diaphragms were coupled to RP-1 and RP-2, respectively, to simulate the supports. In addition, two reference points, RP-3 and RP-4, were defined at the loading points and coupled to the edges on the top flange located at the same cross-section. Equal vertical displacements were prescribed at RP-3 and RP-4 to load the model.

The material properties for these preliminary models consisted of an idealized elastic-plastic material for all segments, stiffeners, and diaphragms. Young's modulus was taken as 29,000 ksi, and the yield stress was set at 50 ksi.

Figure 4.22 shows the test segment corresponding to the Design Concept A models with PT bars that extend continuously through the test segment. Only two PT bars were included in the half models to provide the same amount of steel crossing the crack as in the models with a staggered layout of the PT bars. Each PT bar was modeled with one truss element, as is highlighted in Figure 4.22. Both ends of the truss element were coupled to the nodes corresponding to the holes on anchor points. The anchor sections were meshed with 1-in. C3D8R elements. The PT bars were assumed to be elastic-perfectly plastic, with a Young's modulus of 29,000 ksi and yield stress of 150 ksi.

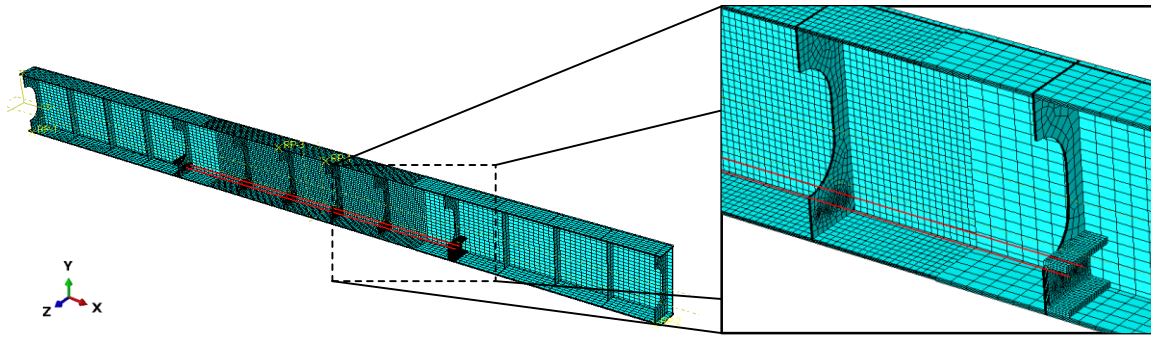


Figure 4.22: Specimen A: FE models with continuous PT bars

Figure 4.23 shows Design Concept A test segment models with a staggered PT bar arrangement. As in the previous models, each PT bar was simulated with one truss element, the ends of which were coupled to nodes corresponding to the holes in the anchor sections.

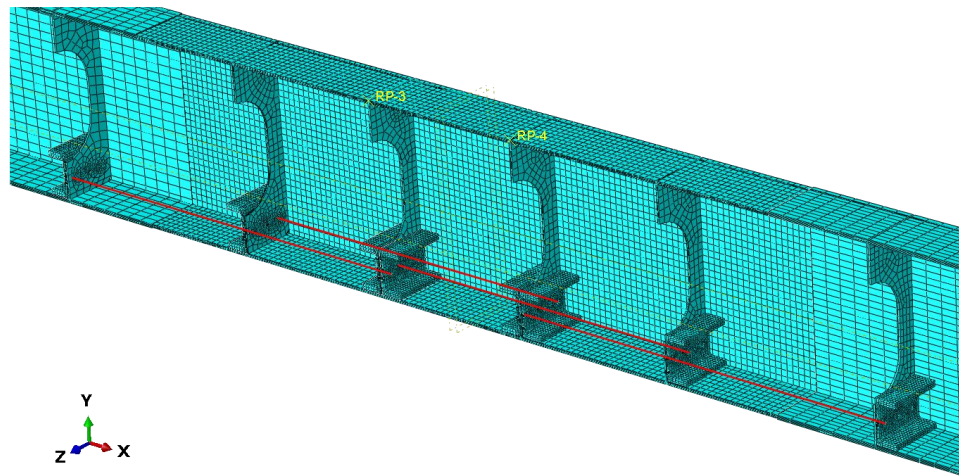


Figure 4.23: Specimen A: FE models with staggered PT bars

The FE model of Specimen B1 is shown in Figure 4.24, and Figure 4.25 shows the different parts created for the model. The half diaphragms, web, half top flange, and flange connection plate were connected with tie constraints defined at their intersections. Around each bolt hole, the nodes on the flange connection plate were tied to the nodes on the bottom flange to simulate the bolted connection. The top portion of the cross-section (top flange, web, and flange connection plate) and the bottom flange were partitioned in coincidence with each bolt hole to achieve a good quality mesh. The mesh around the holes is shown in Figure 4.24.



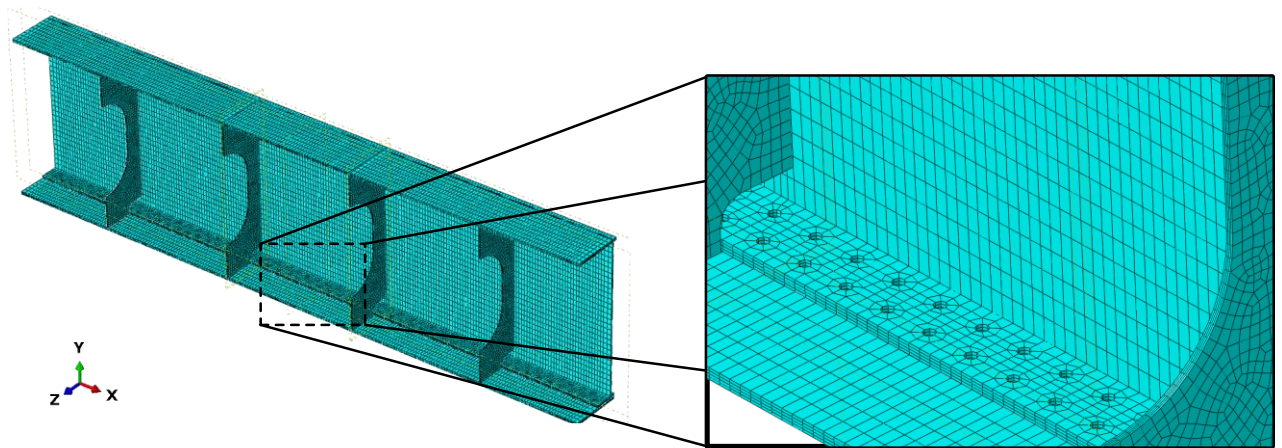


Figure 4.24: Specimen B1 FE model

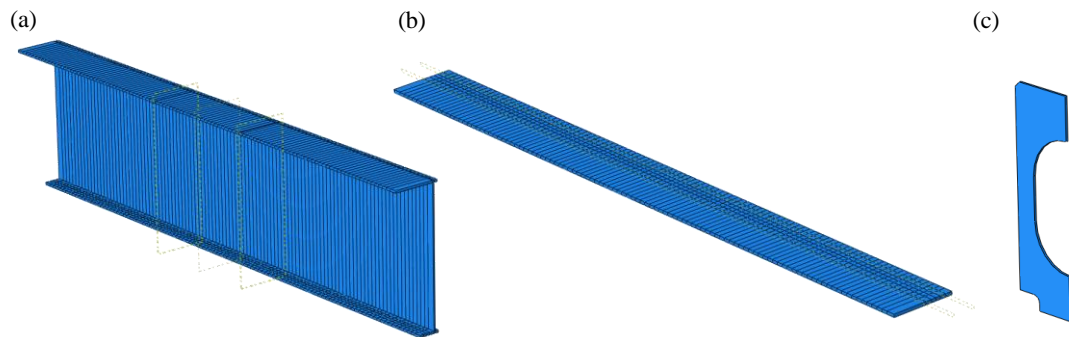


Figure 4.25: Specimen B1 FE model: parts created for the test segment (a) Upper cross-section; (b) bottom flange; and (c) diaphragm.

### 4.2.1. Results of Preliminary Analyses

Load-deflection curves for two different crack scenarios are shown in Figure 4.26 and Figure 4.27. In the cases displayed in Figure 4.26, the bottom flange is assumed to have a crack of 10 in. from each edge, corresponding to the case where one-half of the total width of the bottom flange is cracked. Therefore, the web crack length is defined at 10 in. from the intersection with the bottom flange (Figure 4.18-Center). The curves include a label “A” or “B” to depict the behavior of the two different concepts, with “A” representing the PT bar models and “B” representing the bolted bottom flange approach. As mentioned in Section 4.2, it was assumed that the crack could not propagate to the webs in Specimen B; therefore, the web crack is set at 0 in.

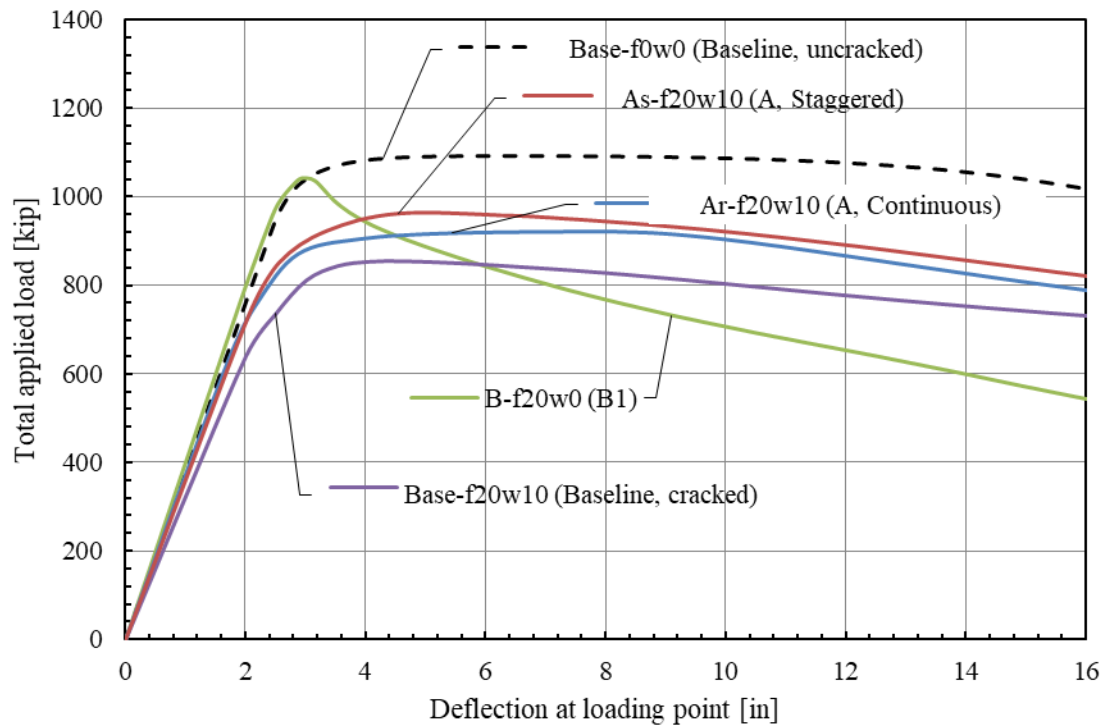


Figure 4.26: Load versus deflection curve for models with cracks that extend through half of the width of the bottom flange for all models and 10 in. in the web in the Baseline and Specimen A models.

In Figure 4.27, the entire width of the bottom flange is considered cracked, and, except for Design Concept B, the web crack length is set at 20 in.



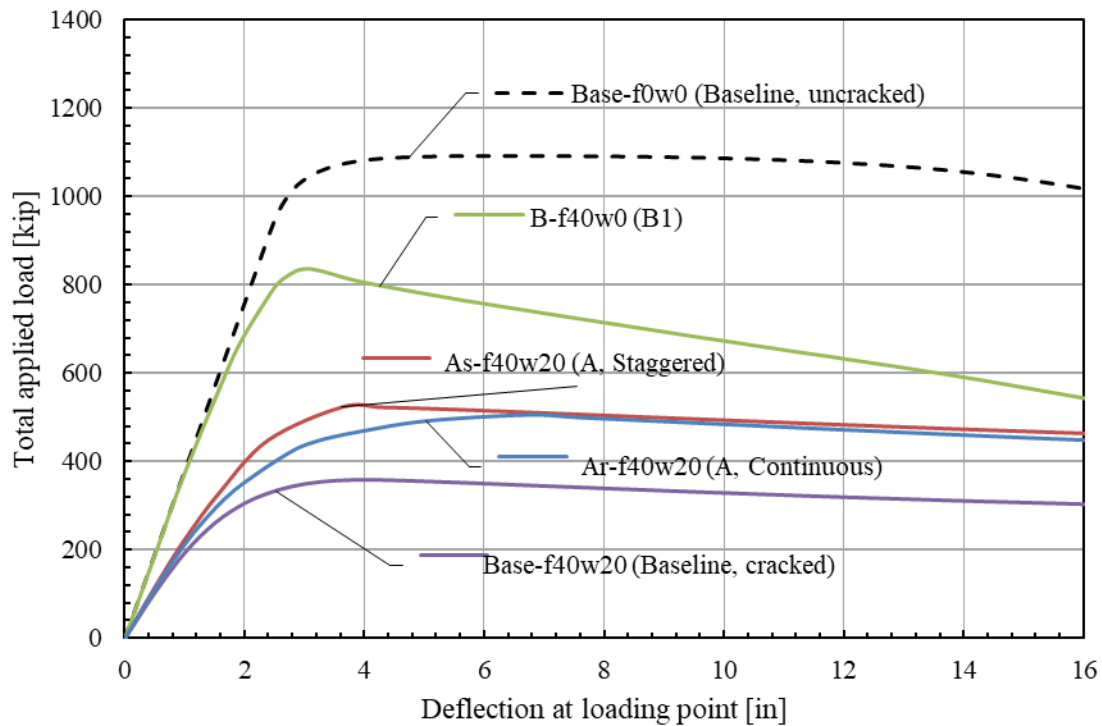


Figure 4.27: Load versus deflection curve for models with cracks that extend through the entire width of the bottom flange and 20 in. on the web in the Baseline and Specimen A models.

Both figures show the load-deflection curve of the uncracked Baseline model as a reference (black dashed line). The analysis of the uncracked Baseline model gives a maximum total capacity of 1091 kips, which was confirmed by a sectional analysis. A clear linear-elastic response is observed until reaching a vertical displacement of approximately 2.5 in. at 87% of the maximum load.

For the cases where one-half of the bottom flange is assumed to be cracked (Figure 4.26), the Baseline model with no redundancy details shows a maximum capacity of 855 kips (78% of the uncracked model) and a reduction in the initial stiffness. The use of post-tensioning bars as a redundancy detail gives a capacity of 85% and 88% of the uncracked baseline model for the continuous and staggered arrangements, respectively. Furthermore, Design Concept B reached a load of 1040 kips (95% of the uncracked Baseline model) with no noticeable loss of stiffness. Additionally, this model indicated potential local buckling of the top flange. Upon a thorough review of the design calculations of the test specimens, it was decided to add a cover plate to the top flange of specimens A and B1 to prevent premature failure of the specimens during the fracture test, as was described in Section 4.1.1

For the cases where the entire bottom flange fractures and the web cracks extend to 20 in. (Figure 4.27), the model without redundancy details (Baseline, cracked) can only carry 33% of the maximum load corresponding to the unfaulted state. Again, adding the PT bars improves this situation, reaching 46% and 48% of the uncracked maximum load for the continuous and staggered arrangements, respectively. In this scenario, with a more extensive cross-sectional loss, the benefit of the staggered arrangement relative to the initial stiffness of the model becomes more evident. Design Concept B can reach 835 kips (77% of the unfaulted maximum load) due to the contribution of the flange connection plates to the flexural response. This result highlights the twofold importance of the flange connection plates: (i) to transfer the load from the bottom flange to the rest of the cross-section while not allowing the crack propagation, and (ii) to provide additional flexural capacity.

These preliminary results suggested that Design Concept A would only deliver satisfactory results if the PT bars effectively arrested the cracks. As the cracks were modeled with seams, this phenomenon was not captured in the analyses and will be assessed during the experimental tests. In turn, Design Concept B showed encouraging results as an internally redundant solution, granted that the fracture of one of the tension components does not affect the adjacent tension components.

### 4.3. Testing Protocol

---

The test protocol for the specimens was divided into two major stages: (i) Fracture Test and (ii) Ultimate Strength Test. The details of each stage are described below.

#### 4.3.1. Fracture Test

The primary goal of the Fracture Test was to evaluate the crack-arresting capacity of the proposed internal redundancy approaches. This test simulates the fracture event of a box straddle cap in service with an existing fatigue crack that suddenly propagates under the passage of traffic. Hence, it was desired to load the specimen dynamically and maintain the load applied on it as it deflected, as the live load would remain on the bridge deck when the straddle cap fractures. Largely based on the work by Hebdon et al. (2015), each Fracture Test involved four steps: (1) initial notching, (2) crack growth by fatigue loading, (3) cooling down, and (4) fracture loading. These steps are described in general terms in the following subsections, while the details corresponding to each specimen are described in Chapter 5.

Two small-scale pilot specimens were designed and fabricated to assess the proposed fracture test protocol and anticipate potential obstacles that may appear during the testing of the full-scale specimens. With these small-scale specimens, the researchers gained experience configuring the closed-loop hydraulic system and data acquisition system (DAQ) to achieve a brittle fracture of the test specimen. Details about the testing of these pilot specimens are provided in Appendix B along with test results and observations.

#### 4.3.1.1. Initial Notching

The tension components of the test specimens were notched to initiate fatigue cracks at predefined locations. The notches were made in the central segment of the specimen, the test segment, midway between internal diaphragms, as shown in Figure 4.28. The size of these initial notches was determined using fracture mechanics equations available in the literature (Tada, Paris and Irwin, *The Stress Analysis of Cracks Handbook* 2000) and preliminary finite element models to ensure that the hydraulic equipment would provide enough loading capacity to produce unstable crack propagation.

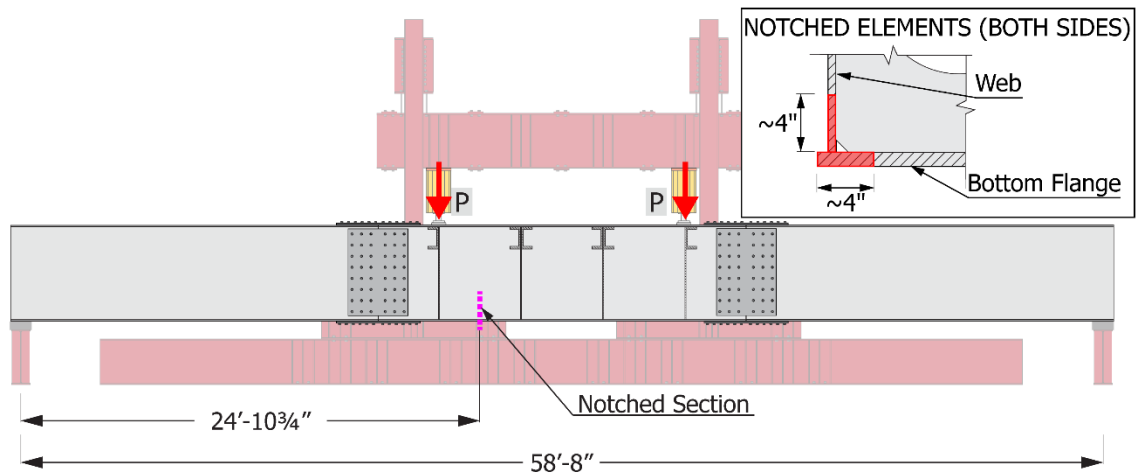


Figure 4.28: Location of the notched section for the Baseline Specimen

In the case of the Baseline Specimen and Specimen A, the initial notches were made on the web-to-flange intersection using a reciprocating saw, as illustrated in Figure 4.29-A. For Specimens B1 and B2, only the bottom flange plate was notched, removing a portion of the flange from the edge of the plate to the first bolt hole and extending a narrow cut beyond the edge of the hole (Figure 4.29-B). A jig saw was utilized for specimen B1 and an oxy-acetylene track-torch cutter for specimen B2.

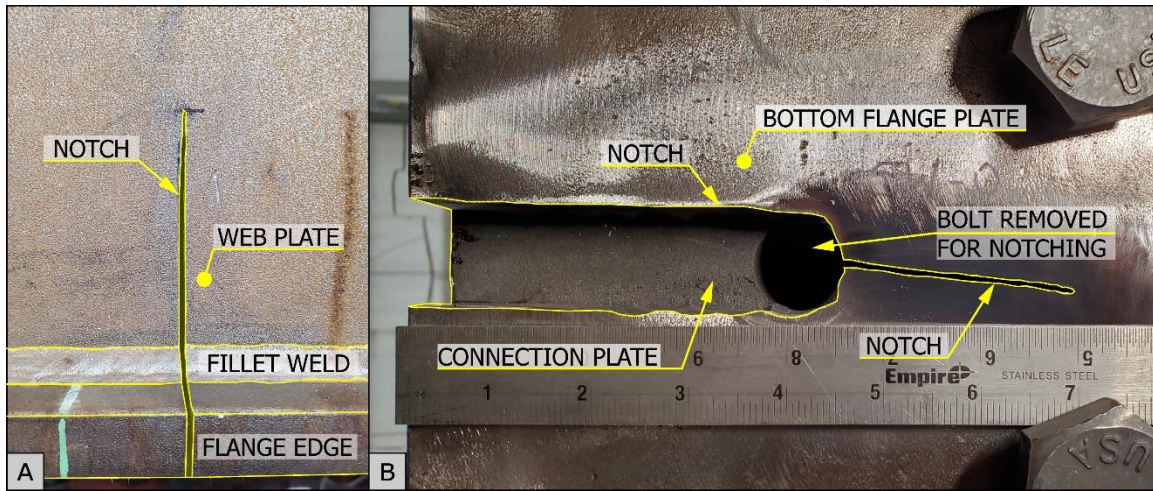


Figure 4.29: Initial notches: (A) Baseline Specimen, and (B) Specimen B1

#### 4.3.1.2. Crack Growth by Cyclic Loading

Although the initial notches create a significant stress concentration, the lack of a sharp crack tip rendered such defects unlikely to produce a brittle crack propagation during the Fracture Test. A sharp fatigue crack was necessary to obtain a brittle failure.

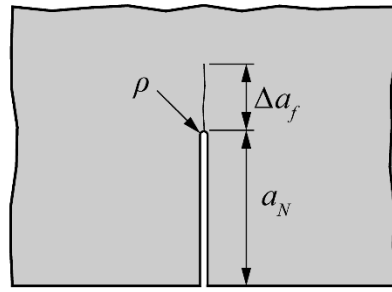
Therefore, the specimens were loaded cyclically to produce fatigue cracks emanating from these initial notches. The applied loads ranged from 10 to 180 kips per actuator at a frequency of 0.125 Hz (1 cycle every 8 seconds) using a cyclic loading procedure on the MTS Testsuite Multipurpose Elite software. The corresponding stress range varied from one specimen to the other based on its corresponding section moduli. A thorough description of the hydraulic equipment is given in Section 4.4.1.

The required fatigue crack length was determined based on the work of Novak and Barsom (1976). Their research showed that a fatigue crack emanating from a notch could be considered a fatigue crack of equivalent length if it satisfied the following equation:

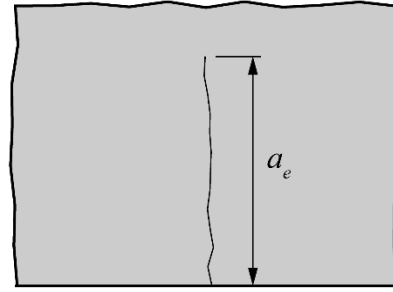
$$\frac{\Delta a_f}{\sqrt{a_N \cdot \rho}} \geq 0.25 \quad \text{Equation 4.1}$$

Where  $a_N$  is the length of the notch,  $\rho$  is the radius of the notch tip, and  $\Delta a_f$  is the length of the fatigue crack that emanates from the notch, as illustrated in Figure 4.30. When Equation 4.1 is satisfied, the added length of the notch and the fatigue crack can be computed as the equivalent length of a fatigue crack,  $a_e$ , as shown in Figure 4.30.

For example: for a 4-in. long initial notch with a tip radius of 0.035 in., the fatigue crack emanating from it must be at least 0.1 in. to be considered a crack of equivalent length.



Fatigue crack emanating from a notch



Fatigue crack emanating from a notch

Figure 4.30: Equivalent fatigue crack length, per Novak and Barsom (1976)

The length of the fatigue cracks was monitored as the cyclic loading progressed to ensure that the criterion described in Equation 4.1 was met. The tips of the notches were polished to facilitate the measurement of the fatigue cracks as the cyclic loading progressed, as depicted in Figure 4.31. In some cases, a dye penetrant was applied on the surface of the steel to enhance the visualization of the cracks.

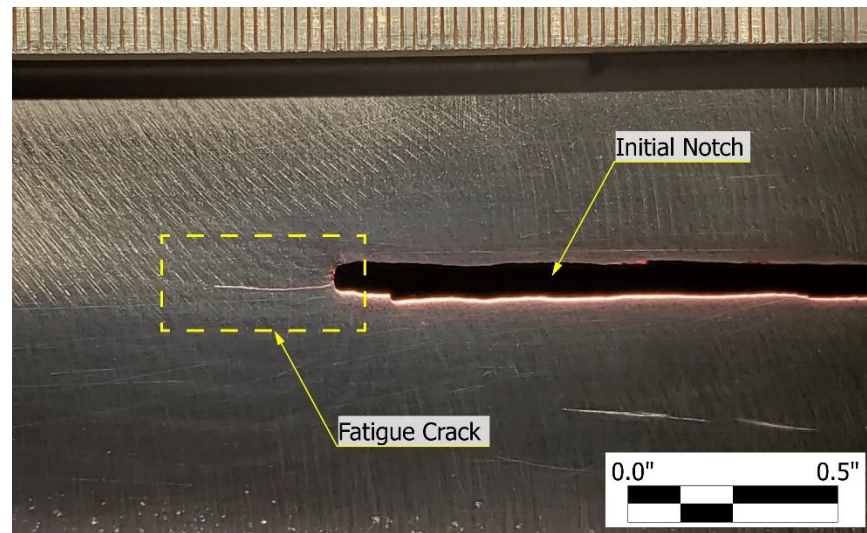


Figure 4.31: Fatigue crack emanating from the initial notch

#### 4.3.1.3. Cooling down procedure

Modern steels, even those not explicitly fabricated to meet the requirements for Fracture Critical Members (AASHTO/AWS 2015), have an inherently high fracture toughness at room temperature. Thus, it was necessary to cool the area surrounding the cracks to temperatures corresponding to the lower-shelf fracture toughness to produce a brittle fracture.



Liquid Nitrogen was introduced inside the specimens in the vicinity of the cracks using pressurized tanks with cryogenic hoses that ran through holes drilled on both webs, as shown in Figure 4.32. The end of each hose was kept at approximately 1 in. from the opposite web plate, and the liquid Nitrogen was allowed to run down the webs to the bottom flange.

Initially, the liquid Nitrogen evaporates quickly, but as the temperature of the steel drops, the Nitrogen stays liquid for longer and decreases the steel temperature further. Insulation foam boards were installed at the interior diaphragms adjacent to the notched section to contain the cold air and improve the effectiveness of the cooling process.

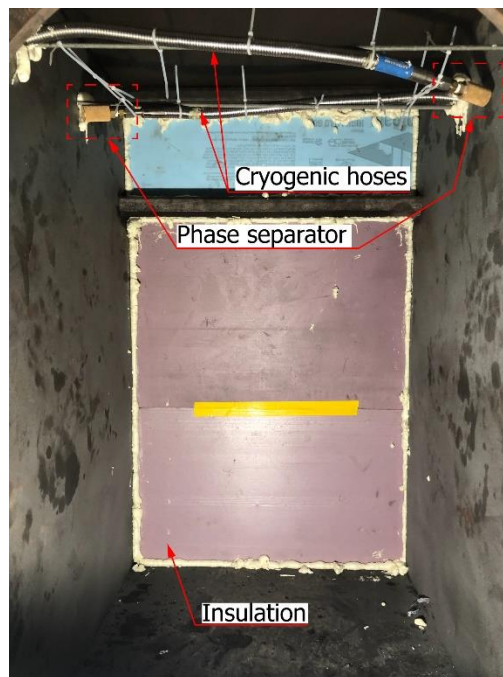


Figure 4.32: Baseline Specimen: cooling equipment inside the box section

The temperature was monitored using Type-K thermocouple wires welded to the outside face of the bottom flange and web plates at the notched section. The cooling procedure was halted once the average temperature measured at the tension portion of the cross-section was in the lower-shelf temperature region. Although most of the CVN tests show negligible energy absorption at  $-120^{\circ}\text{F}$  (refer to Section 4.1.3), the loading of the specimens started once the average temperature at the bottom flange reached  $-200^{\circ}\text{F}$ .

It should be noted that a significant temperature gradient was observed over the height of the specimen as the liquid Nitrogen accumulated at the bottom of the specimen. This temperature gradient produced a fracture toughness variation from the bottom flange

(lower shelf) to the top of the section (transition region), which might prevent the cracks from reaching the upper portion of the webs.

#### **4.3.1.4. Fracture Loading**

Once the temperature corresponding to the lower-shelf fracture toughness was reached, the liquid Nitrogen flow was stopped, and the specimens were subsequently loaded to produce a brittle fracture. The load application for each specimen was performed as follows:

- For the Baseline Specimen, an Enerpac air hydraulic pump was used to supply the actuators and load the specimen until fracture occurred. The slower loading rate of this pump allowed the researchers to halt the loading process after the specimen fractured and prevent excessive damage to the specimen, considering that this specimen had to be repaired and reused to test Specimen A.
- The pump was operated manually, and the applied load was monitored using load cells and pressure transducers.
- The MTS Hydraulic Power Unit (HPU) connected to the closed-loop system was used to load specimens A, B1, and B2 for this stage. With this equipment, it was possible to load the specimens dynamically and restore the load on them almost immediately after the fracture occurred using the force control mode. As it was done for the cyclic loading stage, the loading procedure was specified in the MTS software, in this case, as a ramp loading procedure.

#### **4.3.2. Ultimate Strength Test**

The objective of this stage is to determine the capacity of the specimen in the faulted condition (i.e., its reserve capacity) and assess whether it would meet the requirements to be classified as non-Fracture Critical, as explained in Section 3.1.4.

The Baseline Specimen, which had no internal redundancy, was not re-tested after the initial fracture test, as that would have produced excessive damage and precluded repairing it. On the other hand, the internally redundant specimens (A, B1, and B2) were loaded to reach their theoretical nominal strength (in the faulted condition) or until failure was achieved.

For this stage, the loads were applied using the air-hydraulic pump (which had a higher working pressure than the MTS HPU) to utilize the total capacity of the actuators. Using

this equipment ensured that the theoretical flexural capacity in the faulted condition could be reached for all specimens.

#### 4.4. Test Setup

---

A test setup was designed to accommodate the test protocol requirements and maximize the laboratory equipment capacity. A schematic view of the test specimen and test setup is provided in Figure 4.33, and elevation and plan views of the test setup are included in Figure 4.34.

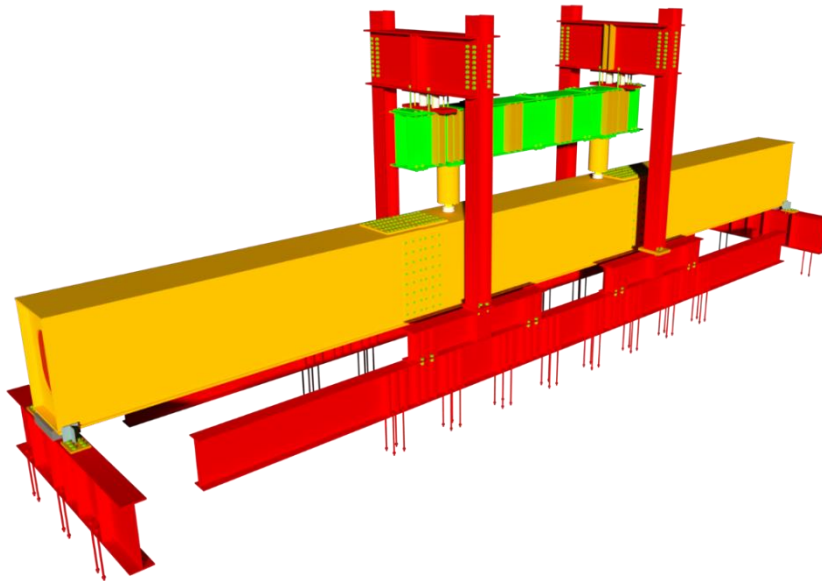


*Figure 4.33: Full-scale test setup: schematic view (strong floor not shown for clarity)*

The test specimen was supported at each end on a 12 in.×24 in.×5 in. elastomeric bearing resting on a W36×150 support beam anchored to the strong floor. In addition, two lateral stops were placed at each end to prevent lateral displacements of the specimens, particularly during the cyclic loading stage (see Figure 4.35-A).



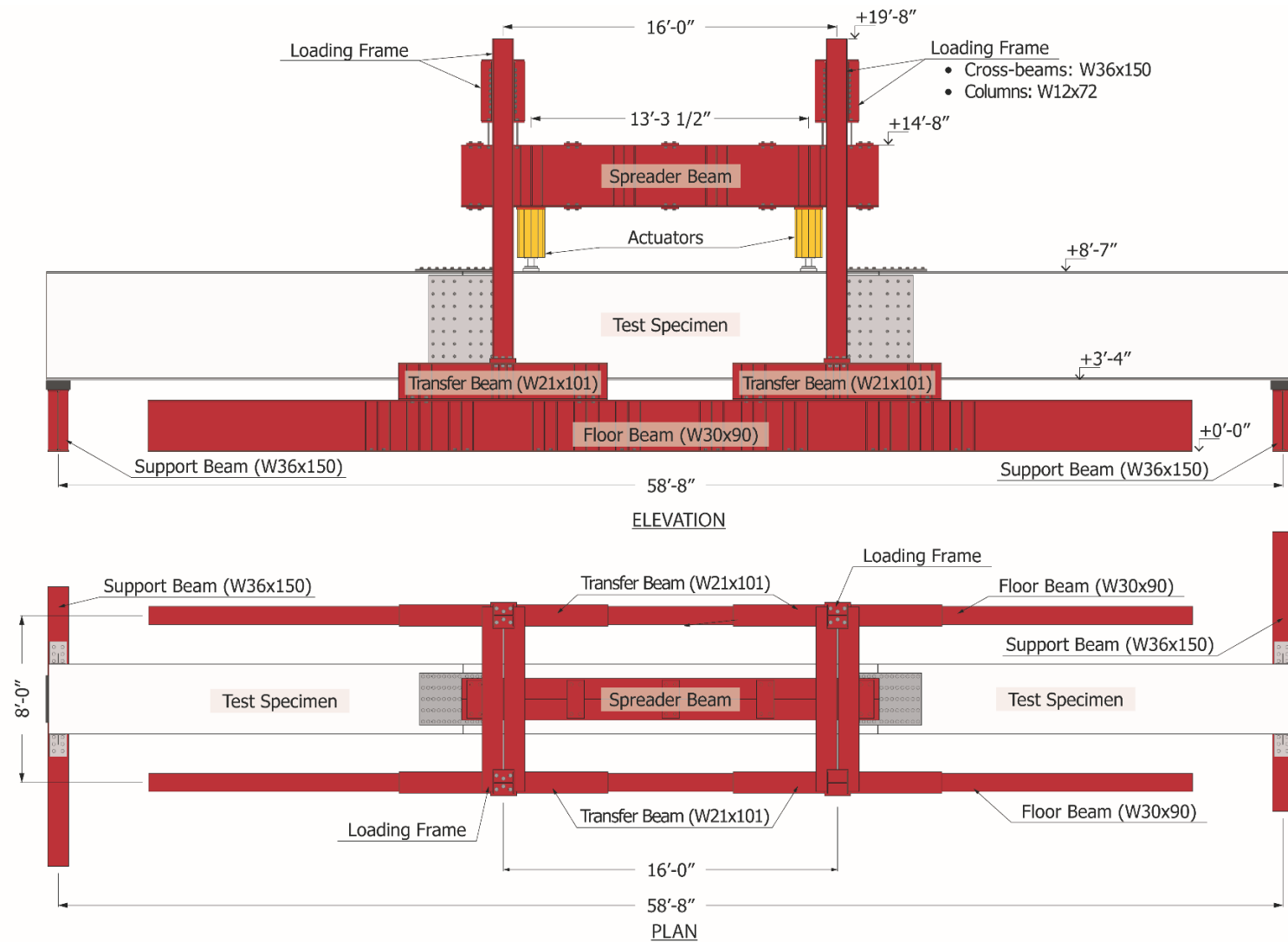


Figure 4.34: Test Setup: elevation and plan views

The specimens were loaded in four-point bending using two Enerpac CLRG-40012 hydraulic actuators with a capacity of 800 kips at 10,000 psi, each equipped with a pressure transducer and a linear displacement transducer, as shown in Figure 4.35-C. The operation of the actuators for each test stage is described in Sections 4.4.1 and 4.4.2. The actuators were attached to a 20-ft long spreader beam made of two W36×150, shown during erecting in Figure 4.35-D.

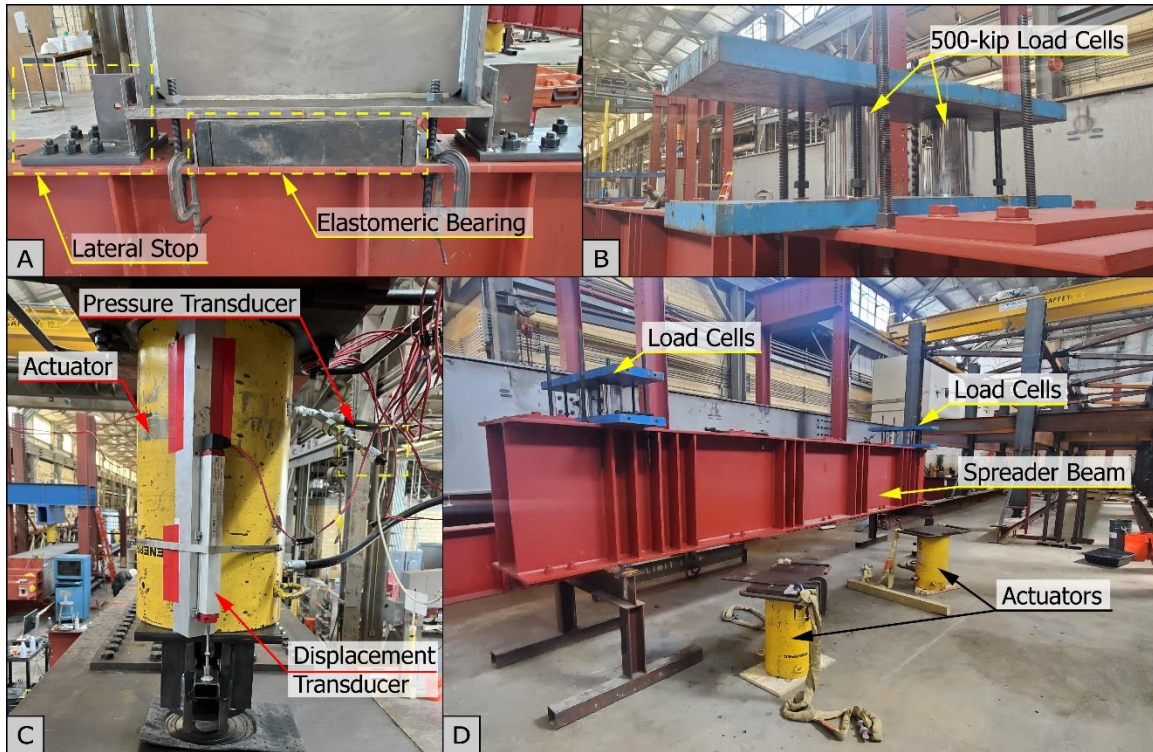


Figure 4.35: Test Setup components: (A) North support elastomeric bearings and lateral stops; (B) pair of load cells on top of the spreader beam; (C) hydraulic actuator; and (D) spreader beam, load cells, and actuators.

The spreader beam was necessary to adjust the position of the actuators to the dimensions of the specimens and the spacing of the anchor points on the strong floor. It hung from the two loading frames, as shown in Figure 4.34. Each column of the loading frames was connected to a W21×101 transfer beam, which was then bolted to a W30×90 floor beam that was anchored to the strong floor with 32 threaded rods (see scheme in Figure 4.34). Two 500-kip load cells, shown in Figure 4.35-B and Figure 4.35-D, were installed between each end of the spreader beam and load frame to measure the loads applied to the specimen.

#### 4.4.1. Hydraulic Actuators Operation for Cyclic Loading and Fracture Test

The hydraulic actuators were operated within a closed-loop system for all the cyclic loading stages and the fracture tests of the internally redundant specimens. The process chart depicted in Figure 4.36 describes the operation of the closed-loop system used in this project. Each actuator was connected to a 30 GPM MTS servo valve, and both were controlled with an MTS Hydraulic Service Manifold (HSM) supplied by a 3,000 psi MTS Hydraulic Power Unit (HPU). Additionally, a 10-gallon bladder accumulator was installed between the HPU and the HSM, which stored pressurized hydraulic fluid to allow for a more stable cyclic loading and a faster displacement of the pistons during the fracture loading stage.

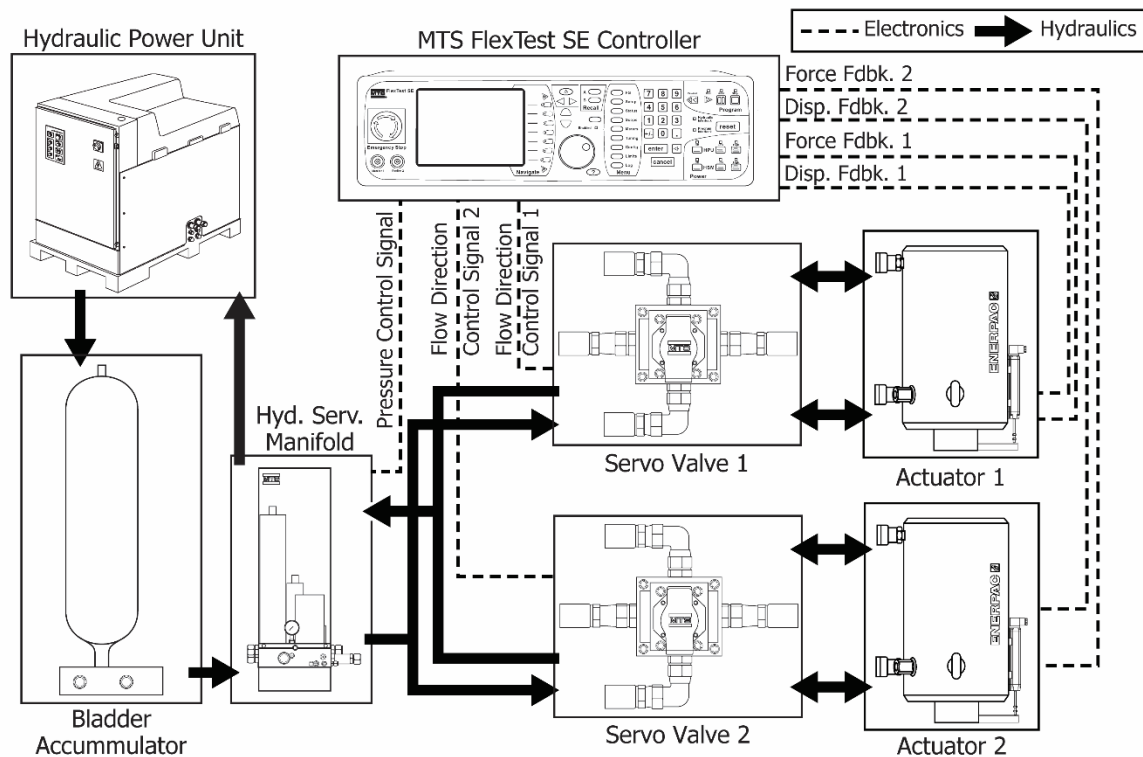


Figure 4.36: Closed-loop system operation process chart

An MTS FlexTest 40 Controller was wired to the load cells installed between the spreader beam and the loading frames to provide the force feedback to the software. The linear potentiometers attached to the body of the actuators and the end of their pistons provided displacement feedback. Based on this feedback, the controller would adjust the command signals to the servo valves to load or unload the specimen as needed. Several of these components depicted in Figure 4.36 are shown in Figure 4.37.

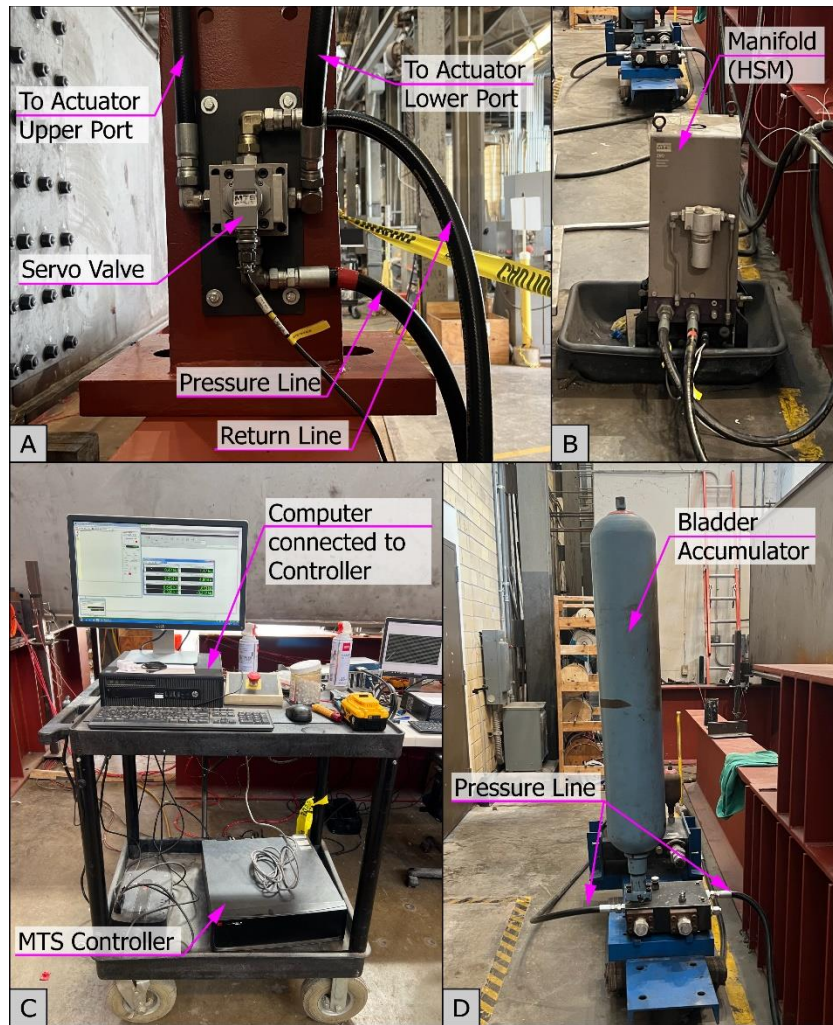


Figure 4.37: Closed-loop system components: (A) servo valve; (B) hydraulic service manifold (HSM); (C) computer and MTS controller; and (D) bladder accumulator

The closed-loop system has two features that were instrumental to this stage of the experimental testing program:

1. Automating the cyclic loading: the controller determines the flow direction of the hydraulic fluid through the servo valves to load and unload the specimens based on user-specified parameters. The force range, loading cycle frequency, and the number of cycles can be specified in the controller according to the loading protocol. This feature allowed the application of cyclic loading to develop fatigue cracks from the notches.



Loading the specimen dynamically: by operating the system in force control, the specimen can be loaded at a defined loading rate until the feedback from the load cells matches the target load.

2. When the specimen fractures, the sudden loss of stiffness produces a reduction in pressure in the hydraulic system and the consequent decline in applied load. However, by operating the equipment in force control, the actuators will reload the specimen after fracture and continue doing so until the feedback from the load cell matches the target force, regardless of the loss of stiffness. Typically, the system would take only a few seconds to reload the specimens.

On the other hand, the closed-loop system has one important drawback: the maximum operating pressure of the MTS Hydraulic Power Unit is 3,000 psi, which limits the maximum force that each actuator can apply to 240 kips. Nonetheless, this loading capacity was sufficient for the execution of the fracture loading stage.

#### **4.4.2. Hydraulic Actuators Operation for Ultimate Strength Test**

To evaluate the ultimate capacity of the specimens in the faulted condition, tests were conducted with an Enerpac air hydraulic pump with a maximum pressure rating of 10,000 psi. A hydraulic manifold was used to deliver equal pressure to the two actuators with the pump.

The main advantage of the Enerpac air hydraulic pump is that it enables to use the total capacity of the actuators and, therefore, reach the load levels required to evaluate the ultimate strength of the faulted specimens. On the other hand, the loading rate using this pump is significantly slower than the MTS system and is manually controlled. Due to the slow loading rate, the system requires significantly longer to reload the specimen when cracks propagate and cannot simulate a dynamic loading.

#### **4.5. Instrumentation**

---

All specimens were instrumented to record their structural performance during both testing stages by monitoring the applied loads, stresses, vertical deflections, and temperature during the cooling process. The data was recorded using a National Instruments data acquisition system (DAQ) operated with a LabView program developed specifically for these tests (Figure 4.38).

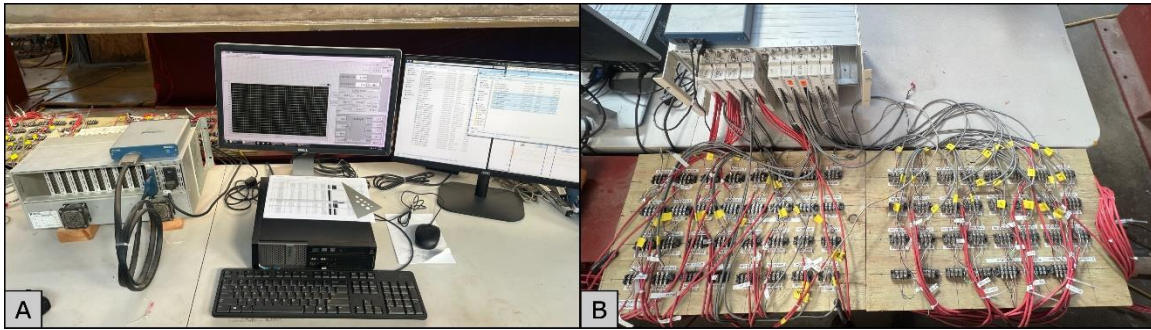


Figure 4.38: DAQ system: (A) NI chassis and desktop computer, and (B) wiring from chassis to connection board and sensors

The loads were recorded using four 500-kip capacity load cells located in pairs between the top flange of the spreader beam and the bottom flange of the cross beams of each loading frame. The location of the load cells is shown in Figure 4.39, and Figure 4.35-B shows two load cells placed on top of the spreader beam before it was lifted in place. Additionally, each actuator was equipped with a Honeywell LM pressure transducer to monitor the hydraulic pressure at its top port and confirm the readings from the load cells.

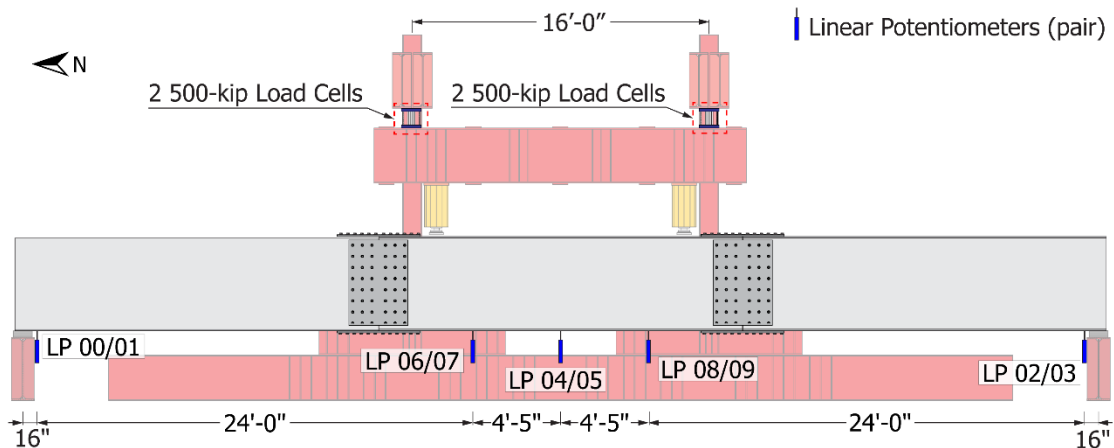


Figure 4.39: Instrumentation: location of linear potentiometers and load cells

Vertical deflections were measured using linear potentiometers. The sensors were supported by a stand and attached to the underside of the bottom flange, as shown in Figure 4.40. Deflections were recorded at various locations, as shown in Figure 4.39. A pair of displacement transducers were placed at the middle point between intermediate diaphragms in the test segment (designated LP 04/05 through 08/09 in Figure 4.39). These sections correspond to the locations where the cracks were initiated. Additionally, a pair of linear potentiometers were installed near each support to monitor the compression of the

elastomeric bearings. These deflections were subtracted from the readings at the other locations to remove the rigid-body motion component.

The temperature in the vicinity of the crack section was monitored as the liquid Nitrogen was poured inside the specimen using Type-K thermocouple wires welded to the outer faces of the webs and bottom flange (Figure 4.41-A). The tip of each TC wire was insulated with foam sealant to prevent eddy currents produced by the temperature difference between the specimen and the surrounding air from altering the temperature readings (Figure 4.41-B). Each wire was connected to an Omega DRSL TC ISO signal conditioner wired to the data acquisition system (Figure 4.41-C and D). Each signal conditioner read the voltage difference between the Chromel and Alumel wires and produced a normalized output voltage that the DAQ recorded.

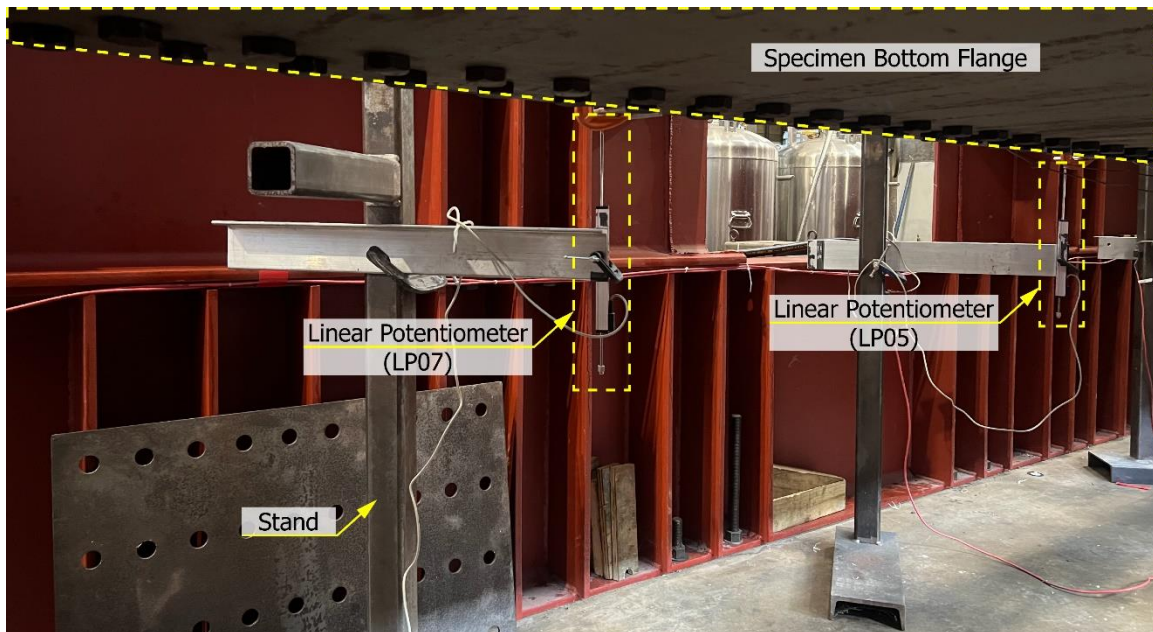


Figure 4.40: Instrumentation: linear potentiometers attached to the underside of the bottom flange



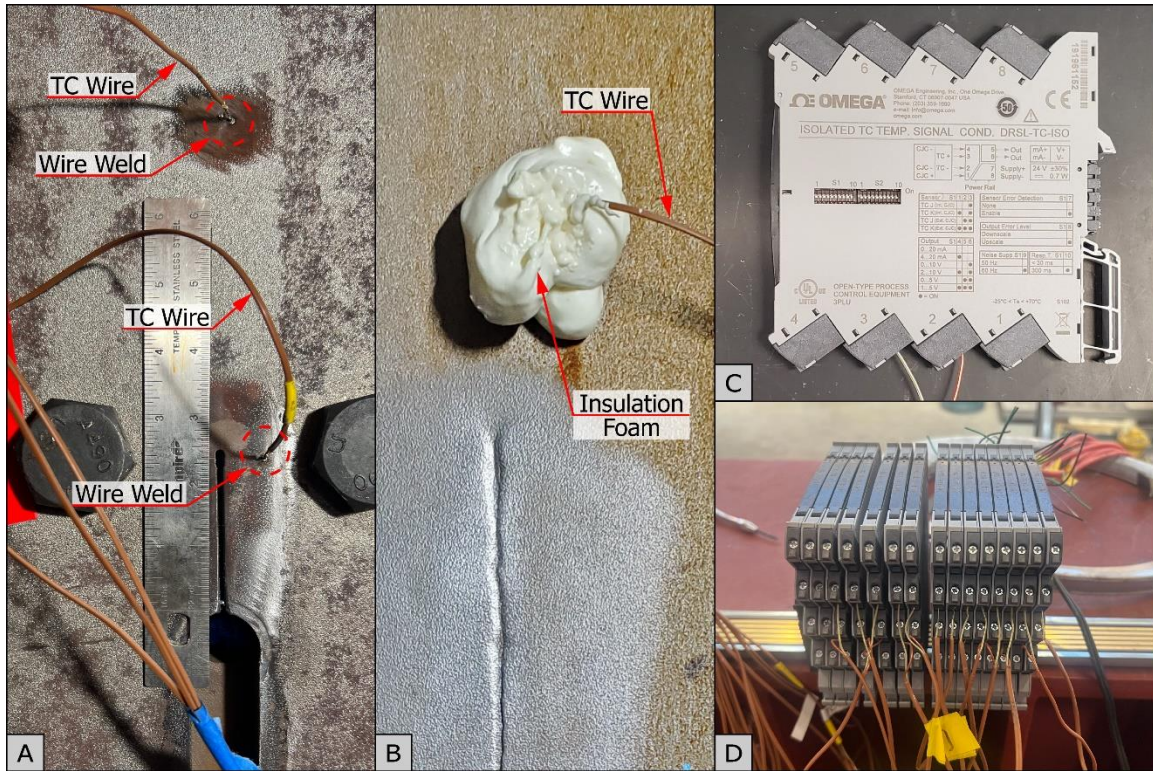


Figure 4.41: Instrumentation for temperature monitoring: (A) TC wires welded to the bottom flange of specimen B2; (B) TC wire tip insulated with foam; (C) Omega DRSL TC ISO Signal conditioner; and (D) stack of signal conditioners wired to the power supply and DAQ.

Strain gauges were installed at several sections of the specimens to calculate the average bottom flange stresses during the fracture test and the force distribution between the tension components. The layout of the strain gauges for each specimen is schematically shown in Figure 4.42.

- For Specimen A, strain gauges were installed on the bottom flange plate and the PT bars. In addition, one load cell was installed at one end of each PT bar to record the axial forces developed in them.
- For Specimen B1 and Specimen B2, the strain gauges were installed at the bottom flange plate and the flange connection plates. The instrumented PT bars and the insulation material that was used to protect them from the liquid Nitrogen are shown in Figure 4.43.

Besides the data recorded with the instrumentation equipment, visual observations of the damage produced to the specimen during all stages of the testing protocol were performed.



The crack propagation trajectories and the deformation of the tension components were photographically documented for the internally redundant specimens.

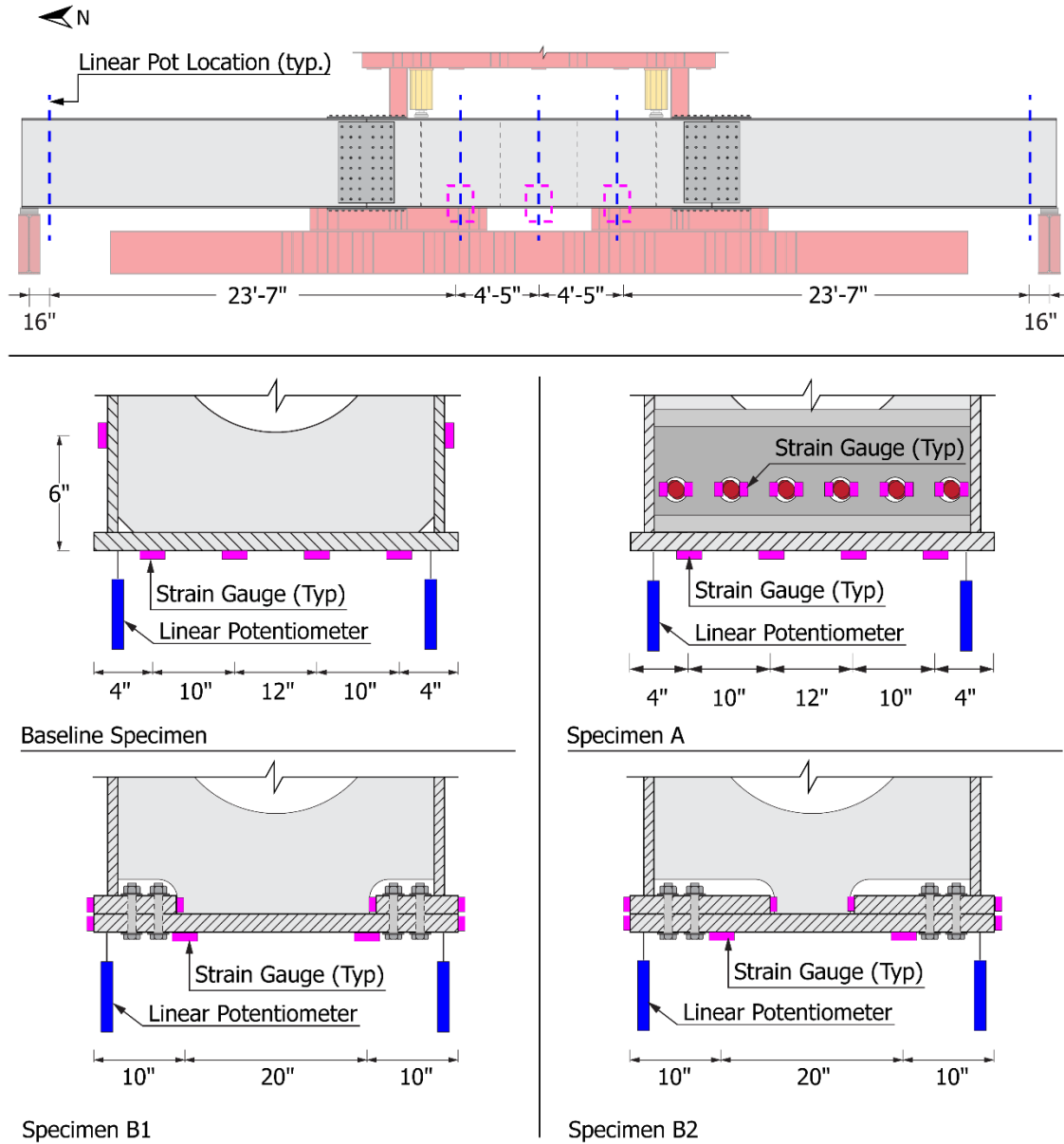


Figure 4.42: Instrumentation: typical locations of strain gauges and linear potentiometers for all test specimens

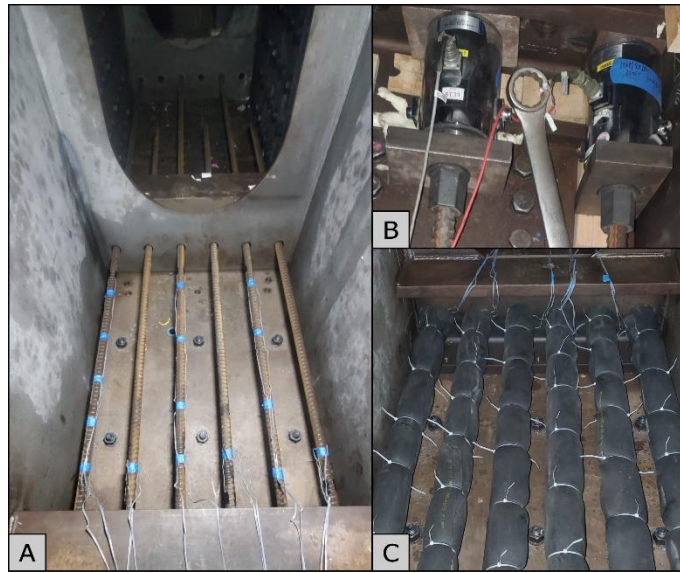


Figure 4.43: Specimen A: instrumentation of PT bars: (A) Strain gauges; (B) load cells; and (C) insulation.

## 4.6. Summary

This chapter describes the experimental testing program developed to evaluate the internal redundancy approaches proposed in Chapter 3. The test specimens were designed in three pieces: a central segment constituting the actual test specimen with the corresponding internal redundancy details and two end segments designed to be reused throughout the experimental program.

One test segment was designed and fabricated per Design Concept A, incorporating post-tensioning bars to act as a secondary tension element after the fracture of the tension portion of the section. The capacity ratio between faulted and undamaged/intact capacities for this specimen is approximately 44%. Furthermore, this specimen would be flipped upside-down and tested to fracture as the Baseline Specimen.

For Design Concept B, two test segments were designed and fabricated. Specimen B1 was designed to provide the minimum practical width for the flange connection plates to accommodate the bolts. This made the bottom flange plate larger than permitted by the AASHTO Guide Specifications for IRMs (2018-1). For this specimen, the ratio of the nominal capacity in the faulted condition relative to the undamaged/intact section is approximately 70%. Specimen B2 was designed with wider flange connection plates that comply with the AASHTO Guide Specifications (2018-1), which reduces the amount of energy transferred to the flange connection plates during the fracture. This specimen was

designed to provide 77% of the undamaged/intact nominal capacity when loaded with the bottom flange fractured.

The test protocol for the test specimens is divided into two primary stages. First, the specimen is loaded to fracture to study the crack-arresting effectiveness of the design approach. This test is conducted after fatigue cracks have been initiated in the specimen and the steel has been cooled to lower-shelf temperatures using liquid Nitrogen. Secondly, the ultimate capacity of the internally redundant specimens was evaluated by loading the fractured specimens to failure.

A test setup that accommodates the requirements of each testing stage and maximizes the capacity of the testing equipment was designed and erected at FSEL. Additionally, an instrumentation plan was developed to monitor and record the quantities of interest for each specimen. The results of the full-scale tests conducted for all specimens are presented in the next chapter.

## **Chapter 5. Experimental Results and Observations**

This chapter outlines the results of the full-scale experimental tests conducted in the study. A total of three specimens were tested; however, one of the specimens was inverted and tested as a baseline specimen. Therefore, there were a total of four experimental setups. For the specimens with details to improve the redundancy, the specimens were first subjected to a fracture test, which was then followed up with an ultimate strength test. This chapter outlines the results from each of the tests. In this chapter, the results of the different specimens that were tested are presented in the following order:

- Fracture Test of Baseline Specimen (Section 5.1)
- Fracture Test of Specimen A (Section 5.2.1)
- Ultimate Strength Test -in faulted condition- of Specimen A (Section 5.2.2)
- Fracture Test of Specimen B1 (Section 5.3.1)
- Ultimate Strength Test -in faulted condition- of Specimen B1 (Section 5.3.2)
- Fracture Test of Specimen B2 (Section 5.4.1)
- Ultimate Strength Test -in faulted condition- of Specimen B2 (Section 5.4.2)

In the interest of minimizing the complexity of repairing the Baseline Specimen, which was actually Specimen A inverted, the Baseline Specimen was not loaded to its ultimate strength in the faulted condition. All tests were conducted following the steps outlined in Section 4.3.

### **5.1. Fracture Test of Baseline Specimen**

---

The locations of the initial notches for this specimen were selected considering that the same test segment was to be repaired and reused to test Specimen A with the addition of the PT bars. Therefore, the decision was made to notch the Baseline Specimen at 24.89 ft from the North support, as shown in Figure 5.1, at the midpoint between internal diaphragms within the maximum moment region. Further details of the experimental testing of the Baseline Specimen can be found in Williams et al. (2022).

The self-weight of the box girder was negligible compared to the applied load. Therefore, the region between the point loads was essentially a constant moment region. For the test of Specimen A, the notches could be made at midspan. Since, in both cases, the notches were located within the constant-moment region of the girder, the results of these specimens could be compared.

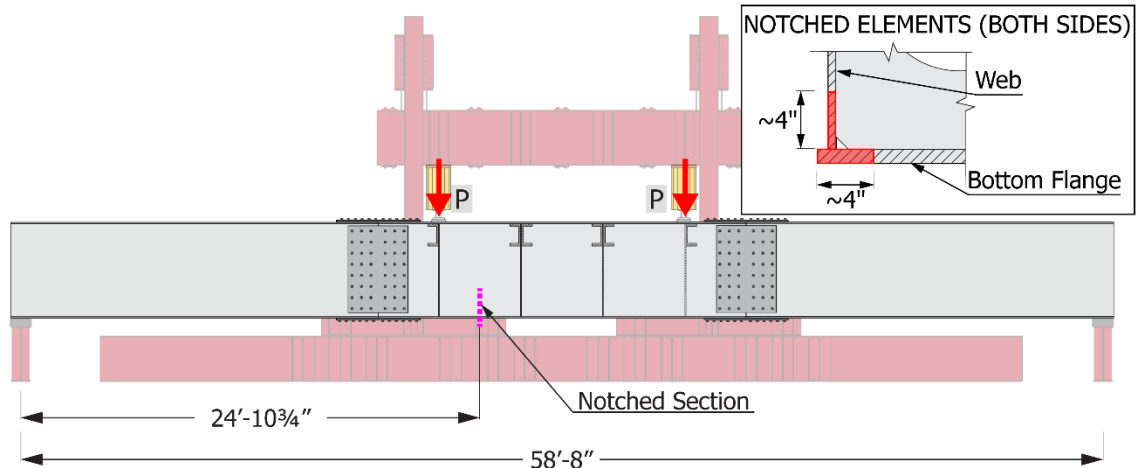


Figure 5.1: Baseline Specimen: location of the notched section

A reciprocating saw with a 0.035 in.-wide blade was used to cut the initial notches at the edges of the bottom flange and the lower portion of the webs, as shown in Figure 5.2. The flange edge notches were approximately 4-in. long, measured from the flange edge. The notches on the webs were also approximately 4-in. long, measured from the top face of the bottom flange plate.

A groove approximately 1/8" deep was ground into the surface of the plates from each notch toward the top flange to induce a preferred propagation path for the cracks. Moreover, as the top flange was to become the bottom flange for Specimen A, a dumbbell-shaped crack arrester was cut on either web a distance 8 in. from the top flange to prevent the cracks from propagating into the top flange. These crack arresters were made by drilling two 1.5-in. diameter holes with a magnetic annular drill and then connecting the holes with a horizontal cut made with a reciprocating saw. This effort was intended to limit the damage to the specimen and simplify the specimen repair tasks following the completion of the Baseline Test. The crack arrester and groove are shown in Figure 5.3, which also illustrates how these holes served as the entry for the cryogenic hoses on each web.

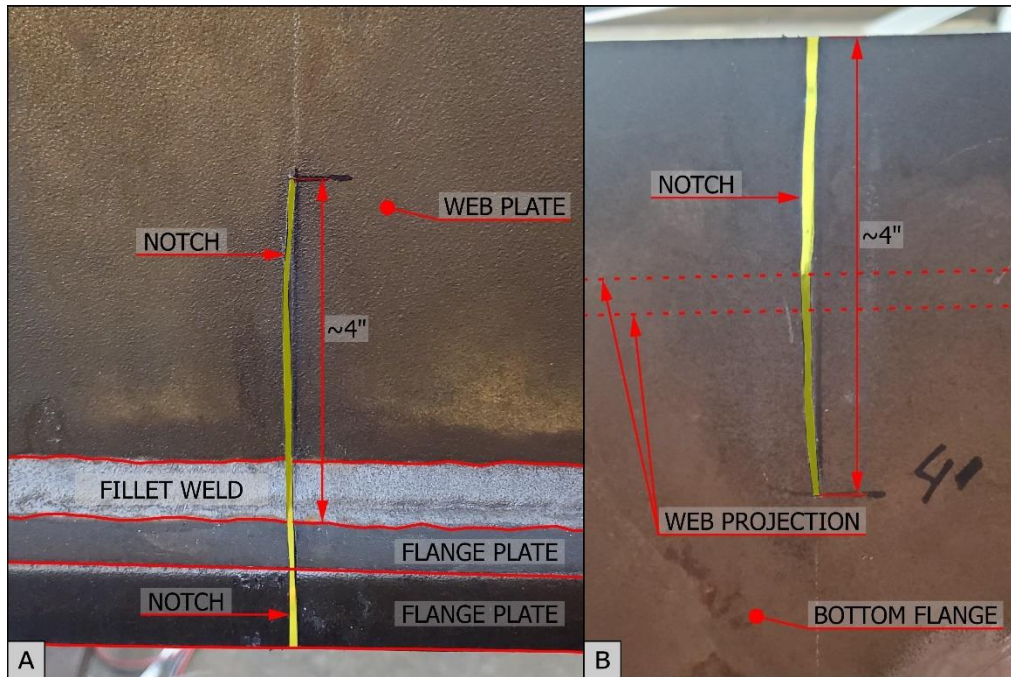


Figure 5.2: Baseline Specimen: initial notches made (A) on the lower portion of the webs and (B) bottom flange edge

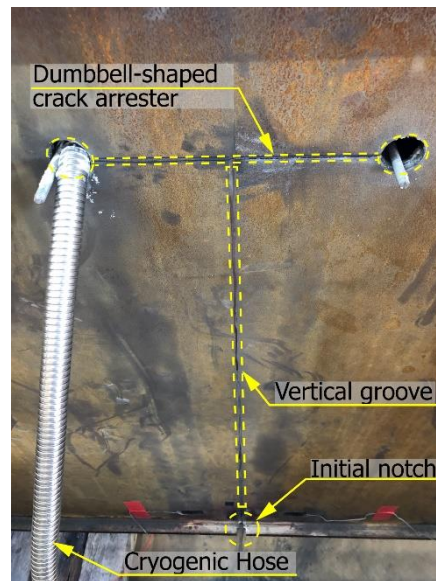


Figure 5.3: Baseline Specimen: dumbbell-shaped crack arrester and vertical groove

Using the closed-loop hydraulic system, the Baseline Specimen was subjected to 9,000 load cycles to produce fatigue cracks emanating from the initial notches. The total load applied by the two hydraulic actuators ranged from 20 kips to 360 kips, corresponding to a 15.2 ksi stress range at the extreme fiber of the bottom flange. The fatigue cracks



emanating from the initial notches following the completion of the cyclic loading was completed are depicted in Figure 5.4.



Figure 5.4: Baseline Specimen: fatigue cracks emanating from notches: (A) West flange and (B) West web

Liquid Nitrogen was used to decrease the temperature of the steel in the vicinity of the notched section, which was monitored with the thermocouple wires described in Section 4.5. The temperature distribution at the notched section immediately before loading the specimen is shown in Figure 5.5, which also shows the frost formed on the outside of the West web of the specimen surrounding the region being cooled. With an average temperature below -230 F, the fracture toughness bottom flange plate was well into the lower-shelf region (see Section 4.1.3).

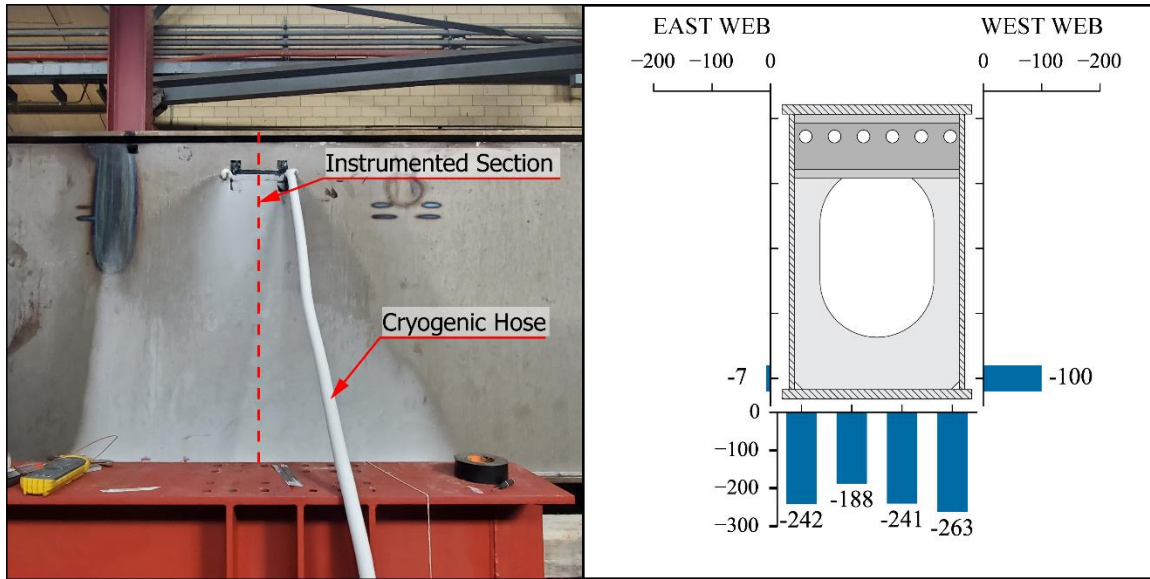


Figure 5.5: Baseline Specimen: temperature distribution at the notched section ( $^{\circ}\text{F}$ )

Subsequently, liquid Nitrogen flow was stopped, and the specimen was loaded with the pneumatic hydraulic pump to produce a brittle fracture. The pneumatic pump was used instead of the closed-loop system due to uncertainty in whether the 3000 psi maximum pressure for the closed-loop system would fracture the specimen. However, the pneumatically controlled pump provided more of a static loading that allowed better control for minimizing the damage to the specimen. The behavior of the Baseline Specimen during the fracture test is shown in Figure 5.6 by plotting the applied bending moment against the deflection measured at the cracked section. The plot also includes a secondary vertical axis normalized to the undamaged/intact section's yield moment. The loading sequence can be summarized as follows (each step is identified in Figure 5.6):

1. The load was monotonically applied to the specimen until the cracks suddenly propagated. The load required to produce the fracture (approximately 94 kips) was significantly lower than the preliminary estimations (approximately 400 kips), which was attributed to the extremely low temperatures at the bottom flange plate. Consequently, the steel was at its minimum fracture toughness during the fracture loading and exhibited a purely brittle behavior. The bending moment at the notched section when the cracks propagated was 1,089 kip·ft, equivalent to a 4.2 ksi tensile stress at the bottom fiber of the bottom flange.

The first peak in the plot (Figure 5.6) corresponds to the applied bending moment when the specimen fractured for the first time: the bottom flange cracks propagated



across its entire width, and the web cracks propagated upwards a distance of 15 in. before arresting.

2. The specimen suddenly deflected when it fractured, and, as expected, the hydraulic equipment could not pump oil quickly enough to maintain the applied load. Therefore, the load cells indicated a drop in the applied load, as shown in the plot after the first fracture occurred. In addition, the oscillations in the plot depict the free vibration undergone by the specimen after the fracture occurred.
3. After assessing the damage, the pneumatic pump was used to continue loading the specimen to determine to what extent the cracks would continue propagating in the webs. The slope of the reloading branch shows the loss of stiffness following the first fracture.

The web cracks propagated approximately 15 in. further when the total applied load reached 223 kips. The corresponding bending moment at the cracked section was 2,550 kip·ft (equivalent to an average stress of 9.8 ksi at the bottom flange), indicated in the second peak in the curve. It should be noted that due to a vertical temperature gradient on the cross-section, these portions of the webs were not likely at the lower shelf temperatures and, therefore, exhibited a more ductile behavior, as confirmed by the appearance of the crack surfaces in that region.

4. The propagation of the cracks induced a further loss of stiffness and a drop in pressure in the hydraulic system, evidenced by the drop after the second peak in the plot.
5. At that point, the cracks had propagated approximately to the mid-depth of the webs, and it was deemed reasonable to end the test to prevent further damage. A permanent deflection of 0.6 in. was measured upon complete unloading.

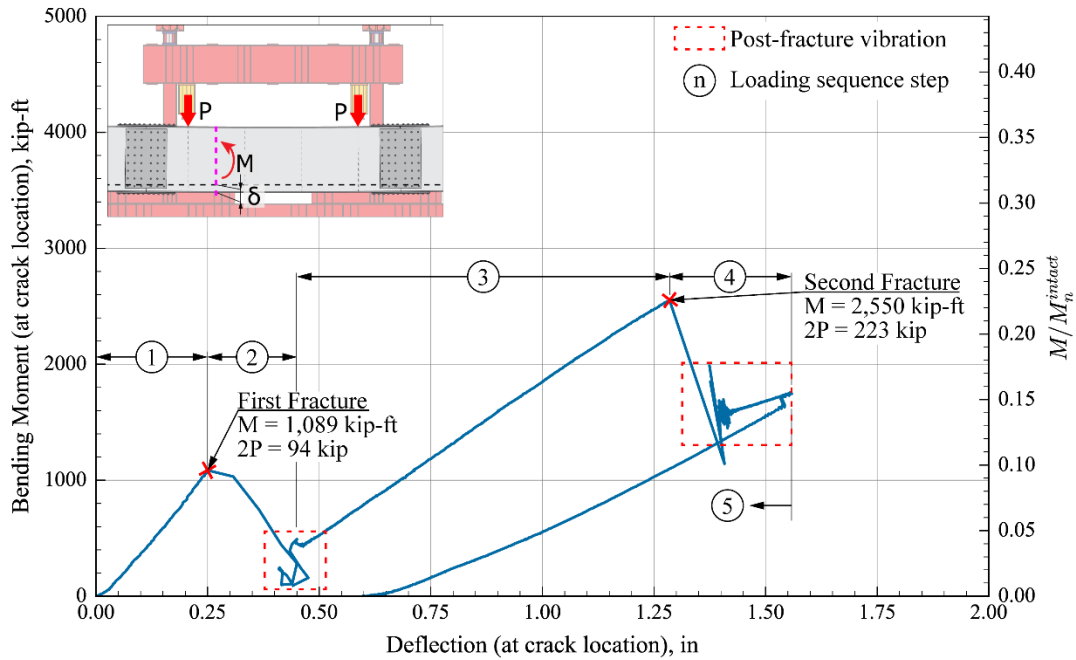


Figure 5.6: Baseline Specimen Fracture Test: applied bending moment versus deflection at the cracked section

To enhance the visualization of the cracks produced on this Baseline Specimen, a pictorially “unfolded view” is presented in Figure 5.7. The figure shows the West web, bottom flange, and East web plates in a single plane, which allows for identifying the trajectories of the cracks.

In this view, it is possible to observe the initial notches and the different branches of the cracks identified with an alphanumeric character. The number refers to the loading stages in which the crack occurred (1 or 2). In addition, each label has a pair of letters that refer to the notch from where each branch originated. For example, the cracks that started from the notches on the bottom flange plate, either on its East or West side, are labeled as “EF” or “WF,” respectively. Likewise, the cracks that originated from the notches on the webs are identified as “EW” or “WW” for East and West webs, respectively.

- The first crack propagation resulted in the total fracture of the bottom flange plate, and the propagation of the web cracks up the webs, as indicated by the crack branches 1-WF, 1-EF, 1-WW, and 1-EW.

It is believed that the crack that initiated from the notch on the East edge of the bottom flange, 1-EF, propagated first, running across the entire bottom flange width and continuing upwards on the West web by propagating through the fillet weld.

This fact shows how a single fatigue crack growing on one side of a box girder can sever the entire bottom flange and continue propagating on the opposite web. Furthermore, the crack that started on the opposite notch (1-WF) also propagated during this first loading but was arrested when it intersected the branch from the East edge (1-EF).

The cracks emanating from the web notches (1-EW and 1-WW) propagated upwards approximately 13 in. during the first fracture loading attempt.

- During the second fracture loading, the cracks located in the webs (1-EW, 1-WW, and 1-EF) propagated even further. However, as mentioned before, this propagation was more directly related to a high-strain ductile behavior than a brittle crack propagation due to the relatively higher temperature of the webs.

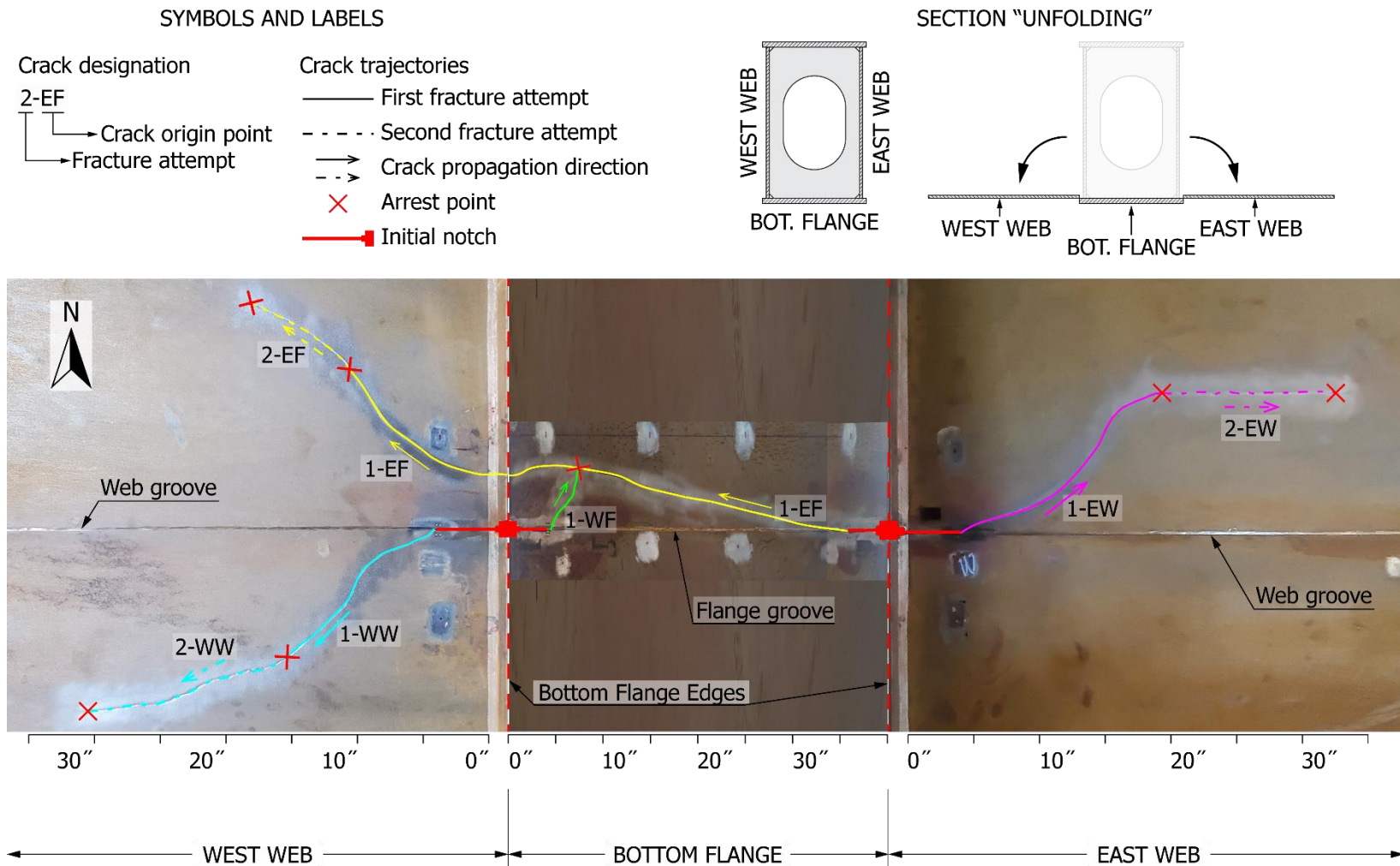


Figure 5.7: Baseline Specimen: cracks after completion of Fracture Test

### 5.1.1. Observations

The results of this test confirmed that, under test conditions that minimize the fracture toughness of the material and in the presence of large defects, the specimen without any internal redundancy would behave relatively poorly. The Baseline Specimen was only loaded to 8.4% of its yield moment when it fractured, making it very undesirable from an in-service point of view. Moreover, the second fracture event occurred at 19.6% of its undamaged/intact yield moment.

As was previously pointed out, welded connections between the tension components create a direct path for cracks to propagate from one component to another, even if the cracks initiate at the opposite side of the section.

Additionally, conducting the test provided verification that the test protocol was indeed effective:

- The fatigue loading was effective in initiating sharp fatigue crack tips that resulted in crack sizes large enough to produce the fracture of the specimen within the loading capacity of the testing equipment.
- The cooling procedure was also found to be adequate, reducing the fracture toughness of the material to its lower-shelf values.
- The data acquisition system and the hydraulic equipment performed as expected.

## 5.2. Experimental Testing of Specimen A

As explained in Section 4.1.1, after the Baseline Specimen fractured, the specimen was repaired and inverted to the intended orientation with the details for the PT bars at the bottom of the girder. Thus, the fractured flange was in compression for Specimen A tests, as shown in Figure 5.8. A total of 120 holes were drilled for the splice plates on each web using a magnetic annular cutter. Additionally, 90 holes were drilled on the compression flange. All bolts were 1-in. in diameter ASTM F3125 Grade A490. Plates were included inside the box for the compression flange, and therefore, these bolts were in double shear. For the webs, the splice plates were only placed outside the box, putting the bolts in single shear. All bolts were pretensioned using a turn-of-the-nut electronic wrench to ensure adequate capacity to prevent slip during subsequent tests.

The repair work done on this specimen is depicted in Figure 5.9. One of the web splice plates is shown on the right-hand side of the picture. The fractured flange, corresponding to the top flange in Figure 5.9, was also spliced at the fractured location.

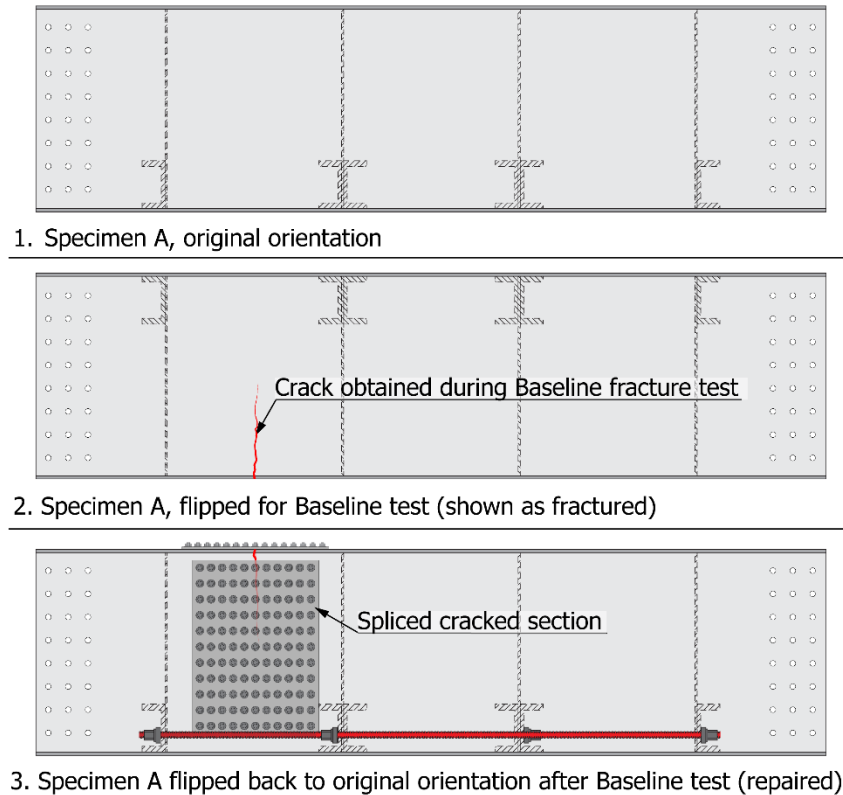


Figure 5.8: Specimen A: testing sequence

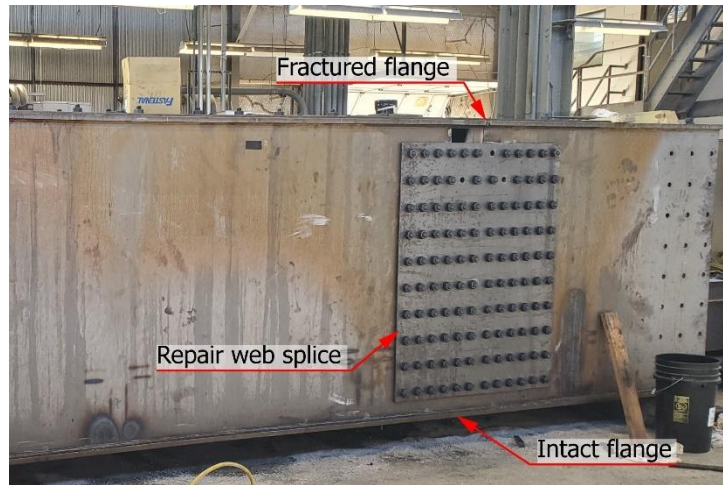


Figure 5.9: Repair process for Specimen A following Baseline Test

Once the repairs were completed, the PT bars were installed, and the test segment was connected to the reusable end segments to assemble the test specimen. Since the PT bars were not intended to introduce a significant prestressing force to the specimen, the bars were tightened using wrenches only to remove the slack and ensure their immediate engagement when the tension portion of the webs fractured.

### 5.2.1. Fracture Test of Specimen A

The procedures for preparation and testing for Specimen A were similar to those used on the Baseline Specimen. Initially, the specimen was notched at 33.77 ft from the North Support at the midpoint between internal diaphragms. The initial notches were approximately 4 ½ in. long in the bottom flange and approximately 4 in. long on the lower portions of the webs, as in the Baseline Specimen. After subjecting the specimen to cyclic loading to produce fatigue cracks emanating from the initial notches, the specimen was cooled using liquid Nitrogen.

During the cooling procedure, the fatigue crack on the East edge of the bottom flange propagated approximately 6.7 in. under self-weight (before any load was applied by the actuators), as shown in Figure 5.10, and the test was terminated. The data from the thermocouples indicated an uneven temperature distribution across the width of the bottom flange, with a significantly lower temperature on the East side. In addition, measurements of the transverse inclination of the specimen showed that the East side was approximately ¾ in. lower than the West side, promoting the accumulation of liquid Nitrogen on the East side of the Specimen. These observations seemed to indicate that the significant temperature gradient was responsible for the fracture event under self-weight.



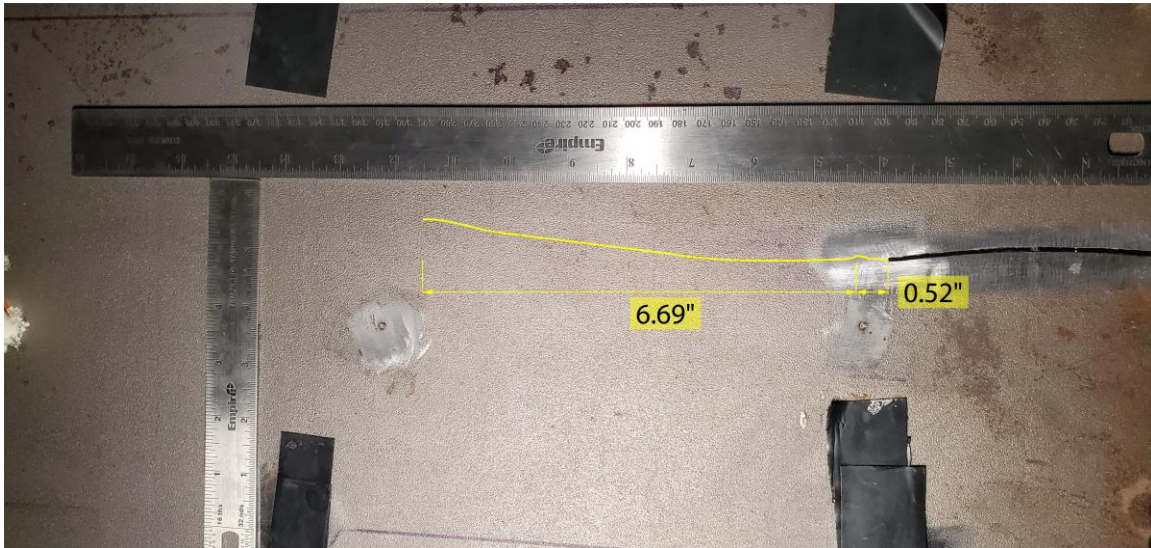


*Figure 5.10: Specimen A: propagation of fatigue crack on the East edge of the bottom flange during the cooling down under self-weight only*

To address this issue and proceed with the testing of this specimen, the fractured section was spliced (plates were used inside and outside the box girder), as shown in Figure 5.11. Additionally, shim plates were used at the end supports to level the specimen and prevent the accumulation of liquid nitrogen on one side.



*Figure 5.11: Specimen A: spliced section after fracture due to uneven distribution of liquid Nitrogen (photo taken inside the specimen)*



Once these repair tasks were completed, the experimental testing was resumed with new notches made at midspan, and the PT bars relocated accordingly. The notches were introduced using a reciprocating saw to initiate fatigue cracks at midspan, as illustrated by Figure 5.12. Initial notches with a length of approximately 2 ½ in. were introduced in the bottom flange, which were slightly shorter than in the Baseline Specimen. The web notches were 4-in. long, which were the same as in the Baseline Specimen.

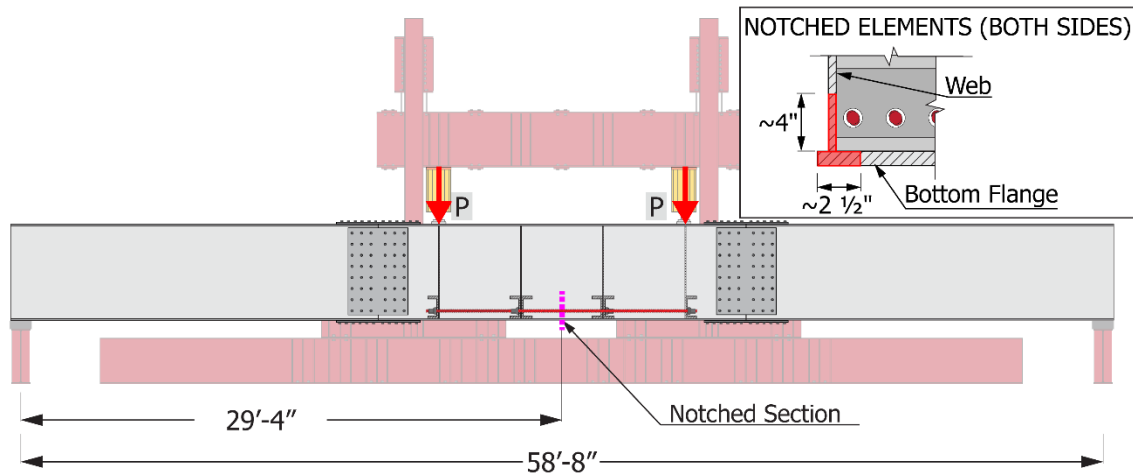


Figure 5.12: Specimen A: location of the notched section

This specimen was subjected to 6,000 load cycles ranging from 10 to 180 kips per actuator, equivalent to a stress range of 14.1 ksi. As desired, sharp fatigue cracks emanated from the initial notches. The lengths of the fatigue cracks on the West flange edge and the West web are shown in Figure 5.13.

The temperature distribution measured in the notched section is shown in Figure 5.14. It can be observed that the entire bottom flange is at lower-shelf temperature (refer to Section 4.1.3). In addition, the temperature gradient is provided from the upper portion of the web, where the liquid Nitrogen was introduced, to the bottom flange, where the Nitrogen accumulated.

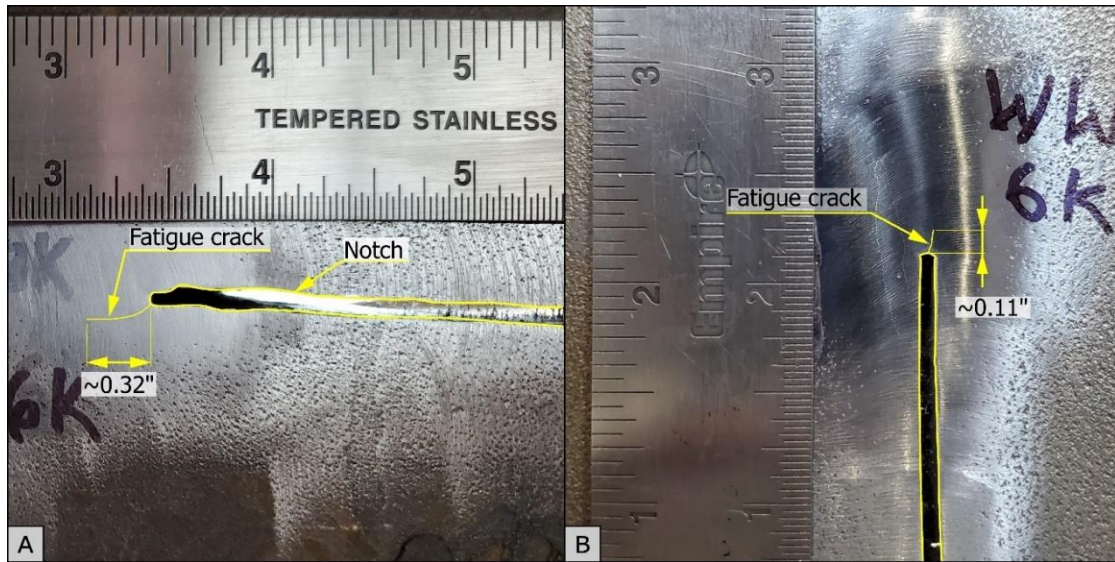


Figure 5.13: Specimen A: fatigue cracks emanating from the initial notches: (A) East flange, and (B) West web

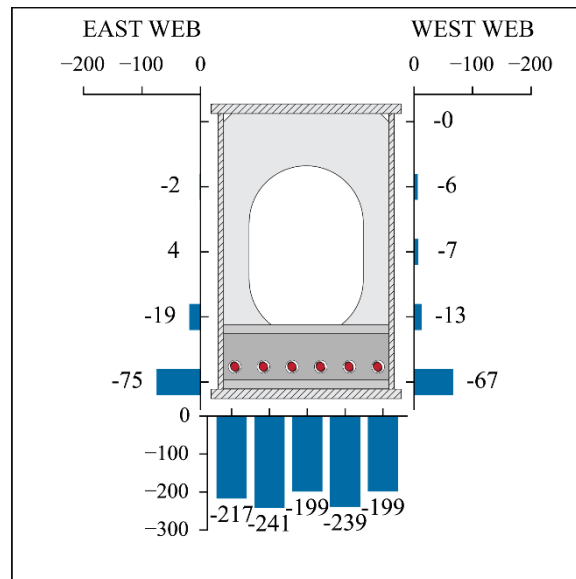


Figure 5.14: Specimen A: temperature distribution at the notched section ( $^{\circ}\text{F}$ )

The loading sequence of Specimen A during the Fracture Test is shown in Figure 5.15. The top plot shows the total load applied by the two hydraulic actuators, while the bottom plot corresponds to the forces developed in the PT bars as the loading progressed. For clarity, the dashed lines indicate the force developed on each PT bar, and the solid line is the average force in the PT bars during the fracture test.

The first 10 seconds of the Fracture Test loading are depicted in Figure 5.16, which more clearly illustrates the sequence of events immediately before and after the cracks propagated. The specimen was loaded quickly, reaching the capacity of the actuators (approximately 400 kips) in approximately 5 seconds. Even before the fracture occurred, the PT bars contributed to the flexural response of the specimen, as indicated by the average of 8.4 kips of axial force developed in each PT bar (considering the six PT bars, a total tensile force of 50.4 kips was developed). When the maximum load was reached, the specimen suddenly fractured, and the load was transferred from the bottom flange of the box to the PT bars, evidenced by the spike in the orange lines in Figure 5.16.

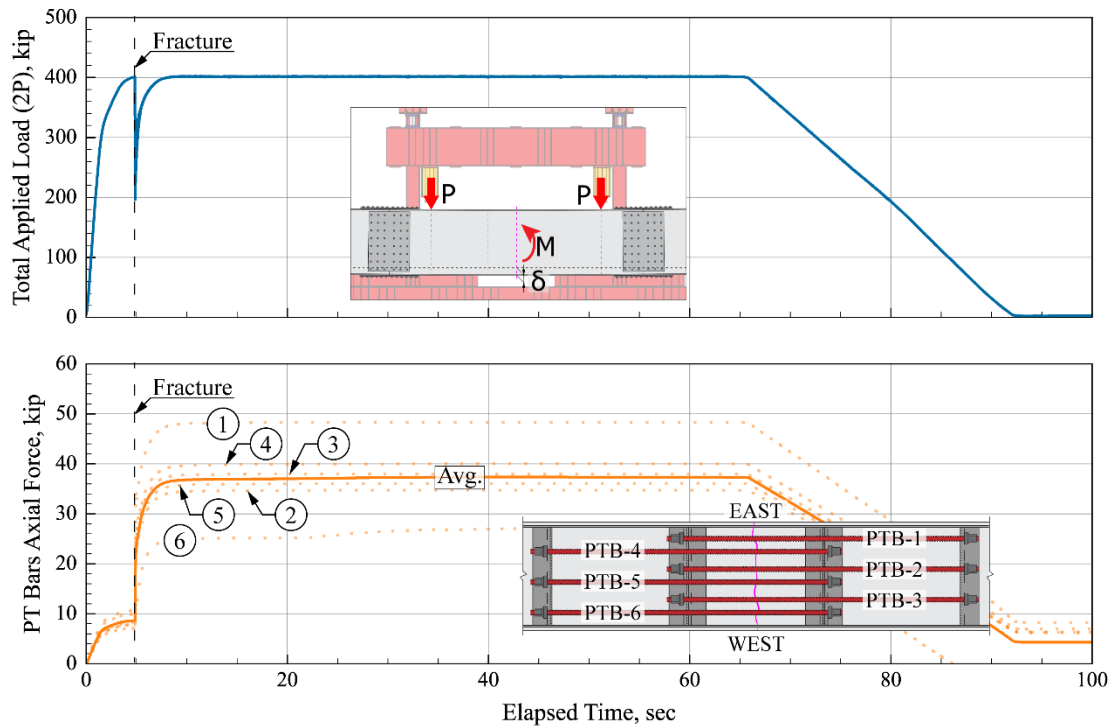


Figure 5.15: Specimen A: loading history during the fracture test: total applied load (top) and axial force developed in the PT bars (bottom).

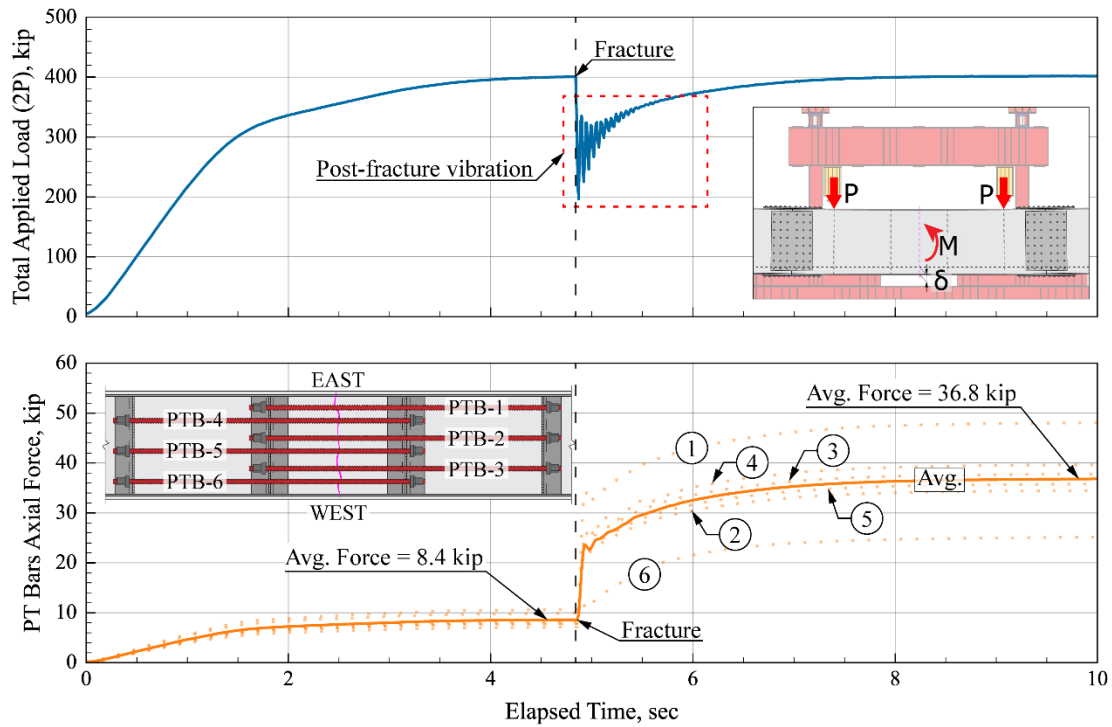


Figure 5.16: Specimen A: loading history (first 10 seconds) during the fracture test: total applied load (top) and axial force developed in the PT bars (bottom).

While the load dropped from the fracture, within approximately 3 seconds, the MTS closed-loop system brought the load on the specimen back to 400 kips. At this point, the average force developed in the PT bars was 36.8 kips (total force in PT bars = 220.8 kips). The load level on the specimen was maintained at the maximum value for 60 seconds, and the specimen was then unloaded.

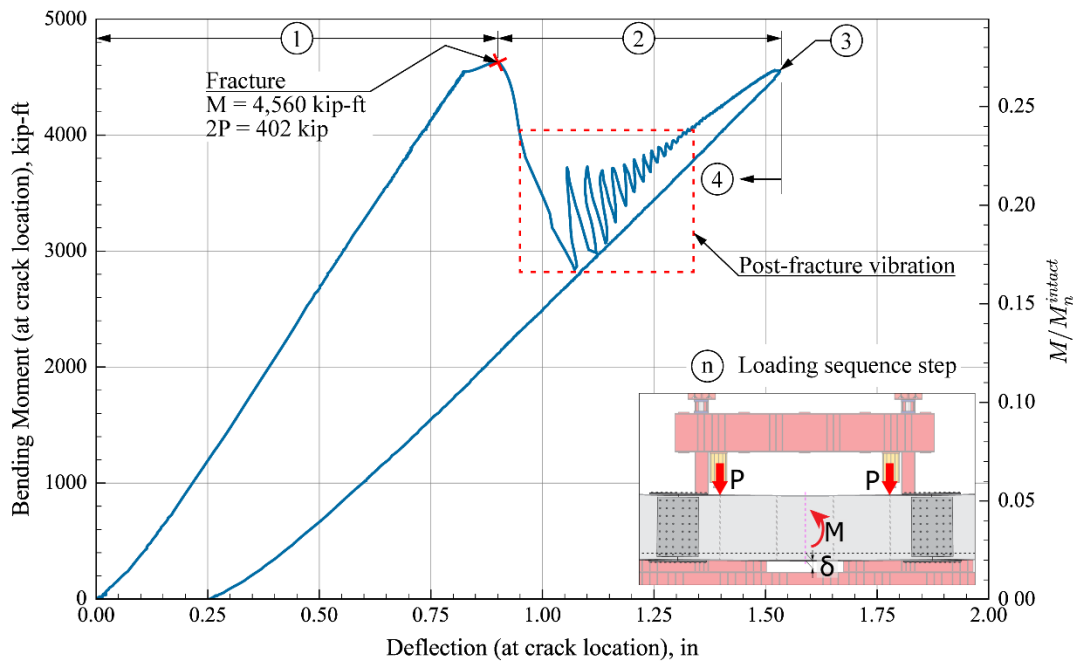


Figure 5.17: Specimen A Fracture Test: bending moment versus deflection at the crack location

The behavior of Specimen A during the fracture test is shown in Figure 5.17 in terms of the bending moment and the deflection measured at the crack location. The secondary axis on the right shows the applied bending moment normalized by the yield moment of the undamaged/intact section. The different stages of the fracture test are as follows:

1. Initially, the response of the specimen was practically linear as the load increased.
2. The fracture occurred at a total load level in both actuators of 402 kips producing a maximum moment of 4,560 kip·ft. After the fracture occurred -at 4,560 kip·ft- the specimen deflected approximately 5/8 in. (from 0.90 in. to 1.55 in.) as the hydraulic system brought the load back to the level at fracture. The post-fracture vibration that happened during the reloading is indicated in the plot.
3. The peak load level was reached again in the fractured condition, with the PT bars acting as the primary tension element at midspan.
4. Subsequently, the specimen was unloaded, and a residual deflection of approximately 0.25 in. was measured.

The cracks produced during the Fracture Test of Specimen A are shown in Figure 5.18, where the cross-section has been “unfolded” for enhanced visualization. The cracks are designated based on the notch from where they originated:

- EF: crack initiated from the notch of the East edge of the bottom flange.
- WF: crack initiated from the notch on the West edge of the bottom flange.
- EW: crack initiated from the notch on the East web. The crack length was approximately 17.6 in. long up the web, measured from the flange-to-web juncture.
- WW: crack initiated from the notch on the West web. The length of this crack after fracture was approximately 17.7 in. long up the web, measured from the flange-to-web juncture.

Based on these trajectories, it is believed that the EF crack propagated first, severing the entire bottom flange plate and propagating upwards on the West web (see Figure 5.18). The EF crack also propagated through the welded connection to the West web, as indicated by the partial-thickness crack (the edge of the bottom flange was not fractured) and the “EF” segment indicated on the West web. Next, the WF crack arrested when it encountered the crack propagating from the opposite flange edge. Finally, the web cracks (EW and WW) propagated upwards approximately 13.5 in.

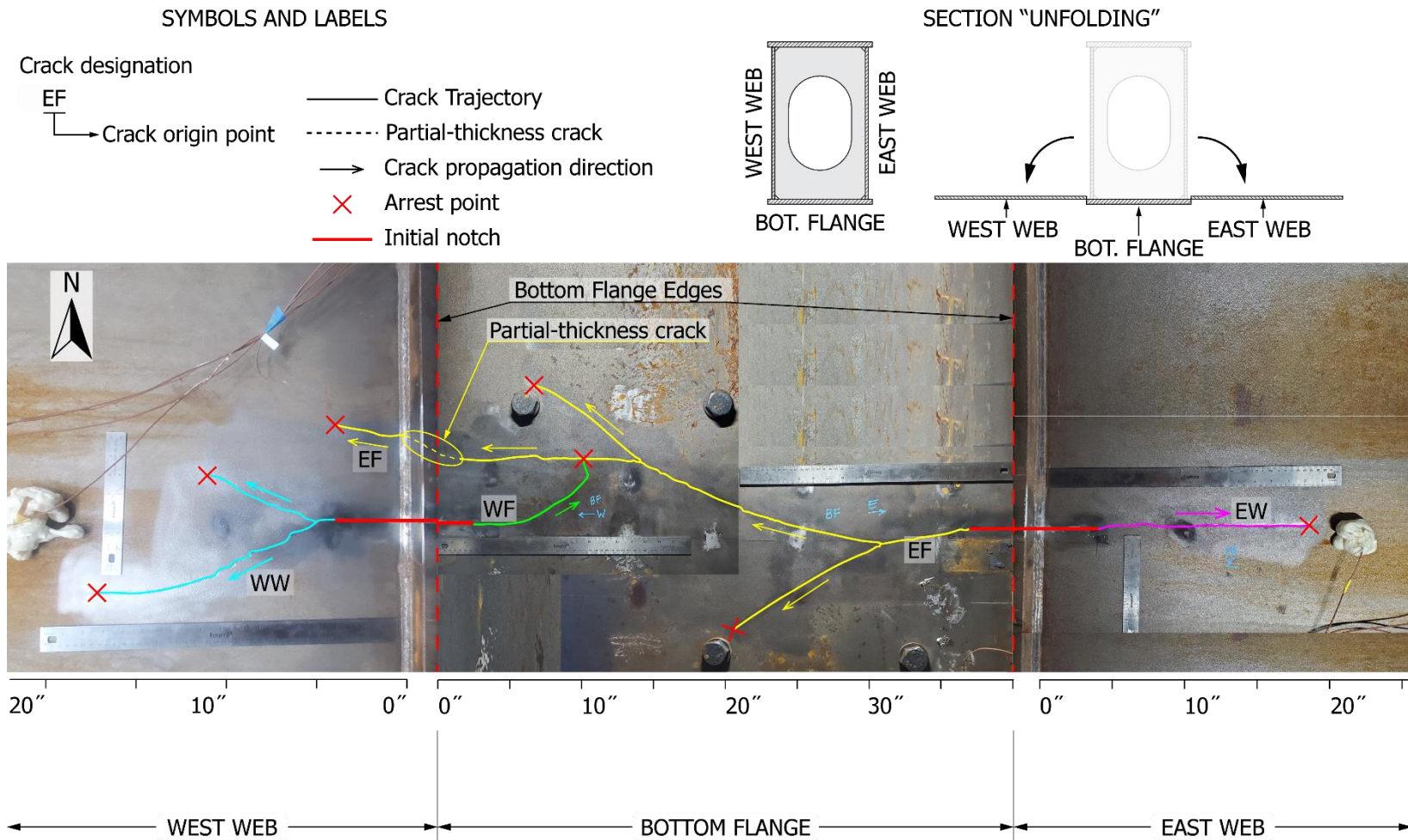


Figure 5.18: Specimen A: cracks after completion of Fracture Test



### 5.2.2. Ultimate Strength Test of Specimen A

Specimen A was tested in the fractured condition to assess the reserve capacity. In this condition, the PT bars were the primary tension component at the cracked section.

The behavior of Specimen A, when it was loaded with the bottom flange fractured, is shown in Figure 5.19. This test was conducted with the crack region at lower-shelf temperatures to produce a worst-case scenario.

1. As the specimen was loaded from the faulted configuration, it displayed an elastic response until the cracks that resulted from the previous Fracture Test (Section 5.2.1) propagated further. This behavior is shown in Figure 5.19 in the first peak of the diagram at 4,843 kip-ft. Based on the temperature readings at that portion of the webs, it is believed that this extension of the cracks was more closely related to high-strain rupture than brittle fracture propagation.

As observed in Figure 5.20, the PT bars experienced a sudden increase in the axial force (from an average of 31 kips per bar to approximately 56 kips per bar) when the cracks propagated. Moreover, it was detected that the PT bar No 6, located closer to the West web, fractured when the web cracks propagated upwards. This might have occurred due to the large volume of liquid Nitrogen pumped inside the specimen, which made the PT bar brittle. However, since this only happened to one of the bars (and under cryogenic temperatures, which were only introduced to make the fracture of the bottom flange and webs feasible), it was not considered a potential issue for applications of this design concept.

2. Because the pneumatic hydraulic pump was used, the load acting on the specimen could not be restored quickly, and the applied load dropped as the specimen suddenly deflected. The plot also shows the vibration/oscillation of the specimen following the fracture event.
3. Following the extension of the crack, the pumps kept displacing the pistons of the actuators until the specimen was reloaded. A continuous loss of stiffness was observed in this reloading stage, which was attributed to the yielding of the remaining portions of the webs. During the reloading, the average forces in the PT bars increased nearly linearly from an average force of 56 kips up to a value of approximately 140 kips.

At 6,687 kip-ft, the cracks on the West web propagated even further, almost reaching the top flange of the section. Only the West web experienced this second



crack extension, which correlates with the fracture of PT bar No 6, which was located on the west side of the girder. This crack extension was also credited to high strain rather than brittle behavior.

Because of this crack extension, the average force in the PT bars increased from 140 kips to 151 kips, while the total applied load dropped from 590 kips to approximately 400 kips. This increased force in the PT bars with a reduction in the total load is explained by the loss of the portion of the web that was in tension.

4. The extension of the cracks produced a sudden deflection of the specimen and a subsequent drop in pressure in the hydraulic equipment, as indicated in the plot in Figure 5.19.
5. Based upon the severe level of damage, it was decided to unload the specimen as it was judged that its ultimate capacity in the faulted state had been reached. Further loading the specimen would not have provided any additional information and would have complicated the specimen removal from the test setup.

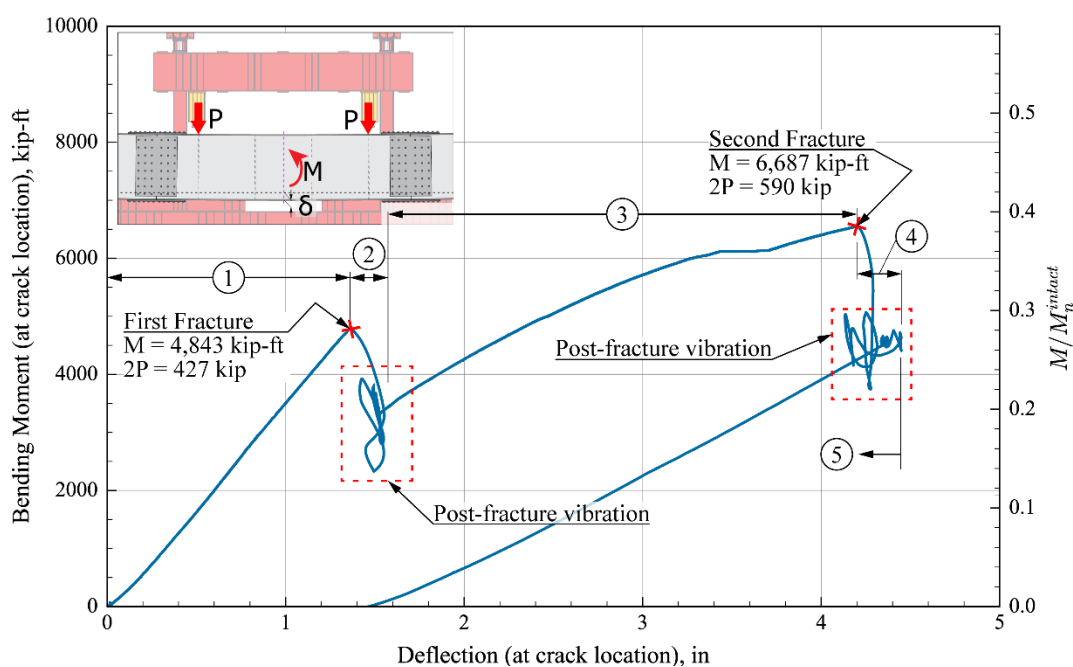


Figure 5.19: Specimen A Ultimate Strength Test: applied bending moment versus deflection at the cracked section

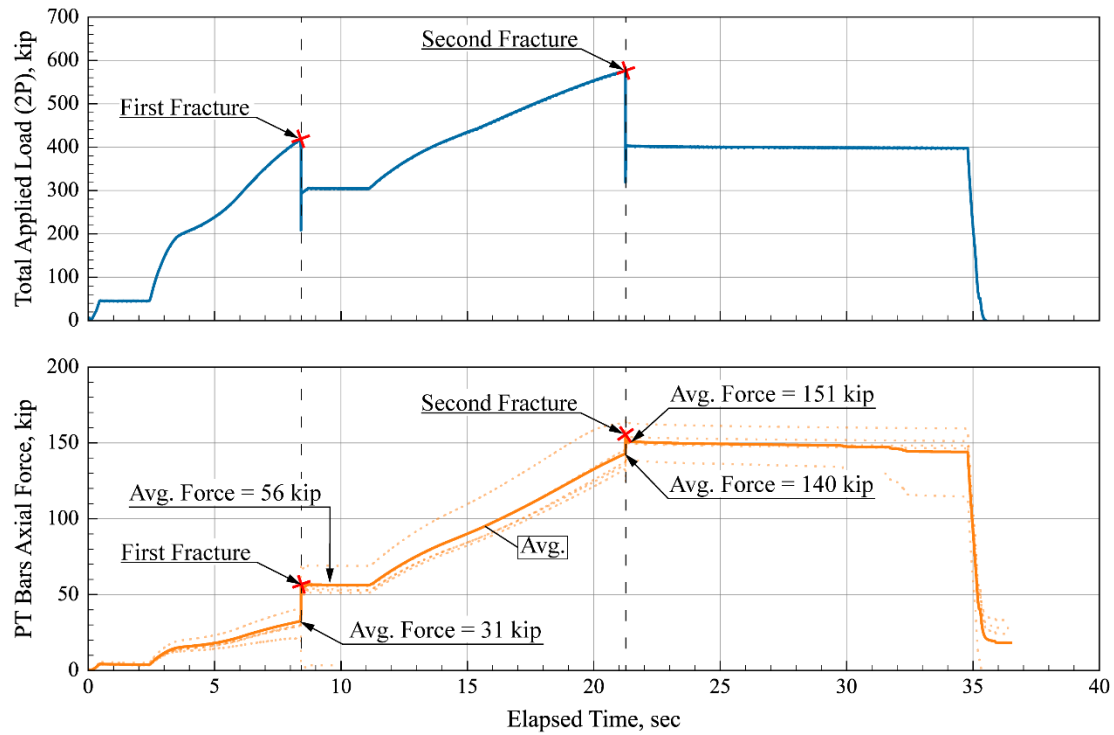


Figure 5.20: Specimen A Ultimate Strength Test: Loading sequence; total applied load (top) and axial force developed in the PT bars (bottom)

The cracks produced in the webs during all loading stages of Specimen A are indicated in Figure 5.21.

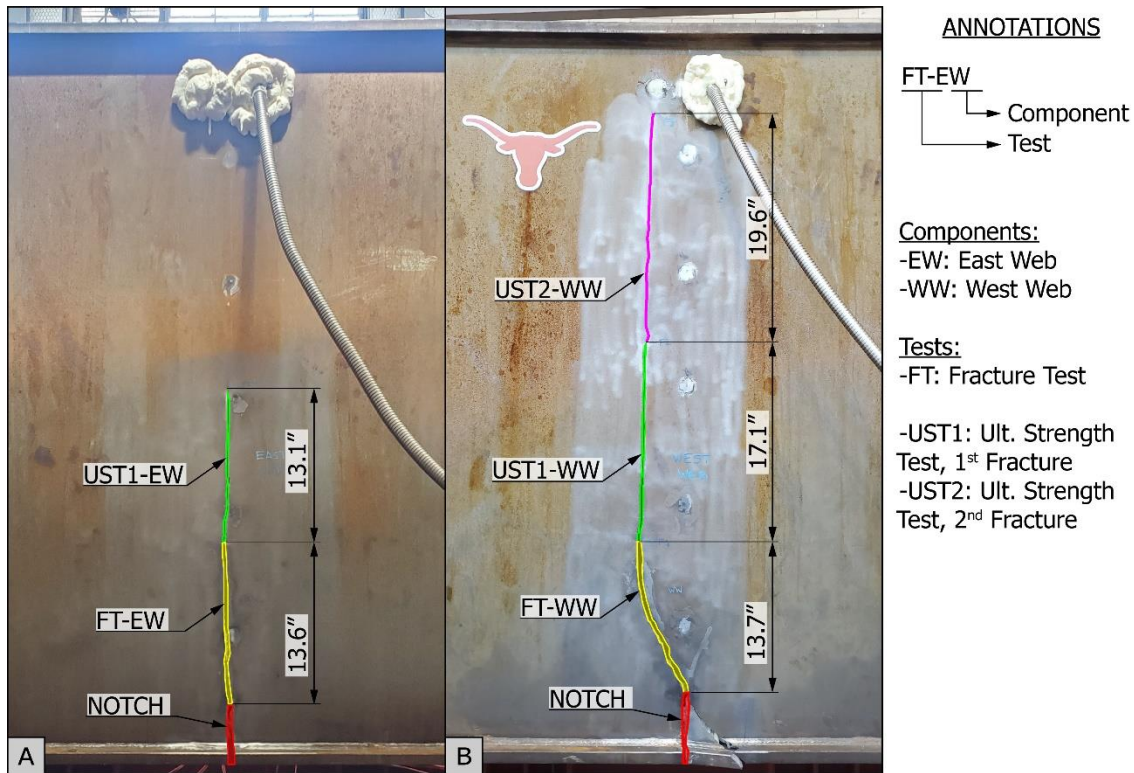


Figure 5.21: Specimen A: cracks observed on the webs through the different test stages: (A) East web; and (B) West web.

### 5.2.3. Observations

The results of the tests conducted on Specimen A provided insight into the performance of Design Concept A, which relies on the added PT bars to arrest the cracks and provide flexural capacity in the faulted condition.

As indicated in Section 4.1.1, adding the cover plate to the top flange of this specimen changed the ratio between the capacity in the assumed faulted condition and the undamaged/intact state from 70% to 45%. The faulted section is considered to have reached its flexural resistance at the first yield of any of its components; this capacity is reached when the stress at the tip of the crack (i.e., the lower edge of the remaining web plate) reaches the yield stress, corresponding to a bending moment of 4,903 kip·ft. As such, Specimen A was capable of surpassing this target load before the cracks on the webs continued to propagate.

Although the 70-percent target redundancy load level was not met, adding the PT bars significantly increased the stresses required to fracture the tension flange from 4 ksi for the Baseline Specimen to 13.3 ksi for Specimen A. In terms of the load level required to

produce the first fracture, Specimen A reached 27% of the yield moment of the undamaged/intact section, while the Baseline Specimen fractured at 9% of the undamaged/intact section yield moment. This improvement was largely in part due to the engagement of the PT bars in the flexural response before the specimen fractured, even though the bars were not pretensioned. Although the fracture delay is beneficial, the engagement of the PT bars in the undamaged/intact condition could introduce fatigue problems in the regions where the bars are anchored.

When tested in the faulted condition (i.e., after the fracture had occurred), the PT bars acted as the tension component of the section. The ultimate capacity of Specimen A was 6,687 kip·ft, equivalent to 49% of the yield moment of the undamaged/intact section. However, the webs ruptured during this test stage due to the large strains produced, ultimately leading to the almost complete loss of the West web. This observation highlights the most important drawback of this design concept, as the faulted section would have a drastic loss of shear strength.

Adding more PT bars could increase the flexural capacity of the faulted section, but it would likely not prevent the extension of the cracks to the point where a large portion of the webs is lost. However, increasing the amount of reinforcement would require stiffer and stronger anchor regions for the bars, which would complicate the implementation of this retrofitting approach. In addition, changes to the PT bar arrangement, such as stiffening the system by employing double nuts at each internal diaphragm, could delay the yielding of the web plates, reducing the likelihood of crack propagation in the webs. However, even if the cracks were arrested at some point (as it happened during the Fracture Test of Specimen A), the large deformations required to develop the full strength of the bars could still produce high strains in the remaining portions of the webs and potentially rupture them, substantially dropping the shear capacity of the faulted section.

Parametric FE analyses, presented in Chapter 6, were conducted to address these points.

## 5.3. Experimental Testing of Specimen B1

### 5.3.1. Fracture Test of Specimen B1

The initial notches of Specimen B1 were made only on the bottom flange plate (illustrated in Figure 5.22) so that a fracture event could be simulated in the largest component of the cross-section. The initial notches were located at 33.77 ft from the North support, midway between intermediate diaphragms, as illustrated in Figure 5.23.

To ensure that the cracks would not arrest at the adjacent holes, the researchers first made two cuts tangent to a bolt hole on the outer line. Then, a single cut from the bolt hole was made using a jigsaw extending to the second bolt line, as shown in Figure 5.24.

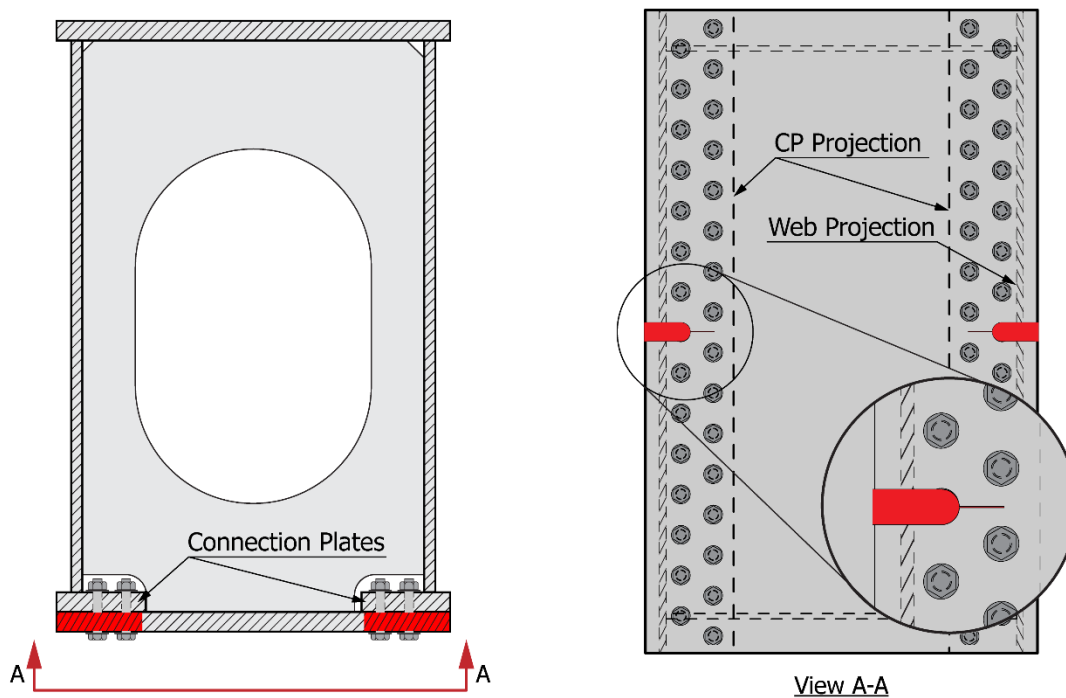


Figure 5.22: Specimen B1: initial notches

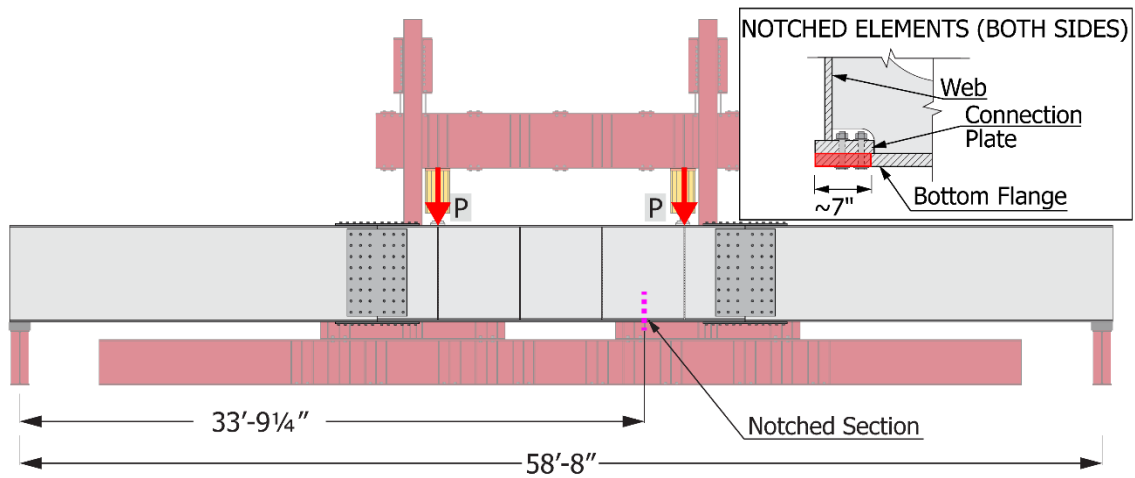


Figure 5.23: Specimen B1: location of the notched section

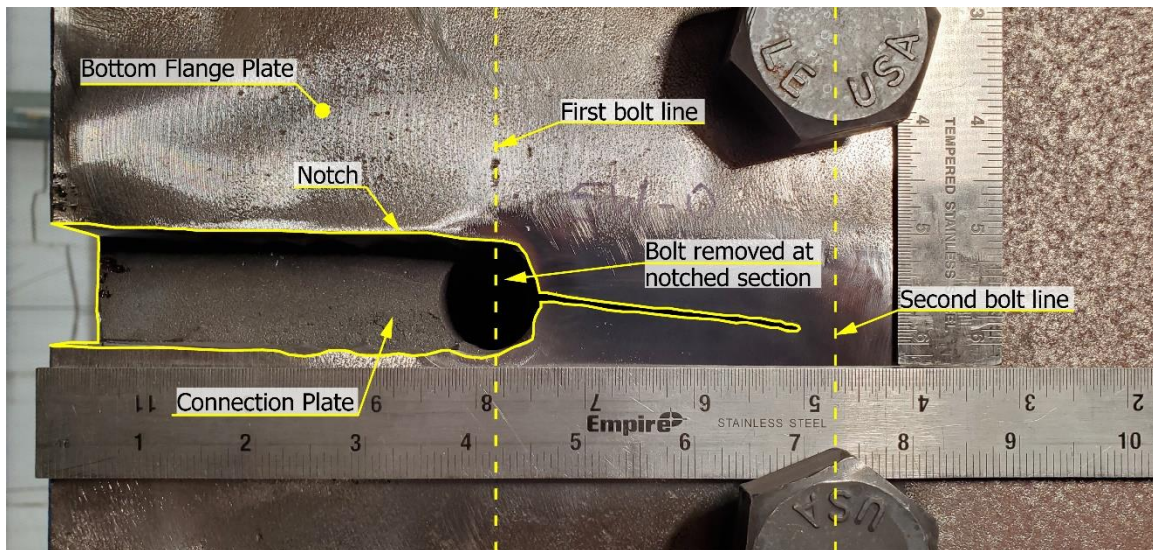
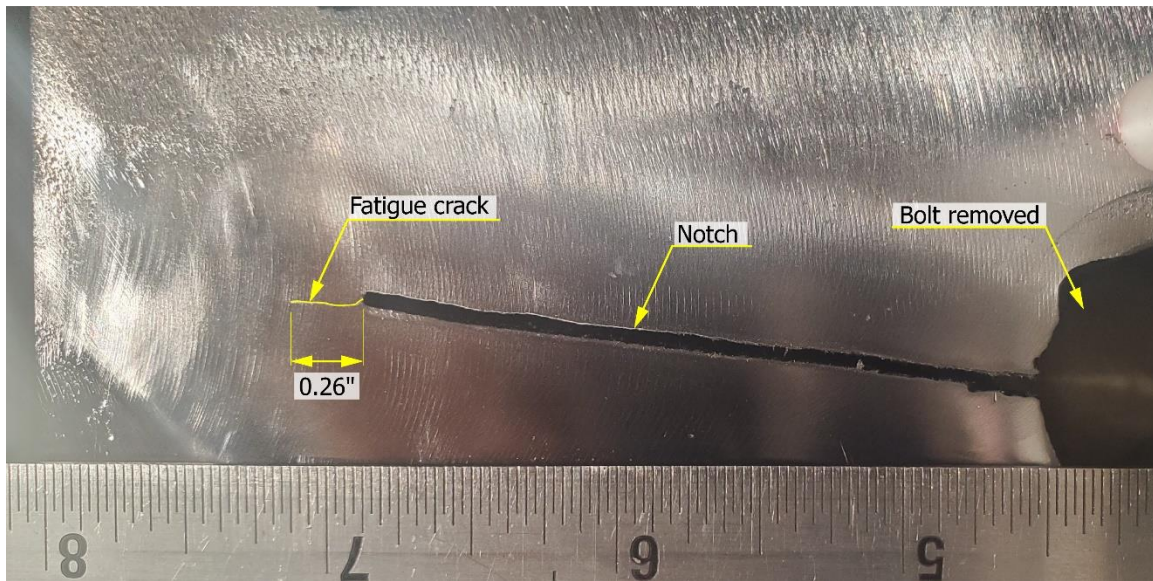


Figure 5.24: Specimen B1: initial notches on the East bottom flange edge

Specimen B1 required 11,000 load cycles to develop the necessary fatigue cracks. As with the other specimens, the load range was set from 10 to 180 kips per actuator (corresponding to a stress range of 11.3 ksi) at a frequency of 0.125 Hz. Figure 5.25 illustrates the fatigue cracks obtained from the cyclic loading.





*Figure 5.25: Specimen B1: fatigue crack emanating from the notch on the bottom flange*

The temperature distribution measured at the notched section at the start of the fracture loading is illustrated in Figure 5.26. Although the temperature readings show a highly uneven distribution and values above the previous tests, an Omega thermocouple thermometer was used to verify that the temperature was in the lower-shelf region (see Section 4.1.3). The discrepancy with the thermocouples was attributed to poor insulation of the thermocouple wires at the welded tips and the eddy currents produced by the temperature difference between the specimen and the surrounding air.

Besides ensuring that the bottom flange plate was in the lower-shelf region, it was verified that the flange connection plates were also in that temperature range. This situation would make the flange connection plates brittle and make it more likely for the cracks to sever the plates if they propagated to that component or as a consequence of the energy release produced during the fracture event.



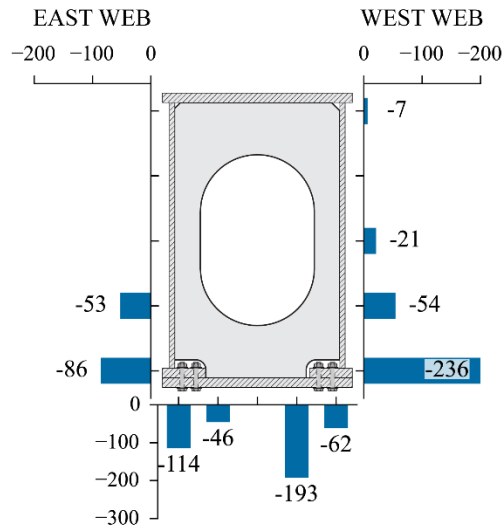


Figure 5.26: Specimen B1: temperature distribution at the notched section ( $^{\circ}\text{F}$ ). Readings from thermocouples affected by eddy currents at the tips of the wires.

The loading sequence corresponding to the Fracture Test of Specimen B1 is described subsequently and illustrated in Figure 5.27:

1. This specimen was loaded attempting to simulate dynamic loading. As with the tests previously described, the behavior of the specimen was approximately linear until the occurrence of the fracture. When the applied bending moment reached 4,382 kip·ft (for a total applied load of 391 kips), corresponding to a maximum tensile stress of 12.7 ksi in the bottom flange plate, the fatigue cracks propagated and severed the entire bottom flange, as shown in Figure 5.28.
2. The drop in load and the vibration following the fracture were less significant than in the previous specimens, partly due to the use of the MTS hydraulic equipment but also because the loss of cross-sectional area was restricted to the bottom flange plate. The loading for this first stage continued until the capacity of the hydraulic pump was reached, producing a maximum bending moment of 4,933 kip·ft.
3. Following reaching the hydraulic pump capacity, the specimen was unloaded completely, showing a permanent deflection of only 0.06 in.

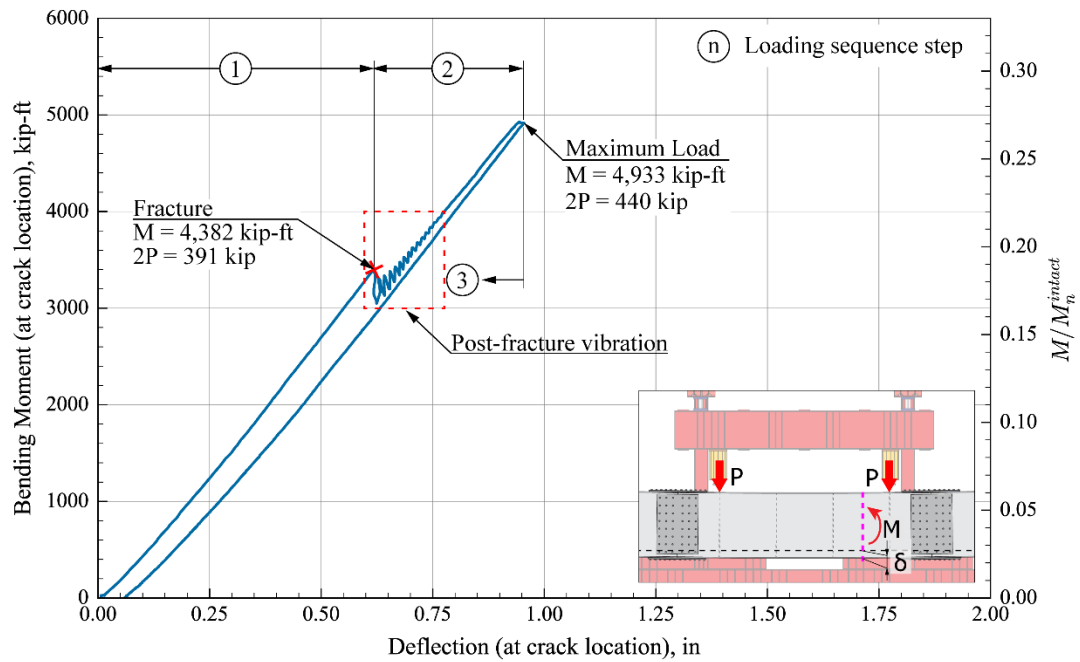


Figure 5.27: Specimen B1 Fracture Test: bending moment versus deflection at the cracked section

The trajectory of the cracks on the bottom flange is shown in Figure 5.28, which shows how the crack that started from the East flange edge (EF) seems to have propagated more rapidly across the width of the plate. On the other hand, the crack that initiated from the West edge of the flange (WF) could only grow a few inches until it arrested against the EF crack.

# SYMBOLS AND LABELS

Crack designation

EF

→ Crack origin point

— Crack Trajectory

→ Crack propagation direction

× Arrest point

Initial notch

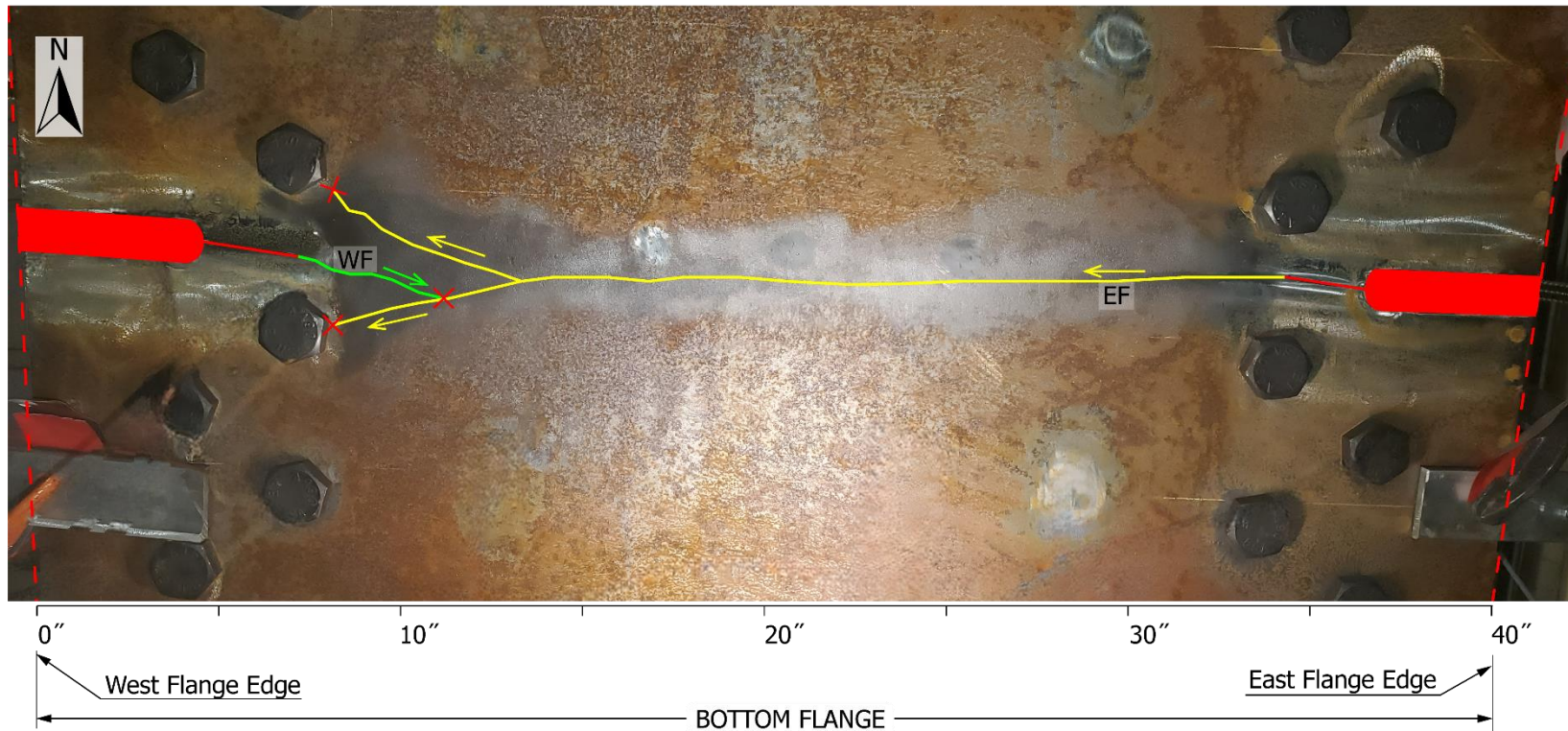


Figure 5.28: Specimen B1: cracks after completion of Fracture Test

As mentioned in Table 4.4 of Section 4.1.1, the area of the bottom flange plate accounts for 69% of the total area of the tension flanges. Although these proportions violate the limits of the AASHTO Guide Specification for IRMs (AASHTO 2018-1), the performance of this specimen during the fracture test was highly satisfactory.

### **5.3.2. Ultimate Strength Test of Specimen B1**

As was used for Specimen A, the ultimate strength test was conducted using the 10,000 psi pneumatic hydraulic pump. The ultimate strength evaluation of Specimen B1 was conducted at room temperature first and then at low temperatures to induce the brittle fracture of the tensile components

- At room temperature, the specimen was loaded twice: (1) until reaching the theoretical yield moment of the faulted section (8,700 kip·ft) and (2) up to the theoretical plastic moment of the faulted section (12,800 kip·ft), as shown in Figure 5.29 and labeled RT-1 and RT-2, respectively. The decreasing stiffness with increasing load in Figure 5.29 indicated that permanent deformations in the flange connection plates resulted in the opening of the crack, as seen in Figure 5.30.
- The specimen was cooled to lower-shelf temperatures and loaded once more until it failed due to the buckling of the top flange. This loading stage is labeled as “LT” in Figure 5.29. After reaching the calculated plastic moment of the faulted section (12,800 kip·ft), the stiffness of the specimen decreased until the top flange buckled at approximately 14,000 kip·ft. The buckled top flange is shown in Figure 5.31-A.
- At this point in loading, the specimen had experienced extensive deformations (approximately 5 in. of vertical deflection), and it was decided to stop the test so as not to complicate the demobilization tasks. The photo shown in Figure 5.31-B was taken inside the specimen following the experiment. Several bolts were removed from the vicinity of the crack to observe the elongation of the holes as the bolts slipped and were in bearing on the edges of the holes.

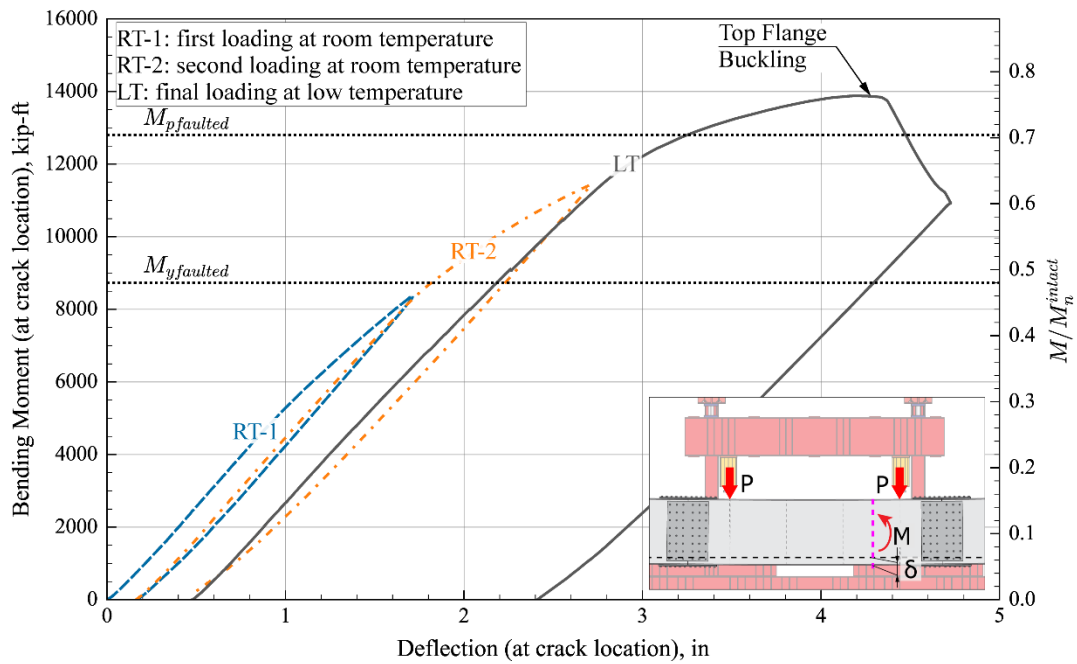


Figure 5.29: Specimen B1 Ultimate Strength Test: bending moment versus deflection at the cracked section

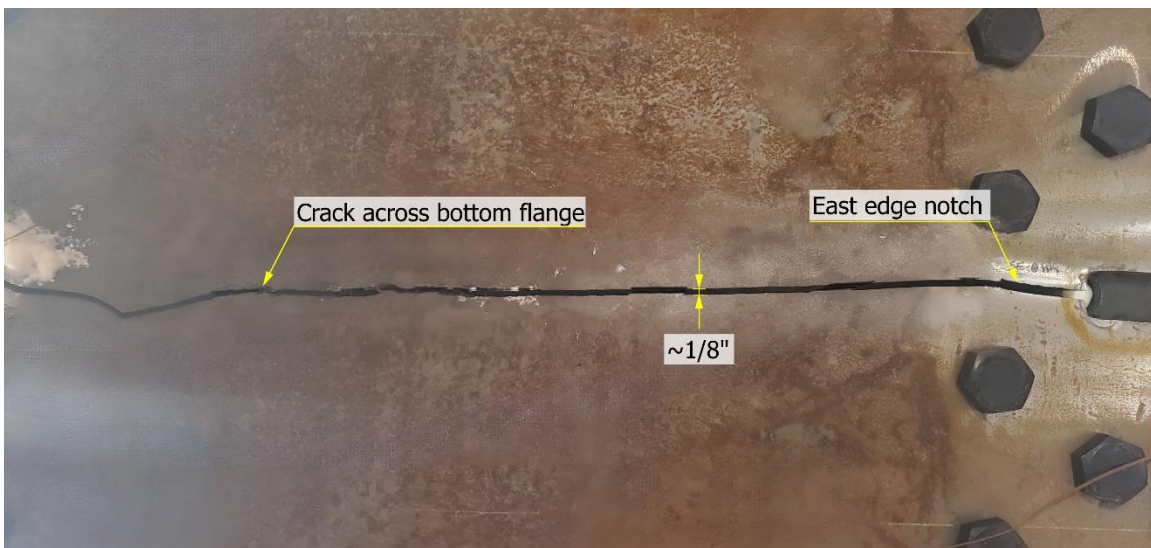


Figure 5.30: Specimen B1 Ultimate Strength Test: bottom flange crack after reaching the calculated plastic moment of the faulted section and unloading the specimen



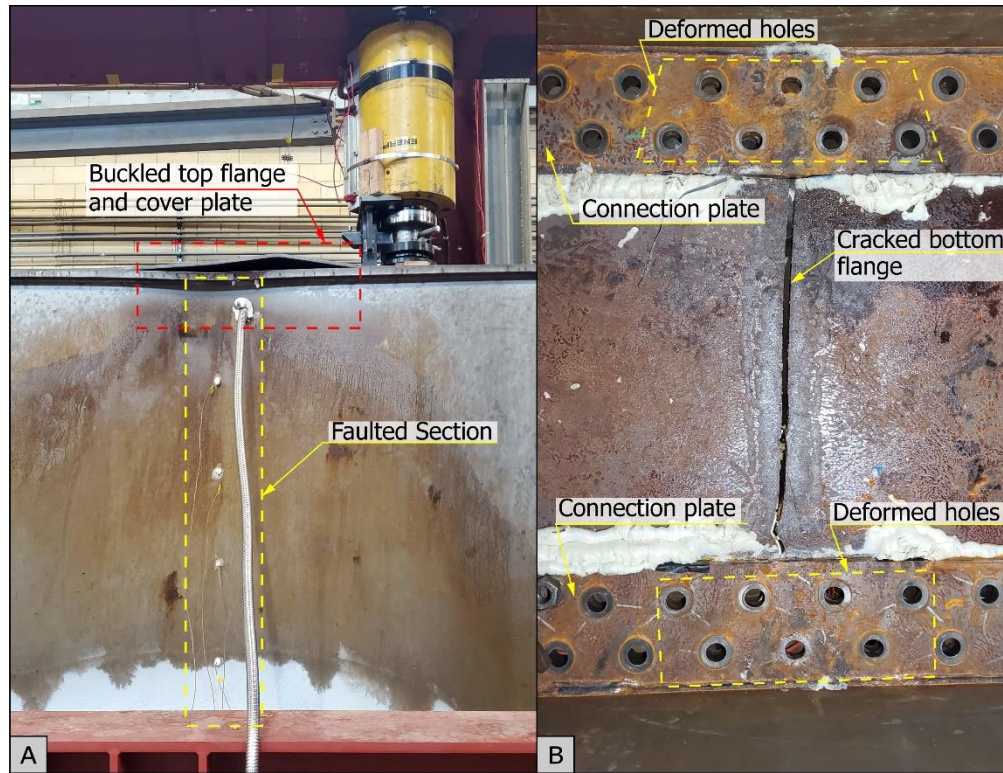


Figure 5.31: Specimen B1 Ultimate Strength Test: (A) Buckled top flange and cover plate, and (B) bottom flange crack and flange connection plates (bolts removed) after final loading.

### 5.3.3. Observations

The most important observation of the testing of Specimen B1 is that the cracks did not propagate from the bottom flange plate to the flange connection plates, despite all those components being at lower-shelf temperatures, and the load was applied dynamically. This result highlights the effectiveness of cross-boundary separation as an internal redundancy approach. Additionally, the performance of this specimen was highly satisfactory, even considering that the dimensions of the bottom flange and the flange connection plates violate the recommendations of the AASHTO Guide Specification for IRMs (AASHTO 2018-1).

Furthermore, the behavior of Specimen B1 during the Ultimate Strength Test showed promising behavior since the target redundancy load was met, the theoretical plastic capacity of the faulted section was exceeded, and the specimen showed large amounts of ductility as it approached the maximum capacity.

## 5.4. Experimental Testing of Specimen B2

### 5.4.1. Fracture Test of Specimen B2

The fracture test of Specimen B2 followed the same sequence as Specimen B1. Both specimens were notched at the same location, as shown in Figure 5.32 and Figure 5.23. The geometry of the notch, depicted in Figure 5.33, was also identical but was made with an acetylene track torch instead of a jig saw. Special care was taken to ensure that the cutting process did not affect the flange connection plate to avoid introducing a defect in this component.

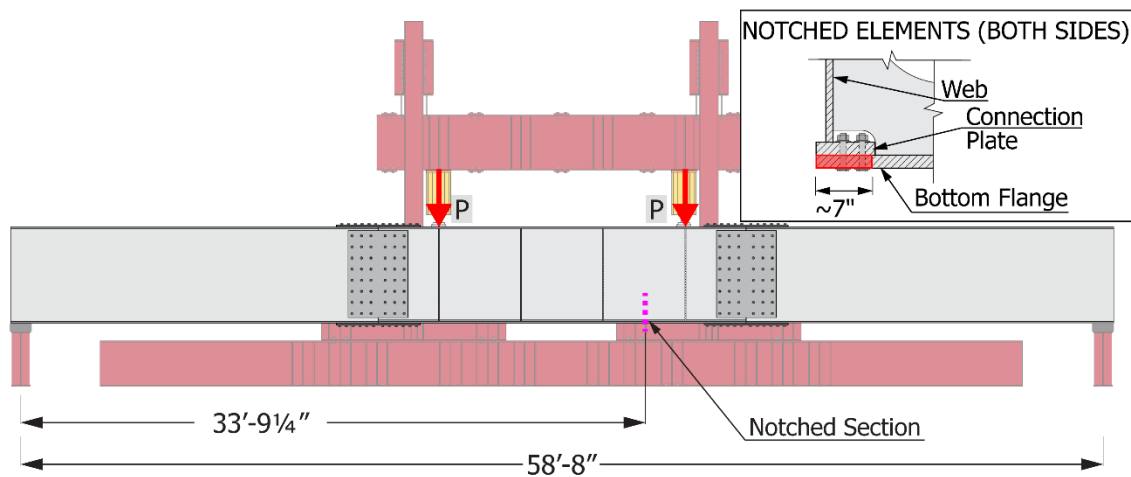


Figure 5.32: Specimen B2: location of the notched section

Because of the larger section modulus of this specimen and the blunt tip radius of the notch created by the torch, 25,000 load cycles were required to produce fatigue cracks emanating from the notches that were long enough to be equivalent to a full-length crack. The fatigue crack emanating from the notch made on the East edge of the bottom flange plate is shown in Figure 5.34.



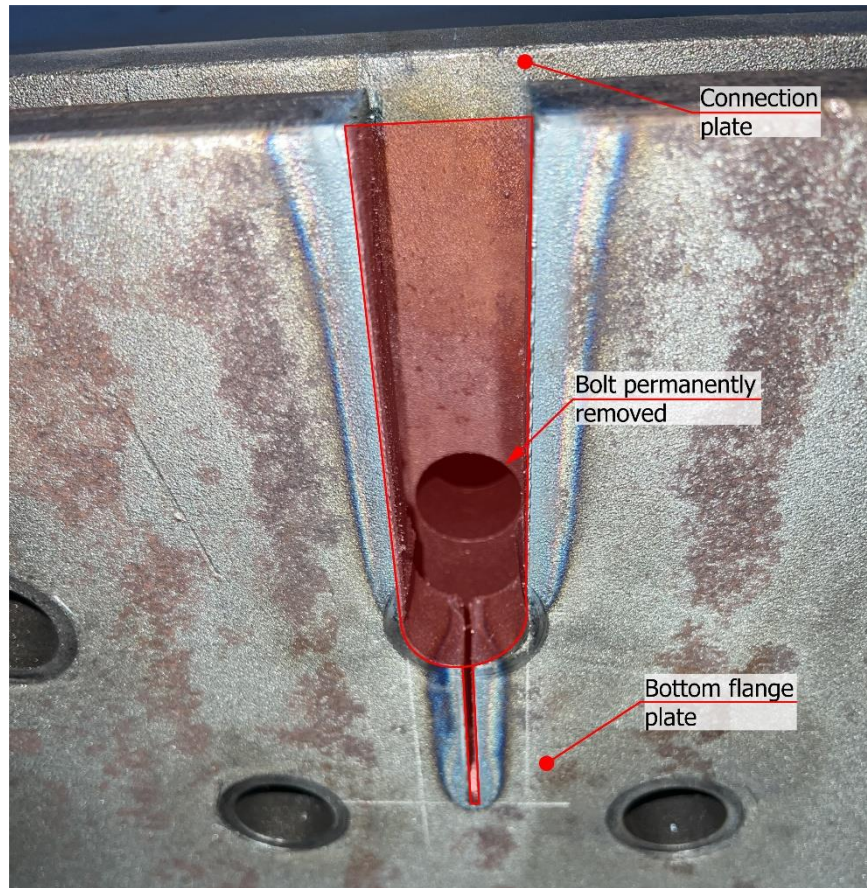


Figure 5.33: Specimen B2: initial notch on the West bottom flange plate

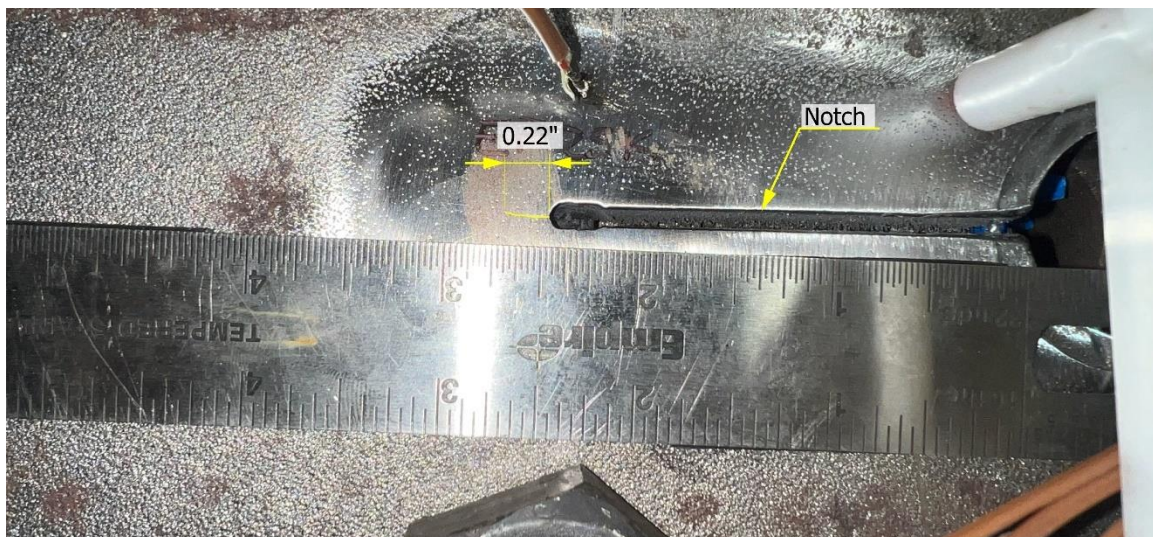


Figure 5.34: Specimen B2: fatigue cracks emanating from the notch on the East flange edge

As with the rest of the specimens, liquid Nitrogen was introduced inside the girder at the top of the webs to lower the temperature of the steel to the lower-shelf toughness range. The temperature profile at the notched section before starting the loading protocol is illustrated in Figure 5.35. The thermocouple wires used in this test were insulated by covering the wire ends with expansive foam. As a result, the temperature readings corresponding to this experiment were less affected by the circulation of air at room temperature, and lower temperatures were recorded. In earlier tests, the circulation of hotter air likely indicated higher temperatures, particularly on the webs.

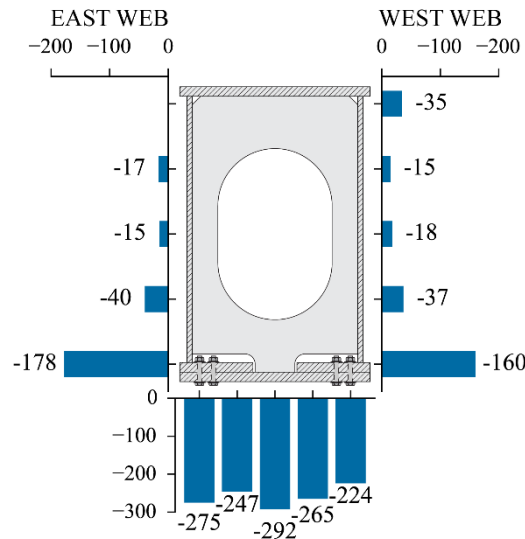


Figure 5.35: Specimen B2: temperature distribution at the notched section (F)

The loading sequence corresponding to the Fracture Test of Specimen B2 is described subsequently and illustrated in Figure 5.36:

1. The hydraulic actuators applied the loads to Specimen B2 dynamically. The response of the specimen was approximately linear until the occurrence of the fracture at a bending moment of 3,609 kip·ft (313 kips), corresponding to a maximum tensile stress of 9.7 ksi in the bottom flange plate. The fatigue cracks propagated and severed the entire bottom flange, as shown in Figure 5.37.
2. The trajectory of the cracks shows how the crack that originated from the East edge of the bottom flange (EF) grew towards the West edge. As it approached the crack initiated at the West edge of the bottom flange (WF), the EF crack bifurcated and arrested in the vicinity of the bolt holes. The WF crack only propagated a few inches and arrested before reaching the EF crack.

3. As was observed with Specimen B1, the drop in load and the vibration following the fracture were minimal, partly due to the use of the MTS hydraulic equipment but also because the loss of cross-sectional area was restricted to the bottom flange plate. The loading continued until the capacity of the hydraulic pump was reached, producing a maximum bending moment of 4,728 kip·ft.
4. Following the fracture and maximum loading in the test, the specimen was unloaded completely, showing a negligible residual deflection of approximately 0.030 in.

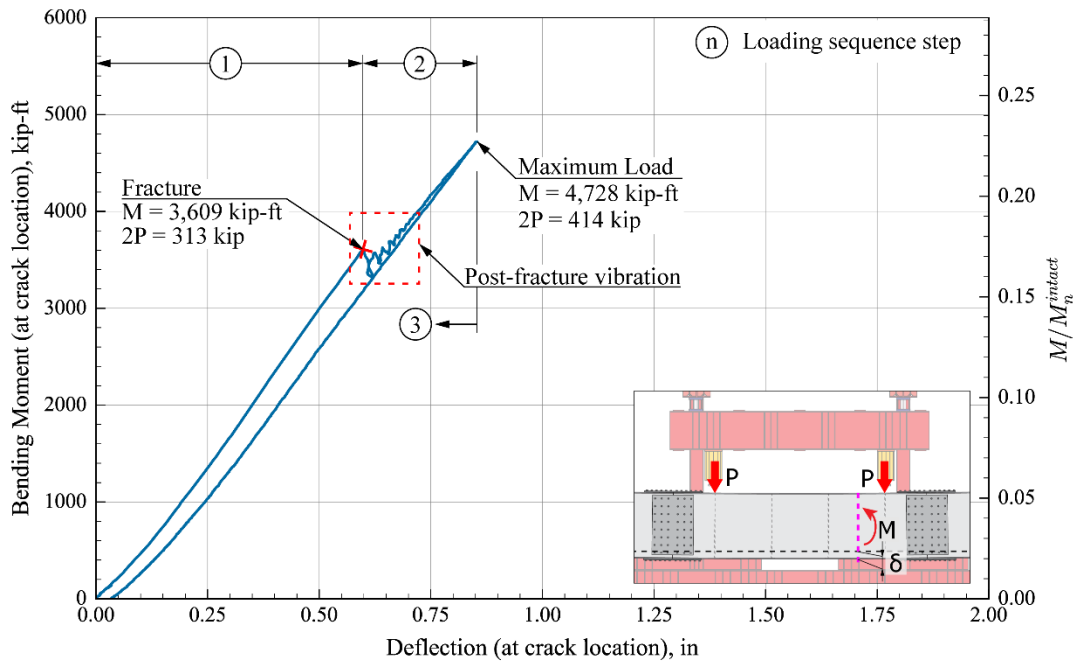


Figure 5.36: Specimen B2 Fracture Test: bending moment versus deflection at the cracked section



# SYMBOLS AND LABELS

Crack designation

EF

→ Crack origin point

— Crack Trajectory

→ Crack propagation direction

× Arrest point

Initial notch

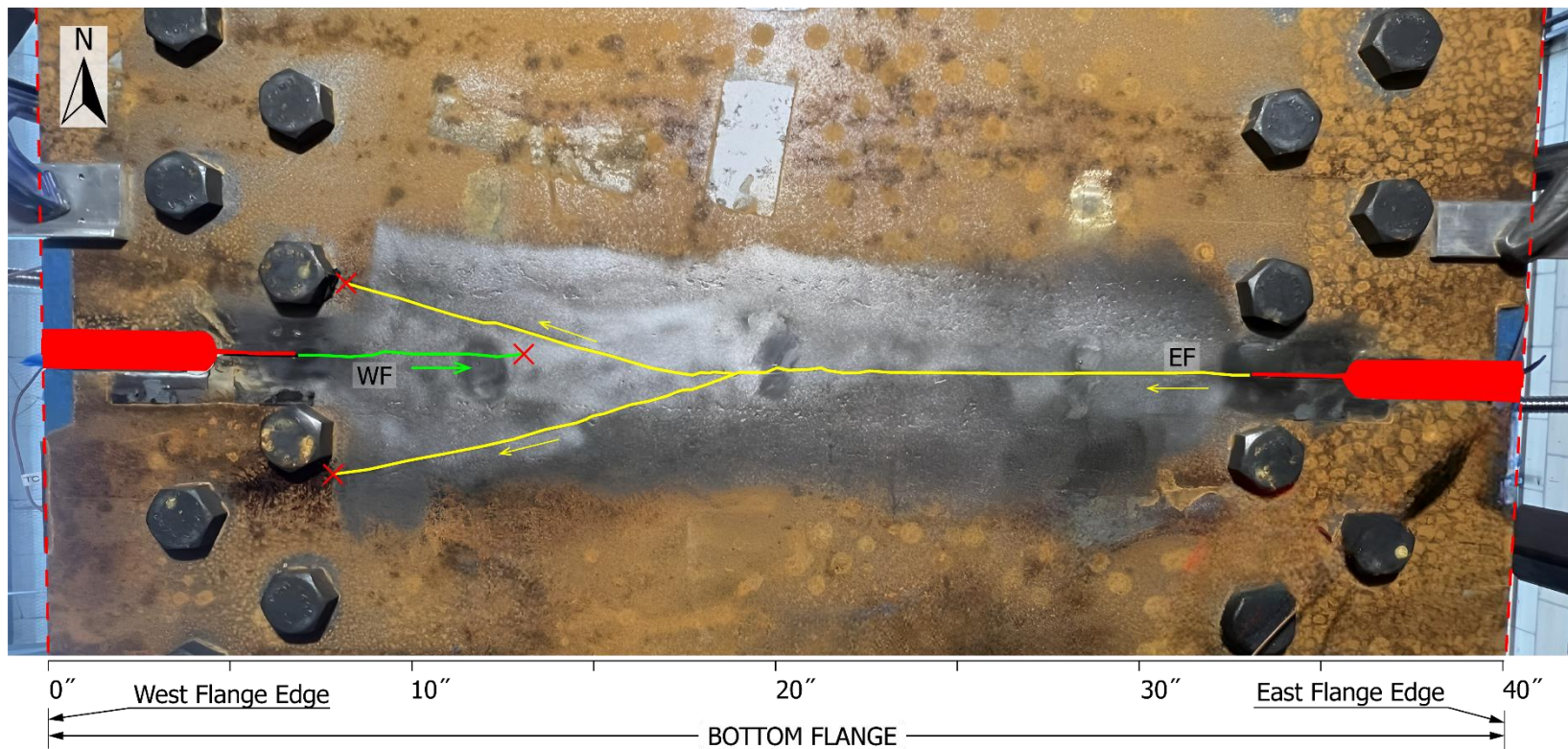


Figure 5.37: Specimen B2: fractured bottom flange plate after Fracture Test

Since the ratio of the area of the bottom flange plate to the area of all the flange components of Specimen B2 is 57% (see Table 4.4), the cross-sectional dimensions of Specimen B2 are in compliance with the provisions of the AASHTO Guide Specification for IRMs (AASHTO 2018-1). The performance of this specimen during the fracture test was highly satisfactory, and the cross-boundary separation provided an effective mechanism for limiting the damage produced by the propagation of the fatigue cracks.

#### **5.4.2. Ultimate Strength Test of Specimen B2**

Finally, the ultimate capacity of Specimen B2 was assessed by loading it in the faulted condition. A 10,000-psi pneumatic pump was utilized for this test to provide enough pressure to supply the actuators to their total capacity. The test was conducted while the specimen was at a temperature corresponding to the lower shelf fracture toughness region to reduce the fracture toughness of the flange connection plates and maximize the potential for cracking/fracture.

The specimen was loaded to a level corresponding to the theoretical plastic moment of the faulted section was reached. This loading stage is illustrated in Figure 5.38. After reaching the calculated yield moment of the faulted section (12,034 kip·ft), the stiffness of the specimen decreased continuously until reaching the maximum moment of 16,815 kip·ft. At that point, the pump had reached its maximum pressure. Upon unloading, a permanent vertical deflection of 0.8 in. was measured.

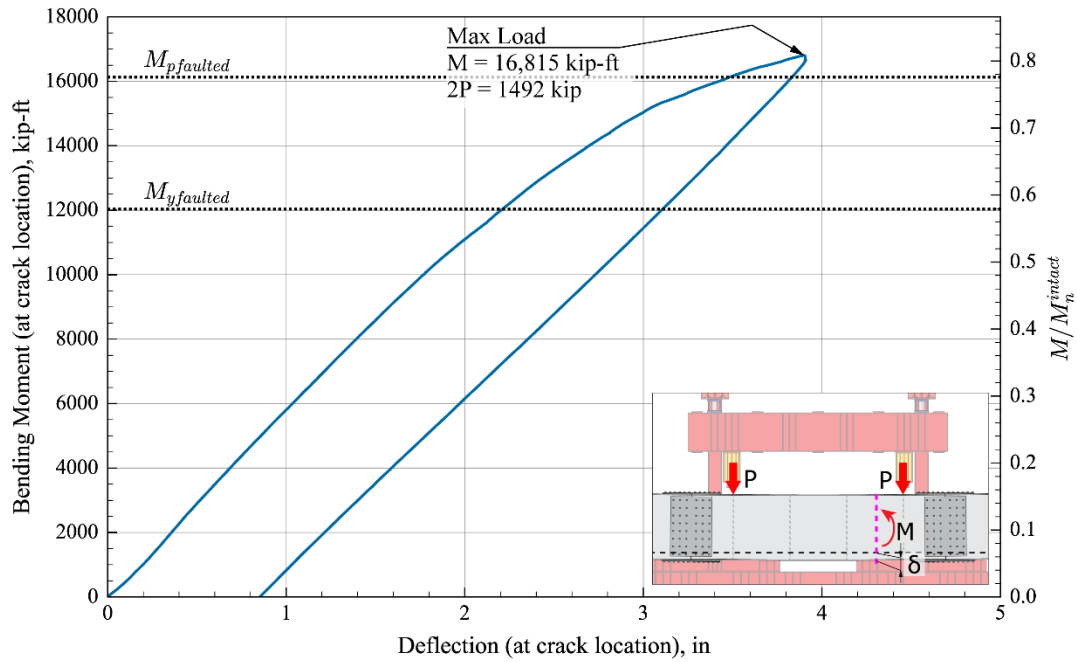


Figure 5.38: Specimen B2 Ultimate Strength Test: bending moment versus deflection at the cracked section

### 5.4.3. Observations

Similar to the observed behavior of Specimen B1, the experimental testing of Specimen B2 showed that the bolted connection between the tension components of the box girder effectively provided cross-boundary separation and prevented the propagation of cracks between the connected components. Moreover, this crack-arresting mechanism worked well despite the fact that the secondary tension components -the flange connection plates- were also in the lower-shelf temperature region.

Regarding the target redundancy load, it was possible to load this Specimen beyond its theoretical plastic moment corresponding to the faulted section without observing signs of premature failure.

## 5.5. Results Comparison

The results of the tests of Specimens A, B1, and B2 are shown in Figure 5.39. The curve corresponding to each specimen combines the data for the fracture test and ultimate strength test to reconstruct the entire loading curve of each specimen, from the initial loading to produce the fracture to the ultimate loading. To enhance the visualization of the

curves in the initial loading branches, a close-up of this area of the plot is provided in Figure 5.40.

The test results corresponding to the fracture test of the Baseline Specimen are also plotted to provide a performance benchmark. It should be noted that no ultimate strength test was performed on the Baseline Specimen to avoid severe damage to the specimen that was to be repaired, flipped, and utilized for Specimen A. Therefore, the results of its fracture test are included only as a reference.

In order to produce valid comparisons between the specimens, the vertical axis shows the bending moment applied at the crack section of each specimen normalized by its nominal flexural resistance in the undamaged/intact condition. The bottom horizontal axis shows the absolute deflections measured at the fractured section for each specimen, and the top horizontal axis shows the vertical deflections normalized by the span length,  $L$ .

Furthermore, horizontal lines are drawn to indicate the estimated capacity of the specimen in the faulted condition based on sectional analysis:

- The estimated capacity Specimen A (indicated as  $M_y^{A\text{ faulted}}$ ) corresponds to the first yield of the remaining web plates when the bottom flange and half of the web depth are assumed fractured, as detailed in Table 4.1.
- For Specimens B1 and B2, the ultimate capacity in the faulted condition is computed as the plastic moment of the faulted section ( $M_p^{B1\text{ faulted}}$  and  $M_p^{B2\text{ faulted}}$ ), as shown in Table 4.2 and Table 4.3.

As seen in Figure 5.39, Specimen A showed a significant improvement with respect to the Baseline Specimen. While the Baseline Specimen fractured below 10% of its undamaged/intact nominal flexural capacity, Specimen A did not fracture until the applied load reached approximately 27% of the flexural capacity of the undamaged/intact section. This significant increase in the fracture load was attributed to the contribution of the PT bars before the fracture occurred, reducing the stress concentration at the crack tips by engaging in the flexural mechanism of the box cap.

When these specimens were loaded beyond the first fracture event, the Baseline Specimen could only support a load corresponding to 22% of the yield moment of the undamaged/intact section before the cracks propagated up to the mid-depth of the webs. Conversely, Specimen A reached 39% of the capacity of the undamaged/intact section when the cracks continued to propagate on both webs.



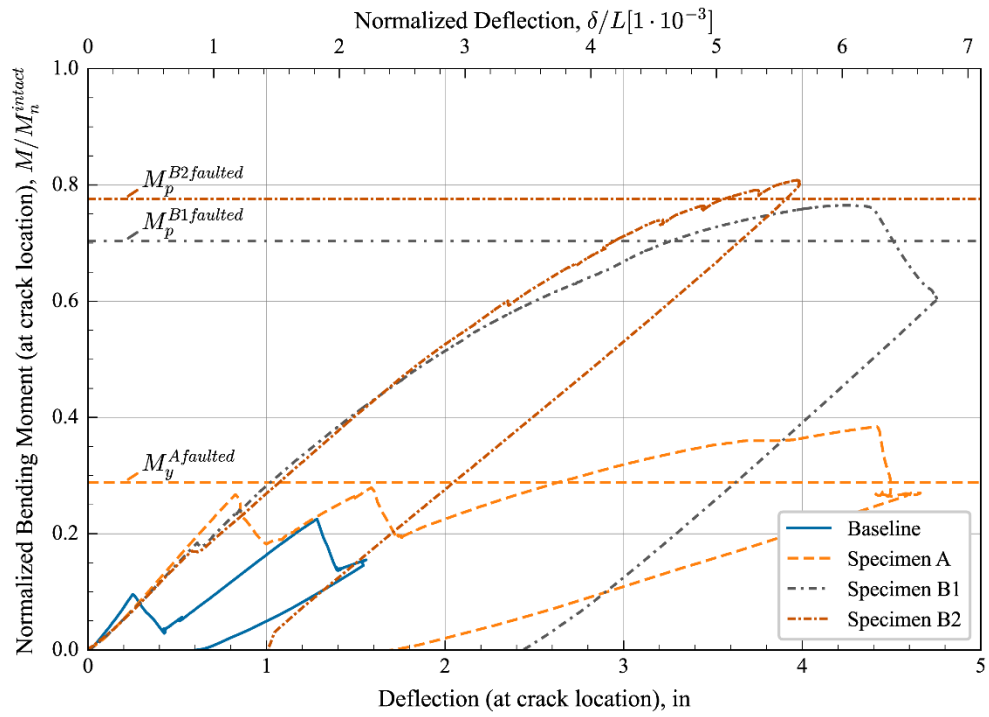


Figure 5.39: Ultimate Strength Tests: comparison of results

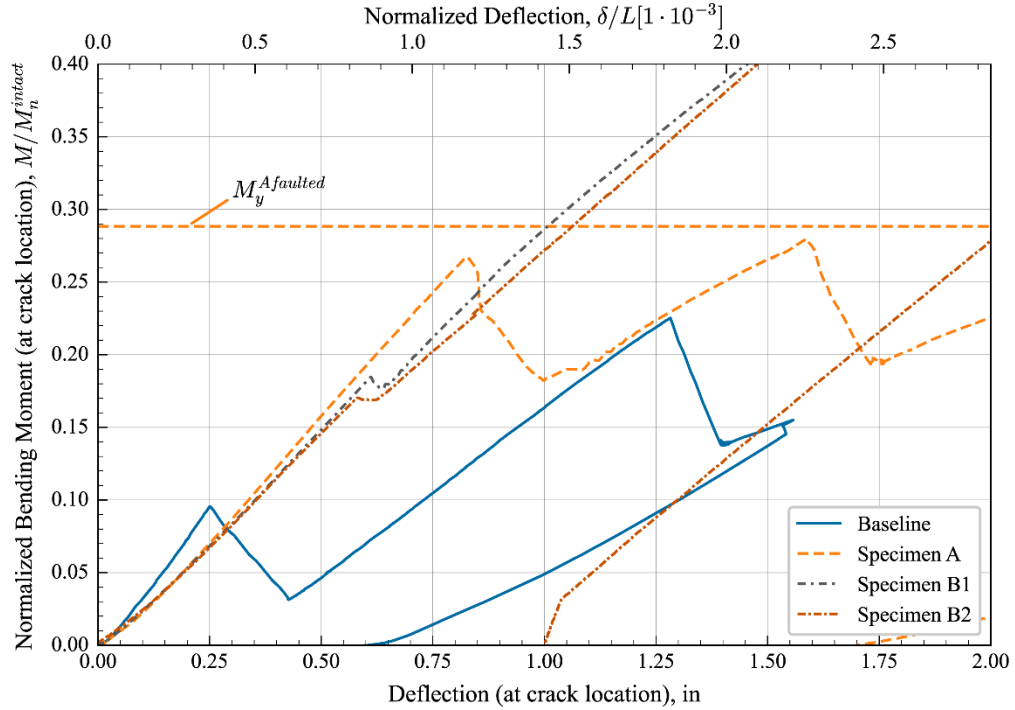


Figure 5.40: Ultimate Strength Tests: comparison of results (close-up view at the origin)

These observations highlight the contribution of the PT bars in delaying the fracture event, arresting the cracks, and acting as the tensile component in the faulted state. However, as mentioned in Section 5.2.3, the PT bars did not prevent the propagation of the cracks on the webs, as the large deformations required to develop their full tension capacity produced large strains at the remaining portions of the webs and the successive fracture events observed during the ultimate strength test. This situation would lead to the loss of the shear strength of the section, providing a much lower capacity if the fracture occurred in a section with high shear demands.

The flexural strength of this design concept can be improved by adding more PT bars or increasing their diameter, granted that the anchor points are designed accordingly. However, the rupture of the webs would still represent an issue as the PT bars reach higher tensile forces, which require large deformations.

On the other hand, Specimens B1 and B2 performed very well and are excellent candidates for achieving the desired redundancy. In both cases, the cracks were limited to the bottom flange plate due to the cross-boundary fracture resistance provided by the bolted connections. Moreover, both specimens were loaded beyond their theoretical plastic moment capacity in the faulted condition, exhibiting a ductile behavior.

For the crack condition studied, the flange connection plates effectively transferred the load back to the undamaged/intact components of the box section and acted as the primary tension element of the cross-section at the fractured section. Based on the fracture test of Specimen B1, no issues were found when the relative proportions of the bottom flange area to the flange connection plates area were 9% above the limit defined by the AASHTO Guide Specification for IRMs (2018-1). Wider flange connection plates, as in Specimen B2, would meet the Guide Specifications requirement and provide a higher capacity in the faulted condition. Ultimately, flange connection plates as wide as half of the width of the bottom flange plate could be utilized.

## 5.6. Summary

The procedures and results of the experimental program conducted in this research study were presented in this chapter. First, all specimens were tested to produce a fracture and assess their performance in conditions that favor the propagation of fatigue cracks (i.e., large fatigue crack-like defects and low fracture toughness due to low temperature). Next, the internally-redundant specimens were tested to evaluate their reserve capacity in the faulted condition. These results were compared with the target load of 70 percent of the

nominal flexural strength in the undamaged/intact condition estimated from a conventional sectional analysis.

The test conducted on the Baseline Specimen showed the extent to which a non-redundant box straddle cap can be damaged in the presence of large fatigue cracks. In addition, the trajectories of the cracks showed how a crack that initiated on one side of the section could extend to the opposite side and fracture the entire section.

For Specimen A, although improvements with respect to the Baseline Specimen were obtained, the addition of the PT bars did not prevent the extension of the cracks on the webs. Fracturing or rupturing the webs would be particularly problematic if the fracture occurred at a section with high shear demands. Increasing the amount of reinforcing steel could potentially increase the flexural strength of the cap in the faulted condition. However, it would also require larger anchor sections and would not likely prevent the extension of the cracks on the webs.

For Specimens B1 and B2, the tests showed that the cross-boundary separation provided by the bolted connection effectively limits the crack propagation to one component of the cross-section and that it is possible to reach the plastic moment of the faulted section with a ductile failure mechanism. Furthermore, the reserve capacity for these specimens with a fractured bottom flange was adequately estimated as the plastic moment of the faulted section.

In Chapter 6, the results of these experiments are used to validate finite element models that were employed to evaluate a broader range of loading conditions and geometries.

## Chapter 6. Computational Studies

Finite element (FE) models with a wide range of geometries were developed to further study the behavior of the proposed design approaches for internally redundant steel box straddle caps using the general-purpose finite element software Abaqus 2022 (Dassault Systèmes, 2022).

Finite element models were developed for design concepts A and B, primarily aiming to study the performance in the faulted condition (i.e., after the fracture of a tension component occurred). First, FE models of the test specimens (shown in Figure 6.1 and Figure 6.2) were created and validated with the results of the laboratory experiments. The validated modeling approach was subsequently used to investigate the effects of various crack sizes, crack locations, and loading conditions on box girders of different geometries.

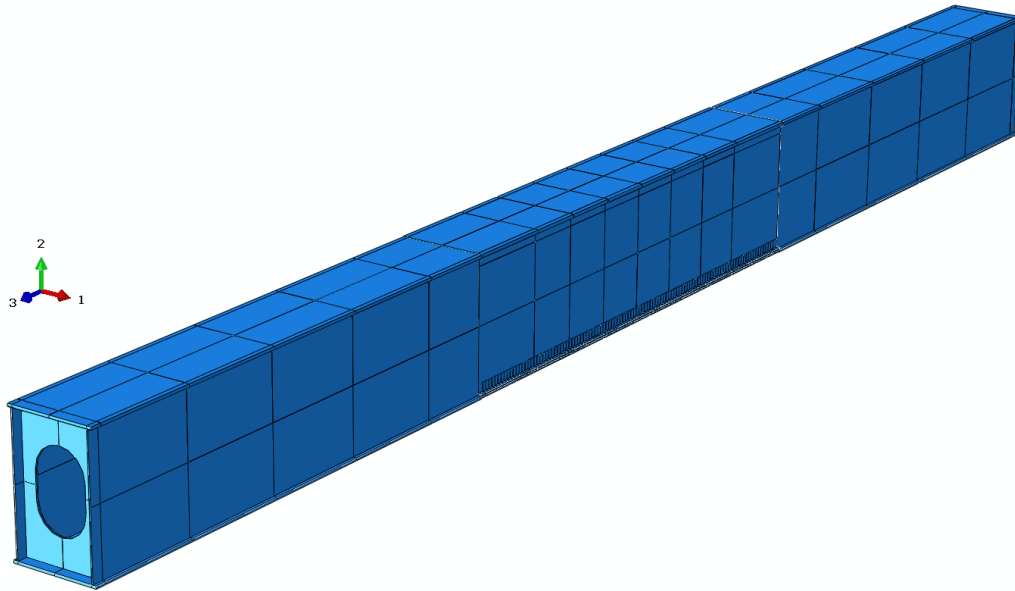


Figure 6.1: Abaqus FE model for Specimen B2 (shell thickness rendered)

Following a description of the modeling techniques employed, this chapter presents the results of the model validation process and the primary outcomes of the parametric studies for each design concept.

### 6.1. Box girder modeling

A longitudinal cut view of the FE model of Specimen B2 is shown in Figure 6.2. All plate elements (top and bottom flanges, webs, diaphragms, and stiffeners) were modeled using

three-dimensional S4R shell elements. These 4-node quadrilateral elements with reduced integration have five integration points through the thickness and six degrees of freedom at each node and can capture in-plane and bending deformations.

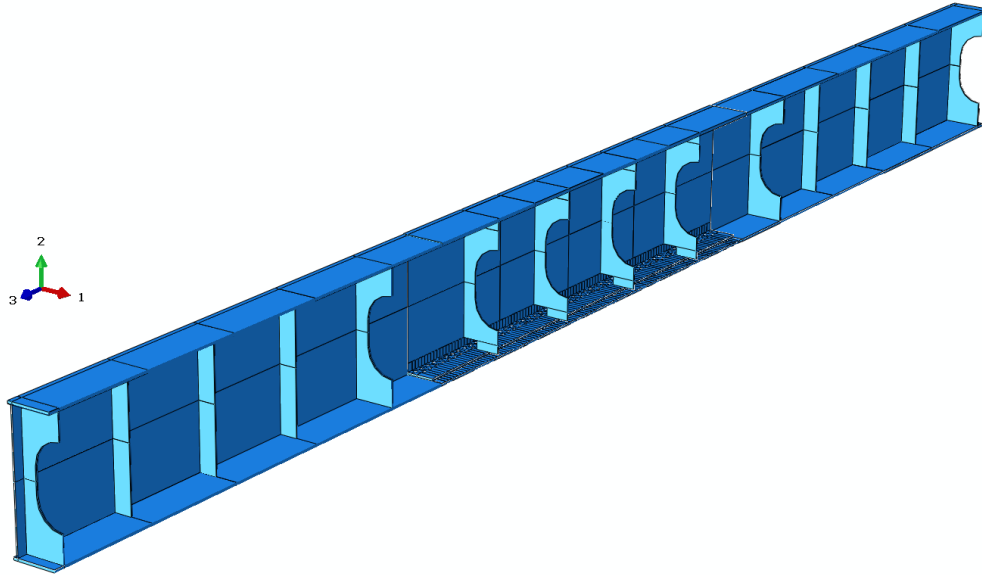


Figure 6.2: Longitudinal cut view of Abaqus/CAE model for Specimen B2

For the validation models (i.e., the models that reproduce the test specimens), each segment of the specimen was created as a single part by merging the individual parts corresponding to the flanges, webs, and diaphragms. The bolted splices between the three segments were not directly modeled; instead, the three segments were connected using tie constraints between the edges of the boxes at the location of the splice, as shown in Figure 6.3 for the FE model of Specimen B2. The constraint is applied to a pair of “sets” containing the edges of the flanges and web plates at the splice location for each segment. The edges of the end segments were selected as the main surface, while the secondary surface corresponds to the edges on the test segment.

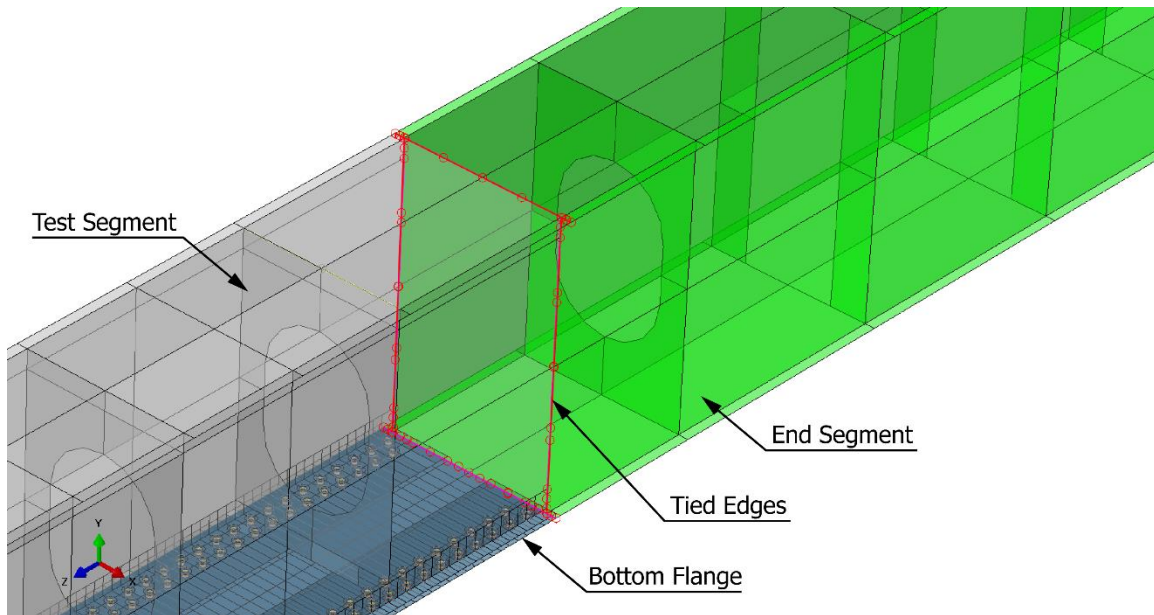


Figure 6.3: Specimen B2 FE Model: tie Constraint between the end segment and test segment (shell thickness not rendered)

For the shell elements that were selected, the user specifies the thickness, material, and positive normal direction. In addition, proper specification of the position of the shell surfaces relative to the reference plane is important since changes in the plate location can significantly impact the stiffness of the girder. The models constructed with shell elements agreed well with the experimental test results (see Section 6.1.7) at a significantly lower computational cost than solid/continuum elements.

After conducting a mesh sensitivity and quality assessment, the global mesh size for the test segment instance was set at 2 in., while the instances corresponding to the end segments were meshed with a global mesh size of 4 in. In addition, the holes and curved edges were seeded with smaller elements to avoid mesh distortion in these regions. Figure 6.4 depicts the meshed model corresponding to Specimen B1, and the detail shows the mesh around the edges of the bolt holes in the bottom flange and flange connection plates. With these mesh sizes, the results from the simulations were satisfactory while keeping the total analysis time under 30 minutes for the largest models.

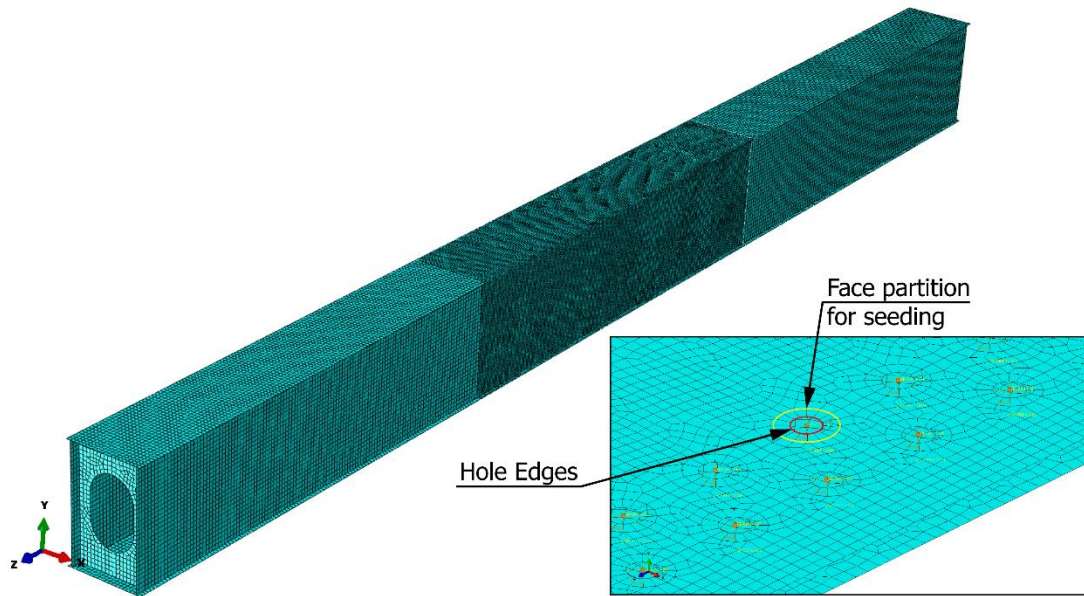


Figure 6.4: Specimen B1 FE model: meshed assembly and detail around bolt holes

Python scripts were developed to modify the geometry of the models, the boundary conditions and applied loads, the crack location and assumed fractured components, and output requests. Furthermore, these scripts allowed using the Abaqus kernel without the graphic user interface and extracting the nodal and element results of interest for post-processing.

### 6.1.1. FE Model for Design Concept A

The finite element models corresponding to the Design Concept A used S4R elements for all the plate components of the box section. The PT bars, however, were modeled using T3D2 truss elements attached to the intermediate diaphragms by coupling their end nodes to the edges of the holes. In addition, two horizontal shells were created on each side of the intermediate diaphragms to model the flanges of the anchor channels. The arrangement of the PT bars and the constraint between the bar and the diaphragms are illustrated in Figure 6.5.



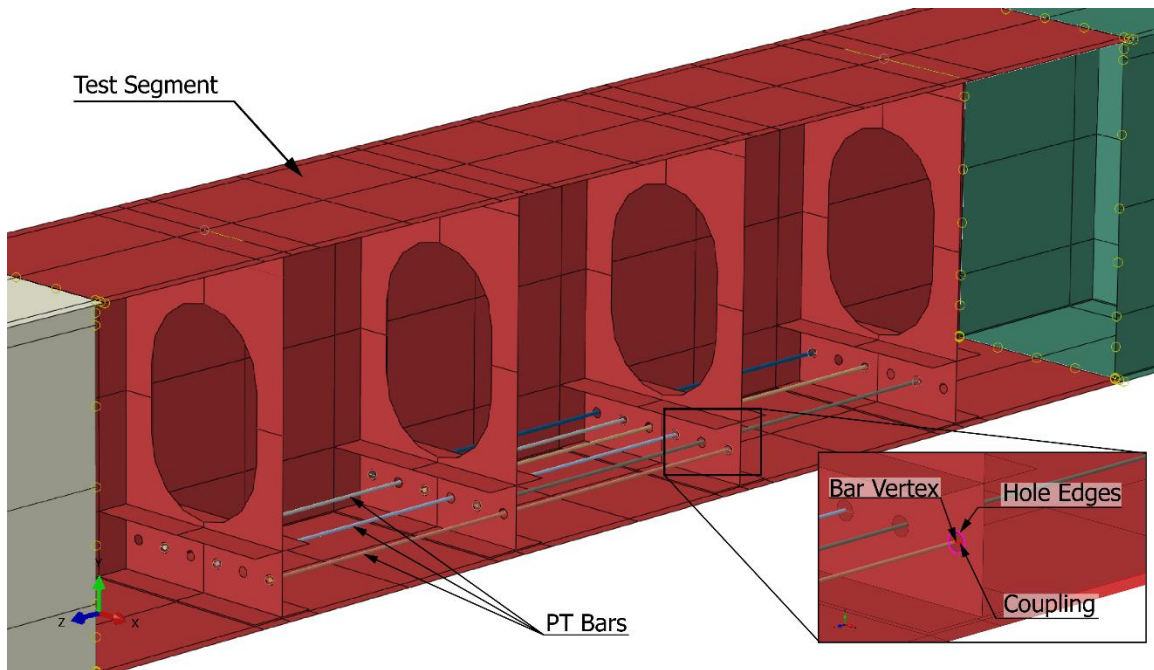


Figure 6.5: PT bars (truss elements) anchored at intermediate diaphragms (shell elements). Front web elements were removed from view for clarity.

### 6.1.2. Modeling of Design Concept B

A distinctive aspect of the models corresponding to Design Concept B -applicable to the models of Specimen B1 and B2- was modeling the bolted connection between the bottom flange and the flange connection plates. Several modeling approaches of various complexity were investigated to identify models that balanced accuracy and computational cost.

In the most complex variant, the bolts and the connected plates were modeled using three-dimensional continuum C3D8R elements with normal and tangential contact interactions at the bearing and faying surfaces. Moreover, each bolt was pretensioned to the corresponding force specified in the AASHTO LRFD Specifications (2020). On the other end of the spectrum, the plates were modeled using shell elements, and the bolts were modeled using Multi-Point Constraint (MPC) Beam connectors. The definition of the connectors involves the following steps: 1) reference points are created at the center of each hole in the bottom flange and flange connection plates; 2) these reference points are then kinematically coupled to the edges of the corresponding hole; 3) the reference points in the bottom flange and the flange connection plates are linked with a wire feature, to which the connector section is finally assigned. These elements are shown in Figure 6.6.

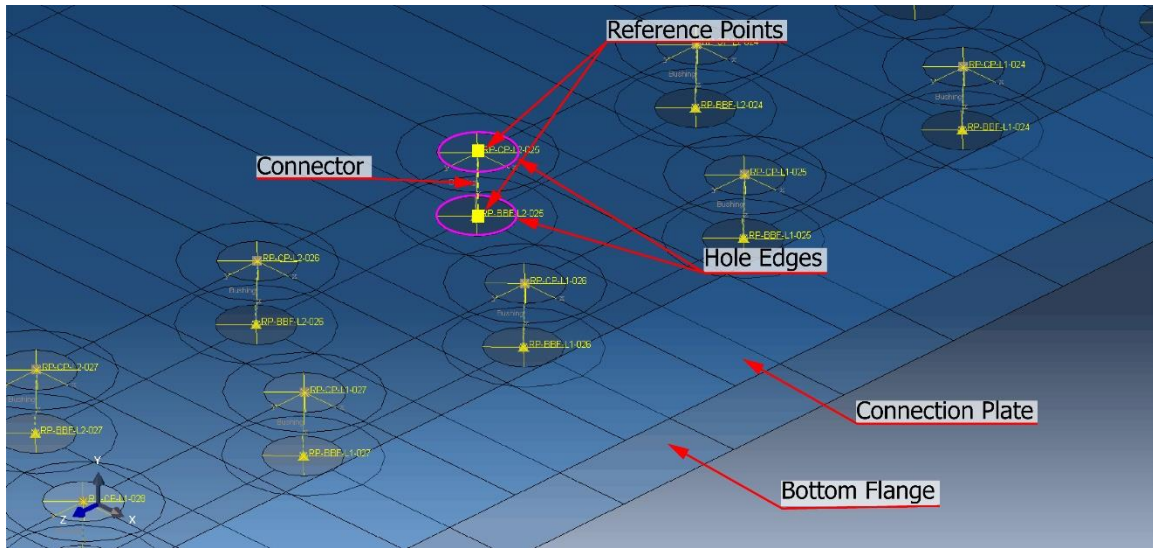


Figure 6.6: Specimen B2 FE model: MPC connectors between the bottom flange and the flange connection plate

The simplified approach with MPC connectors showed good agreement with the solid elements model and the experimental test results with significant reductions in analysis time, relative to the most sophisticated model, from approximately 8 hours to less than 30 minutes per model. As is shown in Section 6.3.1, the simplified model with the MPC connectors had good agreement with the experimental results. Hence, it was decided to utilize the shell models and model the bolts with MPC connectors.

### 6.1.3. Boundary Conditions and Applied Loads

The typical supports for steel box straddle caps used in Texas were described in Section 3.1.2 and illustrated in Figure 3.5, which is repeated in Figure 6.7 for convenience. The anchor bolts provided at each end restrict the displacement in the vertical, transverse, and longitudinal directions of the cap. Additionally, the moment arm between the anchor bolts in the transverse direction restricts the rotation around the longitudinal axis of the box cap. Warping deformation of the section is not considered to be restricted by this type of support.

Vertical supports were provided on the bottom flange at each end of the box girder. The boundary conditions were applied to reference points defined at each support and coupled with the edges of the bottom flange corresponding to the support section. To adequately model the typical supports of steel box straddle caps, the boundary conditions defined at each support corresponded to a pin-roller support with a pin at one end of the cap and a roller support allowing longitudinal deformation at the other end. The support points were

located under each web at the location of the end diaphragm (Figure 6.8). The edges of the support diaphragm and the bottom flange were coupled to the reference points to avoid localized deformations and provide a more realistic support condition.

To achieve the pin-roller condition, on one end of the girder, both reference points under the webs were restrained from displacing in all directions ( $U_1=U_2=U_3=0$ ), as illustrated in Figure 6.8. The reference points at the other end were only restrained vertically and transversely ( $U_1=U_2=0$ ), while the longitudinal displacement ( $U_3$ ) was free. Therefore, the support boundary conditions corresponded to a simply-supported beam. Although in actual straddle caps, the longitudinal displacement is typically restricted by the anchor rods, having a roller support on one end accounts for the conventional use of long-slotted holes for the anchor rods, which would only engage if there is significant deformation. The rotation along the longitudinal axis (torsional rotation) at the supports was restrained by the force couple developed between the two supports on the webs, while the warping of the section was not restrained.

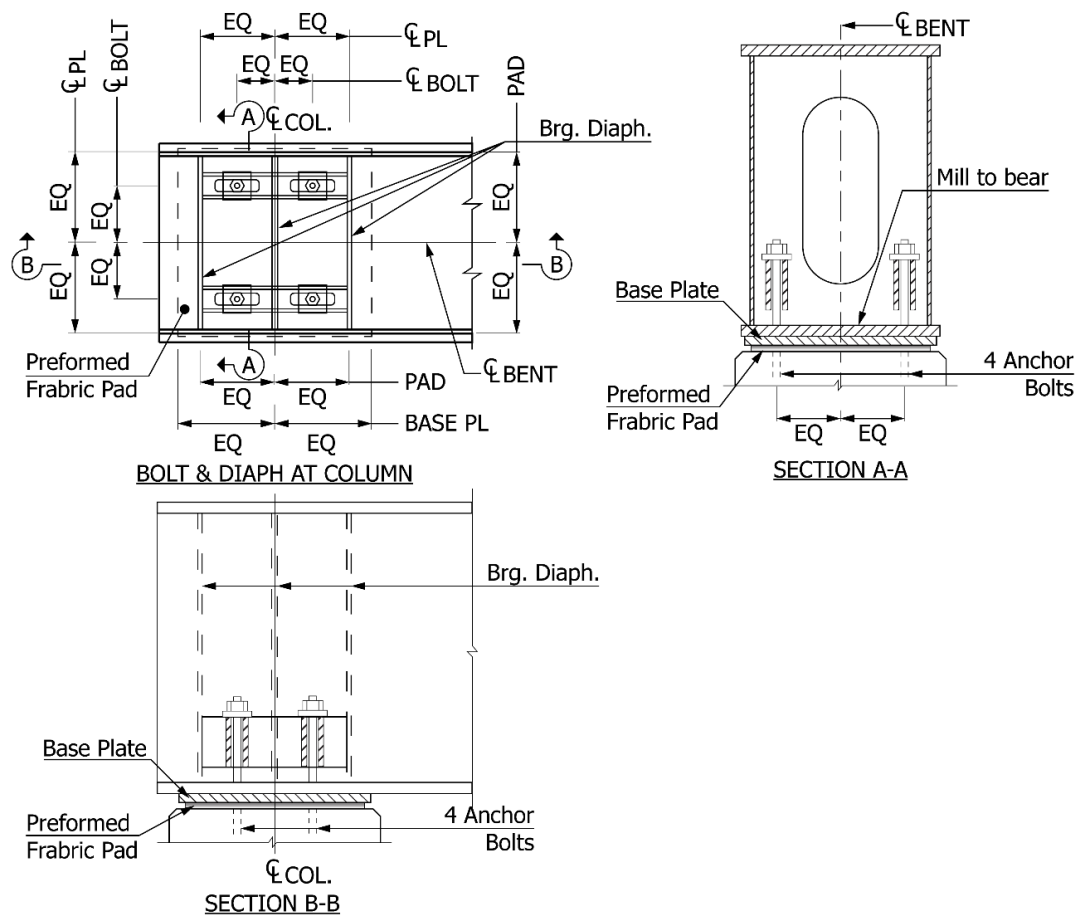


Figure 6.7: Typical support details for the steel box caps

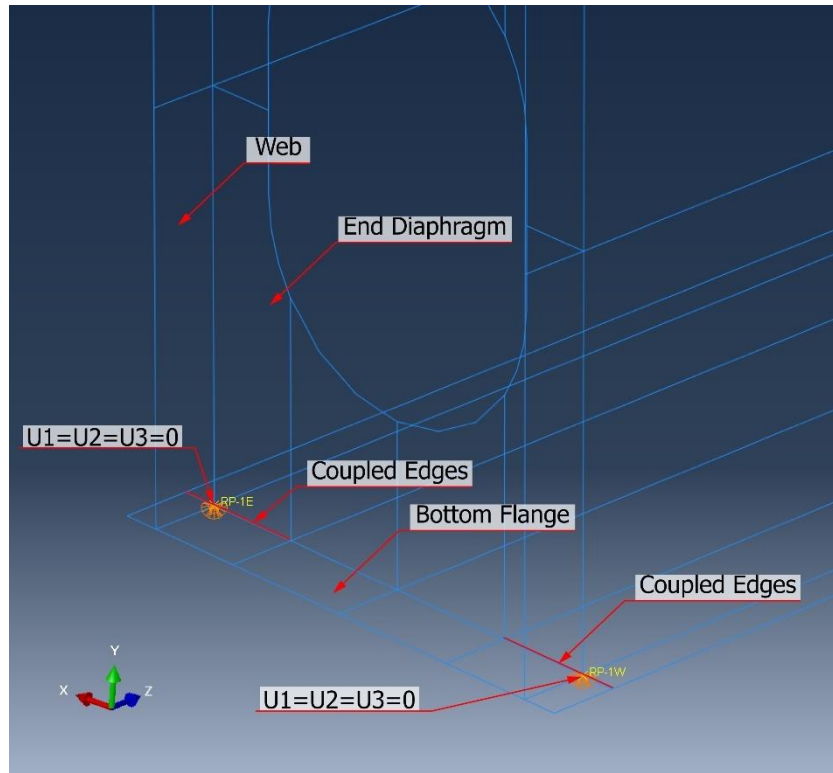


Figure 6.8: Boundary conditions for end supports (pin support depicted)

The vertical loads were applied at the top flange at the locations of the intermediate diaphragms, as would be the case of a non-integral straddle cap with a stacked configuration. Cases were also considered where the loads were applied directly to the webs -also in coincidence with internal diaphragms- to account for the possibility of torsional loads resulting from girders framing to the sides of the cap, as in an integral straddle cap with lateral brackets.

The loads were defined with a ramp amplitude and a final target force. Therefore, during the analysis, a fraction of the target force was added in each time increment. Once equilibrium is satisfied for that increment, another fraction of the target force was applied. In some load increments for points in the analysis involving large deformations, equilibrium may not be satisfied for the current increment, the increment size was automatically reduced. This sequence progresses until the final target force is reached or the analysis is aborted due to a lack of convergence. A target force larger than the theoretical capacity of the girder was always specified to ensure that the ultimate load was captured.

#### 6.1.4. Crack Modeling

Techniques for modeling the propagation of cracks, such as the Extended Finite Element Method (Moës et al., 1999), are available in Abaqus/CAE. However, since the analyses in this study were aimed to determine the capacity of the proposed design concepts in the faulted condition (i.e., the fracture already occurred), the cracks were simulated with seams. In Abaqus/CAE, a seam is a special feature that defines an edge (for shell elements) or face (for continuum elements) that is originally closed but is allowed to open during the analysis, as shown in Figure 6.9, by creating overlapping duplicate nodes along the selected edges or faces when the mesh is generated.

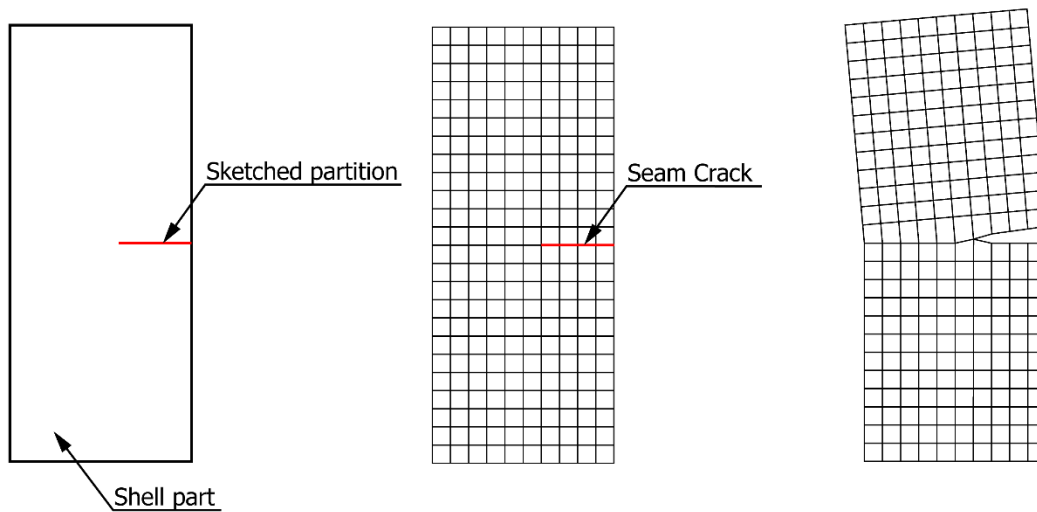


Figure 6.9: Seam crack on a planar shell part. Adapted from Abaqus Reference Manual (Dassault Systèmes, 2022).

Several assumed crack locations and sizes consistent with each design concept were considered in the models by creating partitions and selecting the edges corresponding to the fractured components. For instance, Figure 6.10 illustrates two assumed cracks for Specimen B2, located between intermediate diaphragms and involving (A) the bottom flange plate only and (B) the entire depth of the webs and its corresponding flange connection plate. Similarly, Figure 6.11 depicts two possible crack conditions for the FE model of Specimen A: (A) a crack that affects the bottom flange plate and half of the depth of the webs and (B) a crack that severs the bottom flange and both webs entirely.



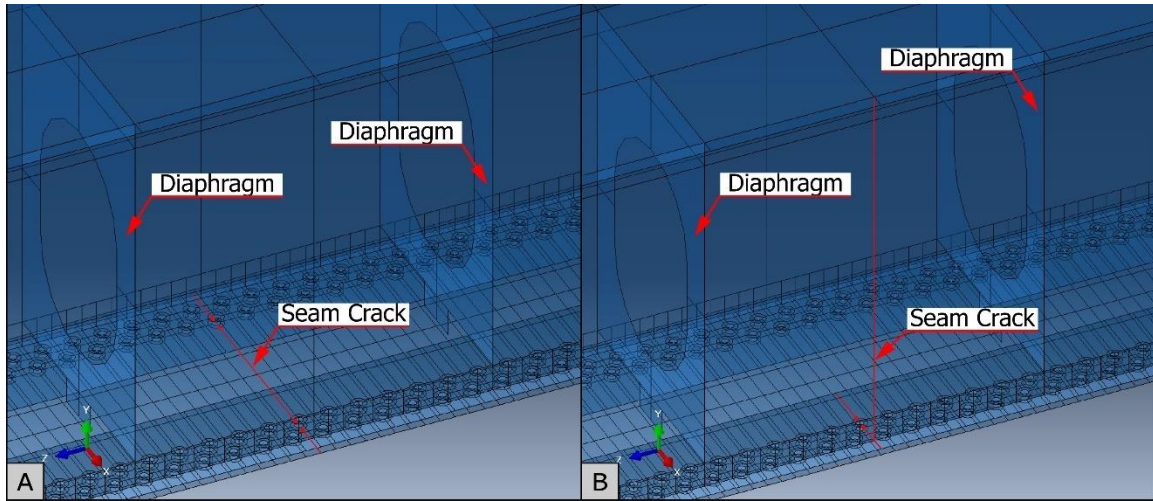


Figure 6.10: Specimen B2 FE model: seam cracks defined on (A) bottom flange plate, and (B) flange connection plate and web plate

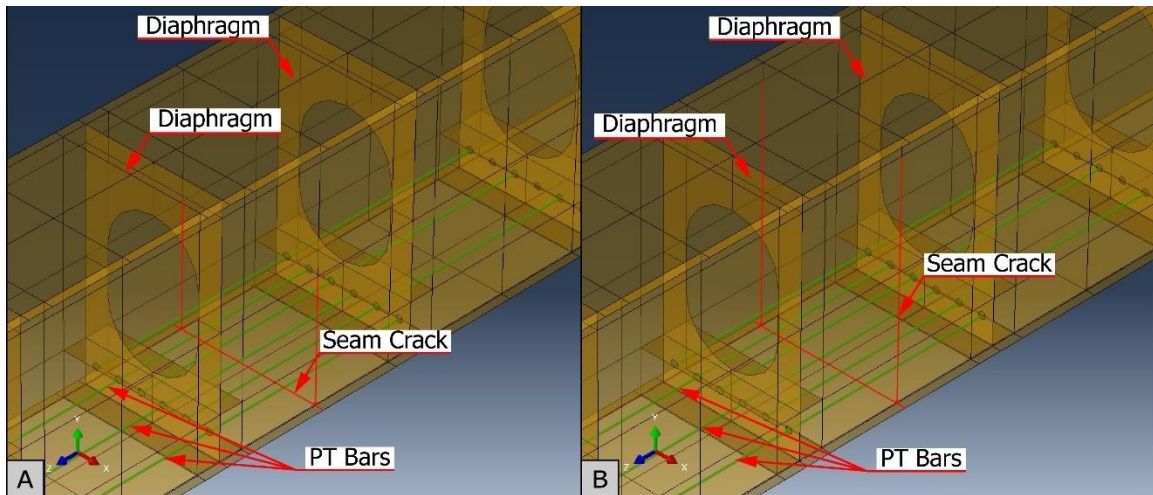


Figure 6.11: Specimen A FE model: seam crack defined on (A) bottom flange and half of the depth of both webs and (B) bottom flange and entire depth of both webs

### 6.1.5. Material Model

The data from the material tests presented in Section 4.1.3 was used for the validation models. For the parametric models, the bilinear elastic material model proposed in the AASHTO Guide Specification for IRMs (2018-1) was used. A Young's modulus of 29,000 ksi and a yield stress of 50 ksi were defined for the elastic portion of the stress-strain curve. Beyond that point, another linear stress-strain relationship was defined, which reaches 65 ksi at 0.05 in./in., as illustrated in Figure 6.12. Using this small amount of strain-hardening provided numerical stability to the models as the ultimate capacity was reached.

For the models corresponding to Design Concept A, the PT bars were modeled as elastic perfectly plastic, with a Young's modulus of 29,000 ksi and nominal yield stress of 150 ksi.

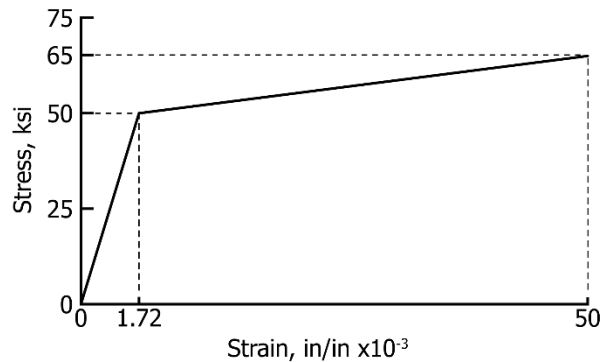


Figure 6.12: Stress-strain model for parametric FE models (not to scale)

### 6.1.6. Analysis Procedure

A Static-General analysis procedure with a full Newton-Raphson solution technique was selected for all analyses. Non-linear geometry was included in the analysis to account for the effects of large displacements. The time incrementation parameters (number of increments, initial, minimum, and maximum increment size) and the output requests were tailored for each model based on the results sought. Multi-thread CPU parallelization and GPU acceleration were enabled on the computer server to expedite the analyses.

### 6.1.7. Finite Element Models Validation

While full-scale experimental results are extremely valuable towards understanding the fundamental behavior, the cost of the specimens and time necessary to carry out each experiment is considerable and therefore the test specimens were proportioned to provide important validation data. Due to the limited number of full-scale specimen tests, a crucial aspect of the investigation is to extend the findings of the experiments via parametric FE models. These studies allow a wider range of specimens to be considered to evaluate the accuracy of proposed design methods and details to the wide range of geometries and load demands found in practice. Therefore, validating the FE models with the results of the large-scale experimental testing program described in Chapter 5 was a critical step to obtaining reliable results from these numerical analyses prior to proceeding to a wider range of cap geometries.

FE models with a range of modeling features were created to model the behavior of specimens A, B1, and B2 during the Ultimate Strength Test. The loading points were



defined according to the test setup dimensions to apply the load at the location where the hydraulic actuators were placed. In addition, seam cracks -explained in Section 6.1.4- were defined at the sections where the specimens were fractured during the fracture tests.

## **6.2. Finite Element Modeling of Design Concept A**

### **6.2.1. Validation of FE models for Specimen A**

Modeling the behavior of Specimen A in the faulted condition was particularly challenging due to the fracture events that occurred during the testing of this specimen. Approximately a quarter of the web depth was already fractured at the start of the ultimate strength test of this specimen, and two more fracture events occurred during the loading when the cracks propagated beyond half of the web depth (refer to Section 5.2).

Per these observations, three crack possibilities were considered for the FE model of Specimen A. In all cases, the bottom flange was assumed to be completely fractured, while three different cases of crack propagation were considered to have occurred consisting of: (i) 25% of the web depth, (ii) 50% of the web depth, and (iii) 100% of the web depth.

The experimental data corresponding to the ultimate strength loading of Specimen A is compared to the results of the FE models in Figure 6.13. The theoretical sectional capacity of Specimen A, computed in Section 4.1.1 as the moment that produces the first yield in the cross-section with half of the web fractured, is also included in Figure 6.13. The model with a quarter of the webs fractured (25%W) reasonably represents the initial loading branch. It should be noted that the experimental data shows some initial deflections, which are associated with initial imperfections of the test setup, that offset the curve from the results of the FE model. After a relatively small amount of load level is reached, the two curves are essentially parallel until the fracture is reached in the experiment and the analysis finishes due to excessive plastic strains in the webs.

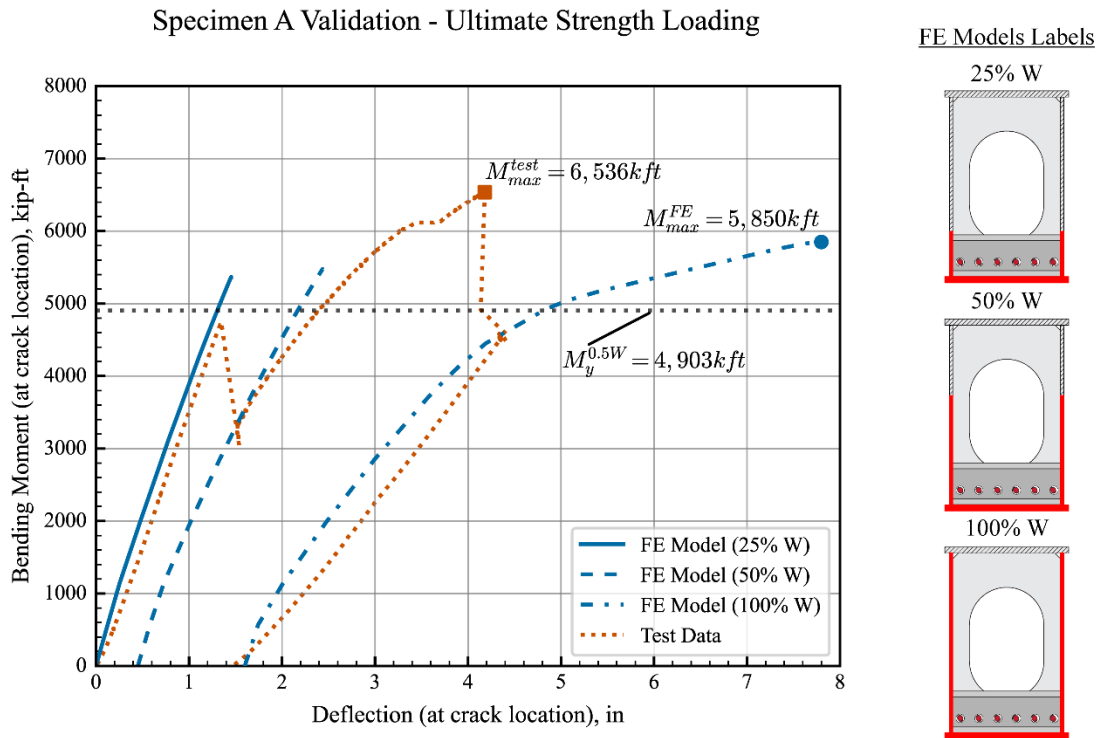


Figure 6.13: Specimen A: experimental test and FEA results

To model the next stage of the fracture test, after the cracks reached approximately half of the depth of the webs, 50% of both webs were assumed fractured using a seam crack. The curve corresponding to this model is offset from the previous stage to match the start of the reloading branch. It is observed that the agreement between the model and the experimental data was not as accurate as the previous step.

For the last stage of the ultimate strength test of Specimen A, the cracks propagated upwards on the West web almost to the top flange after reaching the maximum load indicated in the plot. Conservatively, the FE model with both webs fully fractured (100% W) was used to estimate the capacity of the specimen after the second fracture event.

The complexity of the behavior of a straddle cap such as Specimen A, where the cracks can continue to grow indefinitely, represents a severe limitation to the seam crack models. Since the goal of this research is to evaluate the capacity of the straddle caps in the faulted condition and determine whether they meet the requirements of the current provisions for redundant members, it was deemed appropriate to conservatively assume a full-web-depth crack for the FE models corresponding to Design Concept A.

### 6.2.2. FE Studies for Design Concept A

The analyses presented in this section focused on two objectives: (i) comparing the performance of Design Concept A with a staggered and continuous PT bar arrangement and (ii) evaluating the strength of the box girder in the faulted condition when the fractured section is subject to flexure and a combination of flexure and shear. The consideration of the continuous arrangement responded to the interest in using this design approach to retrofit existing straddle caps by only anchoring the PT bars at the ends of the girder. For this analysis, a 60-ft-long box girder was modeled, with two equal concentrated loads applied in four-point bending, as shown in Figure 6.14.

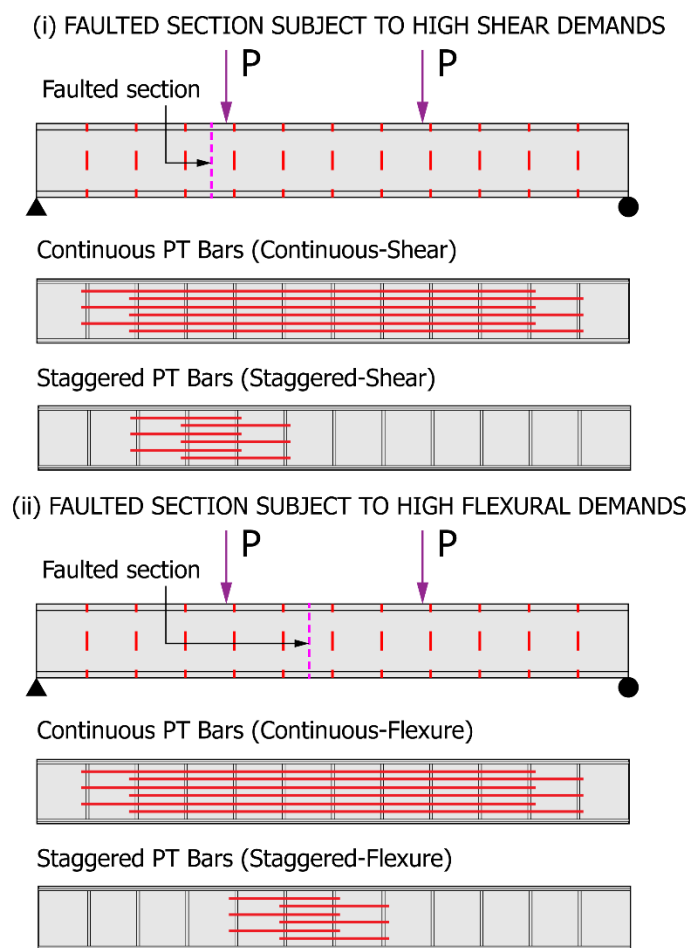


Figure 6.14: Design Concept A: loading conditions and PT arrangements considered

Two cases were considered regarding the location of the faulted section: in one case, the faulted section was assumed to be adjacent to one of the concentrated loads, between the

point of application and the nearest support, in a region with both shear and flexural demands; in the other, the fractured section was defined within the constant-moment region (zero shear). Both cases contemplated the use of a continuous and staggered PT bar arrangement. For the purposes of referencing the results, the respective cases are labeled Cont-Shear and Cont-Flexure for details with continuous bars and the failure located in the regions with shear versus flexure only. Similarly the terms Staggered-Shear and Staggered-Flexure apply to details with staggered bars and the defects located in the regions with shear versus flexure-only, respectively. Because the failure for the cases with combined shear and flexure are located relatively close to the support, the shear-demand is relatively large. A box girder in undamaged/intact condition was also modeled under the same loading conditions to provide a benchmark performance.

The base cross-sectional dimensions of the model are presented in Figure 6.15. Additionally, all models were provided with the same amount of reinforcing steel across the faulted section by adding six 2 ½-in. diameter Grade 150 PT bars that can provide enough tensile force to compensate for the loss of the tension flange in the faulted condition. It should be noted that the channels used to anchor the PT bars required 2 ½-in. thick webs in order to develop the PT bars fully, twice as thick as the channel shapes fabricated from w\_shpaes used in test specimen A.

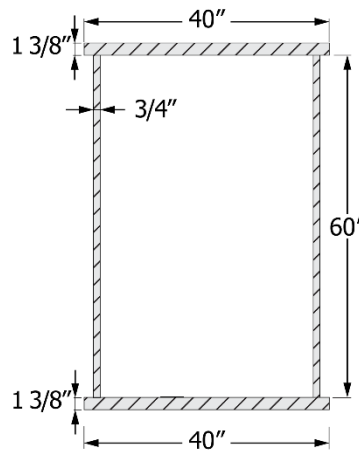


Figure 6.15: Base cross-section for Design Concept A FEA studies

The results of these analyses are shown in Figure 6.16, where the maximum load reached during the analysis is plotted versus the deflection at the location of the fractured section. The solid blue line corresponds to the undamaged/intact model and is included as a benchmark. The models in which the fractured location is assumed in the constant moment region are indicated with solid grey (staggered PT bars) and orange (continuous PT bars)

lines. Finally, the dashed lines correspond to the cases where the fractured section is located in a location of combined shear and flexural demands.

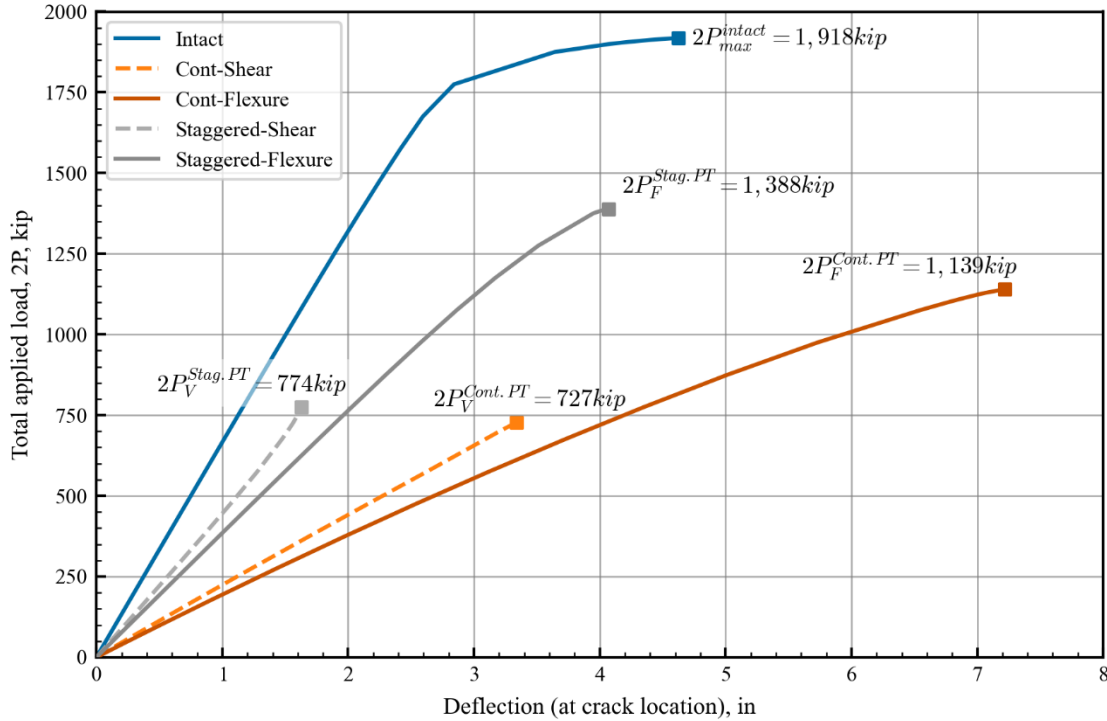


Figure 6.16: Design Concept A: comparison of results from parametric FE studies

The results presented in Figure 6.16 indicate that using staggered PT bars would provide an acceptable performance, reaching 72% of the maximum load of the undamaged/intact section, if the fracture occurred within the constant moment region. However, the capacity dropped to approximately 40% of the strength of the undamaged/intact model when the fractured section was subject to shear and flexure, as the shear force had to be transferred solely by the top flange and the PT bars. The models with a continuous PT arrangement showed similar ultimate strengths to those with the staggered arrangement but required approximately twice as much deformation. The lower stiffness of the continuous arrangement was directly related to the longer PT bars.

The results of these analyses indicate that, although enough reinforcing steel could be provided to compensate for the loss of the bottom flange, the propagation of the cracks on the webs would make the section susceptible to failure in shear. Based on these remarks and the results of the experimental testing program, this design concept was considered unsuitable for general implementation, and no further analyses were conducted.

## 6.3. Finite Element Modeling of Design Concept B

### 6.3.1. Validation of FE models for Specimen B1 and B2

This section presents the results of the FE analyses conducted on models that replicated the geometry and material properties of the test specimens with Design Concept B. The main goal was to determine the adequacy of the modeling approach to capture the behavior of the specimens in the faulted condition. This assessment allowed the researchers to implement the same modeling techniques in the parametric studies presented in the subsequent section.

For the FE models of Specimen B1 and B2, a seam was defined to cut the bottom flange plate while leaving the remaining components undamaged/intact. The seam was located 25 ft from the North support, in coincidence with the location of the crack in the experimental tests. The comparison between the FE model and the Ultimate Strength Test results corresponding to specimen B1 is presented in Figure 6.17. The theoretical plastic capacity of the faulted section calculated per the AASHTO LRFD Specifications (2020),  $M_{p,theoretical}^{faulted}$ , is also shown in the plot.

The FE model had good agreement with the stiffness of the girder and showed excellent agreement with the test data in the loading branch as evidenced by the nearly coincident curves in this region. The discrepancies in the ultimate strength between the FE model and the test results are attributed to the buckling of the top flange and bolted cover plate in the experiments, which were modeled as a monolithic plate. Like the experimental test, the FE model also has a higher ultimate strength than its theoretical design value. This is because of the assumption of elastic-perfectly plastic material used in calculating the plastic moment capacity. In reality, the large strains likely put some of the cross-section into the strain hardening region on the stress-strain curve.



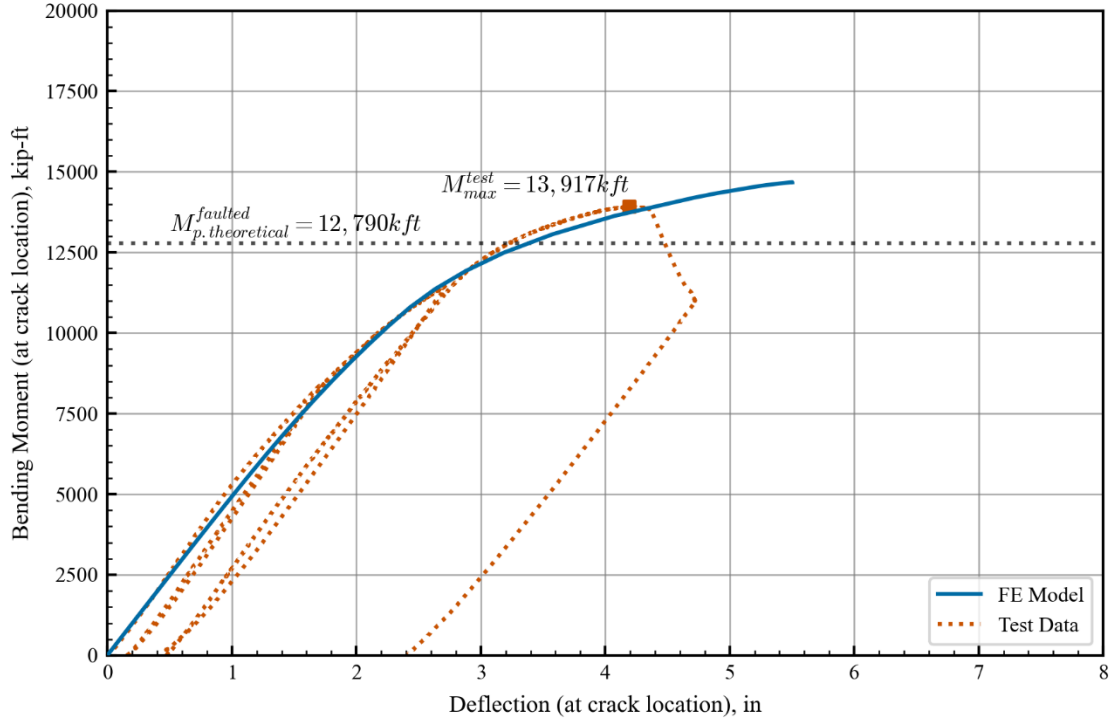


Figure 6.17: Specimen B1: experimental test and FEA results

Similarly, the FE model of Specimen B2, presented in Figure 6.18, exhibited good agreement with the experimental data in the loading branch of the plot, satisfactorily capturing the initial stiffness and yielding of the box girder. Since Specimen B2 was unloaded after surpassing the load corresponding to the theoretical plastic moment of the faulted section, there is no marked peak load as in the case of Specimen B1. This fact also explains why the higher load levels indicated by the FE results (at larger deflections and in the inelastic range) were not captured in the experimental test.

Based on the observed results, the shell FE models with MPC connectors and seam cracks were found suitable for studying the performance of box girders with internal redundancy per Design Concept B. Therefore, the modeling techniques described in this chapter are applied to the parametric studies reported in the following section.

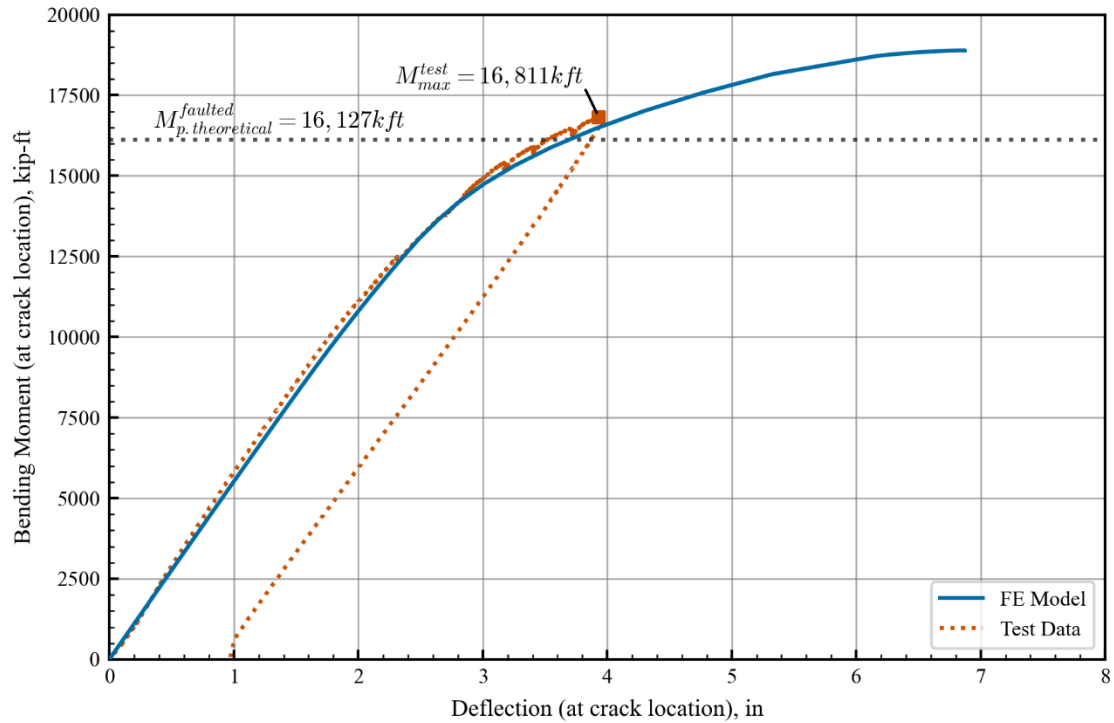


Figure 6.18: Specimen B2: experimental test and FEA model results

The force transference between the bottom flange plate and the flange connection plates was also of interest. The Von Mises stress contours around the fractured section corresponding to the FE model of Specimen B1 are depicted in Figure 6.19, which shows the pronounced stress concentration that occurs at the flange connection plate at the location of the crack. Furthermore, it shows that the stress concentration is dissipated through the bolted connection within three to four bolt rows on each side of the crack. These observations agree with the findings of Hebdon et al. (2015) regarding the force redistribution between mechanically fastened components, and they also correlate with the comments made in Figure 5.31, which shows the deformed bolt holes around the fractured section.

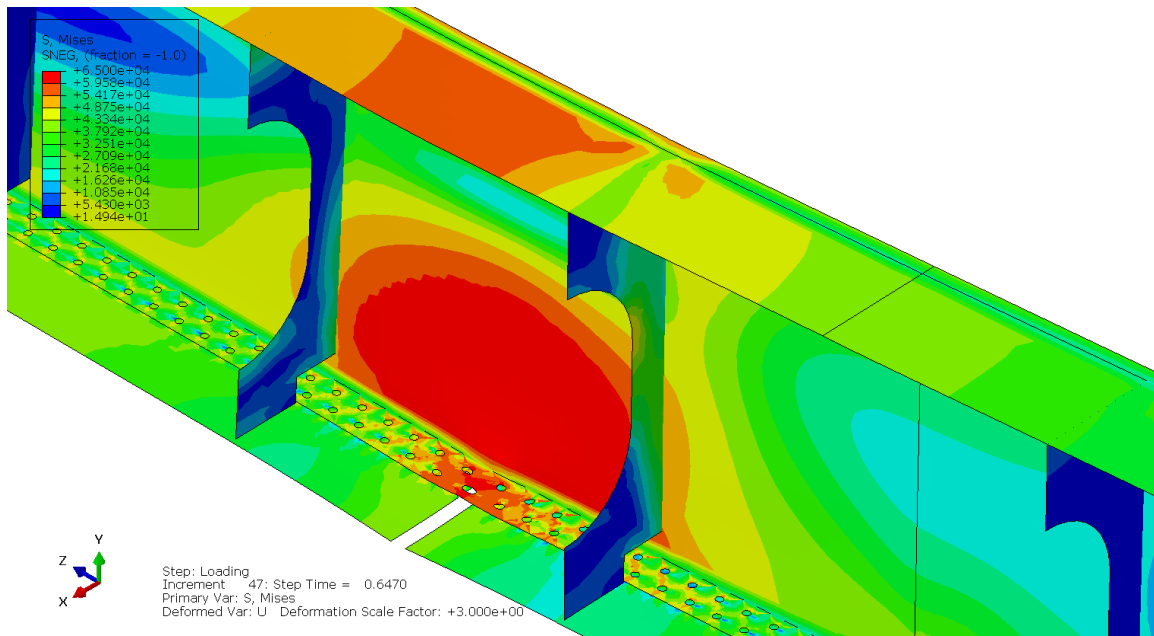


Figure 6.19: Specimen B1: screenshot of the FE model showing equivalent Von Mises stress contours around the fractured section at the maximum load (deformation scale factor of 3)

### 6.3.2. Parametric Studies for Design Concept B

Recognizing that Design Concept B was the most promising alternative for internally redundant steel box straddle caps, the FE studies presented in this section focused on assessing its capacity for several geometries, loading conditions, crack types, and crack locations. Specifically, the goal was to determine design equations that can be used to determine the strength of such a steel box straddle caps with the Design Concept B in the faulted condition. Accurate strength equations for predicting the capacity in the failed state can then be used to develop a comprehensive design methodology for providing sufficient redundancy of steel box straddle caps.

The computation of the flexural resistance of a box section member with an unstiffened compression flange is defined in Article 6.12.2.2.2 of the AASHTO LRDF Specifications (2020). This computation involves the following steps:

1. Verify the slenderness of webs and flanges and the sectional proportion limits per Article 6.12.2.2.2b.
2. Calculate the effective width of the compression flange and compute the effective section moduli per Article 6.12.2.2.2c. Compute the yield moment of the

compression flange considering early nominal yielding of the tension flange,  $M_{yce}$ , and depth of web in compression,  $D_{ce}$ .

3. Check web slenderness and compute the Web Plastification Factor,  $R_{pc}$ , per Article 6.12.2.2.2c.
4. Check the compression flange slenderness and calculate the Compression Flange Slenderness Factor,  $R_f$ , per Article 6.12.2.2.2c.
5. Compute the limiting unbraced length to achieve the yielding flexural capacity,  $L_p$ , and the limiting unbraced length for the onset of nominal yielding in either flange,  $L_r$ , per Article 6.12.2.2.2c.
6. Compute the nominal flexural resistance,  $M_n$ , based on yielding, local buckling, and lateral torsional buckling.

The calculation of the limiting unbraced lengths  $L_p$  and  $L_r$  in step 5 depends on the effective sectional properties, as shown in Equation 6.1 and Equation 6.2, which correspond to Equations 6.12.2.2.2e-4 and 6.12.2.2.2e-5 of the AASHTO LRFD Specifications (2020), respectively:

$$L_p = \frac{0.1 \cdot r_{22e} \cdot E \cdot \sqrt{J_e \cdot A_{ge}}}{M_{yce}} \quad \text{Equation 6.1}$$

$$L_r = \frac{0.6 \cdot r_{22e} \cdot E \cdot \sqrt{J_e \cdot A_{ge}}}{0.5 \cdot F_y \cdot S_{33ce}} \quad \text{Equation 6.2}$$

Where  $E$  is the Young's Modulus,  $F_y$  is the yield stress of the material,  $r_{22e}$  is the effective minor radius of gyration of the section,  $A_{ge}$  is the effective gross area of the section,  $S_{33e}$  is the effective section moduli of the section,  $J_e$  is the effective St. Venant torsional constant, and  $M_{yce}$  is the yield moment of the compression flange, considering early nominal yielding of the tension flange.

Special consideration was given to the computation of the St. Venant torsional constant, which for box sections can be computed per equation 6.12.2.2.2e-4, which is reproduced in Equation 6.3:

$$J = \frac{4 \cdot A_0^2}{\sum \frac{b_m}{t}} \quad \text{Equation 6.3}$$

Where  $A_0$  is the cross-sectional area enclosed by the mid-thickness of the walls of the box section,  $b_m$  is the gross width of each plate of the box section taken between the mid-thickness of the adjacent plates, and  $t$  is the thickness of each plate.

For the sectional proportions generally used in steel box straddle caps, outlined in Section 3.1.2, the St. Venant torsional constant of the sections is relatively large, leading to values of  $L_p$  that usually exceed the unbraced length of the box. In the analyses presented in this section, the span length of the cap is conservatively taken as its unbraced length. Hence, the capacity of the section is typically governed by the yielding of the cross-section or local buckling of the compression flange and webs. This situation is illustrated in Figure 6.20: each marker on the plot corresponds to the nominal flexural resistance of the surveyed steel box straddle caps (Section 3.1.2) and their corresponding unbraced length, normalized by their plastic moment,  $M_p$ , and their limiting unbraced length to achieve the plastic moment under a uniform moment,  $L_p$ , respectively. The sections that contain slender elements are indicated with blue square markers, and those that contain compact or non-compact elements (i.e., non-slender) are plotted with orange circles. The solid black line indicates the nominal flexural resistance based on the unbraced length of the girder for a compact section. For  $L_b/L_p \leq 1$ , the nominal flexural resistance is governed by the yielding of the section or the local buckling of non-compact and slender elements. For  $L_b/L_p \geq 1$ , the flexural resistance decreases linearly due to lateral torsional buckling. The reduction in capacity is approximately 50% for  $L_b = L_r$ .

It can be inferred from this plot that the lateral torsional buckling limit state does not generally control the capacity of steel box section caps with typical cross-sectional proportions. This observation concurs with the commentary provided in C6.12.2.2.2e of the AASHTO LRFD Specifications (2020).

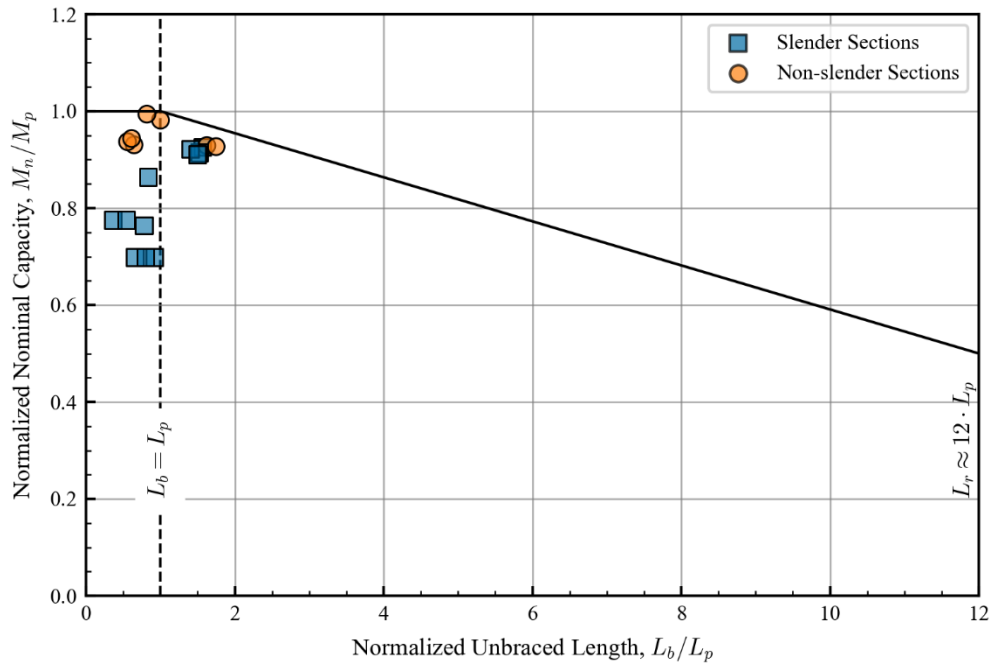


Figure 6.20: Normalized nominal capacity and unbraced length for surveyed box straddle caps

However, when a component of the box section is fractured, the section becomes open at that location. Consequently, the torsional resistance of the faulted section drops by several orders of magnitude because the section has to resist the torsion with a lever arm that is in the order of the thickness of the plates. An example of a box section with different fractured components is shown in Figure 6.21 to illustrate the reduction in the torsional constant as the section becomes open. However, it should be recognized that the reduction in  $J$  is highly localized around the faulted section.

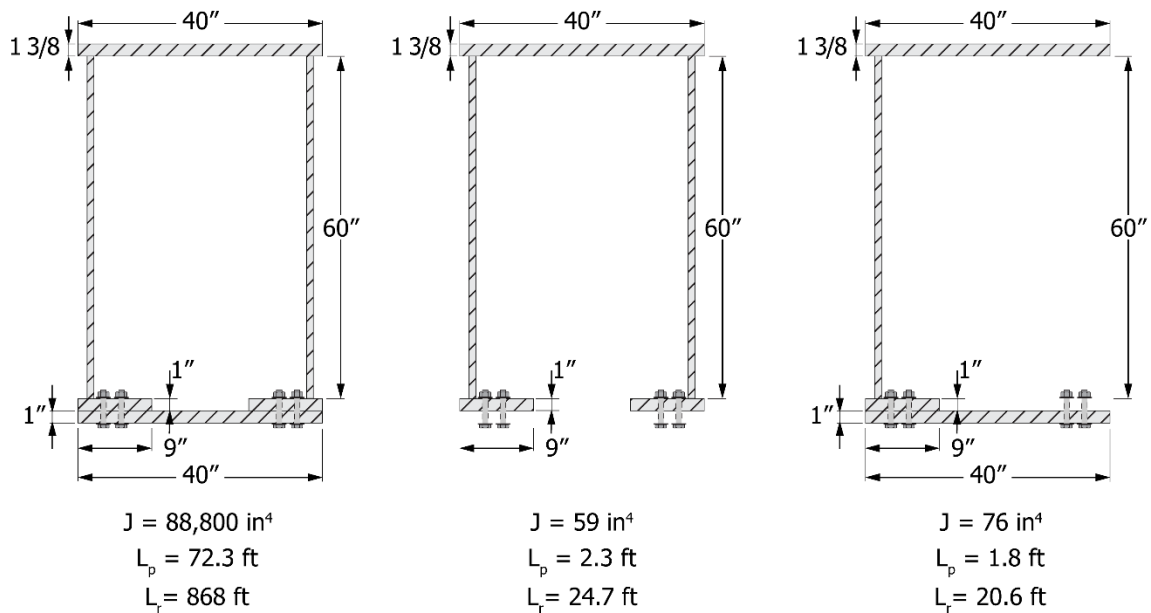


Figure 6.21: Torsional constant for undamaged/intact and assumed fractured sections

If the nominal capacity of the faulted straddle cap were computed based solely on a sectional analysis using the St. Venant torsional constant of the fractured section, the resulting limiting unbraced lengths ( $L_r$  and  $L_p$ ) would be very small, as shown in Figure 6.21. Consequently, there would be a considerable reduction in capacity due to lateral torsional buckling. This approach was considered overly-conservative, as the remaining box girder (undamaged/intact) would still provide significant torsional stiffness to the system away from the fractured section.

The following two subsections summarize the results of two parametric studies. First, the influence of a single fractured section in the global torsional stiffness of the box cap was studied. Based on these results, the second study investigated the adequacy of the current design provisions of the AASHTO LRFD Specifications (2020) to compute the nominal strength of box members in the fractured condition.

### 6.3.2.1. Parametric study for evaluation of torsional stiffness in the faulted condition

A parametric FE study was conducted to investigate the influence of a single fractured section on the global torsional stiffness of a box member. The parameters considered in this study are listed in Table 6.1. Three span lengths (60 ft, 90 ft, and 120 ft) were analyzed, corresponding to the lower, mid-point, and upper end of the range identified in the bridge survey (Section 3.1.2). Moreover, three possibilities were considered for the intermediate



spacing of the internal diaphragms: (i) one web depth (1D), (ii) two web depths (2D), and (iii) three web depths (3D).

**Table 6.1: Parameters considered for the evaluation of the St. Venant torsional constant**

Parameter	Values	Model Keys
Span Length	{ 60 ft; 90 ft; 120 ft }	{ 60, 90, 120 }
Intermediate diaphragm spacing	{ 1D; 2D; 3D }	{ 1D; 2D; 3D }
Cracked Components	{ None; Bottom Flange; Flange connection plate and Web }	{ UC <sup>a</sup> , FBF <sup>b</sup> , FW <sup>c</sup> }

<sup>a</sup> **UC**: uncracked

<sup>b</sup> **FBF**: **F**ractured **B**ottom **F**lange

<sup>c</sup> **FW**: **F**ractured **W**eb and the corresponding flange connection plate

Three conditions were analyzed concerning the assumed fractured components (see Figure 6.22): (i) the model was undamaged/intact -or uncracked,- (ii) the bottom flange plate was fractured, and (iii) one entire web and its corresponding flange connection plate were fractured. Modeling each girder in an undamaged/intact condition provided a benchmark for the models in the faulted state. A single cracked section was assumed for each faulted model, and the various permutations were considered for the location of the cracked section.

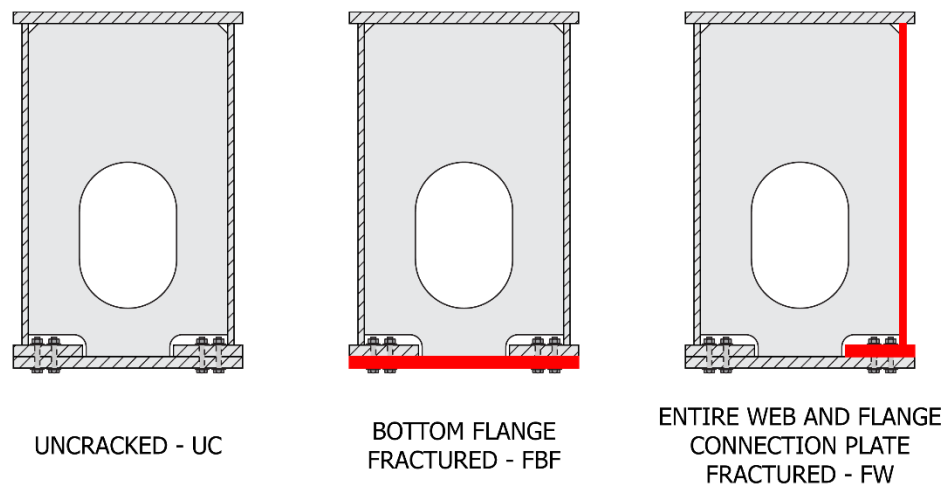


*Figure 6.22: Design Concept B parametric FE study: assumed fractured sections*

For each span length, the geometry of the section was defined considering a typical span-to-depth ratio of 12 and a depth-to-width ratio of 1.5. The thickness of the plates was kept constant along the girder. For all models, the top flanges were sized to be compact such that the entire top flange width was effective, and the webs were made noncompact or compact.

The bottom flange and the flange connection plates were sized to the same thickness, and the ratio between the gross area of the bottom flange plate to the total gross area of the tension flanges was approximately 60% for all girders, per the requirements of the AASHTO Guide for IRMs (AASHTO 2018-1). Internal diaphragms were sized to have sufficient bearing and buckling resistance to carry the plastic shear strength of the webs. Finally, all plate dimensions were sized up to the nearest 1/8" to simplify the geometry and meshing of the models. The dimensions of the cross-sections of these three models are illustrated in Figure 6.23.

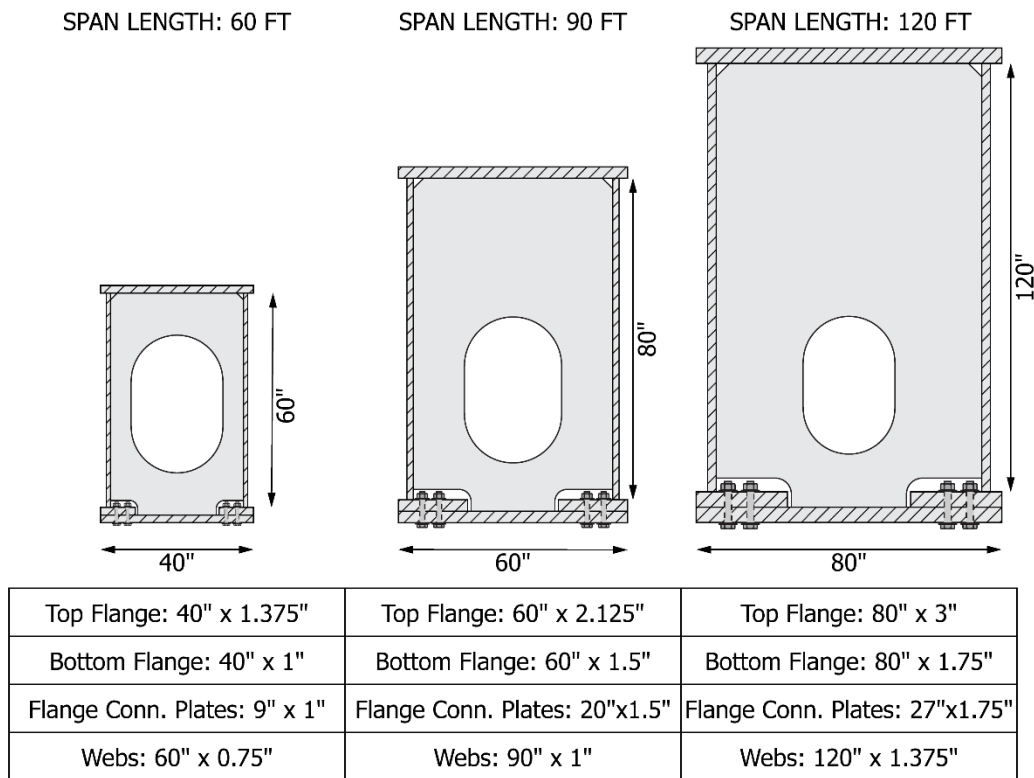


Figure 6.23: Design Concept B parametric FE study: cross-sectional dimensions considered

Each model (illustrated in Figure 6.24) was fixed to translation and rotation about the longitudinal axis on one end ("Fixed End") and to vertical and transverse translation on the

other (“Free End”). On the latter end, a torque was applied to subject the girder to a pure torsion condition.

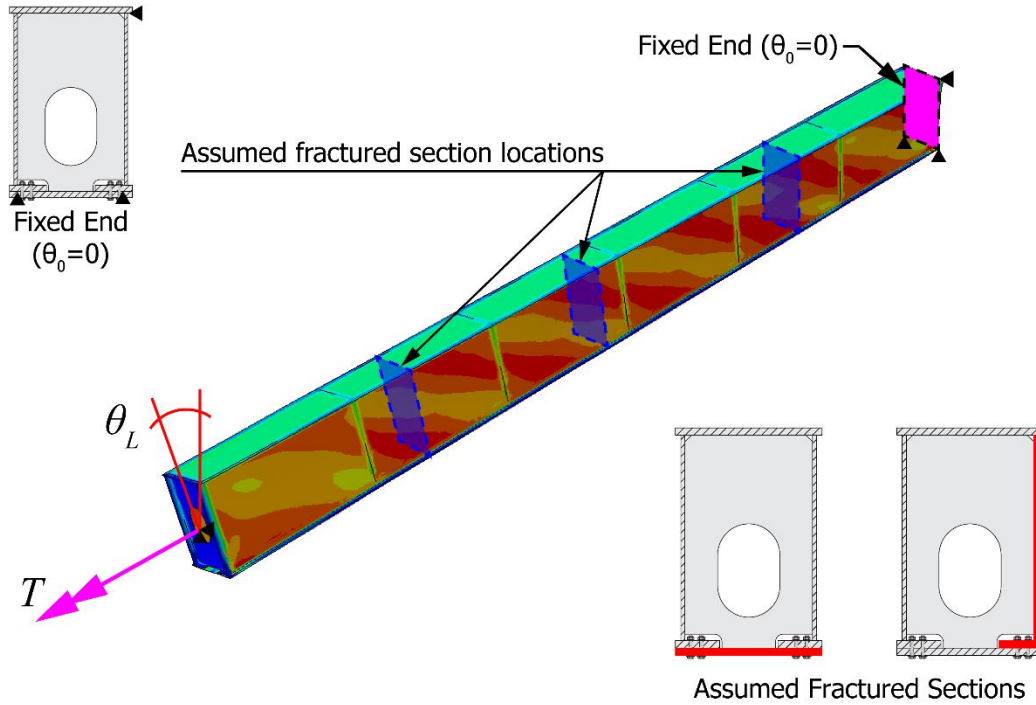


Figure 6.24: FE model of box member subject to pure-torsion demands

Then, the angle of rotation of the end where the torque was applied was extracted, and the effective torsional constant of the box girder was computed per Equation 6.4:

$$J_{FEA} = \frac{T \cdot L}{\phi_L \cdot G} \quad \text{Equation 6.4}$$

Where  $J_{FEA}$  is the torsional constant determined from the FE analyses,  $T$  is the applied torque,  $G = \frac{E}{2(1+\nu)}$  is the shear modulus of the material, and  $\phi_L$  is the angle of rotation of the section where the torque is applied.

The results of these analyses are illustrated in Figure 6.25 for the 60-ft-long model with an internal diaphragm spacing of 1D. Three cases are shown: the undamaged/intact model (UC), a model with the bottom flange fractured (FBF), and a model with an entire web and the corresponding flange connection plate fractured (FW). The crack is located at the

midspan in both faulted models. Additionally, the value for the torsional constant obtained from Equation 6.3 is included for comparison (labeled as “theoretical”). The upper plot shows the relationship between the applied torque,  $T$ , and the rotation of the free end,  $\phi$ , for the three models and the theoretical results from Equation 6.3. The bottom plot depicts the calculated torsional constant,  $J_{tg}$ , of the girder as a function of the rotation, which was calculated from the first derivative of the  $T - \phi$  curve on the upper plot.

These results showed that the initial stiffness of the models is approximately 10% lower than the theoretical value computed from Equation 6.3, which was attributed to the discrete connection between the bottom flange plate and the flange connection plates with the connectors (corresponding to the bolted connections). Moreover, it was noted that the behavior of the model with a fractured bottom flange does not differ significantly from the undamaged/intact model: the differences in torsional stiffness are within 2% for rotations smaller than 0.02 radians. At this point, the curve corresponding to the fractured model deviates from the undamaged/intact model. On the other hand, a fractured web seems to have a higher impact: the initial torsional constant is lower than in the other two models (approximately 5% lower than the undamaged/intact model) and shows a more abrupt decay as the rotations increase. This more rapid decrease seems to indicate that the loss of one web has a more significant impact on the torsional capacity of the box member than the loss of the bottom flange.

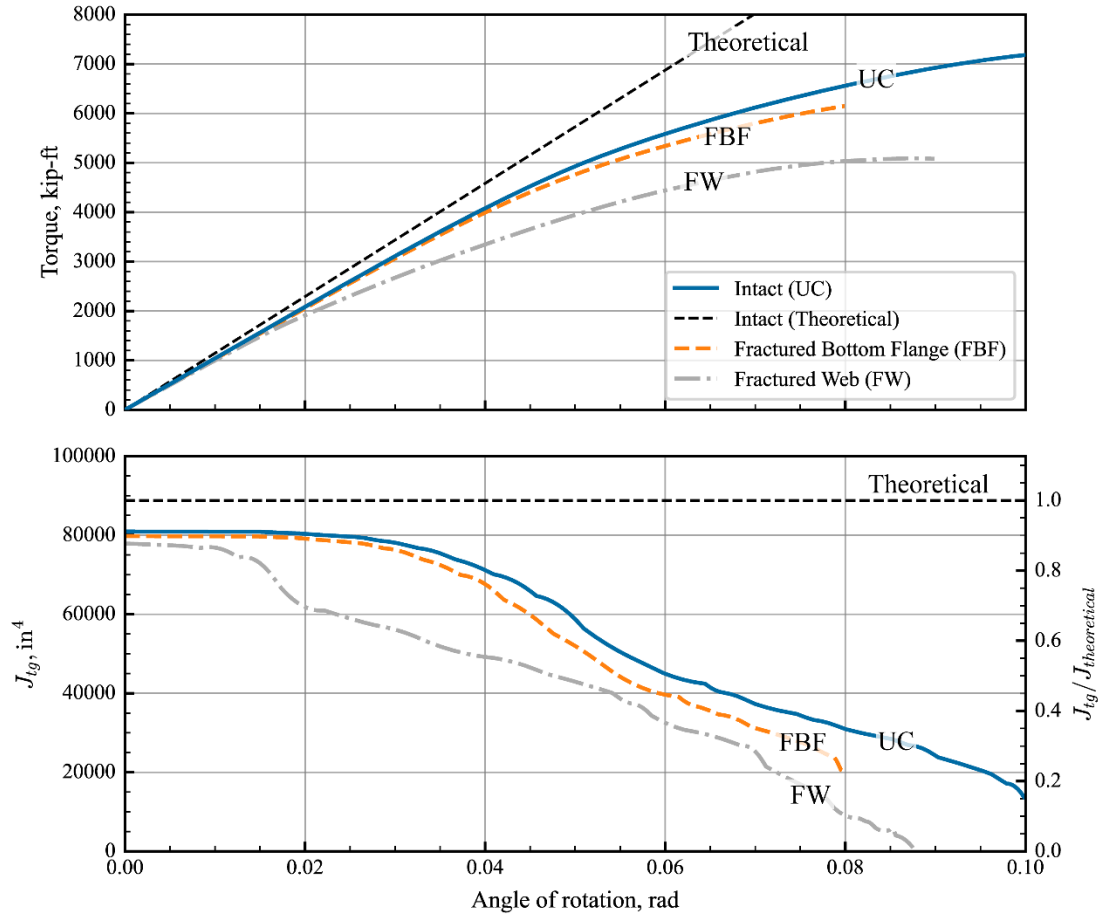


Figure 6.25: Design Concept B Parametric Studies: influence of a fractured section on the torsional stiffness

Furthermore, the influence of the diaphragm spacings on the torsional stiffness is shown in Figure 6.26 for the undamaged/intact and fractured models. To normalize the horizontal axis, the applied torque is expressed as the web shear stress due to torsion,  $f_{ve}$ , per Equation 6.5 (Equation C6.9.2.2.2-2 from the AASHTO LRFD Specifications (2020):

$$f_{ve} = \frac{T}{2 \cdot A_0 \cdot t_w} \quad \text{Equation 6.5}$$

Where  $T$  is the applied torque,  $A_0$  is the enclosed area within the undamaged/intact box section, and  $t_w$  is the thickness of the web plates.

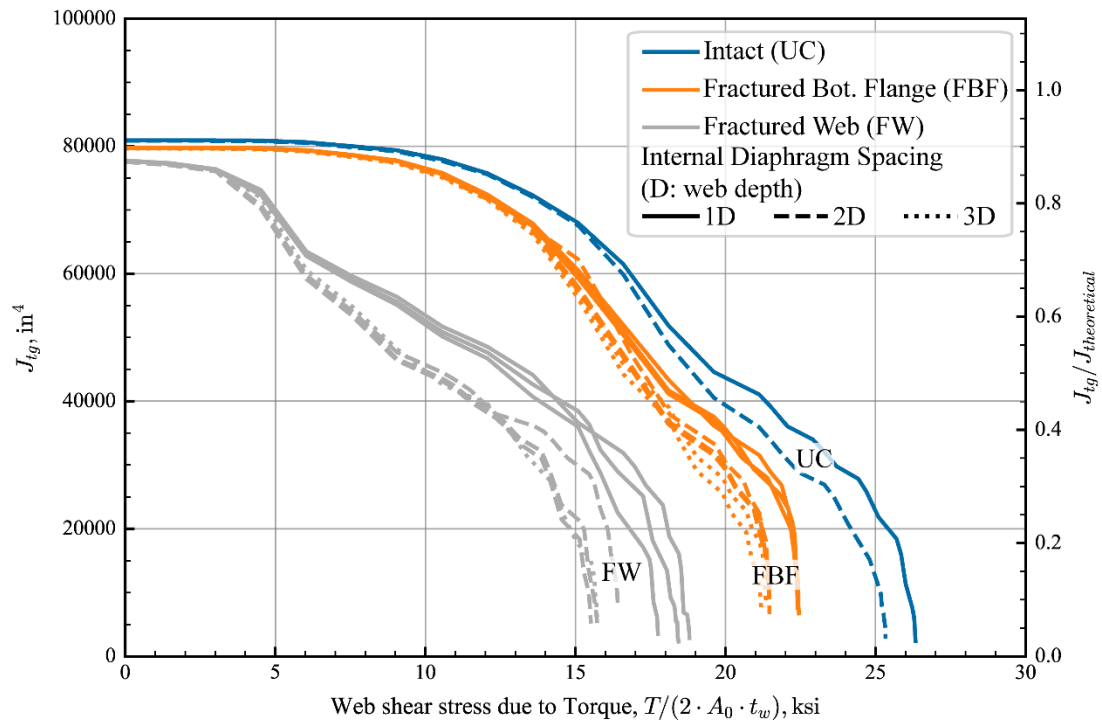


Figure 6.26: Design Concept B: influence of the spacing of internal diaphragms

The curves are grouped by color based on the fractured components considered: undamaged/intact (UC) models are shown in blue, models with the bottom flange fractured (FBF) are depicted in orange, and those with the entire web fractured (FW) are plotted in grey. The different line styles correspond to the spacing of the internal diaphragms.

In the undamaged/intact models (UC) and those with a fractured bottom flange (FBF), increasing the diaphragm spacing has a negligible effect (less than 2%) on the torsional stiffness for torsional shear stresses below 12 ksi. On the other hand, the diaphragm spacing has more influence on the torsional stiffness of the models with a fractured web, particularly as the applied shear stresses exceed 3 ksi. Beyond that point, the torsional stiffness decreases significantly (as much as 50% at 15 ksi).

These analyses were conducted for all the models described in Table 6.1. The results are presented in Figure 6.27, where the torsional constant is normalized by the length of the girder,  $L$ , and plotted against the web shear stress due to torque. The curves are grouped by colors according to the span length of the model.

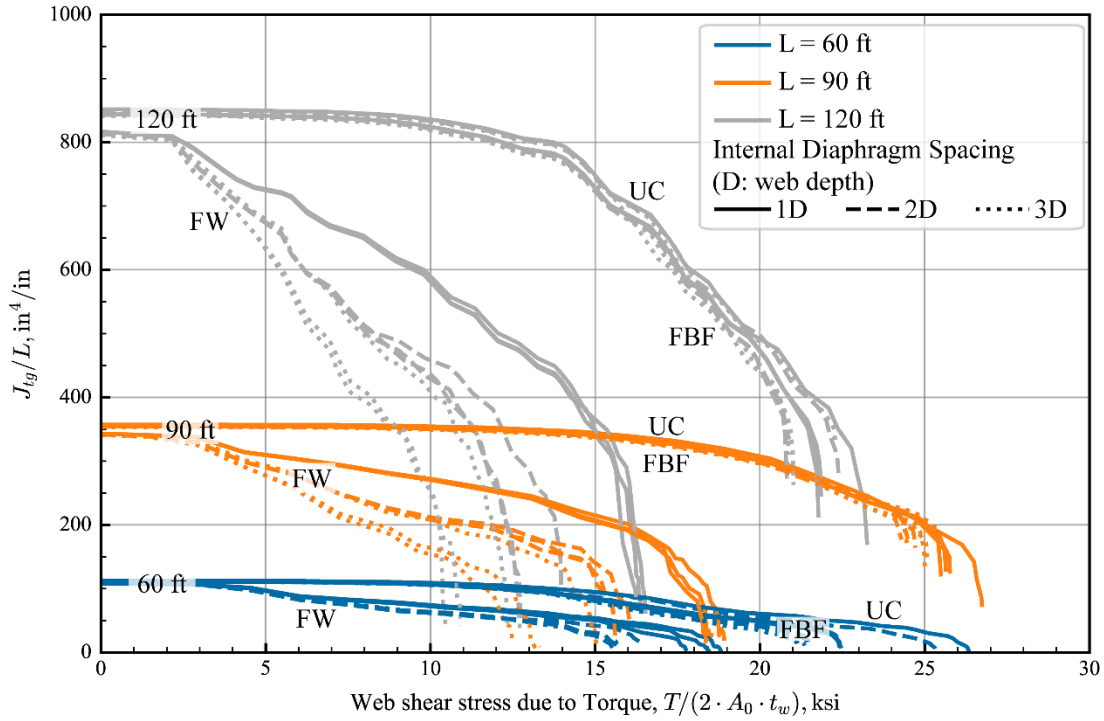


Figure 6.27: Design Concept B: torsional constant normalized by span length versus web shear stress due to torsion

The solid lines correspond to the undamaged/intact models, while the dashed and dotted lines represent the models with a fractured bottom flange and a fractured web, respectively. As observed previously, the most pronounced reductions in torsional stiffness correspond to the models with a fractured web.

The same results are presented in Figure 6.28, in which the torsional constant of each model was normalized by its initial value. It can be observed from this plot that the reduction in the torsional stiffness is less than 8% for web shear stresses due to torsion below 2 ksi. Moreover, the reduction in torsional stiffness is bound at 20% for 4 ksi, and the reduction continues as the torsional demands increase.



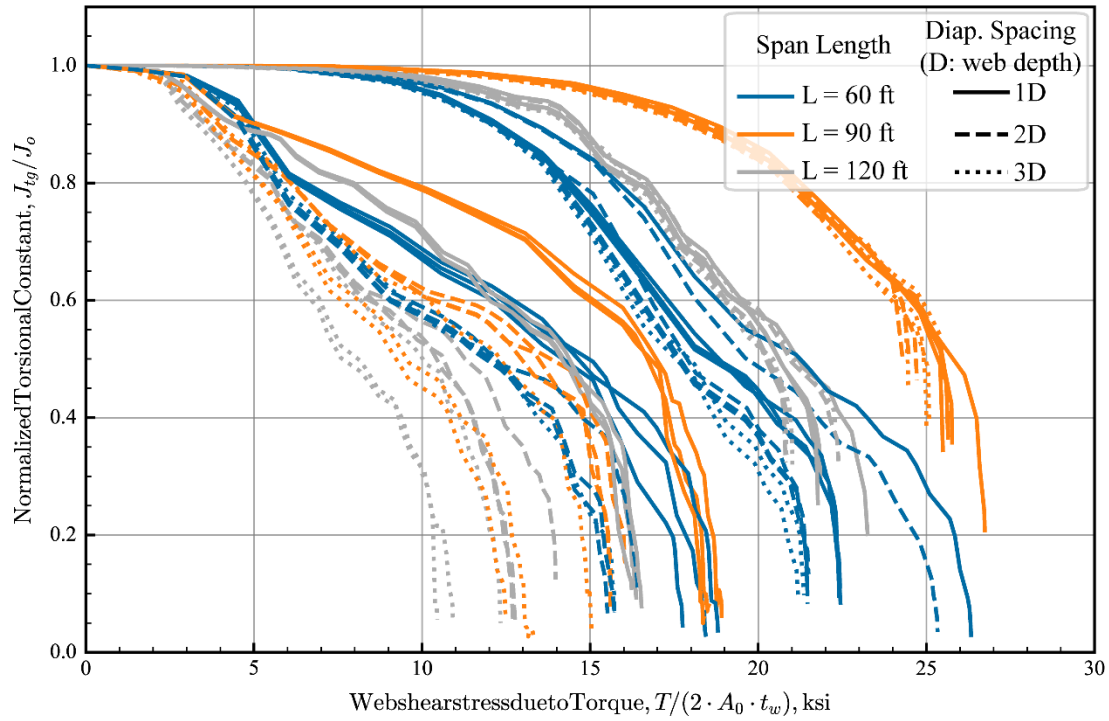


Figure 6.28: Design Concept B: normalized torsional constant versus web shear stress due to torsion

The results indicate that the torsional stiffness of the box section member with a fracture remains relatively unaffected for low torsional demands (i.e., producing less than 5 ksi of web shear stresses due to torsion). As a reference, web shear stresses of 5 ksi on the 60-ft-long model correspond to the eccentric loading the box girder with four factored HS-20 design trucks (AASHTO, 2020), illustrated in Figure 6.29.

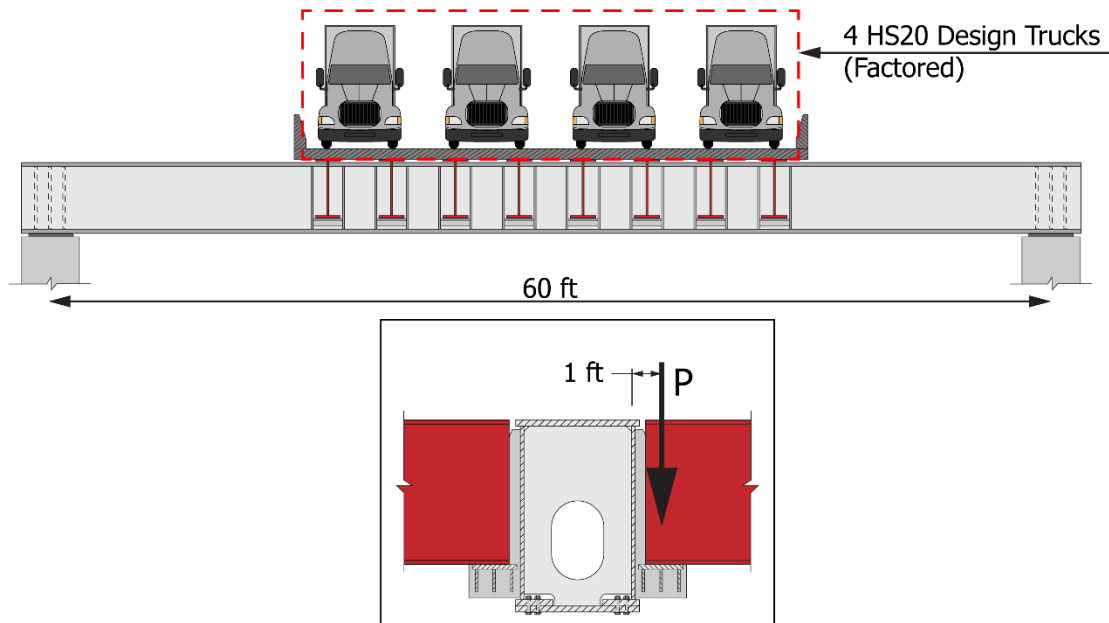


Figure 6.29: Application of four factored HS-20 trucks for a 60-ft long box cap

A conservative and straightforward assumption is to consider 50% of the torsional constant of the undamaged/intact section to estimate the capacity of box section caps in the faulted condition. Due to the nonlinearity of Equation 6.1 and Equation 6.2, a 50% reduction in the torsional constant reduces the limiting unbraced lengths by 30%. This conservative approach will be applied to assess the current design provisions to estimate the strength of faulted box caps presented in the following subsection.

#### 6.3.2.2. Parametric study for adequacy of current design equations

The models described in the previous subsection were analyzed under the loading conditions, shown in Figure 6.30. The loading conditions included symmetric and unsymmetric loading with one or two concentrated loads that were applied coincidentally with internal diaphragms. For the first set of models, the loads were applied through the shear center of the box section; in the second set, eccentrically applied loads equivalent to four factored HS-20 trucks (AASHTO 2020) were applied to each girder before applying the centered loads. These eccentric loads were aimed at introducing realistic torsional demands on the box girder to assess the influence on the capacity of the box girder. Considering the different loading conditions, crack types, and crack locations, a total of 360 models were included in the study.

Three scenarios were analyzed relative to the fractured components of the box cap (see Figure 6.22): (i) the model was undamaged/intact -or uncracked,- (ii) the bottom flange

plate was fractured, and (iii) one entire web and its corresponding flange connection plate were fractured. The assumed locations of the cracked sections were selected to consider situations with high flexural demands and a combination of high shear and flexural demands on the faulted section, as depicted in Figure 6.30. In addition, modeling each girder in an undamaged/intact condition provided a benchmark for the models in the faulted state.

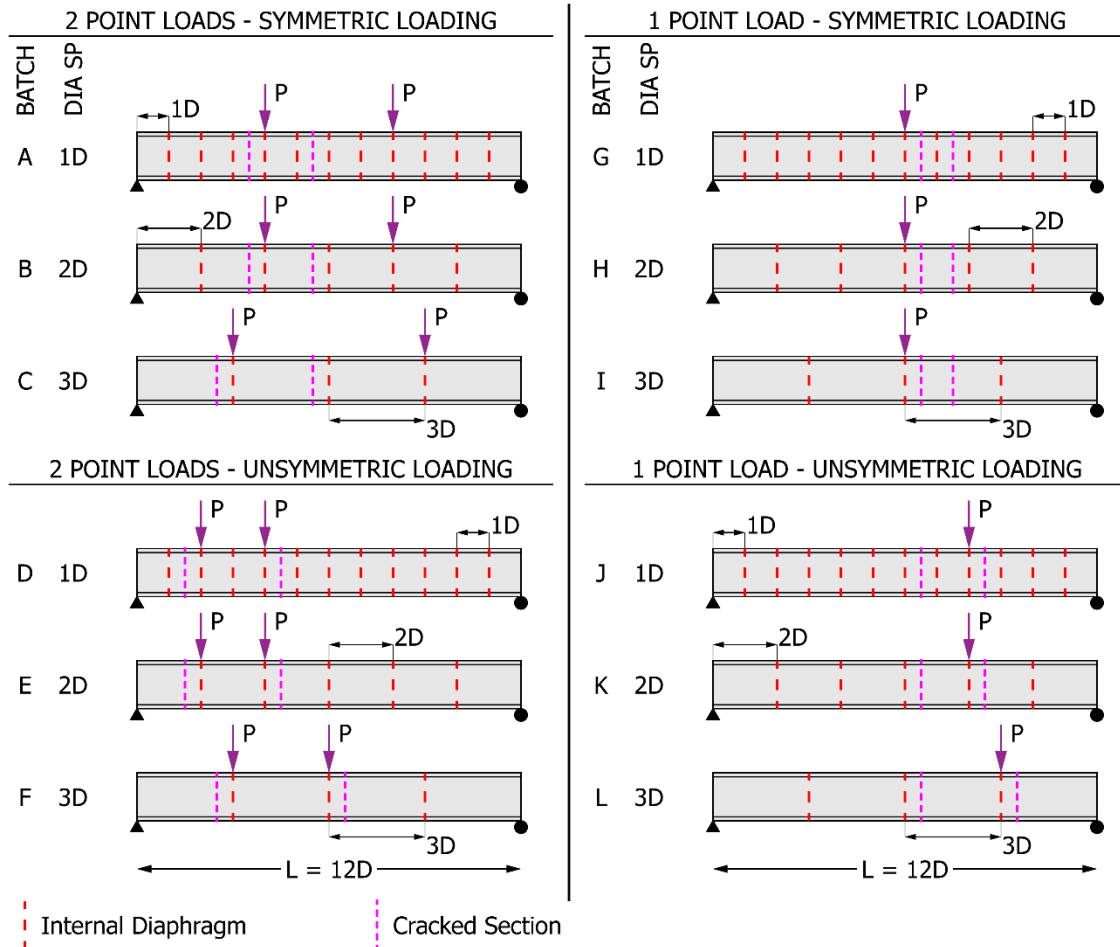


Figure 6.30: Design Concept B parametric FE study: loading conditions and crack locations

An example is provided in Figure 6.31 for the 60-ft-long model with the internal diaphragms spaced every one web depth. For the case shown, the model was subject to two concentrated symmetric loads applied at the shear center, and the fractured section is located to the left of the first concentrated load, at 17.5 ft from the left support. The plot on the right-hand side of the figure shows the total applied vertical load versus the vertical deflection at the fractured section. It should be noted that although no fractured section

exists in the undamaged/intact model, the deflection is measured at the same location as in the other two cases. The plot on the left depicts the lateral displacement at the fractured section. Three curves are shown: the undamaged/intact or uncracked (UC) model, the model with a fractured bottom flange (FBF), and the model with one entire web and its corresponding flange connection plate fractured (FW).

The decrease in the maximum load the girder can carry for different assumed crack configurations is evidenced in Figure 6.31. Moreover, it is noted that there is essentially no lateral deflection for the uncracked model (UC) and the model with a fractured bottom flange (FBF), as the cross-section remains symmetric with respect to the vertical axis in the faulted condition.

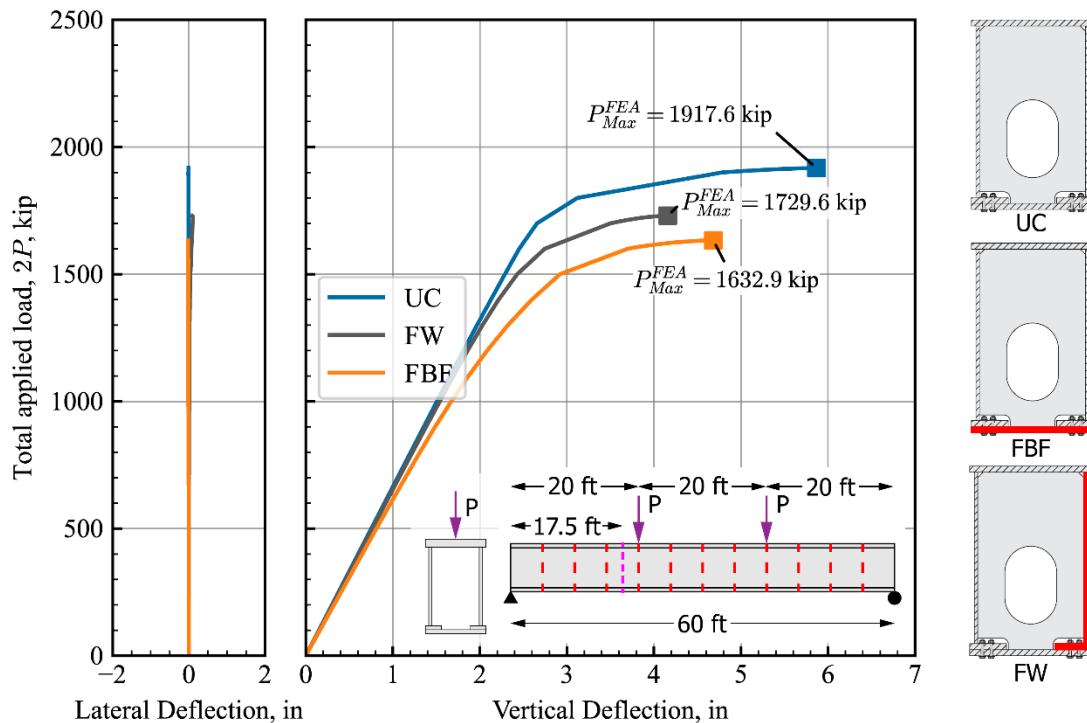


Figure 6.31: Design Concept B parametric FE study: load versus displacement at the fractured section.

However, a slight lateral deflection of approximately 3/10,000 of the length of the girder was observed for the model with the fractured web and flange connection plate (FW).

For each of these models, the flexural and shear strengths were calculated based on the provisions of Article 6.12.2.2.2 of the AASHTO LRFD Specifications (2020) and compared with the results of the FE models. Sample calculations are provided in Table 6.2,

Table 6.3, and Table 6.4 for the 60-ft-long girder with internal diaphragms spaced at one web depth. Next, the maximum load the girder can sustain in each loading configuration was derived from the calculated flexural and shear strengths. In several cases, it was found that the maximum load reached in the FE analyses was in between the flexural and shear strengths of the faulted section calculated with the provisions of AASHTO LRFD (2020). Hence, the interaction between moment and shear was also reflected in the analyses. Since AASHTO removed the flexure-shear interaction provisions from the LRFD Specifications in 2005, the equation of the American Institute of Steel Construction (AISC) Manual of 1999 was used. Table 6.11 provides a sample calculation of the maximum loads for the 60-ft-long box girder with internal diaphragms spaced at 1D.

**Table 6.2: Sample calculation of Flexural Strength (Undamaged/intact Condition)**

	Top Flange Thickness, in	$t_{tf}$	1.375
	Top Flange Width, in	$b_{tf}$	40.0
	Bottom Flange Thickness, in	$t_{bf}$	1.0
	Bottom Flange Width, in	$b_{bf}$	40.0
	Web Thickness, in	$t_w$	0.75
	Web Depth, in	$d_w$	60.0
	Flange Connection Plate Thickness, in	$t_1$	1.0
	Flange Connection Plate Width, in	$b_1$	9.0
	Clear Projecting Width, in	$b_p$	2.0
	Yield Stress, ksi	$F_y$	50.0
	Young's Modulus, ksi	$E$	29,000
	Unbraced Length, in	$L_b$	720.0
<b>1. Computation of top flange effective width, <math>b_e</math>, and effective sectional properties (Article 6.12.2.2.2c)</b>			
Flange width $b = b_{tf} - 2 \cdot b_p - 2 \cdot t_w = 34.5 \text{ in}$ (Table 6.9.4.2.1-1)			
Flange Slenderness $\lambda_f = \frac{b}{t_{tf}} = 25.1$ (Table 6.9.4.2.1-1)			
Limiting Slenderness $\lambda_r = 1.09 \cdot \sqrt{\frac{E}{F_y}} = 26.3$ (Table 6.9.4.2.1-1)			
$\rightarrow \lambda_f < \lambda_r \therefore b_e = b_{tf} = 40.0 \text{ in}$			
Depth of the webs in compression in the elastic range $D_{ce} = 30.6 \text{ in}$			
Yield moment with respect to the compression flange $M_{yce} = S_{33te} \cdot F_y = 17,616 \text{ kip} \cdot \text{ft}$			
Depth of the webs in compression in the plastic range $D_{cep} = 31.0 \text{ in}$			
Plastic moment $M_{pe} = Z_{33e} \cdot F_y = 20,189 \text{ kip} \cdot \text{ft}$			
	Gross Area, in <sup>2</sup>	$A_{ge}$	203.0
	Elastic Neutral Axis, in	$y_{ge}$	31.4
	Plastic Neutral Axis, in	$y_{pe}$	31.0
	Moment of Inertia about 33 axis, in <sup>4</sup>	$I_{33e}$	135,170
	Radius of Gyration about 33 axis, in	$r_{33e}$	25.8
	Section Moduli about 33 axis (top), in <sup>3</sup>	$S_{33te}$	4,228
	Section Moduli about 33 axis (bot), in <sup>3</sup>	$S_{33be}$	4,304
	Plastic Section Mod about 33 axis, in <sup>3</sup>	$Z_{33e}$	4,845
	Moment of Inertia about 22 axis, in <sup>4</sup>	$I_{22e}$	45,075
	Radius of Gyration about 22 axis, in	$r_{22e}$	14.9
	Section Moduli about 22 axis, in <sup>3</sup>	$S_{22e}$	2,254
	St. Venant Torsional Constant, in <sup>4</sup>	$J_e$	88,800

**Table 6.2: Sample calculation of Flexural Strength (Undamaged/intact Condition) (Cont.)**

<p><b>2. Web Classification (Article 6.12.2.2.2c)</b></p> <p>Limiting Slenderness for a compact web,</p> $\lambda_{pw} = 3.1 \frac{D_{ce}}{D_{cep}} \sqrt{\frac{E}{F_y}} = 73.7$ <p>Limiting Slenderness for a noncompact web,</p> $\lambda_{rw} = 4.6 \sqrt{\frac{E}{F_y}} = 110.8$ <p>Web Slenderness</p> $\lambda_w = 2 \cdot \frac{D_{ce}}{t_w} = 81.6 \rightarrow \text{Noncompact web}$ <p>Web Plastification Factor for noncompact webs (Equation 6.12.2.2.2c-4, 7 &amp; 8)</p> $R_{pc} = \left[ 1 - \left( 1 - \frac{M_{yce}}{M_{pe}} \right) \cdot \left( \frac{\lambda_w - \lambda_{pw}}{\lambda_{rw} - \lambda_{pw}} \right) \right] \frac{M_{pe}}{M_{yce}} = 1.11$ <p>Limiting Slenderness for noncompact webs</p> $\lambda_{rws} = 4.6 \sqrt{\frac{E}{F_y}} \leq \left( 3.1 + \frac{5}{a_{wc}} \right) \sqrt{\frac{E}{F_y}} \leq 5.7 \sqrt{\frac{E}{F_y}} = 137.3$ <p>Web Load Shedding Factor</p> $\rightarrow \lambda_w < \lambda_{rws} \therefore R_b = 1.0$	<p><b>3. Compression Flange Classification (Article 6.12.2.2.2d)</b></p> <p>Limiting Slenderness for a compact flange</p> $\lambda_{pf} = 1.09 \cdot \sqrt{\frac{E}{F_y}} = 26.3$ <p>Limiting Slenderness for a noncompact flange</p> $\lambda_{rf} = 1.56 \cdot \lambda_{pf} = 40.9$ <p>Flange Slenderness</p> $\lambda_f = 25.1 \rightarrow \text{Compact Flange}$ <p>Compression Flange Slenderness Factor for a compact flange</p> $R_f = 1.0$ <p><b>4. General Yielding, compression flange local buckling, and Lateral Torsional Buckling (Article 6.12.2.2.2e)</b></p> <p>Limiting unbraced length to achieve the nominal flexural resistance <math>R_f R_b R_{pc} M_{yce}</math></p> $L_p = \frac{0.1 \cdot r_{22e} \cdot E \cdot \sqrt{J_e \cdot A_{ge}}}{M_{yce}} = 868 \text{ in} \approx 72.3 \text{ ft}$ <p>Limiting unbraced length for the calculation of the lateral torsional buckling resistance</p> $L_r = \frac{0.6 \cdot r_{22e} \cdot E \cdot \sqrt{J_e \cdot A_{ge}}}{0.5 \cdot F_y \cdot S_{33te}} = 10,415 \text{ in} \approx 868 \text{ ft}$ <p><math>\rightarrow L_b &lt; L_p \therefore M_n = R_b R_{pc} R_f \cdot M_{yce} = 19,641 \text{ kip} \cdot \text{ft}</math></p>
<p><b>5. Shear Strength of Interior Panels</b></p> <p>Plastic Shear Force (per web)</p> $V_p = 0.58 \cdot F_y \cdot t_w \cdot d_w = 1,305 \text{ kip}$ <p>Transverse Diaphragm Spacing</p> $d_o = 60 \text{ in}$ <p>Shear buckling coefficient</p> $k = 5 + \frac{5}{\left( \frac{d_o}{d_w} \right)^2} = 10$ $\frac{d_w}{t_w} = 80 < 1.12 \cdot \sqrt{\frac{E \cdot k}{F_y}} = 85.3 \rightarrow C = 1.0$ $\frac{2 \cdot d_w \cdot t_w}{\left( \frac{b_{tf}}{2} t_{tf} + \frac{b_{bf}}{2} t_{bf} \right)} = 1.89 < 2.5$ $\rightarrow V_n = V_p \cdot \left( C + \frac{0.87(1-C)}{\sqrt{1 + \left( \frac{d_o}{d_w} \right)^2}} \right) = 1,305 \text{ kip (per web)}$	<p><b>6. Shear Strength of End Panels</b></p> <p>Plastic Shear Force (per web)</p> $V_p = 0.58 \cdot F_y \cdot t_w \cdot d_w = 1,305 \text{ kip}$ <p>Transverse Diaphragm Spacing</p> $d_o = 60 \text{ in}$ <p>Shear buckling coefficient</p> $k = 5 + \frac{5}{\left( \frac{d_o}{d_w} \right)^2} = 10$ $\frac{d_w}{t_w} = 80 < 1.12 \cdot \sqrt{\frac{E \cdot k}{F_y}} = 85.3 \rightarrow C = 1.0$ $\frac{2 \cdot d_w \cdot t_w}{\left( \frac{b_{tf}}{2} t_{tf} + \frac{b_{bf}}{2} t_{bf} \right)} = 1.89 < 2.5$ <p><math>\rightarrow V_n = V_p \cdot C = 1,305 \text{ kip (per web)}</math></p>



**Table 6.3: Sample calculation of Flexural Strength (Fractured Bottom Flange)**

	Top Flange Thickness, in	$t_{tf}$	1.375
	Top Flange Width, in	$b_{tf}$	40.0
	<del>Bottom Flange Thickness, in</del>	<del><math>t_{bf}</math></del>	<del>0.0</del>
	<del>Bottom Flange Width, in</del>	<del><math>b_{bf}</math></del>	<del>0.0</del>
	Web Thickness, in	$t_w$	0.75
	Web Depth, in	$d_w$	60.0
	Flange Connection Plate Thickness, in	$t_l$	1.0
	Flange Connection Plate Width, in	$b_l$	9.0
	Clear Projecting Width, in	$b_p$	2.0
	Yield Stress, ksi	$F_y$	50.0
	Young's Modulus, ksi	$E$	29,000
	Unbraced Length, in	$L_b$	720.0

**1. Computation of top flange effective width,  $b_e$ , and effective sectional properties (Article 6.12.2.2c)**

Flange width

$$b = b_{tf} - 2 \cdot b_p - 2 \cdot t_w = 34.5 \text{ in} \quad (\text{Table 6.9.4.2.1-1})$$

Flange Slenderness

$$\lambda_f = \frac{b}{t_{tf}} = 25.1 \quad (\text{Table 6.9.4.2.1-1})$$

Limiting Slenderness

$$\lambda_r = 1.09 \cdot \sqrt{\frac{E}{F_y}} = 26.3 \quad (\text{Table 6.9.4.2.1-1})$$

$$\rightarrow \lambda_f < \lambda_r \therefore b_e = b_{tf} = 40.0 \text{ in}$$

Depth of the webs in compression in the elastic range

$$D_{ce} = 16.9 \text{ in}$$

Yield moment with respect to the compression flange

$$M_{yce} = 13,445 \text{ kip} \cdot \text{ft}$$

(early nominal yielding of tension flange)

Depth of the webs in compression in the plastic range

$$D_{cep} = 17.7 \text{ in}$$

Plastic moment

$$M_{pe} = Z_{33e} \cdot F_y = 13,994 \text{ kip} \cdot \text{ft}$$

Gross Area, in <sup>2</sup>	$A_{ge}$	163.0
Elastic Neutral Axis, in	$y_{ge}$	38.0
Plastic Neutral Axis, in	$y_{pe}$	43.3
Moment of Inertia about 33 axis, in <sup>4</sup>	$I_{33e}$	87,593
Radius of Gyration about 33 axis, in	$r_{33e}$	23.2
Section Moduli about 33 axis (top), in <sup>3</sup>	$S_{33te}$	3,592
Section Moduli about 33 axis (bot), in <sup>3</sup>	$S_{33be}$	2,306
Plastic Section Mod about 33 axis, in <sup>3</sup>	$Z_{33e}$	3,359
Moment of Inertia about 22 axis, in <sup>4</sup>	$I_{22e}$	39,741
Radius of Gyration about 22 axis, in	$r_{22e}$	15.6
Section Moduli about 22 axis, in <sup>3</sup>	$S_{22e}$	1,987
St. Venant Torsional Constant, in <sup>4</sup>	$J_e$	44,400 <sup>a</sup>

<sup>a</sup> Corresponding to 50% of the undamaged/intact section

**Table 6.3: Sample calculation of Flexural Strength (Fractured Bottom Flange) (Cont.)**

<p><b>2. Web Classification (Article 6.12.2.2.2c)</b></p> <p>Limiting Slenderness for a compact web,</p> $\lambda_{pw} = 3.1 \frac{D_{ce}}{D_{cep}} \sqrt{\frac{E}{F_y}} = 71.7$ <p>Limiting Slenderness for a noncompact web,</p> $\lambda_{rw} = 4.6 \sqrt{\frac{E}{F_y}} = 110.8$ <p>Web Slenderness</p> $\lambda_w = 2 \cdot \frac{D_{ce}}{t_w} = 45.2 \rightarrow \text{Compact web}$ <p>Web Plastification Factor for noncompact webs (Equation 6.12.2.2.2c-4, 7 &amp; 8)</p> $R_{pc} = \frac{M_{pe}}{M_{yce}} = 1.04$ <p>Limiting Slenderness for noncompact webs</p> $\lambda_{rws} = 4.6 \sqrt{\frac{E}{F_y}} \leq \left( 3.1 + \frac{5}{a_{wc}} \right) \sqrt{\frac{E}{F_y}} \leq 5.7 \sqrt{\frac{E}{F_y}} = 137.3$ <p>Web Load Shedding Factor</p> $\rightarrow \lambda_w < \lambda_{rws} \therefore R_b = 1.0$	<p><b>3. Compression Flange Classification (Article 6.12.2.2.2d)</b></p> <p>Limiting Slenderness for a compact flange</p> $\lambda_{pf} = 1.09 \cdot \sqrt{\frac{E}{F_y}} = 26.3$ <p>Limiting Slenderness for a noncompact flange</p> $\lambda_{rf} = 1.56 \cdot \lambda_{pf} = 40.9$ <p>Flange Slenderness</p> $\lambda_f = 25.1 \rightarrow \text{Compact Flange}$ <p>Compression Flange Slenderness Factor for a compact flange</p> $R_f = 1.0$ <p><b>4. General Yielding, compression flange local buckling, and Lateral Torsional Buckling (Article 6.12.2.2.2e)</b></p> <p>Limiting unbraced length to achieve the nominal flexural resistance <math>R_f R_b R_{pc} M_{yce}</math></p> $L_p = \frac{0.1 \cdot r_{22e} \cdot E \cdot \sqrt{J_e \cdot A_{ge}}}{M_{yce}} = 755 \text{ in}$ $\approx 62.9 \text{ ft}$ <p>Limiting unbraced length for the calculation of the lateral torsional buckling resistance</p> $L_r = \frac{0.6 \cdot r_{22e} \cdot E \cdot \sqrt{J_e \cdot A_{ge}}}{0.5 \cdot F_y \cdot S_{33te}} = 8140 \text{ in}$ $\approx 659 \text{ ft}$ <p><math>\rightarrow L_b &lt; L_p \therefore M_n = R_b R_{pc} R_f \cdot M_{yce}</math></p> $= 13,994 \text{ kip} \cdot \text{ft}$
--	--

**Table 6.3: Sample calculation of Flexural Strength (Fractured Bottom Flange) (Cont.)**

5. Shear Strength of Interior Panels	6. Shear Strength of End Panels
Plastic Shear Force (per web) $V_p = 0.58 \cdot F_y \cdot t_w \cdot d_w = 1,305 \text{ kip}$	Plastic Shear Force (per web) $V_p = 0.58 \cdot F_y \cdot t_w \cdot d_w = 1,305 \text{ kip}$
Transverse Diaphragm Spacing $d_0 = 60 \text{ in}$	Transverse Diaphragm Spacing $d_0 = 60 \text{ in}$
Shear buckling coefficient $k = 5 + \frac{5}{\left(\frac{d_0}{d_w}\right)^2} = 10$	Shear buckling coefficient $k = 5 + \frac{5}{\left(\frac{d_0}{d_w}\right)^2} = 10$
$\frac{d_w}{t_w} = 80 < 1.12 \cdot \sqrt{\frac{E \cdot k}{F_y}} = 85.3 \rightarrow C = 1.0$	$\frac{d_w}{t_w} = 80 < 1.12 \cdot \sqrt{\frac{E \cdot k}{F_y}} = 85.3 \rightarrow C = 1.0$
$\frac{2 \cdot d_w \cdot t_w}{\left(\frac{b_{tf}}{2} t_{tf} + \frac{b_{bf}}{2} t_{bf}\right)} = 1.89 < 2.5$	$\frac{2 \cdot d_w \cdot t_w}{\left(\frac{b_{tf}}{2} t_{tf} + \frac{b_{bf}}{2} t_{bf}\right)} = 1.89 < 2.5$
$\rightarrow V_n = V_p \cdot \left( C + \frac{0.87(1-C)}{\sqrt{1 + \left(\frac{d_0}{d_w}\right)^2}} \right) = 1,305 \text{ kip (per web)}$	$\rightarrow V_n = V_p \cdot C = 1,305 \text{ kip (per web)}$

**Table 6.4: Sample calculation of Flexural Strength (Fractured Web)**

	Top Flange Thickness, in	$t_{tf}$	1.375
	Top Flange Width, in	$b_{tf}$	40.0
	Bottom Flange Thickness, in	$t_{bf}$	1.0
	Bottom Flange Width, in	$b_{bf}$	40.0
	Web Thickness, in	$t_w$	0.75
	Web Depth, in	$d_w$	60.0
	Flange Connection Plate Thickness, in	$t_l$	1.0
	Flange Connection Plate Width, in	$b_l$	9.0
	Clear Projecting Width, in	$b_p$	2.0
	Yield Stress, ksi	$F_y$	50.0
<p><b>1. Computation of top flange effective width, <math>b_e</math>, and effective sectional properties (Article 6.12.2.2.2c)</b></p> <p>Flange width  <math>b = b_{tf} - 2 \cdot b_p - 2 \cdot t_w = 34.5 \text{ in}</math> (Table 6.9.4.2.1-1)</p> <p>Flange Slenderness  <math>\lambda_f = \frac{b}{t_{tf}} = 25.1</math> (Table 6.9.4.2.1-1)</p> <p>Limiting Slenderness  <math>\lambda_r = 1.09 \cdot \sqrt{\frac{E}{F_y}} = 26.3</math> (Table 6.9.4.2.1-1)</p> <p><math>\rightarrow \lambda_f &lt; \lambda_r \therefore b_e = b_{tf} = 40.0 \text{ in}</math></p> <p>Depth of the webs in compression in the elastic range  <math>D_{ce} = 25.5 \text{ in}</math></p> <p>Yield moment with respect to the compression flange  <math>M_{yce} = S_{33be} \cdot F_y = 15,505 \text{ kip} \cdot \text{ft}</math></p> <p>Depth of the webs in compression in the plastic range  <math>D_{cep} = 26.0 \text{ in}</math></p> <p>Plastic moment  <math>M_{pe} = Z_{33e} \cdot F_y = 16,189 \text{ kip} \cdot \text{ft}</math></p>	Young's Modulus, ksi	$E$	29,000
	Unbraced Length, in	$L_b$	720.0
	Gross Area, in <sup>2</sup>	$A_{ge}$	149.0
	Elastic Neutral Axis, in	$y_{ge}$	33.0
	Plastic Neutral Axis, in	$y_{pe}$	36.0
	Moment of Inertia about 33 axis, in <sup>4</sup>	$I_{33e}$	113,212
	Radius of Gyration about 33 axis, in	$r_{33e}$	27.6
	Section Moduli about 33 axis (top), in <sup>3</sup>	$S_{33te}$	3,731
	Section Moduli about 33 axis (bot), in <sup>3</sup>	$S_{33be}$	3,428
	Plastic Section Mod about 33 axis, in <sup>3</sup>	$Z_{33e}$	3,885
	Moment of Inertia about 22 axis, in <sup>4</sup>	$I_{22e}$	23,033
	Radius of Gyration about 22 axis, in	$r_{22e}$	12.4
	Section Moduli about 22 axis, in <sup>3</sup>	$S_{22e}$	877
	St. Venant Torsional Constant, in <sup>4</sup>	$J_e$	44,400 <sup>a</sup>
	<sup>a</sup> Corresponding to 50% of the undamaged/intact section		

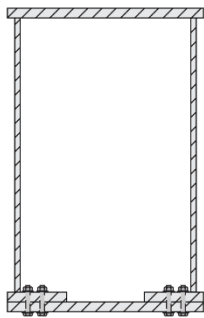
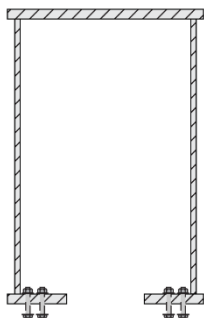
**Table 6.4: Sample calculation of Flexural Strength (Fractured Web) (Cont.)**

<p><b>2. Web Classification (Article 6.12.2.2.2c)</b></p> <p>Limiting Slenderness for a compact web,</p> $\lambda_{pw} = 3.1 \frac{D_{ce}}{D_{cep}} \sqrt{\frac{E}{F_y}} = 73.3$ <p>Limiting Slenderness for a noncompact web,</p> $\lambda_{rw} = 4.6 \sqrt{\frac{E}{F_y}} = 110.8$ <p>Web Slenderness</p> $\lambda_w = 2 \cdot \frac{D_{ce}}{t_w} = 68.1 \rightarrow \text{Compact web}$ <p>Web Plastification Factor for noncompact webs (Equation 6.12.2.2.2c-4, 7 &amp; 8)</p> $R_{pc} = \frac{M_{pe}}{M_{yce}} = 1.04$ <p>Limiting Slenderness for noncompact webs</p> $\lambda_{rws} = 4.6 \sqrt{\frac{E}{F_y}} \leq \left(3.1 + \frac{5}{a_{wc}}\right) \sqrt{\frac{E}{F_y}} \leq 5.7 \sqrt{\frac{E}{F_y}} = 137.3$ <p>Web Load Shedding Factor</p> $\rightarrow \lambda_w < \lambda_{rws} \therefore R_b = 1.0$	<p><b>3. Compression Flange Classification (Article 6.12.2.2.2d)</b></p> <p>Limiting Slenderness for a compact flange</p> $\lambda_{pf} = 1.09 \cdot \sqrt{\frac{E}{F_y}} = 26.3$ <p>Limiting Slenderness for a noncompact flange</p> $\lambda_{rf} = 1.56 \cdot \lambda_{pf} = 40.9$ <p>Flange Slenderness</p> $\lambda_f = 25.1 \rightarrow \text{Compact Flange}$ <p>Compression Flange Slenderness Factor for a compact flange</p> $R_f = 1.0$ <p><b>4. General Yielding, compression flange local buckling, and Lateral Torsional Buckling (Article 6.12.2.2.2e)</b></p> <p>Limiting unbraced length to achieve the nominal flexural resistance <math>R_f R_b R_{pc} M_{yce}</math></p> $L_p = \frac{0.1 \cdot r_{22e} \cdot E \cdot \sqrt{J_e \cdot A_{ge}}}{M_{yce}} = 498 \text{ in} \approx 42 \text{ ft}$ <p>Limiting unbraced length for the calculation of the lateral torsional buckling resistance</p> $L_r = \frac{0.6 \cdot r_{22e} \cdot E \cdot \sqrt{J_e \cdot A_{ge}}}{0.5 \cdot F_y \cdot S_{33te}} = 5,966 \text{ in} \approx 497 \text{ ft}$ <p style="text-align: center;"><math>\rightarrow L_p &lt; L_b &lt; L_r \therefore</math></p> $M_n = R_b (R_{pc} R_f \cdot M_{yce} - (R_{pc} R_f M_{yce} - 0.5 F_y S_{33te}) \alpha)$ $\alpha = \frac{L_b - L_p}{L_r - L_p} = 0.04$ $M_n = 15,848 \text{ kip} \cdot \text{ft}$
--	---

**Table 6.4: Sample calculation of Flexural Strength (Fractured Web) (Cont.)**

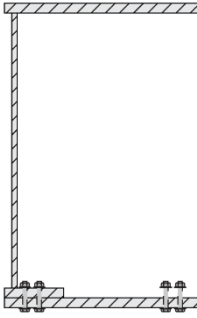
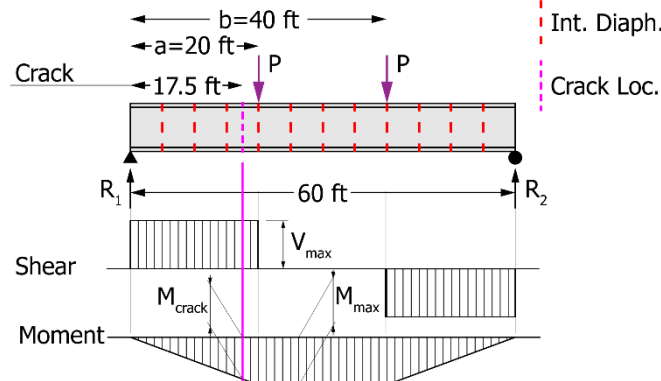
<p><b>5. Shear Strength of Interior Panels</b></p> <p>Plastic Shear Force (per web)  <math>V_p = 0.58 \cdot F_y \cdot t_w \cdot d_w = 1,305 \text{ kip}</math></p> <p>Transverse Diaphragm Spacing  <math>d_0 = 60 \text{ in}</math></p> <p>Shear buckling coefficient  <math display="block">k = 5 + \frac{5}{\left(\frac{d_0}{d_w}\right)^2} = 10</math></p> $\frac{d_w}{t_w} = 80 < 1.12 \cdot \sqrt{\frac{E \cdot k}{F_y}} = 85.3 \rightarrow C = 1.0$ $\frac{2 \cdot d_w \cdot t_w}{\left(\frac{b_{tf}}{2} t_{tf} + \frac{b_{bf}}{2} t_{bf}\right)} = 1.89 < 2.5$ $\rightarrow V_n = V_p \cdot \left( C + \frac{0.87(1 - C)}{\sqrt{1 + \left(\frac{d_0}{d_w}\right)^2}} \right) = 1,305 \text{ kip (per web)}$	<p><b>6. Shear Strength of End Panels</b></p> <p>Plastic Shear Force (per web)  <math>V_p = 0.58 \cdot F_y \cdot t_w \cdot d_w = 1,305 \text{ kip}</math></p> <p>Transverse Diaphragm Spacing  <math>d_0 = 60 \text{ in}</math></p> <p>Shear buckling coefficient  <math display="block">k = 5 + \frac{5}{\left(\frac{d_0}{d_w}\right)^2} = 10</math></p> $\frac{d_w}{t_w} = 80 < 1.12 \cdot \sqrt{\frac{E \cdot k}{F_y}} = 85.3 \rightarrow C = 1.0$ $\frac{2 \cdot d_w \cdot t_w}{\left(\frac{b_{tf}}{2} t_{tf} + \frac{b_{bf}}{2} t_{bf}\right)} = 1.89 < 2.5$ $\rightarrow V_n = V_p \cdot C = 1,305 \text{ kip (per web)}$
---	---

**Table 6.5: Sample calculation of Maximum Load**

UNDAMAGED/INTACT SECTION (UC)		
	<p><b>Required load to reach flexural strength</b></p> $M_{max} = \frac{P_{max}}{L} (2bL - ab - b^2 - bL + aL)$ $\therefore P_n^F = \frac{M_n L}{(2bL - ab - b^2 - bL + aL)} =$ $\frac{19,641 \text{ k}' \cdot 60'}{(2 \cdot 40' \cdot 60' - 20' \cdot 40' - (40')^2 - 40' \cdot 60' + 20' \cdot 60')} =$ $P_n^M = 982.1 \text{ kip}$ $\therefore 2P_n^M = 1,964.2 \text{ kip (controls)}$	<p><b>Required load to reach shear strength</b></p> $V_{max} = R_1 = \frac{P_{max}}{L} (2L - a - b)$ $\therefore P_n^V = \frac{(2V_n) \cdot L}{(2L - a - b)} =$ $\frac{(2 \cdot 1,305k) \cdot 60'}{(2 \cdot 60' - 20' - 40')} = 2,610 \text{ kip}$ $\therefore 2P_n^V = 5,220 \text{ kip}$
	<p><b>M-V Interaction per AISC (1999)</b></p> $0.625 \frac{V_u}{V_n} + \frac{M_u}{M_n} \leq 1.375$ $0.625 \frac{\frac{P_{max}}{L} (2L - a - b)}{V_n} + \frac{\frac{P_{max}}{L} (2bL - ab - b^2 - bL + aL)}{M_n} = 1.375$ $\rightarrow P_n^{M-V} = 1,093.2 \text{ kip}$ $\therefore 2P_n^{M-V} = 2,186.4 \text{ kip}$	
SECTION WITH FRACTURED BOTTOM FLANGE (FBF)		
	<p><b>Required load to reach flexural strength</b></p> $M_{crack} = R_1 \cdot c = \frac{P}{L} (2L - a - b) \cdot c$ $\therefore P_n^F = \frac{M_n L}{(2L - a - b) \cdot c} =$ $\frac{15,031 \text{ k}' \cdot 60'}{(2 \cdot 60' - 20' - 40') \cdot 17.5'} =$ $P_n^F = 799.7 \text{ kip}$ $\therefore 2P_n^F = 1,599.4 \text{ kip (controls)}$	<p><b>Required load to reach shear strength</b></p> $V_{crack} = R_1 = \frac{P}{L} (2L - a - b)$ $\therefore P_n^V = \frac{(2V_n) \cdot L}{(2L - a - b)} =$ $\frac{(2 \cdot 1,305k) \cdot 60'}{(2 \cdot 60' - 20' - 40')} = 2,610 \text{ kip}$ $\therefore 2P_n^V = 5,220 \text{ kip}$
	<p><b>M-V Interaction per AISC (1999)</b></p> $0.625 \frac{V_u}{V_n} + \frac{M_u}{M_n} \leq 1.375$ $0.625 \frac{\frac{P_{max}}{L} (2L - a - b)}{V_n} + \frac{\frac{P}{L} (2L - a - b) \cdot c}{M_n} = 1.375$ $\rightarrow P_n^{M-V} = 922.8 \text{ kip}$ $\therefore 2P_n^{M-V} = 1,845.6 \text{ kip}$	



**Table 6.5: Sample calculation of Maximum Load (Cont.)**

SECTION WITH FRACTURED WEB AND FLANGE CONNECTION PLATE (FW)		
	<p><b>Required load to reach flexural strength</b></p> $M_{crack} = R_1 \cdot c = \frac{P}{L} (2L - a - b) \cdot c$ $\therefore P_n^F = \frac{M_n L}{(2L - a - b) \cdot c} =$ $\frac{16,839 \text{ k'} \cdot 60'}{(2 \cdot 60' - 20' - 40') \cdot 17.5'} =$ $P_n^F = 905.6 \text{ kip}$ $\therefore 2P_n^F = 1,811.2 \text{ kip}$	<p><b>Required load to reach shear strength</b></p> $V_{max} = R_1 = \frac{P}{L} (2L - a - b)$ $\therefore P_n^V = \frac{(V_n) \cdot L}{(2L - a - b)} =$ $\frac{(1,305 \text{ k}) \cdot 60'}{(2 \cdot 60' - 20' - 40')} = 1,305 \text{ kip}$ $\therefore 2P_n^V = 2,610 \text{ kip}$
	<p><b>M-V Interaction per AISC (1999)</b></p> $0.625 \frac{V_u}{V_n} + \frac{M_u}{M_n} \leq 1.375$ $0.625 \frac{\frac{P_{max}}{L} (2L - a - b)}{V_n} + \frac{\frac{P}{L} (2L - a - b) \cdot c}{M_n} = 1.375$ $\rightarrow P_n^{M-V} = 868.5 \text{ kip}$ $\therefore 2P_n^{M-V} = 1,737 \text{ kip (controls)}$	
		

The strengths calculated using the provisions of the AASHTO LRFD Specifications (2020) were compared to the maximum load obtained from the FE analysis. This comparison is presented in Table 6.6 and Figure 6.32, which reproduces Figure 6.31 by adding horizontal lines representing the strength calculated per AASHTO (2020). It is observed that, for the cases presented, the strength estimates obtained following the provisions of the AASHTO LRFD Specifications (2020) are within a margin of -2/+2%.

**Table 6.6: Comparison between maximum loads from FE analyses and calculated strengths per AASHTO (2020)**

Section Condition	$P_{max}$ (FEA)	$P_n$ (AASHTO)	Difference
Undamaged/intact	1,917.6 kip	1,964.2 kip	+ 2%
Fractured Bottom Flange (FBF)	1,632.9 kip	1,599.4 kip	- 2%
Fractured Web and FCP <sup>1</sup> (FW)	1,729.6 kip	1,737.2 kip	+ 1%

<sup>1</sup> FCP: Flange Connection Plate

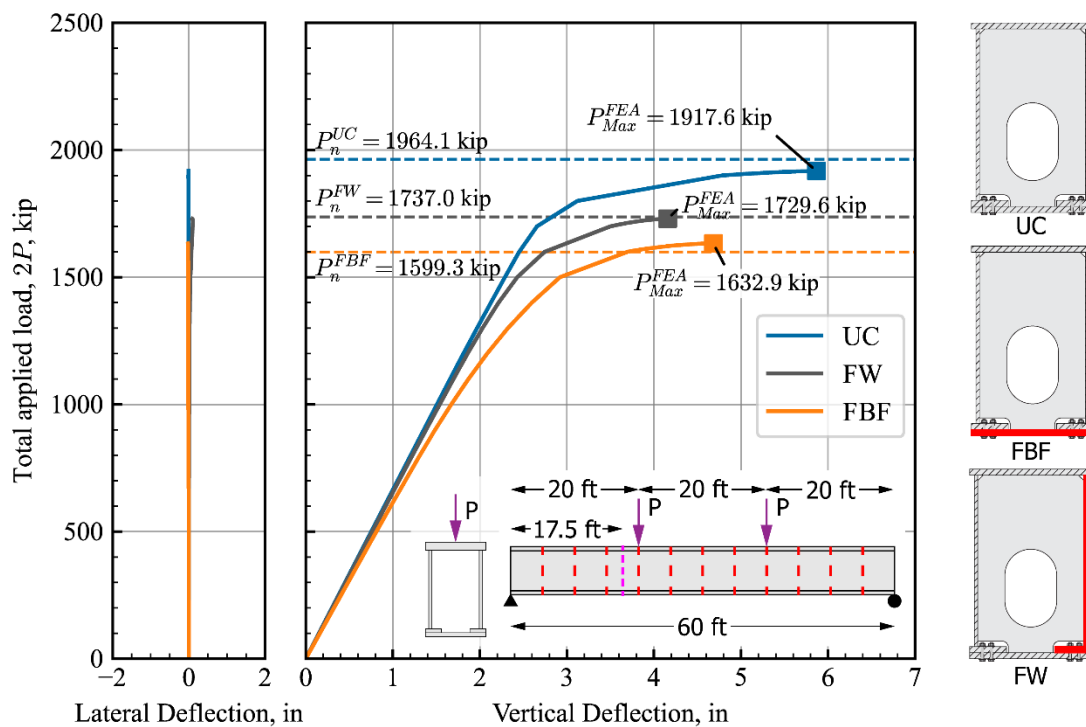


*Figure 6.32: Comparison between FEA results and strength calculations per AASHTO (2020)*

These analyses and calculations were repeated for all the models listed in Table 6.1, subject to the loading conditions shown in Figure 6.30. The results are presented in Figure 6.33. The results were grouped by cracked condition: uncracked models are shown in the top plot, the center plot corresponds to the models with an assumed fractured bottom flange, and the bottom plot contains the results for the models with an assumed fractured web and flange connections plate.

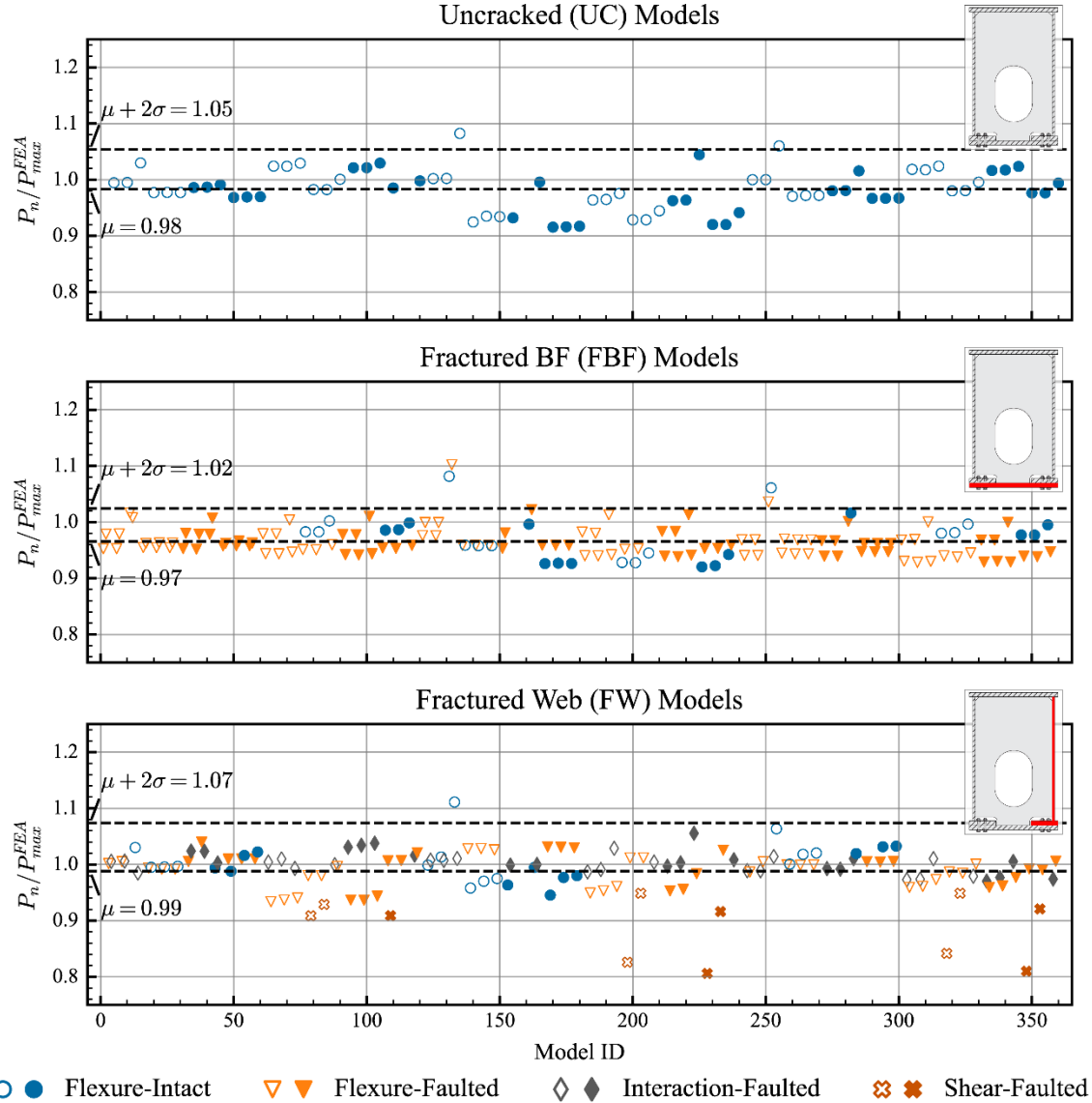


Figure 6.33: Parametric study: comparison of FE models and AASHTO design equations for models with different assumed cracks

In each graph, the ratio between the strength computed with the provisions of Article 6.12.2.2.2 of the AASHTO LRFD Specifications (2020),  $P_n$ , and the maximum load obtained from the corresponding FE analysis,  $P_{max}^{FEA}$ , is plotted for each model. A ratio larger than unity indicates that the design equations provided by AASHTO give a strength estimate higher than that from the FE analyses.

The different markers used in Figure 6.33 indicate the loading conditions and the controlling failure mode for each model:

- Empty markers correspond to models not subject to eccentrically applied loads. In contrast, filled markers were used for the models loaded with eccentrically applied loads equivalent to four factored HS-20 design trucks before applying the centered loads.
- Blue circles indicate failure due to flexure in the undamaged/intact section and correspond to the undamaged/intact and faulted models in which the crack location did not control the capacity of the member. The models labeled with an orange inverted triangle reached the maximum load corresponding to the flexural strength at the fractured section; these typically corresponded to the models with a fractured bottom flange (FBF). Lastly, the models indicated with a grey diamond or an orange cross correspond to the cases where the shear strength of the fractured section or the interaction between flexure and shear at the fractured section was reached. The cases associated with a shear or flexure-shear interaction failure corresponded to the models with a fractured web and flange connection plate.

The mean value,  $\mu$ , and standard deviation,  $\sigma$ , of the strength ratio were computed for each group. The limits corresponding to the mean value and the mean plus two standard deviations were plotted in each graph as a reference. It is observed that, on average, the provisions of the AASHTO LRFD Specifications (2020) provide good agreement with the FE analyses, given that the mean values of the strength ratio are approximately equal to one for the three groups. Considering two standard deviations above the mean value gives a strength ratio of 1.07 for the models with a fractured web (worst of the three groups). Furthermore, there is no appreciable difference between the cases with and without eccentric loading, indicating that the AASHTO Specifications (2020) estimates are adequate for both conditions.

All the models are plotted together in Figure 6.34 following the same criteria described previously. The mean value of the strength ratio was 0.98 for the entire sample, with only seven cases above the mean plus two standard deviations threshold.

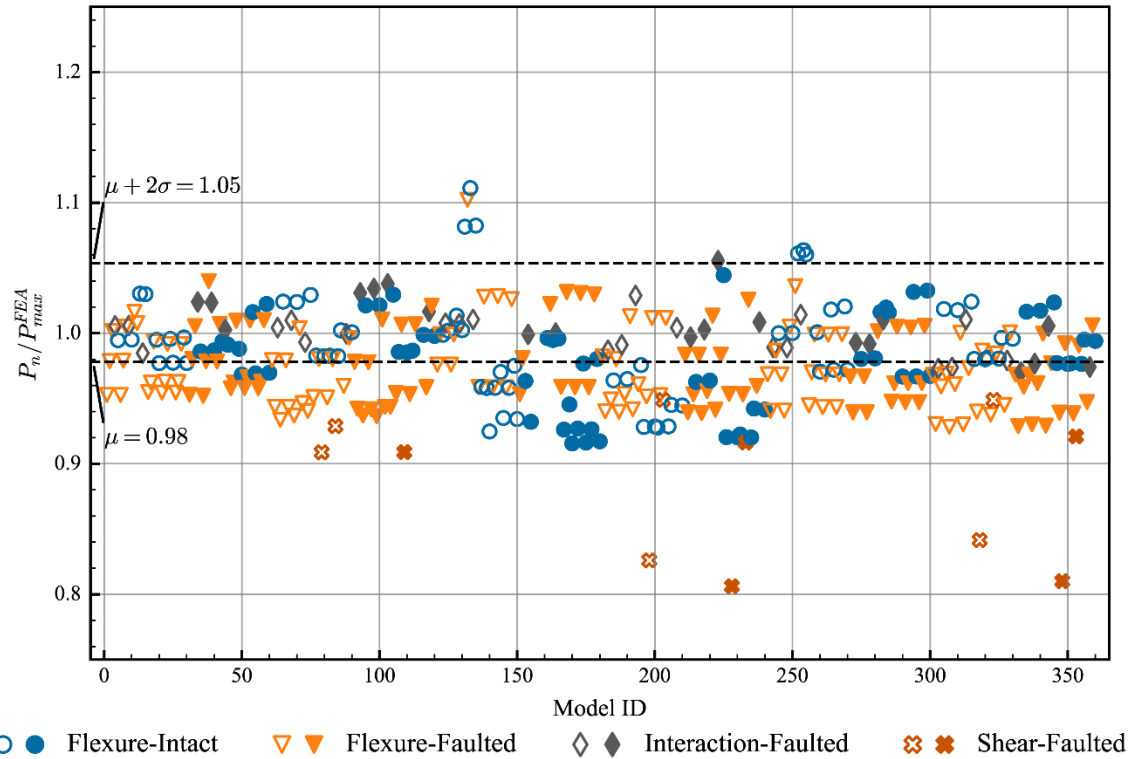


Figure 6.34: Parametric study: comparison of FE models and AASHTO design equations for all models

Based on these observations, a conservatively assumed resistance factor of 0.90 is suggested to be applied when calculating the capacity of a box member in the faulted condition. Applying this strength reduction factor, the strength ratio of all the models falls below one, indicating a conservative estimate from the equations available in the AASHTO LRFD Specifications (2020), as shown in Figure 6.35.

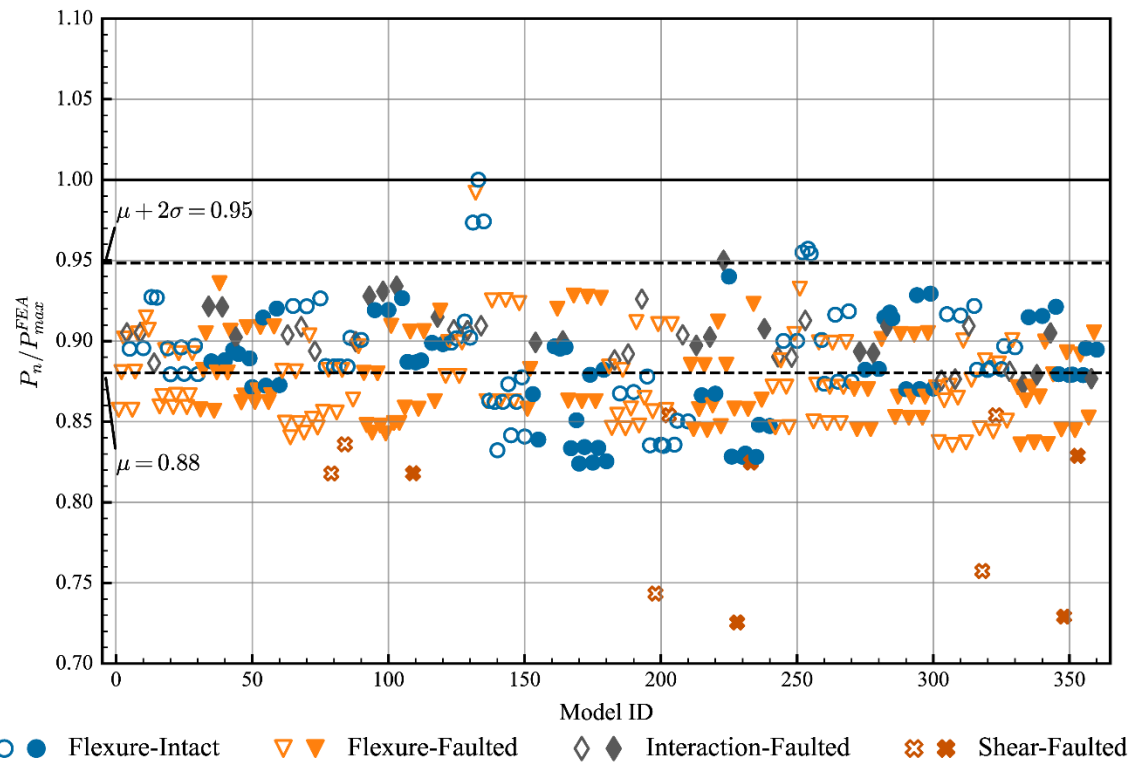


Figure 6.35: Parametric study: comparison of FE models and AASHTO design equations with 0.90 resistance factor

## 6.4. Summary

This chapter describes the analytical work conducted to study the performance of the proposed design concepts using finite element analyses and design equations available in the current design provisions of the AASHTO LRFD Specifications (2020). The chapter began with a discussion of the modeling techniques utilized and details of the FE models developed, including the element type selected, the meshing technique, and the definition of the boundary and loading conditions.

The FE analyses conducted on each design concept were then presented, starting with the validation process of the FE models for each design concept. Next, the results of the parametric studies conducted to evaluate the performance of each design concept were outlined.

In the case of Design Concept A, these studies confirmed the observations that followed the experimental tests: the lack of crack-arresting capacity of the PT bars does not preclude the fracture from severing the webs and, consequently, losing all shear capacity at that section. Furthermore, the area/number of PT bars needed to provide adequate flexural strength to the box cap in the faulted condition requires very large anchor points, which are not deemed viable for installation in the field. Another concern with the PT bars is also the member/plate sizes required at the anchors to develop the bar forces. These results make this design concept unsuitable for general design recommendations.

On the other hand, the results of the parametric studies conducted for Design Concept B show this method promising. The results showed that a fractured section has little impact on the global torsional stiffness of the box member and that the current design equations were adequate to estimate the capacity of box-section caps in the faulted condition with two straightforward modifications: (i) considering 50% of the torsional constant of the undamaged/intact section when computing the flexural strength of the undamaged/intact box member, and (ii) applying a conservative resistance factor of 0.90 in all cases (undamaged/intact and faulted sections of the girder).

Design recommendations and considerations about implementing Design Concept B are provided in Chapter 7. Furthermore, a design example for an internally redundant steel box straddle cap is outlined.



## **Chapter 7. Recommendations And Design Example**

This chapter provides some considerations on the implementation of the design concepts developed in this project and design recommendations based on the outcomes of the experimental testing and the analytical work described in Chapters 5 and 6. Next, a design example for an internally-redundant steel box straddle cap is given according to Design Concept B.

### **7.1. Considerations on Implementation**

The use of high-strength steel bars as a secondary tensile element that would limit the crack propagation and provide sufficient capacity in the faulted condition was considered in this research study in Design Concept A. This design approach was mainly envisioned as a retrofitting methodology to provide internal redundancy to existing steel box straddle caps.

A specimen constructed per this design concept (Specimen A) was tested to evaluate its crack-arresting capacity and ultimate strength in the faulted condition. Although the addition of the PT bars resulted in an improved behavior compared to the non-redundant Baseline Specimen, the crack propagation through the webs was not prevented by this design approach. Consequently, a reinforced straddle cap would lose a substantial portion of its shear capacity in the faulted condition, as shown in the FE analyses presented in Chapter 6. Moreover, several practical complications are associated with this design concept, from mobilizing, placing, and welding heavy steel sections inside the box member to modifying the diaphragms to accommodate the PT bars. Therefore, based on the results offered by this research study, general recommendations for implementing the use of PT bars to provide internal redundancy to steel box straddle caps are not prudent based on the observed behavior.

On the other hand, providing cross-boundary separation between the tensile components of a box member, as in Design Concept B, proved to be an effective method for achieving internal redundancy in steel box caps. The experimental tests demonstrated the effectiveness of this approach, and finite element analyses of steel box section members with a compact compression flange and compact or non-compact webs aided in the study of the performance of these members in the faulted condition. It was found that the flexural and shear strength of these internally redundant box section members can be adequately estimated using the design equations available in the AASHTO LRFD Specifications (2020) with minor modifications for the assumed faulted/fractured conditions. Two

primary faulted/fractured conditions were considered in this study, which correspond to the assumption of the fracture of the entire bottom flange plate and the fracture of an entire web and the corresponding flange connection plate, as shown in Figure 6.22. These potential fractured sections should be assumed to occur in regions of high flexural and combined shear and flexural demands.

Besides the auspicious outcomes of the experimental and analytical work, the positive feedback received from the TxDOT Monitoring Committee and the Industry Advisory Group makes this design approach a promising candidate for implementation for newly constructed steel box straddle caps. In addition, although not explicitly addressed in this study, this design concept could also be implemented as a retrofitting alternative for existing steel box straddle caps: bolting an additional bottom flange plate to an existing straddle cap could provide adequate capacity in the faulted condition to safely carry the load level corresponding to the Redundancy I/II or Extreme Event III load combinations. In a retrofit condition of a fully welded box girder, consideration should be given to providing a longitudinal cut to the existing bottom flange plate to produce a crack arrester and prevent a crack from propagating through both webs. It is noted that these tasks would require significant effort from the construction personnel and thorough planning for the road closure during the installation tasks.

The following recommendations are applicable to internally redundant steel box straddle caps designed according to Design Concept B and are based on the work done in this research study:

- Design sections with compact compression flanges and compact or non-compact webs. The analytical studies and experiments conducted in this project were limited to cross-sections with compact compression flanges and webs that are classified as compact or non-compact. This criterion was adopted to prevent local buckling of the compression elements in the faulted condition.
- Provide internal diaphragms to develop the tension-field action in the web plates. The finite element analyses showed that for the case where one entire web is fractured, a tension field often developed around the undamaged/intact web. Hence, providing internal diaphragms with sufficient strength and stiffness at a maximum spacing of three web depths is recommended.
- Design shear connections between the bottom flange plate and the flange connection plates for the nominal shear capacity of the webs to ensure that the full shear strength of the section can be developed.

- The bolted connection should be made with high-strength bolts and sized to fully develop the bottom flange plate in the undamaged/intact condition. Use standard holes and slip-critical connections to limit the relative displacement between the tensile components when the fracture occurs. The full bearing and bolt shear strength should be accounted for in the Strength limit state. Additionally, a larger number of bolts with a smaller spacing is preferable to larger-diameter bolts with increased spacing. It is therefore suggested to limit the bolt diameter to 1 in. and attend to the stitch bolt spacing defined in Articles 6.13.2.6.2 and 6.13.2.6.3 from the AASHTO LRFD Specifications (2022). These recommendations are intended to transfer the load from the fractured section to the remaining undamaged/intact components in the shortest possible distance to limit the deformations of the cap following the fracture occurrence.

## 7.2. Design Example

This section presents an illustrative example of the design of a steel box straddle cap for new construction with internal redundancy provided by the cross-boundary separation of the tension elements. The straddle cap analyzed in this design example corresponds to one of the bridges the TxDOT Project Monitoring Committee provided. The layout of the bridge and straddle cap analyzed is illustrated in Figure 7.1.

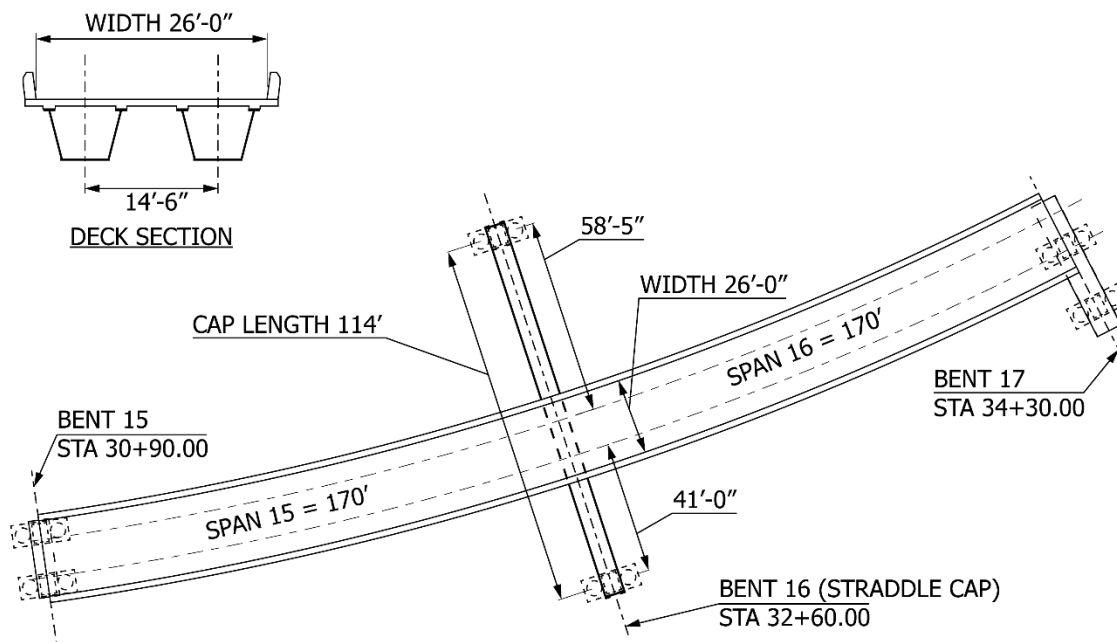


Figure 7.1: Bridge layout for design example. Adapted from TxDOT drawings.

The structural analysis was conducted with a widely-used bridge analysis program commonly used in practice to obtain the required forces (moments and shears) on the straddle cap. The load combinations considered for this example are listed with the corresponding load factors in Table 7.1, adapted from Table 3.4.1-1 from the AASHTO LRFD Specifications (2020). In this illustrative example, only dead loads and gravity vehicular live loads are considered in the analyses. Furthermore, this design example focuses solely on the design of the cross-section for the undamaged/intact and faulted states and omits the design of the diaphragms, bearings, and substructure of the cap, as the design of those components do not differ from a conventional all-welded cap.

**Table 7.1: Load Factors and Load Combinations**

<b>Load Combination</b>	$\gamma_{DC}^1$	$\gamma_{DW}^2$	$\gamma_{LL}^3$	$IM^4$	$DA_R^5$
Strength I	{1.25 – 0.90}	{1.50 – 0.65}	1.75	0.33	
Service II	1.00	1.00	1.30	0.33	
Fatigue I	-	-	1.75	0.15	
Fatigue II	-	-	0.80	0.33	
Redundancy I	1.05	1.05	0.85	0.00	0.40
Redundancy II	1.05	1.05	1.30	0.15	
Extreme Event III	{1.25 – 0.90}	{1.50 – 0.65}	1.10	0.33	

<sup>1</sup> DC: Components and Attachments

<sup>2</sup> DW: Wearing Surfaces and Utilities

<sup>3</sup> LL: Live Load

<sup>4</sup> IM: Dynamic Load Allowance

<sup>5</sup> Dynamic Amplification Factor (AASHTO Guide Specification for IRMs (2018-1))

Three cross-sections (A, B, and C, indicated in Figure 7.2) are proposed to accommodate the flexural demands on the cap by varying the dimensions of the top and bottom flanges. The cross-sectional dimensions are provided in Table 7.2 and Figure 7.3. The dimensions

of the webs and the flange connection plates are kept constant along the entire length to simplify the detailing and fabrication. It should be noted that the width of the flange connection plates could be varied along the length, but the thickness should be maintained to simplify the connection of the bottom flange plate.

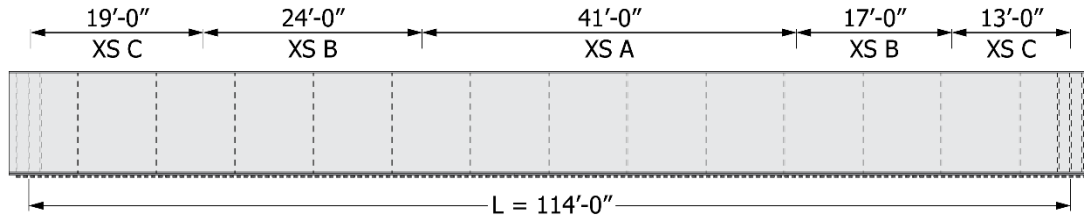


Figure 7.2: Steel box straddle cap geometry

Table 7.2: Cross-section dimensions for Design Example

		Cross-section		
		A	B	C
Top Flange Thickness, in	$t_{tf}$	2.50	2.00	1.50
Top Flange Width, in	$b_{tf}$	70.0	70.0	70.0
Bottom Flange Thickness, in	$t_{bf}$	1.50	1.00	1.00
Bottom Flange Width, in	$b_{bf}$	70.0	70.0	70.0
Web Thickness, in	$t_w$	1.125	1.125	1.125
Web Depth, in	$d_w$	105.0	105.0	105.0
Flange Connection Plate Thickness, in	$t_l$	1.50	1.50	1.50
Flange Connection Plate Width, in	$b_l$	24.0	24.0	24.0
Clear Projecting Width, in	$b_p$	2.0	2.0	2.0
Yield Stress, ksi	$F_y$	50.0	50.0	50.0
Young's Modulus, ksi	$E$	29,000	29,000	29,000
Unbraced Length, in	$L_b$	1368.0		

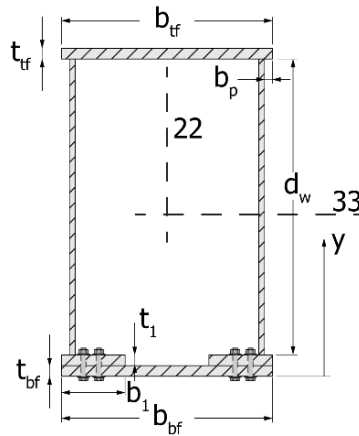


Figure 7.3: Internally redundant steel box straddle cap typical cross-section

First, the flexural and shear strengths of the box-section cap are first computed in the undamaged/intact condition following the provisions of the AASHTO LRFD Specifications (2020). Next, two failed conditions are assumed, and the corresponding strengths are calculated with the modifications proposed in Chapter 6. Finally, the factored strengths are compared with the demands in the undamaged/intact and faulted conditions.

A summary of flexural and shear strengths calculated based on the methodology proposed in Chapter 6 is provided in Table 7.3. Detailed calculations for cross-section A are included in Appendix C.

**Table 7.3: Summary of sectional capacities**

Section	Factored Flexural Strength, kip·ft	Factored Shear Strength, kip	
		Int. Panel	End Panel
A – Undamaged/intact	98,863	6,438	5,892
A – Fractured Bottom Flange	68,121	5,579	5,302
A – Fractured Web and FCP	72,576	2,897	2,651
B – Undamaged/intact	74,087	6,438	5,892
B – Fractured Bottom Flange	58,246	5,579	5,302
B – Fractured Web and FCP	53,709	2,897	2,651
C – Undamaged/intact	49,657	6,199	5,892
C – Fractured Bottom Flange	43,585	5,579	5,302
C – Fractured Web and FCP	35,747	2,897	2,651

The results from the demands and capacity analyses of the box straddle cap are presented graphically in Figure 7.4 and Figure 7.5 for the undamaged/intact condition and in Figure 7.6 and Figure 7.7 for the faulted state. In each plot, the envelope of the flexural or shear demands is plotted for the entire length of the cap for each of the load combinations considered. Additionally, the corresponding capacity estimated per the provisions of the AASHTO LRFD Specifications (2020) modified according to the findings presented in Chapter 6 is shown in each case. Therefore, the proposed sections would satisfy the demands in the undamaged/intact and faulted conditions and can be classified as non-Fracture Critical.



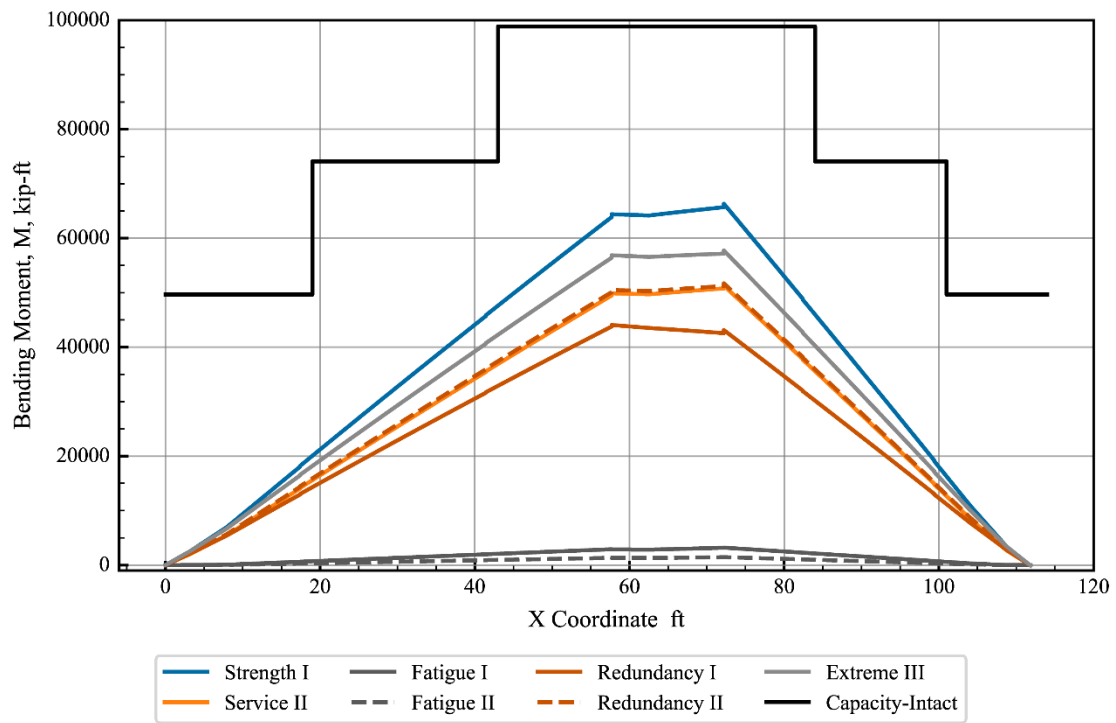


Figure 7.4: Flexural demands and capacity in the undamaged/intact condition

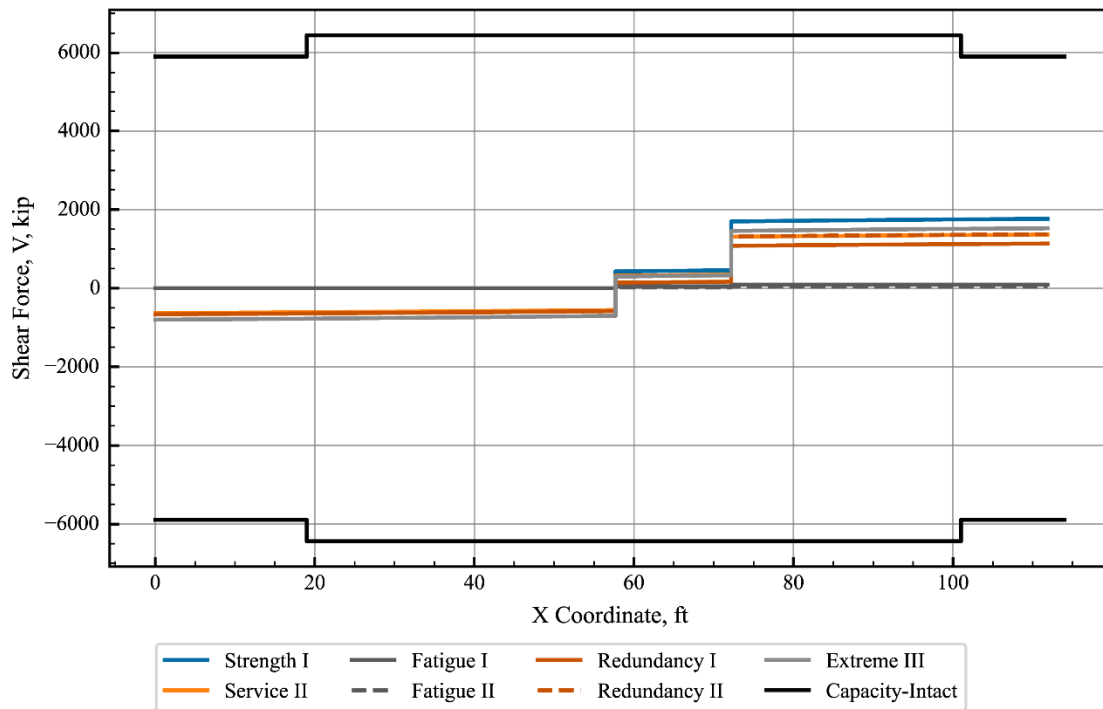


Figure 7.5: Shear demands and capacity in the undamaged/intact condition

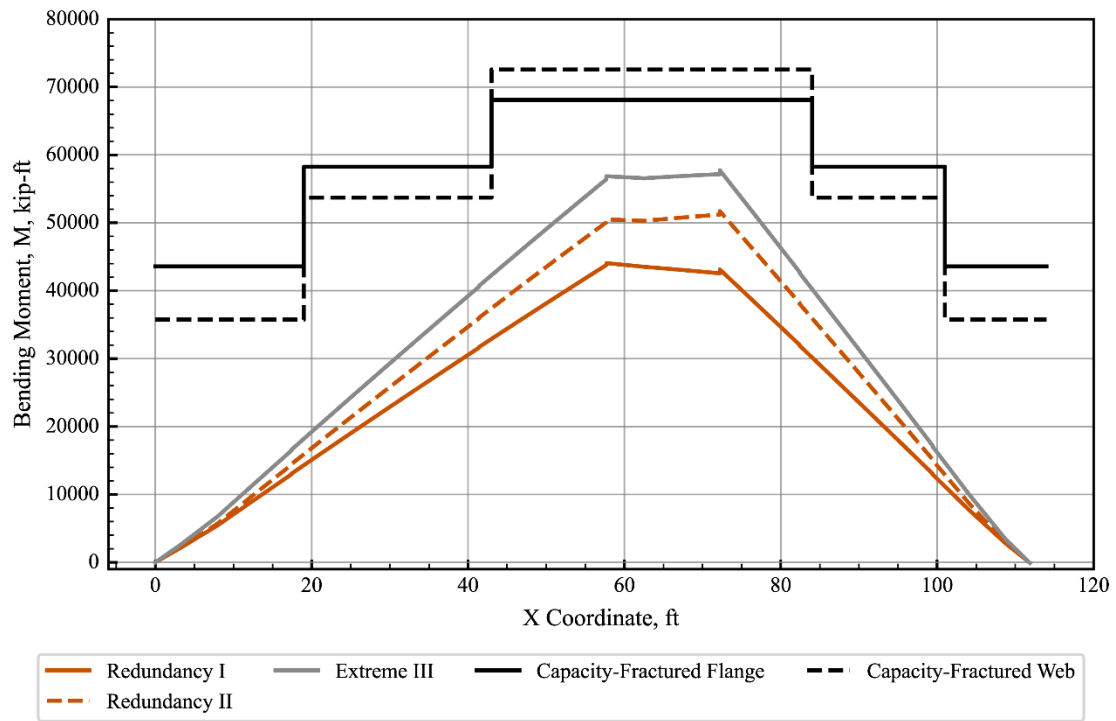


Figure 7.6: Flexural demands and capacity in the faulted condition

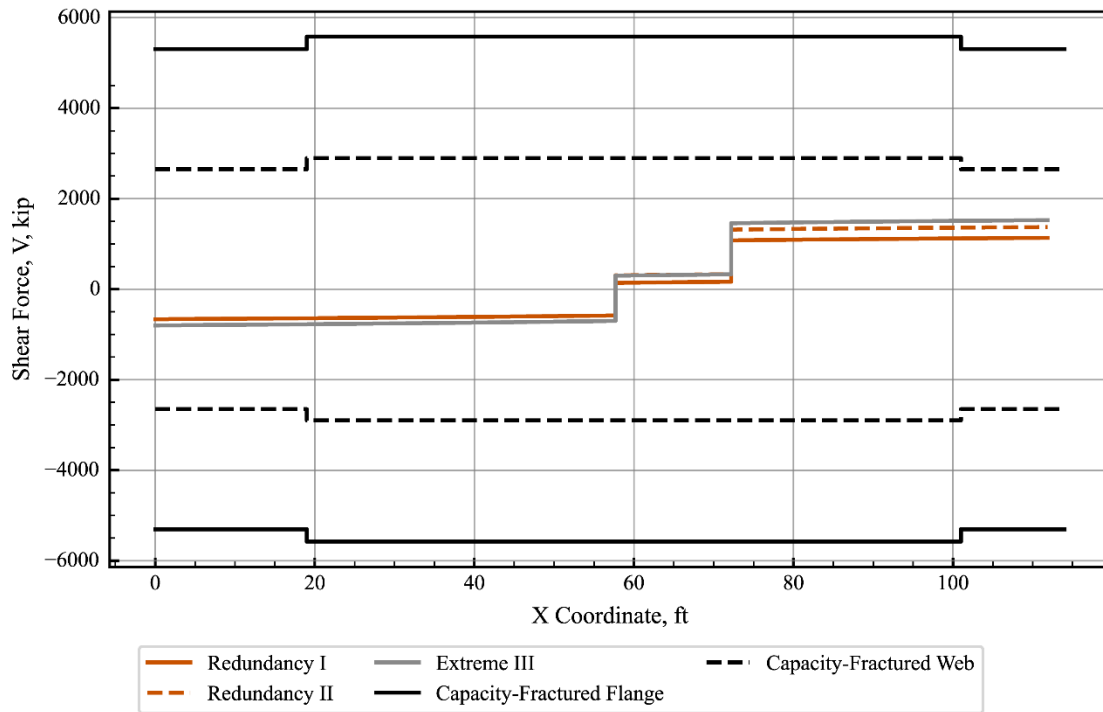


Figure 7.7: Shear demands and capacity in the faulted condition

## **Chapter 8. Summary and Conclusions**

### **8.1. Summary**

The research presented in this report studied two alternatives for providing internal redundancy to steel box straddle caps. The first approach considered, labeled as Design Concept A, used high-strength bars installed inside the box-section cap to arrest the cracks and act as a secondary tensile element in the faulted state. The other option, designated as Design Concept B, provided internal redundancy by providing a bolted connection between the tensile flange (primary tension component) and flange connection plates welded to the webs of the section, thus creating cross-boundary separation. The primary objectives of the study were to assess the crack-arresting capacity and ultimate strength in the faulted condition for both design concepts. Theoretical, experimental, and computational tasks were conducted in the research study.

A thorough literature review on brittle fracture, Fracture Critical Members, and structural redundancy was conducted, which included past research to investigate testing methods and current and past codified design provisions. Additionally, a review of 19 existing steel box straddle caps in Texas was performed to identify typical details that would aid in the design of the test specimens. The selected design concepts and the corresponding test specimens were designed working in conjunction with bridge designers, inspectors, fabricators, detailers, and consultants. The test specimens using Design Concept A and B proposed details were fabricated by W&W AFCCO Steel in San Angelo following established fabrication techniques. The specimens consisted of two reusable end segments (each approximately 20 ft. long), and three 20 ft. long test specimens focusing on the redundancy details to be evaluated. The test specimens had bolted connections to the reusable end segments, resulting in a 60 ft. total length of the tested straddle cap.

Full-scale experiments were carried out. As part of this task, a test setup was designed and fabricated at the Ferguson Structural Engineering Laboratory to allow the investigation of the fracture behavior and ultimate strength of the test specimens. Four 60-ft-long specimens were tested during this stage: one corresponding to a conventional all-welded steel box straddle cap, one with added post-tensioning bars as a secondary tension element, and two incorporating cross-boundary fracture separation by using a bolted connection between the primary tension components.

The results of the experimental tests were complemented with analytical studies that included finite element analysis of box members in the faulted condition. The combination of the experimental and analytical studies resulted in the selection of Design Concept B as

the most promising approach for implementation to result in straddle caps that can be classified as non-fracture critical. Finally, a design example based on the load demands of an existing steel box straddle cap was provided to illustrate the proposed design procedure for achieving an internally redundant solution.

## 8.2. Conclusions

The findings of this research suggest that connecting the bottom flange plate to the remaining components of the box cap using high-strength bolts effectively provides cross-boundary separation between the primary tensile components (bottom flange) and allows sizing the cross-section to have sufficient capacity in the faulted condition. This approach is suitable for newly designed and constructed steel box straddle caps, and it can also be used as the basis for an effective retrofitting technique in which an additional bottom flange plate is bolted to the existing cap and the original bottom flange is slitted to produce the separation between the two webs. The results for Design Concept A, which focused on utilizing high-strength bars to provide internal redundancy to steel box straddle caps, do not support this Design Concept as a plausible solution resulting in a non-fracture critical system based upon the experimental and analytical results which suggested that the use of high-strength bars would not prevent the propagation of cracks on the webs and the corresponding loss of shear resistance.

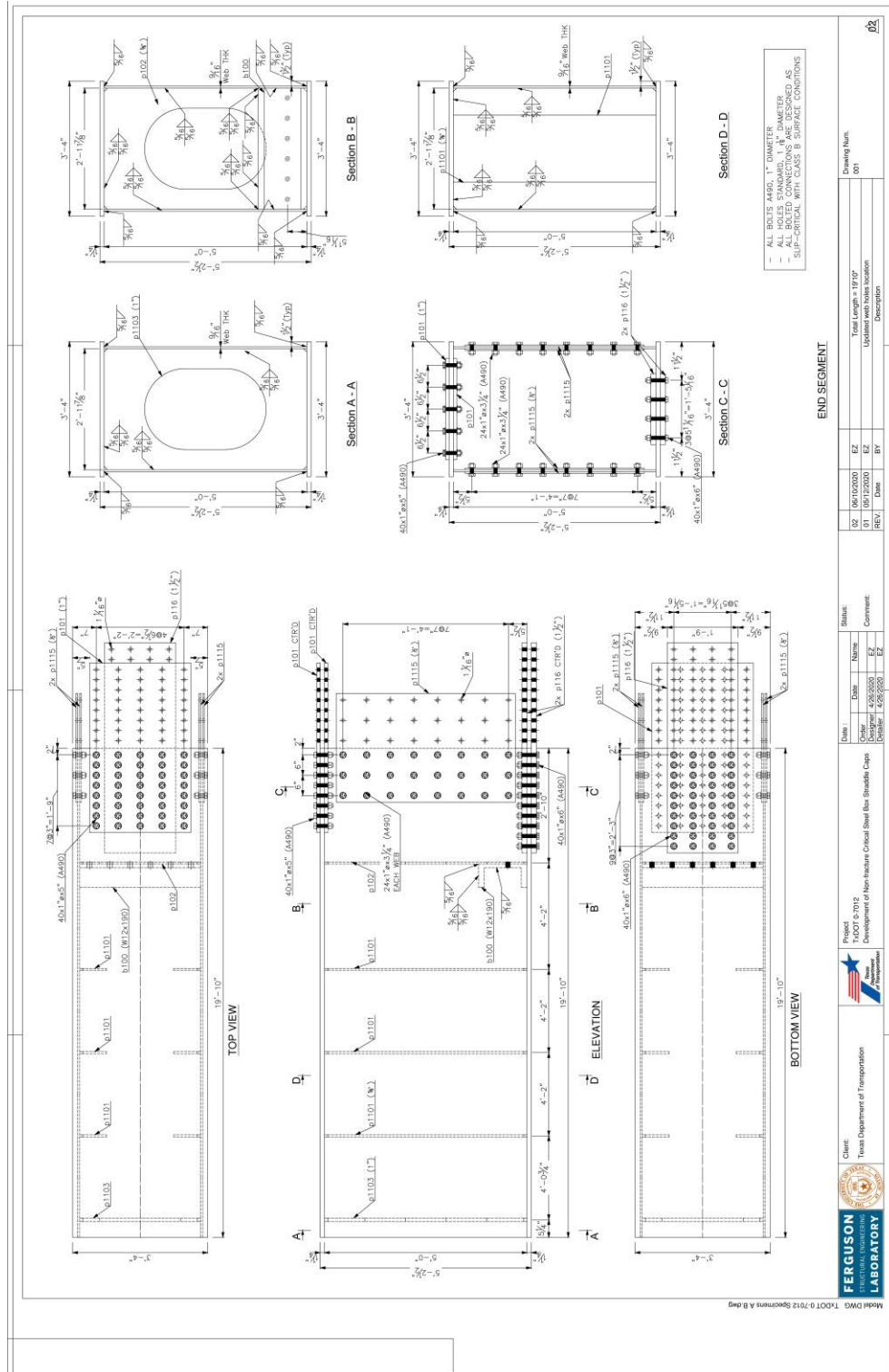
The parametric analyses conducted on the FE models with a bolted bottom flange showed that a fractured section had little influence on the torsional stiffness of the member subject to realistic torsional demands. These observations supported the use of the current design provisions for noncomposite box section members defined in the AASHTO LRFD Specifications (2020) with two straight-forward modifications for the calculation of the capacity in the faulted condition: (i) considering 50% of the torsional constant ( $J$ ) of the undamaged/intact section for the calculation of the Lateral Torsional Buckling limit state, and (ii) applying a resistance factor of 0.90 to account for the scatter of the results obtained from the parametric studies.

## References

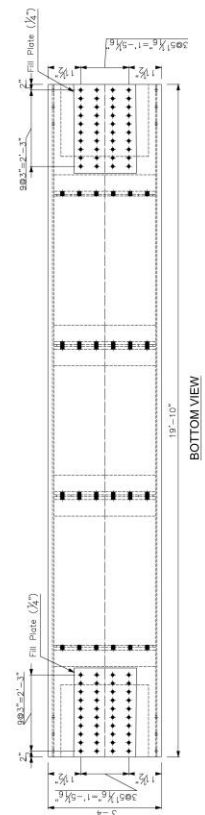
- AASHTO. 2018. *AASHTO Guide Specifications for Analysis and Identification of Fracture Critical Members and System Redundant Members*. 1st. Washington, D.C.: American Association of State Highway and Transportation Officials.
- . 2018-1. *AASHTO Guide Specifications for Internal Redundancy of Mechanically-Fastened Built-up Steel Members*. 1st. Washington, D.C.: American Association of State Highway and Transportation Officials.
- . 2020. *AASHTO LRFD Bridge Design Specifications*. 9th. Washington, DC: American Association of State Highway and Transportation Officials.
- . 2012. *AASHTO LRFD Bridge Design Specifications*. 6th. Washington, DC: American Association of State Highway and Transportation Officials.
- . 2020. *AASHTO LRFD Bridge Design Specifications*. 9th. Washington, D.C.: American Association of State Highway and Transportation Officials.
- . 2018. *AASHTO LRFD Bridge Design Specifications*. 8th. Washington, DC: American Association of State Highway and Transportation.
- . 1978. *Guide Specifications for Fracture Critical Non-redundant Steel Bridge Members*. Washington, DC: American Association of State Highway and Transportation Officials.
- . 2011. *The Manual for Bridge Evaluation*. Washington, DC: American Association of State Highway and Transportation Officials.
- AASHTO/AWS. 2015. *AASHTO/AWS D1.5 Bridge Welding Code*. Washington, D.C.: American Association of State Highway and Transportation Officials/American Welding Society.
- AASHTO/NSBA. 2020. *G12.1 Guidelines to Design for Constructability and Fabrication*. Washington, DC.
- Barnard, T, C Hovell, J Sutton, J Mouras, B Neuman, S Vasileios, K Janghwan, E Williamson, and K Frank. 2010. *Modeling the Response of Fracture Critical Steel Box Girder Bridges*. Austin, TX: Research Report No 9-5498-1, Center for Transportation Research, The University of Texas at Austin, 172.
- Barsom, John M, and Stanley T Rolfe. 1999. *Fracture and Fatigue Control in Structures*. Philadelphia, PA: American Society for Testing and Materials.
- British Standards Institution. 2015. *Guide to methods for assessing the acceptability of flaws in metallic structures (BS 7910:2013 + A1:2015)*. British Standards Institution.
- Connor, J Robert, Karl Frank, Bill McEleney, and John Yadlosky. 2015. "Are you sure that's fracture critical?" *Modern Steel Construction*, January: 17-23.
- Dassault Systèmes Simulia Corp. 2016. "Abaqus/CAE Version 2017 User's Manual."
- Diggelman, L., R. Connor, and R. Sherman. 2012. *Evaluation of Member and Load-Path Redundancy on the US-421 Bridge Over the Ohio River*. West Lafayette, IN: Purdue University.

- Fasl, J., T. Helwig, and S. Wood. 2016. "Fatigue Response of Fracture-Critical Bridge at the End of Service Life." *ASCE Journal of Performance of Constructed Facilities*.
1968. "Federal-Aid Highway Act of 1968." Vols. Pub. L. No. 90-495, 73 Stat. 145. August 23. <https://www.govinfo.gov/content/pkg/STATUTE-82/pdf/STATUTE-82-Pg815.pdf>.
- FHWA. 2012. *Clarification of Requirements for Fracture Critical Members*. Memorandum, Washington, D.C.: US Department of Transportation - Federal Highway Administration.
- FHWA. 2019. *FHWA Requirements for Classification and Treatment of Steel Bridge Members for Fracture Control - Draft Memorandum*. Federal Highway Administration.
- FHWA. 2019. *Proposed LRFD Specifications for Noncomposite Steel Box-Section Members. Publication No FHWA-HIF-19-063*. US Department of Transportation.
- Hebdon, Matthew H., Cem Korkmaz, Francisco Javier Bonachera Martin, and Robert J. Connor. 2015. *Member-Level Redundancy of Built-Up Steel Girders Subjected to Flexure*. West Lafayette, IN: Purdue University.
- MTS. 2009. *MTS Series 793 Tuning and Calibration*. MTS Systems Corporation.
- Novak, S R, and J M Barsom. 1976. "Brittle Fracture (KIC) Hebehavior of Cracks Emanating from Notches." *ASTM STP 601* (American Society of Testing and Materials) 409-447.
- Novak, S. R., and J. M. Barsom. 1976. "Brittle Fracture (KIC) Behavior of Cracks Emanating from Notches." *Cracks and Fracture, ASTM STP 601* (American Society for Testing and Materials) 409-447.
- NTSB. 1968. *Collapse of US 35 Highway Bridge Point Pleasant, West Virginia, December 15, 1967*. National Transportation Safety Board, Washington, DC: US Department of Transportation.
- Tada, Hiroshi, Paul C Paris, and George R Irwin. 2000. *The Stress Analysis of Cracks Handbook*. New York: American Society of Mechanical Engineers.
- Tada, Hiroshi, Paul C. Paris, and George R. Irwin. 2000. *The Stress Analysis of Cracks Handbook*. New York: The American Society of Mechanical Engineers.
- Texas Department of Transportation. 2020. *Bridge Design Manual LRFD*.
- West Virginia Department of Transportation. 2019. *West Virginia Department of Transportation*. September 2019. Accessed September 18, 2019. [https://transportation.wv.gov/highways/bridge\\_facts/Modern-Bridges/Pages/Silver.aspx](https://transportation.wv.gov/highways/bridge_facts/Modern-Bridges/Pages/Silver.aspx).
- Williams, Emma C, Todd A Helwig, and Michael D Engelhardt. 2022. "Experimental Testing of Steel Box Straddle Caps for Evaluation of Internal Redundancy." University of Texas.

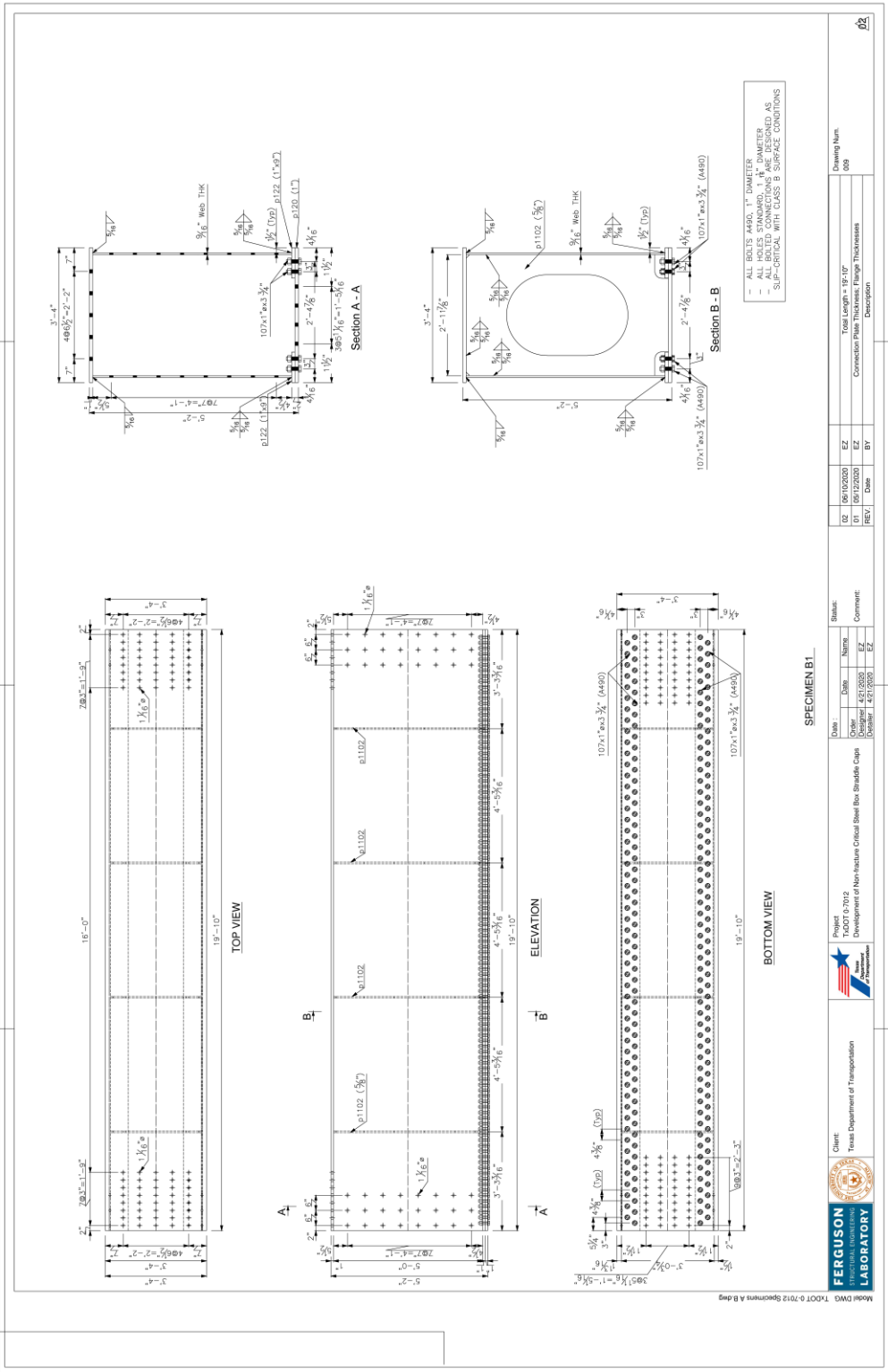
## 181







SPECIMEN A											
 <b>FERGUSON</b> The National Institute for <b>LABORATORY</b>		 Texas Department of Transportation		 Project TxDOT 7-712 Development of Non-Intrusive Critical Steel Bolt Straddle Caps		Status		Drawing Num			
						Date	Name	03	06/15/2020	EZ	p118 replaced by p122 520
						Order	Date	02	06/10/2020	EZ	
						Order	Date	01	07/12/2020	EZ	
						Rev1	Date	01	07/12/2020	EZ	



NOTE: QUANTITIES IN THIS TABLE ONLY SUMMARIZES DRAWINGS 001, 100, 101, 102, AND 103. QUANTITIES FOR DRAWINGS 104, 105 AND 106 ARE INCLUDED DIRECTLY IN THOSE DRAWINGS.



SPECIMEN B2

[illegible]

## Appendix B. Pilot Specimens Tests

Two 14-ft long pilot specimens were designed and fabricated to assess the proposed test protocol and anticipate potential obstacles that may appear during the testing of the full-scale specimens. With these small-scale specimens, the researchers gained experience configuring the closed-loop hydraulic system and data acquisition system (DAQ) to achieve a brittle fracture of the test specimen.

Moreover, different methods for initiating the cracks at the desired location were evaluated, the need to use a wedge driving apparatus or a hydraulic flange spreader to produce a brittle fracture was assessed, and the cooling-down procedure was tested. Finally, testing the pilot specimens provided valuable data to validate preliminary finite element models and allowed the researchers to anticipate potential problems and limitations of the testing equipment.

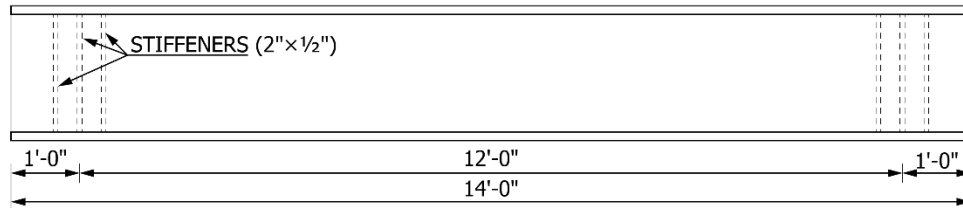
The pilot specimens were designed with a span-to-depth ratio consistent with the full-scale specimens, and the plate thicknesses were selected such that their fracture behavior was representative of that of the full-scale specimens. Two 14-ft long specimens with a 12-ft effective span were designed and fabricated at the Ferguson Structural Engineering Laboratory (FSEL). As shown in Figure B.1, 12-in.  $\times$  1-in. plates were used for the flanges and 14-in.  $\times$  3/8-in. plates were employed for the webs. The sectional properties of the pilot specimens are listed in Table B.1.

A36 steel was utilized for the pilot specimens. Tension and Charpy-V-Notch tests were performed by Chicago Spectro LLC to characterize the material at various temperatures and determine its influence on the material properties. Figure B.2 shows the results of the tension tests for the flange and web plates. Flange plates (1-in. thick, left plot) show a more consistent behavior at the different test temperatures, with a clear linear-elastic initial stress-strain response and a marked yield plateau. The yield strength for these plates increases as the temperature decreases. Table B.2 presents the tension test results corresponding to the flange plates.

The stress-strain behavior of web plates is shown in the plot on the right in Figure B.2. In this case, the behavior is not so well defined: it is not possible to identify a linear-elastic portion of the stress-strain curves, and there are no well-defined yield plateaus. In spite of this, the mechanical properties listed in

Table B.3 (as reported by Chicago Spectro LLC) are fairly comparable to those obtained for the flange plates.

**PILOT SPECIMEN - ELEVATION**



**CROSS SECTION**

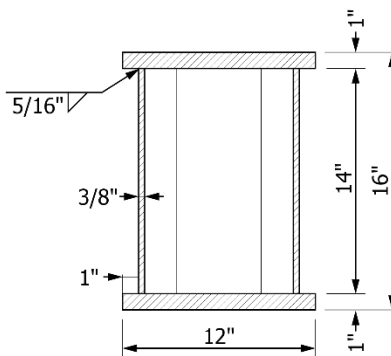


Figure B.1: Pilot Specimen dimensions (elevation and cross-section)

**Table B.1: Pilot Specimen Section Dimensions and Mechanical Properties**

Flange Width	$b_f$	12.0 in.
Flange Thickness	$t_f$	1.0 in.
Web Depth	$h_w$	14.0 in.
Web Thickness	$t_w$	0.375 in.
Area	$A_g$	34.5 in. <sup>2</sup>
Moment of Inertia	$I_g$	1523.5 in. <sup>4</sup>

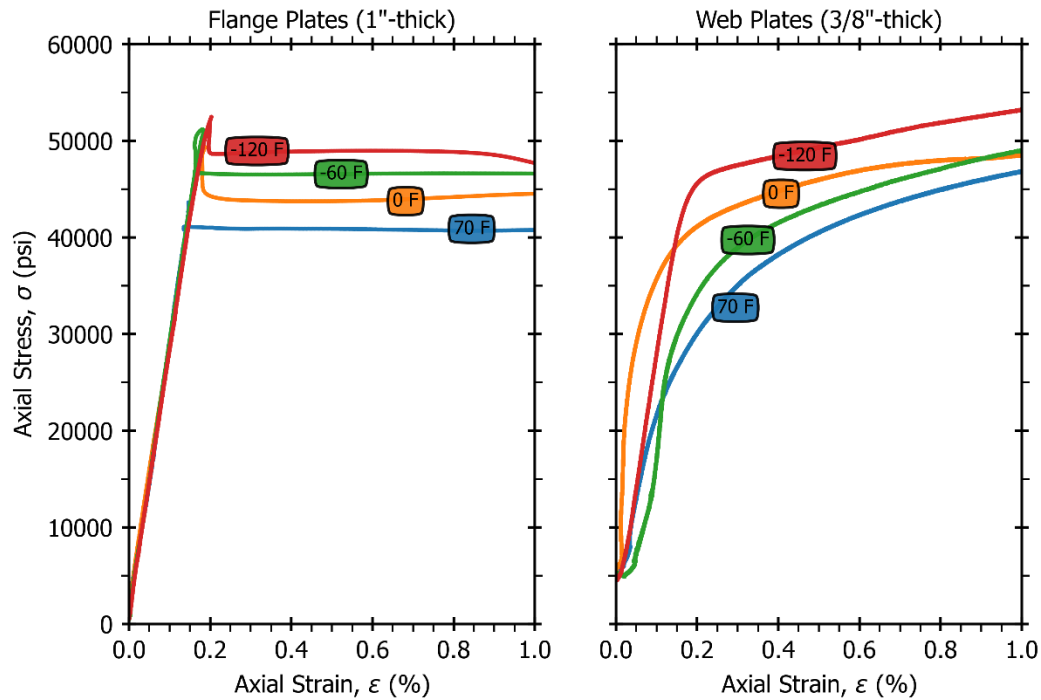


Figure B.2: Tension test results for flange plates (left) and web plates (right).

**Table B.2: Mechanical Properties for 1"-thick plates (Chicago Spectro LLC)**

Test Temperature	RT(~70 °F)	0 °F	-60 °F	-120 °F
Tensile Strength	69.7 ksi	73.5 ksi	74.8 ksi	75.5 ksi
Yield Strength @ 0.2% Offset	40.9 ksi	43.8 ksi	46.5 ksi	48.9 ksi
Elongation in 0.65"	33.9%	36.2%	35.8%	35.7%
Reduction of Area	72.6%	72.2%	70.6%	71.3%

**Table B.3: Mechanical Properties for 3/8"-thick plates (Chicago Spectro LLC)**

Test Temperature	RT(~70 °F)	0 °F	-60 °F	-120 °F
Tensile Strength	71.4 ksi	74.4 ksi	74.1 ksi	76.0 ksi
Yield Strength @ 0.2% Offset	37.8 ksi	43.1 ksi	40.9 ksi	48.1 ksi
Elongation in 0.65"	36.1%	37.8%	39.5%	36.6%
Reduction of Area	77.7%	71.5%	72.3 %	71.8%

Charpy V-Notch test results, presented in Figure B.3 and Table B.4, were used to estimate the material toughness at lower-shelf temperatures based on the guidelines of BS 7910 (2015). The methodology, described in Annex J of BS 7910, uses the absorbed energy obtained in the transition temperature range to define a curve of Material Toughness ( $K_{mat}$ ) versus temperature for the lower-shelf and transition temperature regions. Only the final results of this process are presented in this report. The resulting  $K_{mat}$  curves for each plate thickness are depicted in Figure B.4. Based on these curves, the researchers were able to determine if the temperature reached during the cooling down was sufficiently low to have a brittle behavior.



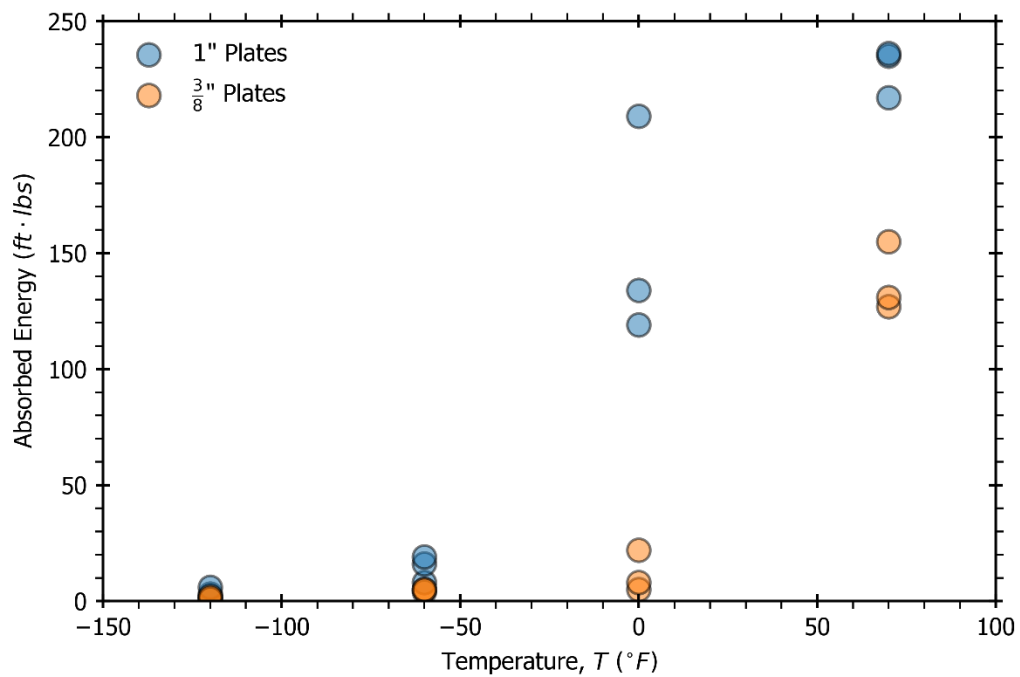


Figure B.3: Charpy V-Notch test results for flange (1 in.) and web (3/8") plates

**Table B.4: Charpy V-Notch impact tests results (Chicago Spectro LLC)**

Temperature (°F)	Thickness (in.)	Specimen Type	Absorbed Energy (ft-lbs)
-120	3/8	Sub-sized	1
-120	3/8	Sub-sized	1
-120	3/8	Sub-sized	2
-60	3/8	Sub-sized	4
-60	3/8	Sub-sized	5
-60	3/8	Sub-sized	5
0	3/8	Sub-sized	5
0	3/8	Sub-sized	8
0	3/8	Sub-sized	22

**Table B.4: Charpy V-Notch impact tests results (Chicago Spectro LLC) (Cont.)**

Temperature (°F)	Thickness (in.)	Specimen Type	Absorbed Energy (ft-lbs)
70	3/8	Sub-sized	127
70	3/8	Sub-sized	131
70	3/8	Sub-sized	155
-120	1	Standard	2
-120	1	Standard	3
-120	1	Standard	6
-60	1	Standard	8
-60	1	Standard	16
-60	1	Standard	19
0	1	Standard	119
0	1	Standard	134
0	1	Standard	209
70	1	Standard	217
70	1	Standard	235
70	1	Standard	236

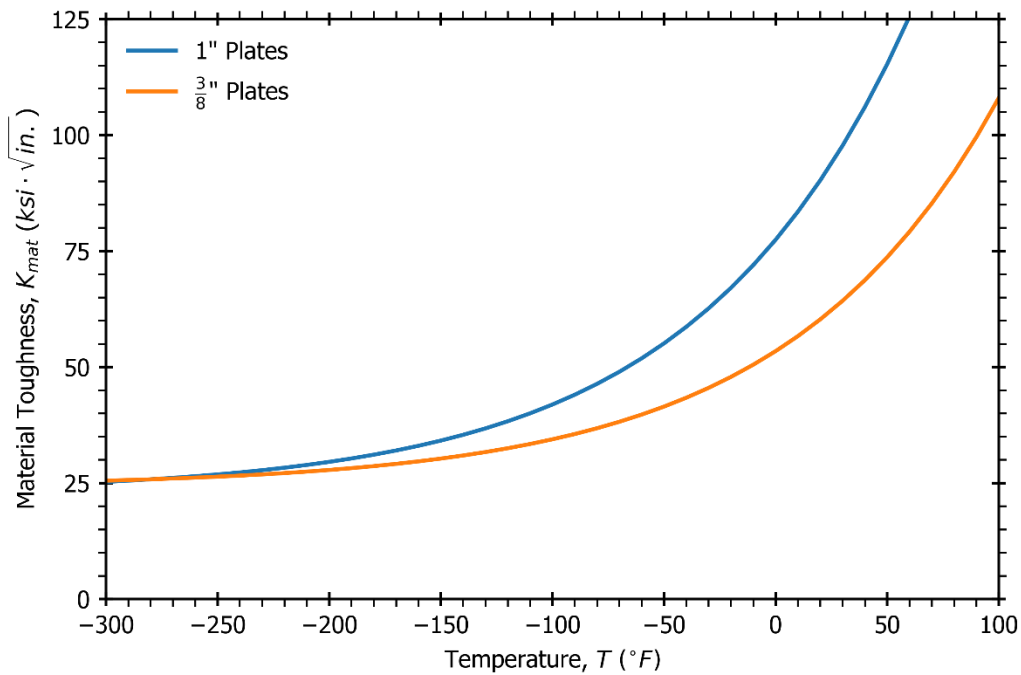


Figure B.4: Lower-shelf and transition region material toughness calculated according to BS 7910 for flange (1 in.) and web (3/8 in.) plates

## Test Setup

To conduct these pilot tests, a small test setup consisting of two support beams and a reaction frame was installed at FSEL. To accommodate the spacing of the anchors on the laboratory floor, the end supports were located 12 ft apart. The specimens were supported on elastomeric bearings providing a simply supported condition.

The load was applied to the specimens using a hydraulic ram, supported by the reaction frame located 4 ft from the North support. Figure B.5 illustrates the pilot specimen test setup elevation, and Figure B.6 shows the actual test setup at FSEL.

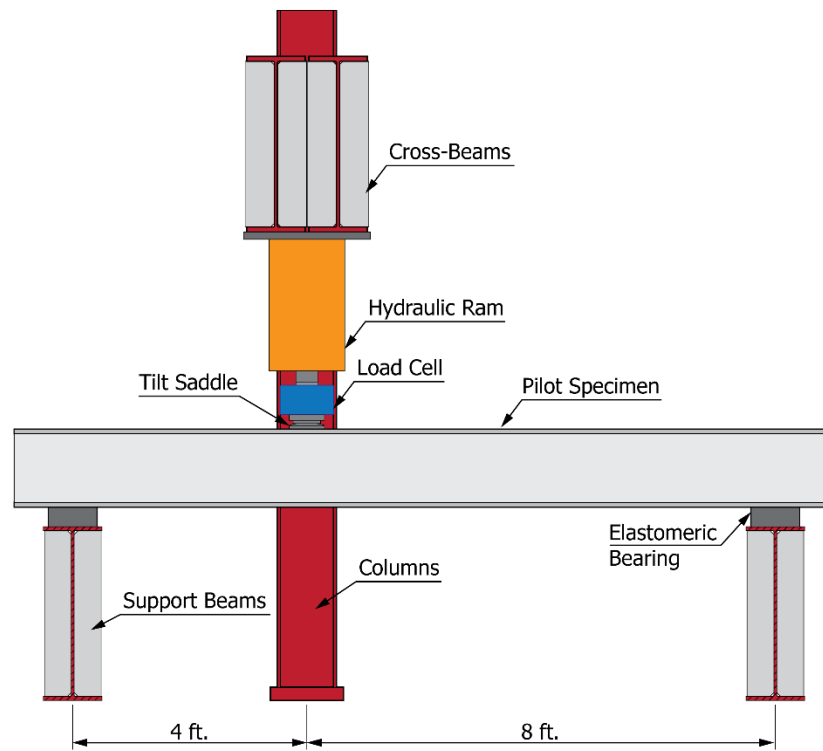


Figure B.5: Schematic of the pilot specimen test setup



Figure B.6: Pilot specimen test setup at FSEL

## Closed-Loop System

A hydraulic closed-loop system, schematized in Figure B.7, was configured to perform the cyclic loading necessary to propagate sharp fatigue cracks from the initial notches on the specimens. The same hydraulic system was later used to load the specimens to induce a brittle fracture.

Typically, a closed-loop system is used with a hydraulic actuator, which integrates a servo valve and force and displacement sensors. However, due to the loads required for this application, the researchers had to use a double-acting hydraulic ram connected to an external servo valve and equipped with a load cell and a linear potentiometer to monitor the applied forces and displacements, respectively.

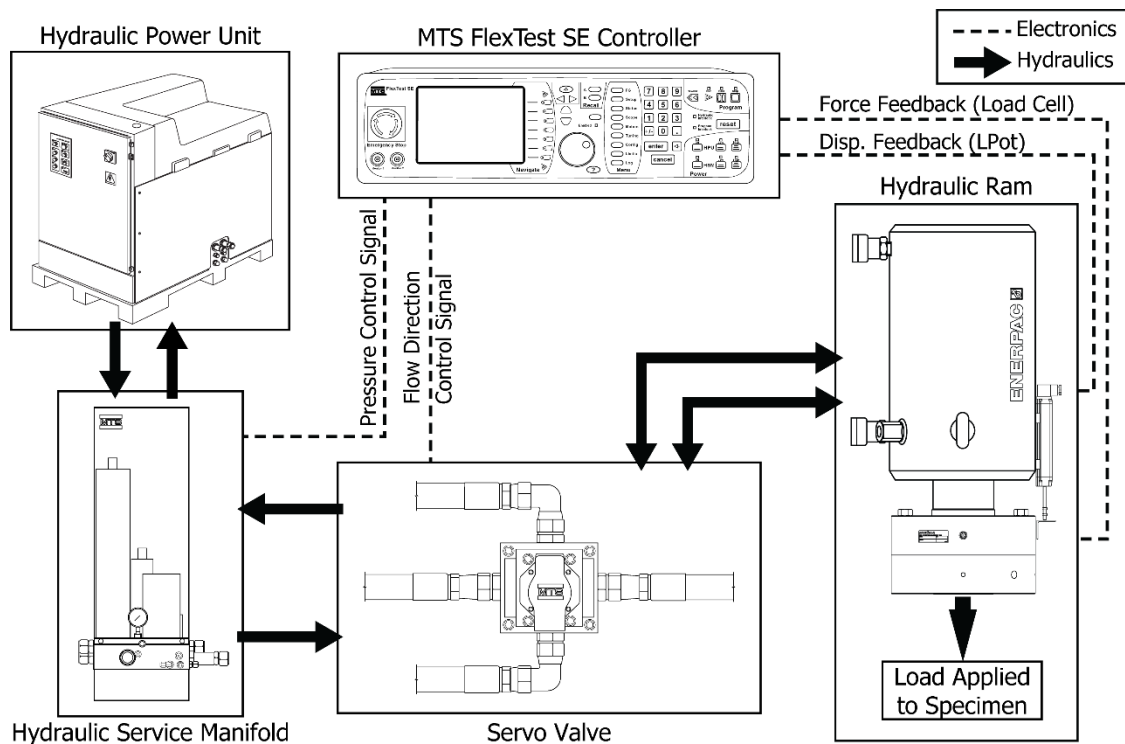


Figure B.7: Flow diagram of the closed-loop system. Dashed lines represent electronic connections between components and the controller, and solid lines symbolize hydraulic connections (arrowheads indicate the oil flow direction)

An MTS FlexTest® SE Controller was used to command the different components of the system and apply the desired loading protocol to the specimen:

- An MTS 290 hydraulic service manifold (HSM) controls the system pressure supplied by the hydraulic power unit (HPU). The HSM (Figure B.8.a) acts as an accumulator, storing a certain volume of oil at a constant pressure of 3,000 psi,

allowing the system to rapidly pump that oil and produce the desired displacement of the ram's rod, which is particularly useful when high-speed loading and large displacements are required.

- From the HSM, the hoses were connected to a servo valve, shown in Figure B.8.b, that controls the oil flow direction. Pressure and return hoses are connected to the bottom and top ports of the servo valve, respectively. The oil is then directed towards the right or left ports by the controller.
- From the servo valve, the hoses are connected to the top and bottom ports of the hydraulic ram. Pumping oil to the top or bottom of the ram allows its rod to extend or retract as needed. A 200-kip Interface load cell, connected in series with the hydraulic ram, provided the force feedback to the controller. Additionally, a linear potentiometer attached to the cylinder monitored the displacement of the rod and provided a displacement feedback signal for the controller. These elements are shown in Figure B.9.

All the elements corresponding to the closed-loop system used to test the pilot specimens are shown in Figure B.10.

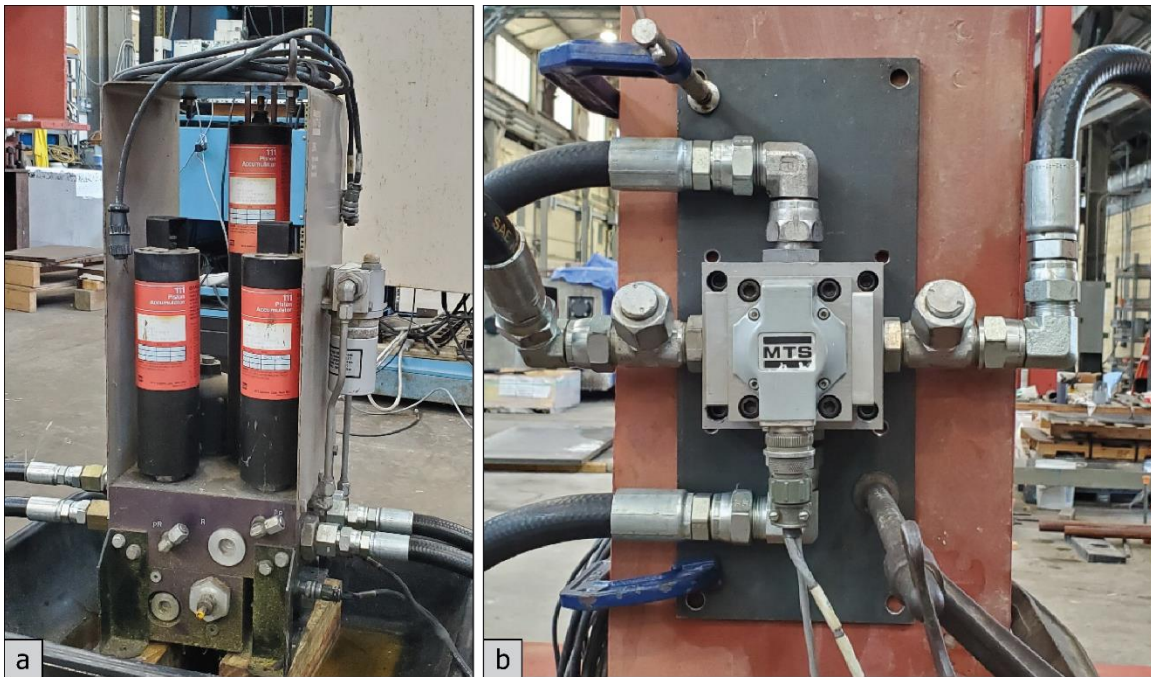


Figure B.8: (a) MTS 290 Hydraulic Service Manifold (HSM), and (b) MTS Servo Valve





Figure B.9: Hydraulic ram with 200-kip Interface load cell for force feedback and linear potentiometer for displacement feedback



Figure B.10: Closed-loop system setup for pilot specimen cyclic loading

### **Closed-loop system operation**

The closed-loop system used for these tests can control either of the two feedback channels: force or displacement. For each of them, the user can specify a target value (for example, a target force of 100 kips), the speed at which that target value has to be reached, the frequency and number of cycles at which that command is to be repeated, et cetera. Moreover, these variables can be combined in one single protocol to stipulate different loading stages.

For instance, during the fracture loading test phase, the load was first raised to a predetermined level controlling the force channel by defining the loading rate and target load. Then, the load was rapidly increased using the displacement control mode by specifying a high displacement rate and a target rod displacement value. Switching from force to displacement control was done in an attempt to maintain load on the specimen even when it had fractured.

The controller has several built-in limits and interlocks designed to shut down the HSM if the limits are triggered. These include minimum and maximum rod displacements and applied forces. For these pilot tests, the displacement limits were set so that the rod did not reach its maximum stroke. Likewise, the load limits were set not to exceed the load cell capacity.

## **Tuning**

Before starting, the closed-loop system was adjusted so that the servo loop responded accurately to its command signal. Each control mode (force and displacement) was tuned separately.

First, the displacement control mode was tuned without the specimen. This allows the controller to adjust the tuning controls (gains) that allow the signal and the feedback to be in close agreement. Second, the load control mode was tuned after installing the specimen. The specimen is required for the load control mode because the system parameters (gains) of this mode depend on the stiffness of the specimen.

In this set of experiments, the auto-tuning feature available on the MTS FlexTest® SE Controller was used. The specifics of the tuning procedure are not described in this Tech Memo. For more details about tuning techniques, refer to the MTS Series 793 Tuning and Calibration Manual (MTS 2009).

## **Fatigue Loading Protocol**

Each specimen was subjected to several thousand load cycles to initiate fatigue cracks from the initial notches. The applied load ranged from 0 to 120 kips at a frequency of 0.25 Hz, which produced a tensile stress of 20 ksi in the bottom flange. The loading protocol was cycled until the desired crack lengths were measured.

## **Fracture Loading Protocol**

Once the fatigue cracks emanating from the notches had grown to the desired size, the specimen was cooled down to lower shelf temperatures and loaded until a brittle fracture occurred. First, the specimen was loaded to approximately 70% of the predicted fracture



load. Then, the loading protocol was switched from force control to displacement control, and the load was applied rapidly until the brittle fracture occurred. The displacement rate was set at 40 in./min, which in practical terms represents a dynamic load.

## **Data Acquisition System Setup and Installation**

Several sensors were installed on the specimens to gather data during the tests. The variables of interest included the temperature at the vicinity of the crack, the bending stresses at the bottom flange, the deflection of the specimen at the different loading stages, and the applied force. The following subsections briefly describe the sensors that were used to measure these variables.

A National Instruments NI SCXI-1001 chassis and SCXI-1314 modules were utilized to collect all this data. After several iterations, the research team set the data collection frequency at 1000 Hz.

### **Thermocouples**

Six type K thermocouple wires were welded to the specimens near the cracks to monitor the temperature evolution until it reached the lower-shelf temperature range. Two thermocouples were placed at the bottom flange, and two were placed on each web at the top and bottom thirds.

Since multiple TC wires were welded to the specimens, it was necessary to isolate their readings using one Omega DRSL-DC2 signal conditioner for each TC wire. These conditioners transform the voltage changes produced in the TC wires into a linearly variable voltage output of 0 to 10 V that is read and recorded by the DAQ.

The signal conditioners have to be programmed for a specific temperature range beforehand. For these experiments, the temperature range was set from -180 °C to 120 °C (-292 °F to 248 °F). It must be noted that liquid Nitrogen has a boiling point of -196 °C (-320 °F).

### **Strain Gages**

Weldable 350Ω strain gages were placed at the top and bottom flanges to monitor the stresses due to bending. These sensors are wired directly into the Data Acquisition System in a quarter bridge configuration.

### **Linear Potentiometers**

Linear potentiometers were installed at several locations along the length of the specimen to monitor vertical deflections:

- Two were located at each side of the elastomeric bearings to monitor the support settlement
- Two were placed at mid-span
- Two were placed at 4 in. from the section where the cracks were initiated

### Load Cell

A 200-kip StrainSense load cell was installed in series with the hydraulic ram to provide feedback to the closed-loop system and record the applied load during the test.

### Optotrak System

The Optotrak Certus System was installed to track the movement and deflections in the crack vicinity during the fracture. A 40 in.  $\times$  16 in. array of 24 infrared light-emitting markers was placed along the west side of the first pilot specimen (PS1). For the second and third pilot tests (PS2A and PS2B), thirteen markers were placed in the arrangement shown in Figure B.11. Additionally, a marker placed on a linear potentiometer was used to synchronize the Optotrak and the DAQ.

The markers and position sensor were connected to the system control unit. The position sensor was aligned to the area using a static rigid body configured in NDI 6D Architect. The maximum sampling frequency for the Optotrak is inversely proportional to the number of markers utilized. For the first pilot test, the maximum frequency was 168.5 Hz; thus, a sampling frequency of 150 Hz was used. As fewer markers were placed in the second pilot test, a higher sampling frequency of 280 Hz was used. The markers were attached to the beam using high-strength velcro. This allowed removing the markers without damage and provided some insulation from the cold temperature.

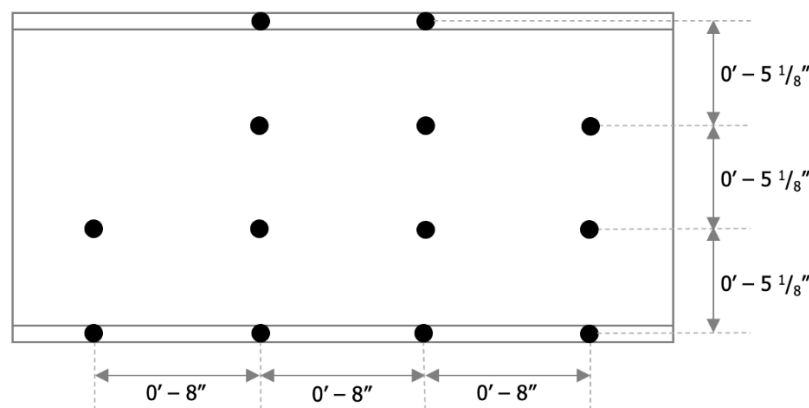


Figure B.11: Marker arrangement for PS2A and PS2B

## Test Outline

Testing of the pilot specimens consisted of four main steps:

1. Notch the bottom flanges and lower portion of the webs at the location where the cracks were desired.
2. Apply cyclic loading to propagate fatigue cracks from the initial notches.
3. Cool down the specimen to reach lower-shelf temperatures in the notched region.
4. Load the specimen to produce a brittle fracture.

Each of these steps is described in the following subsections. In addition, specifics related to each pilot specimen test are mentioned in subsequent sections.

## Initial Notching

The researchers decided to initiate the cracks directly below the loading point, at the section of maximum bending stresses. The crack location was predetermined by notching the edges of the bottom flange and part of the webs. A reciprocating saw with a 0.035 in.-wide blade was used to cut the initial notch at the chosen location.

Figure B.12.a depicts the initial notches done in the webs of the pilot specimens, where the right-hand side image is included to highlight the notch location. Similarly, Figure B.12.b shows the initial notches done in the bottom flange edges (the bottom picture highlights the location of the notches). The initial notch size and the target crack size (i.e., the notch plus the crack emanating from it) were determined based on fracture mechanics equations available in the literature (Tada et al. (2000)) and preliminary FE models.

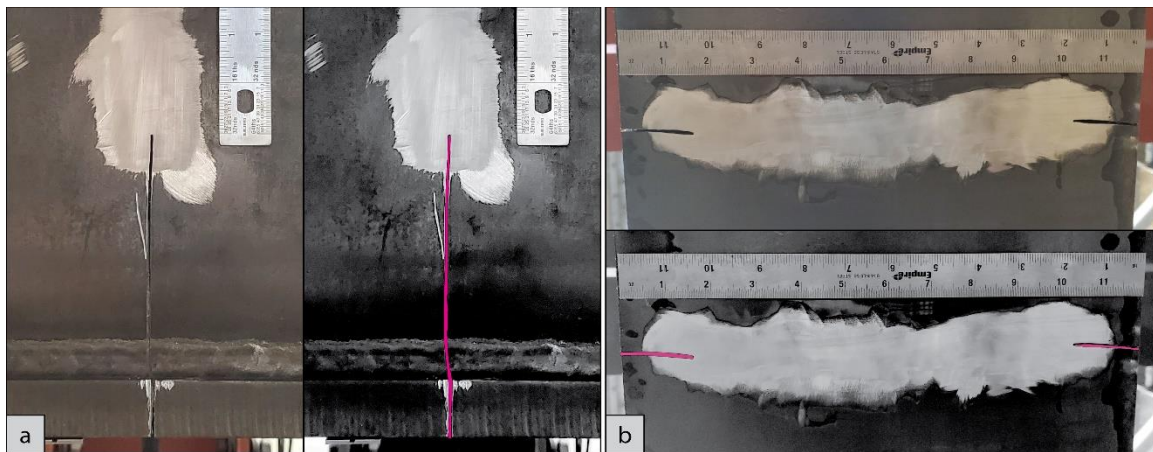


*Figure B.12: Initial notches (a) on the webs and (b) on the bottom flange edges. Each photo is duplicated, and initial notches are highlighted in magenta for the reader's clarity*

## Crack Growth by Cyclic Loading

A crack emanating from a notch can be considered as a crack of equivalent length if it meets the following criteria (Novak and Barsom 1976):

$$\frac{\Delta a_f}{\sqrt{a_N \cdot \rho}} \geq \frac{1}{4} \quad \text{Equation B.1}$$

Where  $a_N$  is the notch length,  $\rho$  is the tip radius, and  $\Delta a_f$  is the length of the crack that emanates from the notch. For simplicity, the ratio shown in Equation B.1 will be referred to as the “N&B Ratio” in the following sections.

To produce that sharp crack, each specimen was subjected to approximately 10,000 load cycles ranging from 0 to 120 kips at a frequency of 0.25 Hz. The researchers measured the crack growth periodically using a dye penetrant.

The notch tip region was previously ground and polished to remove the mill scale and any surface scratches. This permitted the researchers to visualize the fatigue cracks better. In addition, rulers were placed in the vicinity of the notch tips as a reference for crack growth measurements.

The crack inspection procedure using dye penetrant consisted of four steps:

- First, the crack tip area is thoroughly cleaned using a cleaner spray and a clean rag (see Figure B.13.a).
- Next, the red dye penetrant is sprayed on the crack tip region, as shown in Figure B.13.b.
- After 20 minutes, the excess red dye is wiped from the steel surface using the cleaner spray and a clean rag.
- Finally, the developer is applied to the inspected region, and, within a few seconds, the crack tip is exposed on the steel surface, as illustrated in Figure B.13.c.



Figure B.13: Crack inspection using dye penetrant method. (a) Notch tip area polished and cleaned; (b) application of penetrant dye on the notch tip area; (c) developer application that allows the observation of the fatigue crack.

## Cooling down procedure

Commercially available steels, even those not explicitly fabricated to meet Fracture Critical toughness requirements (AASHTO/AWS 2015), have an inherent high fracture toughness at room temperature. Hence, the specimens had to be cooled down to lower-shelf temperatures to obtain a brittle response during the test.

To reach lower-shelf temperatures, liquid Nitrogen was introduced inside the specimens in the vicinity of the cracks using pressurized vessels with cryogenic hoses that ran through holes drilled on both webs, as shown in Figure B.14. Each hose had a phase separator at its end, which was kept at approximately 1 in. from the opposite web plate. The liquid Nitrogen was introduced into the specimen near the top of the webs and allowed to run



down the webs to the bottom flange. In the beginning, the liquid Nitrogen evaporated quickly, producing noticeable amounts of vapor. Later, as the temperature dropped, the Nitrogen could stay liquid for longer, further reducing the steel temperature.

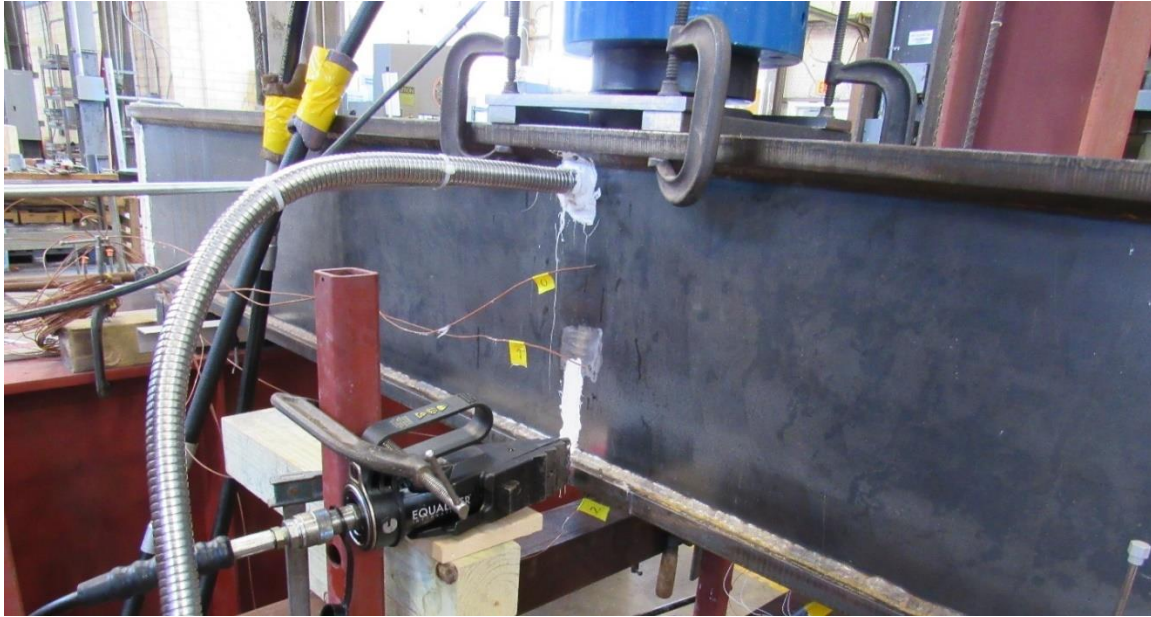


*Figure B.14: Cryogenic hose inserted through the West web of the specimen (there is another cryogenic hose going through the opposite web).*

The specimens were sealed at both ends to prevent the flow of air at room temperature, which would reduce the effectiveness of the process. During the first test, plywood was used to seal the ends of the specimen. For the following experiments, 2-in. thick rigid foam insulation boards were utilized instead.

The liquid Nitrogen was poured into the specimen until lower shelf temperatures were registered by the thermocouples located at the bottom flange. This process took approximately 20 to 25 minutes.

As expected, the bottom flange exhibited the lowest temperatures. The thermocouples located at the bottom flange recorded temperatures as low as -292 °F during one preliminary test. The readings at the other points in the cross-section showed a temperature gradient towards the top flange, which was in some cases only 20 to 30 °F colder than the room temperature. Due to this temperature gradient, the specimen experienced an upward deflection of approximately 3/16 in. before any load was applied.

The research team evaluated the effect of a variation in the fracture toughness between the bottom flange and the webs using FE analyses and concluded that, even though the temperature reached in the bottom half of the web depth was not as low as in the bottom

flange, the corresponding fracture toughness was already in the lower-shelf region. Consequently, this temperature gradient (and, hence, fracture toughness gradient) was deemed negligible for the experiment purposes.

## Fracture Loading

Once the lower-shelf temperature was reached and stabilized, the liquid Nitrogen flow was stopped, and the specimens were loaded to produce a brittle fracture. The loading protocol used for this stage consisted of a first step in which the specimen was slowly loaded until reaching approximately 70% of the estimated fracture load. At that point, most of the upward deflection produced by the cooling down procedure was neutralized. Next, the specimen was loaded in displacement mode control at a 40 in./min rate with a maximum piston displacement of 1.25 in.

Previous work from Hebdon et al. (2015), made use of actuators that drove wedges to initiate the fracture under load, if the dynamic load was not able to achieve fracture. For this study, the Research Team has decided to use two Enerpac SWi2025T hydraulic flange spreader tools (Figure B.15.a) to increase the stress concentration at the crack tip and induce the crack propagation if the specimen did not fracture solely under the load applied by the ram. This tool can produce a spreading force of 26.9 Ton. One of these tools was installed on each bottom flange edge of the pilot specimen, as shown in Figure B.15.b. Both spreader tools were connected to the same hydraulic pump to produce approximately the same force on each crack.

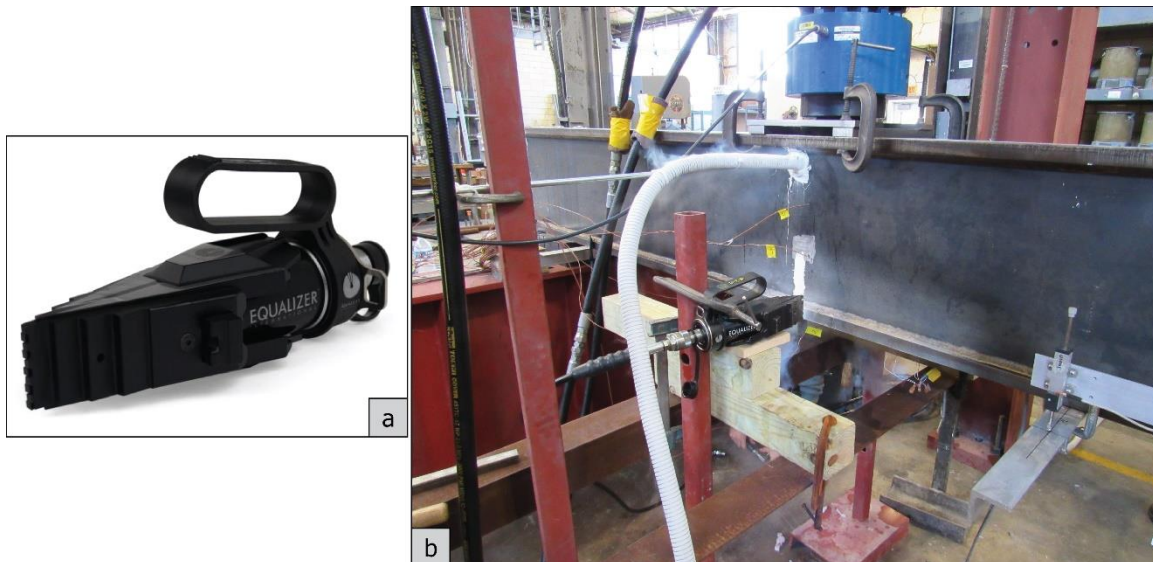


Figure B.15: (a) SWi2025T hydraulic flange spreader tool, and (b) flange spreader tool installed on the bottom flange edge of the pilot specimen.

## Test Results and Commentaries

The present section outlines the results from the tests conducted in the pilot specimens. Pilot Specimen 1 was tested to fracture only once and will be referred to as PS1. Pilot Specimen 2 was tested twice: after the first fracture test was conducted, the cracked section was spliced, and the specimen was re-tested at a different section. The two tests conducted on Pilot Specimen 2 are designated as PS2A and PS2B, respectively.

### Pilot Specimen 1 (PS1)

#### Initial Notching

PS1 was notched using a reciprocating saw with a 0.035 in.-wide blade 4 ft from the North support. The goal was to notch the bottom flange edges just enough to get past the web plate (approximately 1 5/8 in.) and approximately 4 1/2 in. in the tension portion of the webs, measured from the top face of the bottom flange. The size of the initial notches was determined from the preliminary FE analyses conducted by the Research Team.

Notch sizes were measured by taking a photograph of the notch next to a scaled ruler and scaling the photo using AutoDesk AutoCad<sup>®</sup>. The notch sizes corresponding to PS1 are presented in Table B.5 and sketched in Figure B.16.

**Table B.5: Notch sizes for PS1**

Location	Notch Size
East Bottom Flange Edge	1.711 in.
East Web	4.472 in.
West Bottom Flange Edge	1.724 in.
West Web	4.597 in.



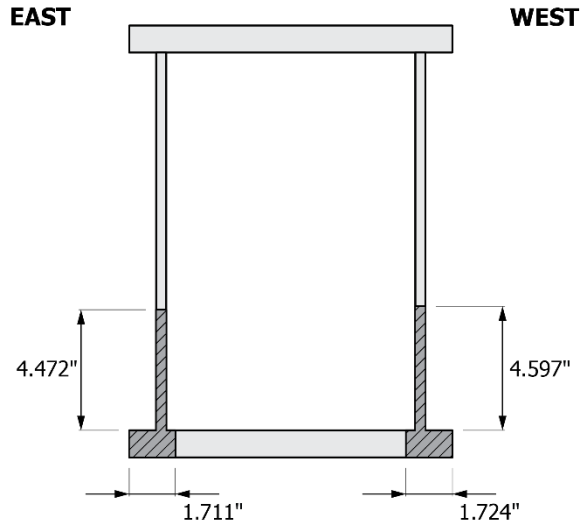


Figure B.16: PS1 Notch Sizes

### Crack Growth by Cyclic Loading

As stated previously, the load was set to fluctuate between 5 and 120 kips at a frequency of 0.25 Hz. This produced tensile stresses of 20.2 ksi at the bottom fiber and 17.6 ksi at the web-to-flange interface.

At first, the cyclic loading was interrupted every few hundred cycles to inspect and monitor the crack growth. Once the researchers gained confidence, the cyclic loading was interrupted only every 2,000 cycles. The fatigue cracks emanating from the notches were inspected using a dye penetrant, as described in previous sections.

Figure B.17 shows the fatigue crack growth at the tip of the four notches of the pilot specimen. No crack growth was detected before 5775 cycles and, hence, those points are not shown in the plot. This plot shows that the fatigue crack growth exhibits a marked linear trend with respect to the number of load cycles. It is also clear that the crack growth in the flange edge notches is much faster than in the web notches due to the higher tensile stresses (and, correspondingly, the higher stress intensity factors) at the bottom flange.

Additionally, for each fatigue crack, the N&B Ratio determined in Equation B.1 was calculated and plotted in Figure B.18. The horizontal dashed line indicates the threshold at which the fatigue crack emanating from a notch can be considered equivalent to a fatigue crack of the same length.

The final crack lengths, computed as the summation of the initial notch length and the fatigue crack extension, are shown in Table B.6, as well as their corresponding N&B Ratio.

Figure B.19 illustrates the fatigue crack observed at the East bottom flange notch using the dye penetrant after 7,200 cycles.

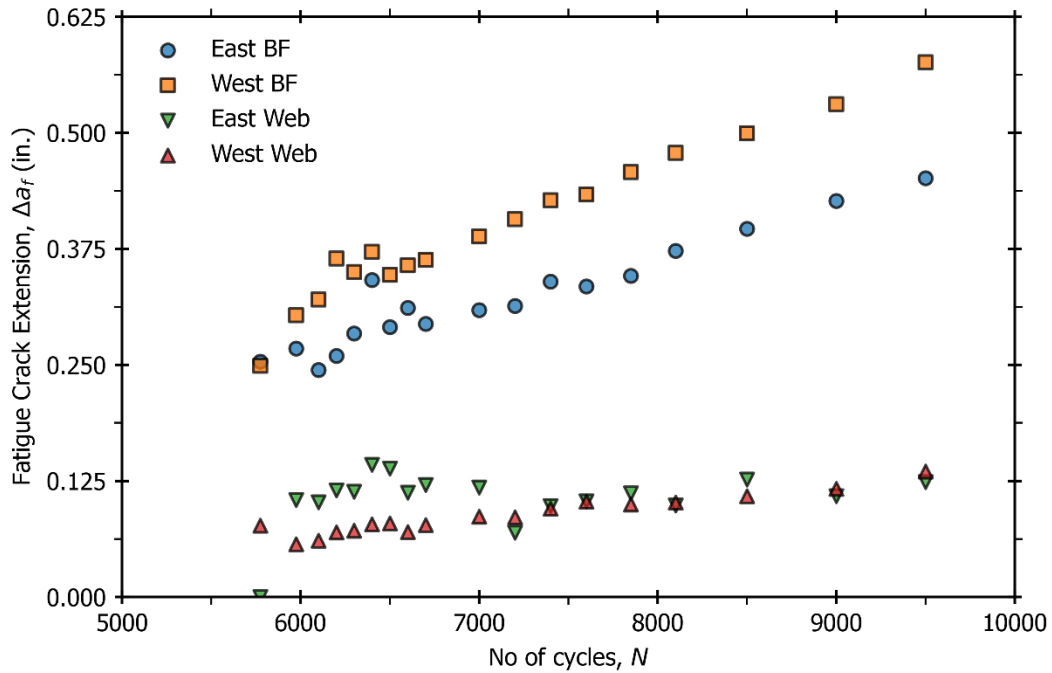


Figure B.17: PS1 Fatigue crack growth

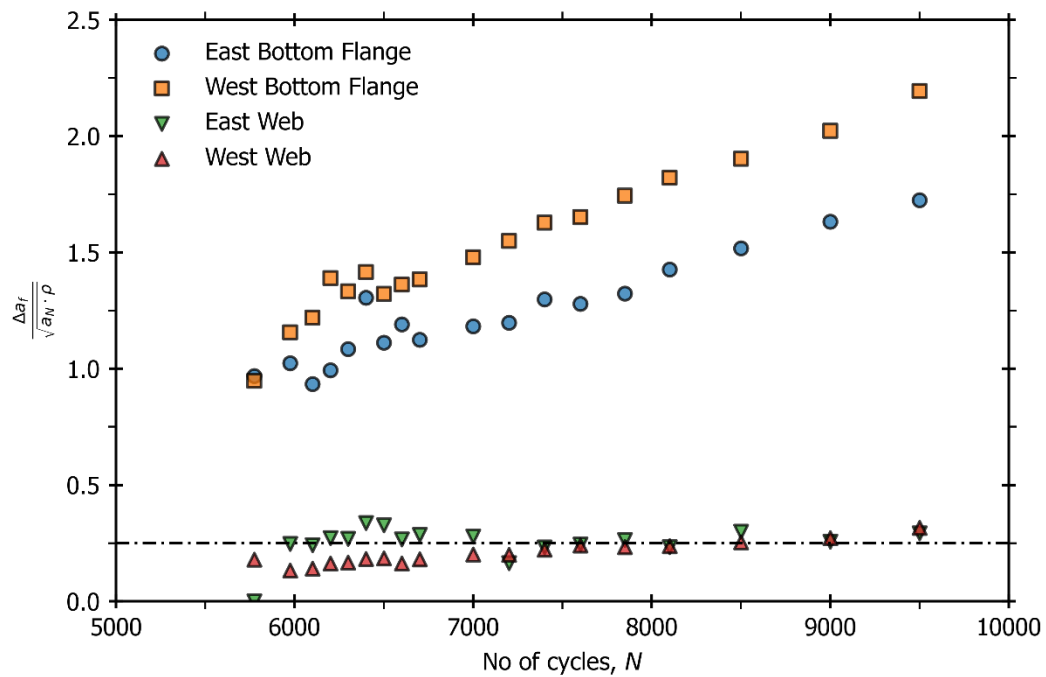
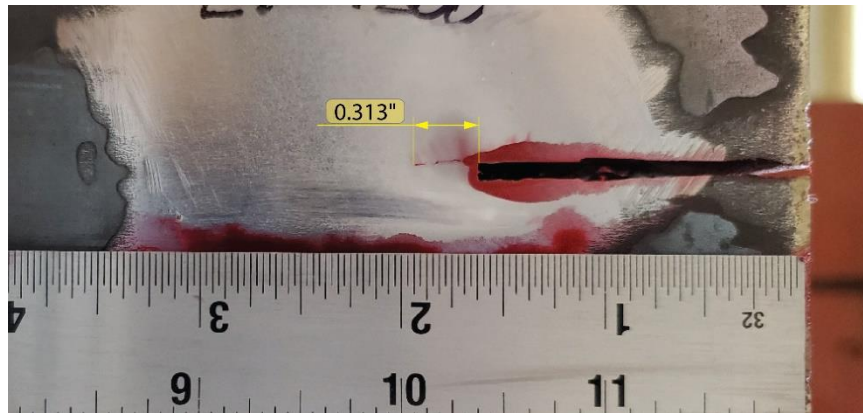


Figure B.18: Novak and Barsom Ratio for PS1; horizontal dashed line indicates the threshold corresponding to Equation B.1

**Table B.6: Final crack lengths (initial notch + fatigue crack) and Novak & Barsom Ratio for PS1**

Location	Notch Size	N&B Ratio
East Bottom Flange Edge	2.162 in.	1.724
East Web	4.595 in.	0.293
West Bottom Flange Edge	2.299 in.	2.193
West Web	4.732 in.	0.315



*Figure B.19: Fatigue crack at the East bottom flange after 7,200 load cycles*

### **Cooling down procedure**

PS1 was cooled down using the procedure described in previous sections. Figure B.20 illustrates the temperature evolution registered at each thermocouple during the cooling down procedure. Thermocouples TC-0 and TC-5 were located in the top third of the web depth on the West and East sides of the specimen, respectively; TC-1 and TC-4 were located in the lower third of the web depth on the West and East sides, respectively; and TC-2 and TC-3 were installed in the bottom flange, on the West and East edges, respectively.

Table B.7 summarizes the final temperatures at the beginning of the fracture loading protocol, which are plotted against the estimated material toughness curves described in Figure B.21. Except for TC-0 and TC-5, all points in the cross-section were assumed to be in the lower shelf temperature region. For TC-0 and TC-5, nonetheless, the material toughness was still very low, and it did not represent an obstacle to achieving a brittle fracture, as was demonstrated in the test.

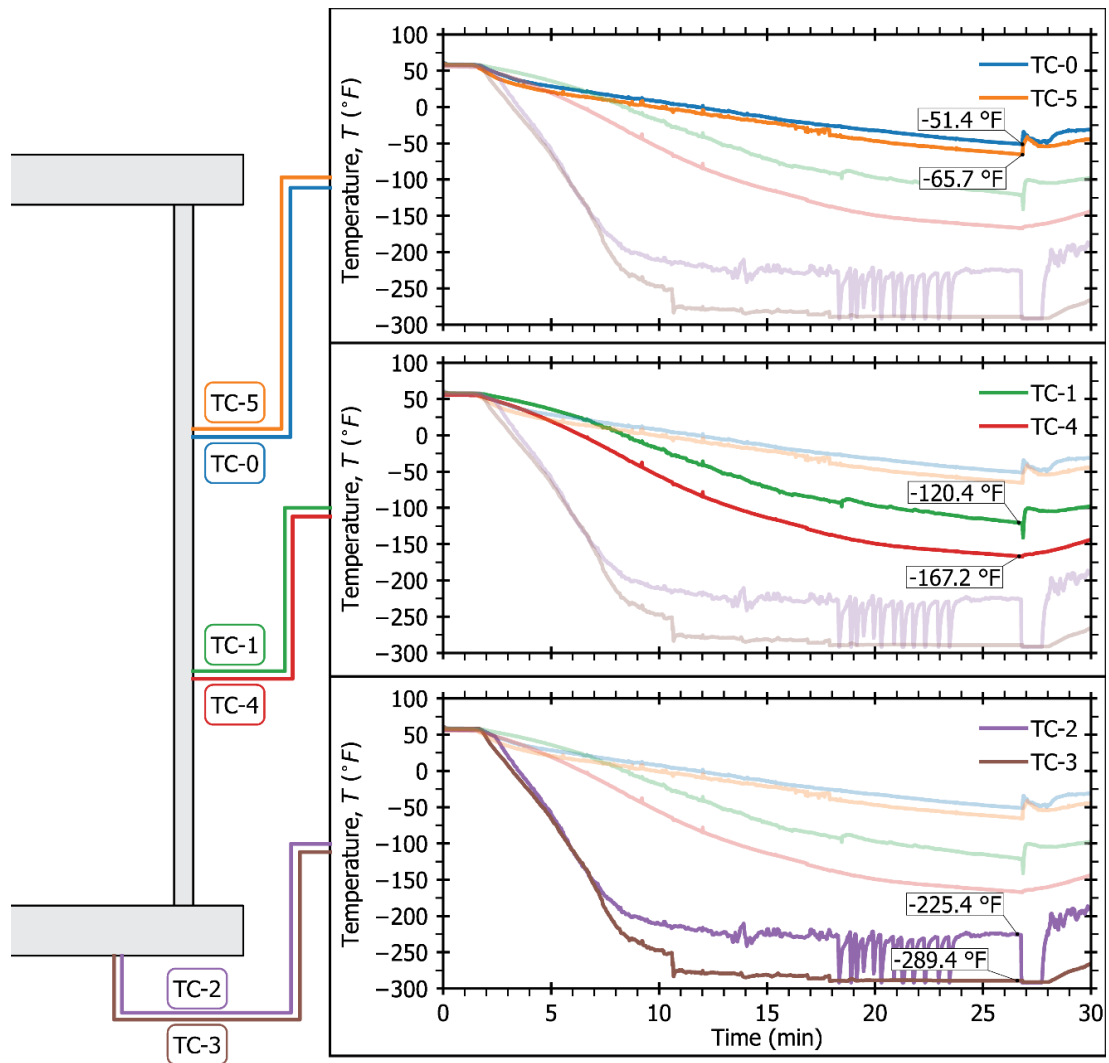
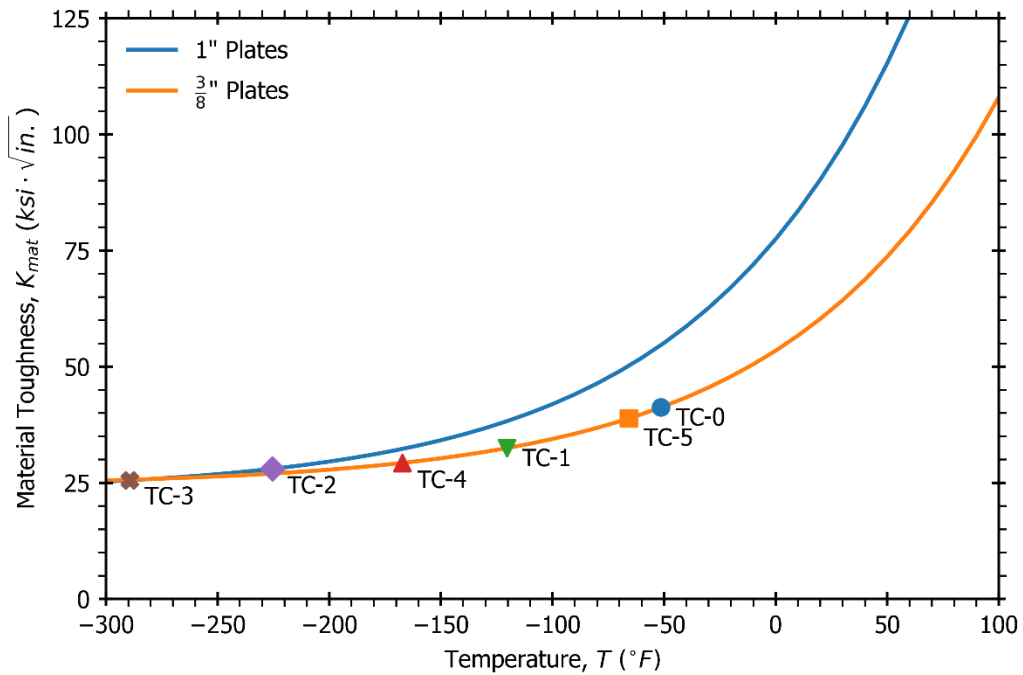


Figure B.20: Temperature evolution at different points in the cross-section. Recorded temperatures when the fracture loading protocol started are pointed out for each thermocouple.

**Table B.7: Temperatures recorded at the cross-section when fracture loading protocol started**

Thermocouple ID	Location	Temperature	Material Toughness
TC-0	West Web – Upper Third	-51.4 °F	41.2 ksi $\sqrt{\text{in.}}$
TC-1	West Web – Lower Third	-120.4 °F	32.4 ksi $\sqrt{\text{in.}}$
TC-2	West Bottom Flange Edge	-225.4 °F	28.0 ksi $\sqrt{\text{in.}}$
TC-3	East Bottom Flange Edge	-289.4 °F	25.5 ksi $\sqrt{\text{in.}}$
TC-4	East Web – Lower Third	-167.2 °F	29.2 ksi $\sqrt{\text{in.}}$
TC-5	East Web – Upper Third	-65.7 °F	38.8 ksi $\sqrt{\text{in.}}$



*Figure B.21: Temperature recorded at the different thermocouples plotted against the material toughness*

## Fracture Loading

Once the temperature had stabilized, the specimen was loaded to produce a brittle fracture. First, the load was slowly increased to 80 kips, approximately 70% of the fracture load estimated from the FE models. After that, the controller was set to reach 120 kips. It must be noted that, during this first test, only the force channel of the system could be controlled.

As a result, all cracks propagated suddenly, producing a brittle failure, completely severing the bottom flange and almost reaching the top flange. Figure B.22 shows the fractured specimen after being cleaned.



Figure B.22: Fracture obtained in the West web (a) and bottom flange (b)

## Observations from PS1 Test

Although the test was successful in achieving the brittle fracture, several issues related to the closed-loop system and data acquisition system were found:

First, the HSM shut down because of the sudden loss of stiffness at the moment of fracture. This situation prompted the researchers to re-assess the hydraulic controller setup and verify that the configuration was adequate. As a result, some errors in the configuration were found and corrected. In addition, a linear potentiometer was attached to the hydraulic ram to monitor its piston displacement accurately. This would allow the Research Team

also to control the closed-loop system using the displacement control mode in the following tests.

The specimen fractured under the applied load, and the flange spreader tools were not required to produce the crack propagation. Based on this observation, the flange spreader tools were not installed in the following pilot specimen tests. Nonetheless, the Research Team expects that the full-size specimens, particularly those with post-tensioning bars and bolted bottom flanges, will not fracture solely under the load application, and the flange spreader tools will be required.

The low temperatures degraded the adhesive used to attach the high-strength velcro (supporting the Optotrak markers) to the steel. Consequently, most of the infrared markers fell off the specimen, making the displacement data collected with this system unreliable. Therefore, the researchers decided to use stronger adhesives for the following tests.

The DAQ did not work adequately. The strain readings were deemed unreliable due to an incorrect shunt calibration of the gages. Moreover, load and displacement readings were also considered unreliable. Unfortunately, the only reliable data from this first experiment was the temperature recorded by the thermocouples and the fact that the specimen fractured when the load was increasing from 80 to 120 kips. In an attempt to solve this issue, the researchers developed a new LabView code to guarantee reliable data collection for the following tests.

## Pilot Specimen 2A (PS2A)

### Initial Notching

Similar to the protocol for PS1, a reciprocating saw was used to notch PS2A at the section of maximum bending stresses. Table B.8 shows the sizes of the notches cut in this specimen, also illustrated in Figure B.23.

**Table B.8: Notch sizes for PS2A**

Location	Notch Size
East Bottom Flange Edge	1.572 in.
East Web	4.742 in.
West Bottom Flange Edge	1.562 in.
West Web	4.433 in.



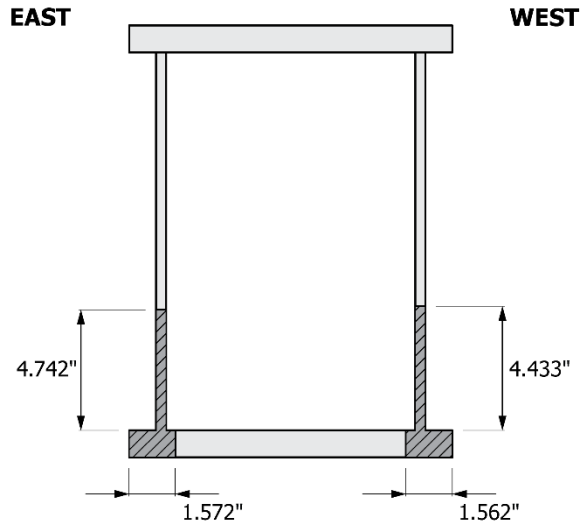


Figure B.23: PS2A notch sizes

### Crack Growth by Cyclic Loading

Pilot Specimen 2A was cyclically loaded between 0 and 120 kips to propagate fatigue cracks from the initial notches, in the same way as it was done on PS1. The loading was stopped every 2,000 cycles to monitor and record the fatigue crack lengths. The dye penetrant method was used again for this task.

Figure B.24 depicts the growth of the fatigue cracks emanating from the initial notches. Fatigue cracks were first detected after 4,000 cycles. As for PS1, fatigue crack growth exhibits a linear trend, higher for the bottom flange cracks where the stresses (and, hence, the stress intensity factors) are higher. For each fatigue crack, the N&B Ratio defined in Equation B.1 was computed and plotted in Figure B.25. Figure B.26 shows a crack detected at the West bottom flange after 6,000 load cycles.

The final crack lengths and their corresponding N&B ratios are shown in Table B.9. It is noted that the fatigue crack extensions are approximately of the same magnitude as in PS1, as are the N&B ratios. However, the N&B ratios for the web cracks do not actually exceed the threshold defined in Equation B.1. Despite this, the researchers decided to halt the cyclic loading for this specimen for consistency since the crack lengths were already of similar length to those obtained in PS1.

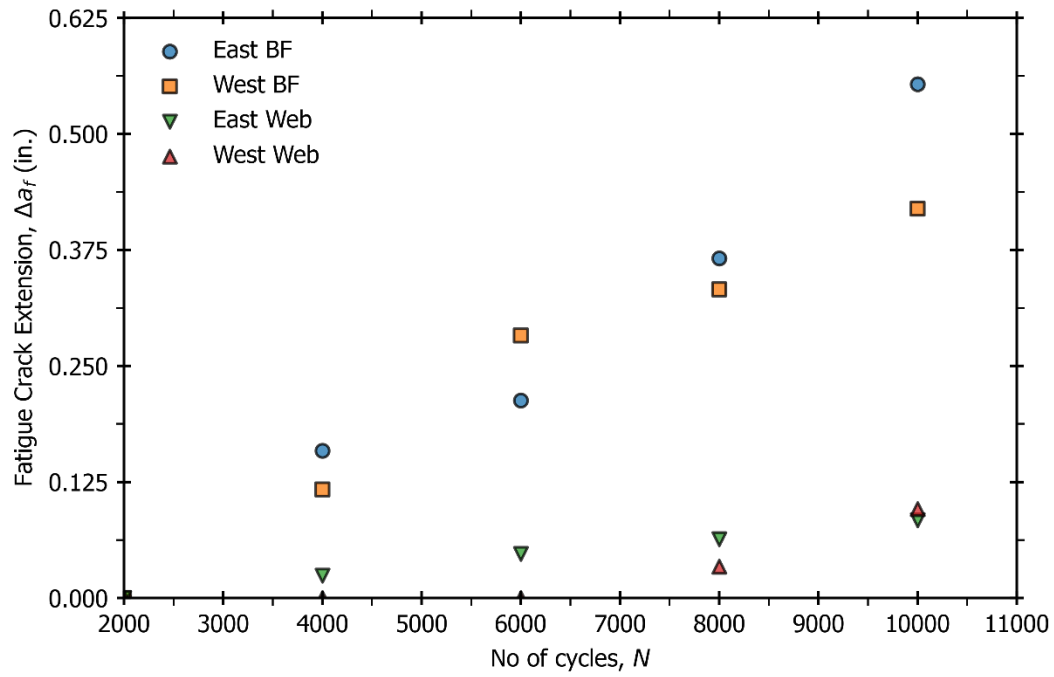


Figure B.24: PS2A fatigue crack growth

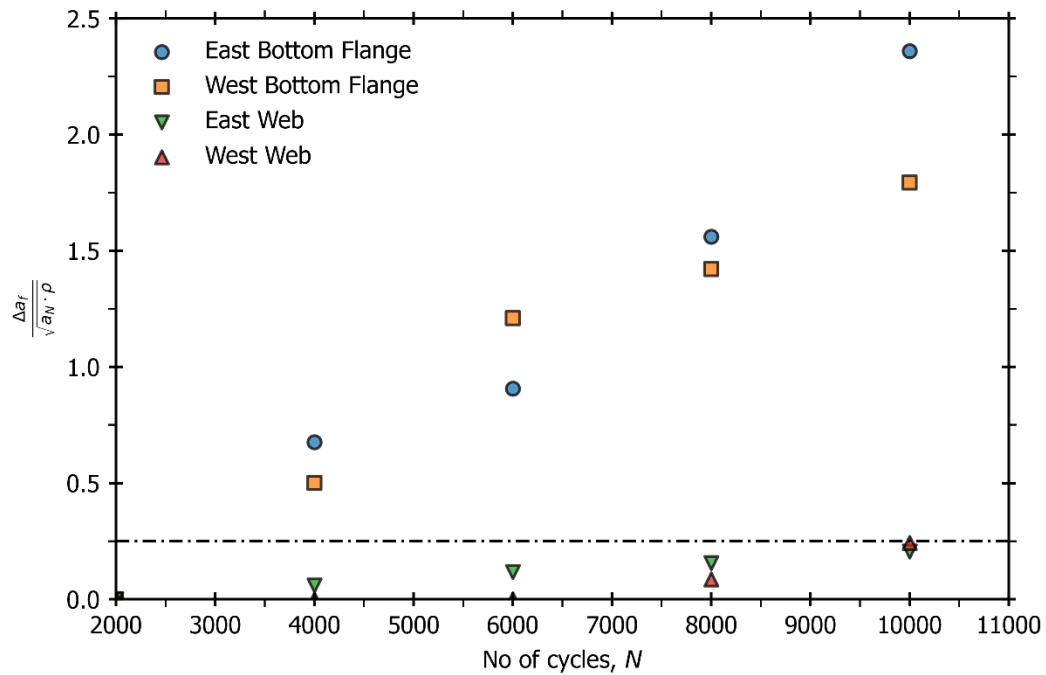


Figure B.25: Novak and Barsom Ratio for PS2A; horizontal dashed line indicates the threshold corresponding to Equation B.1

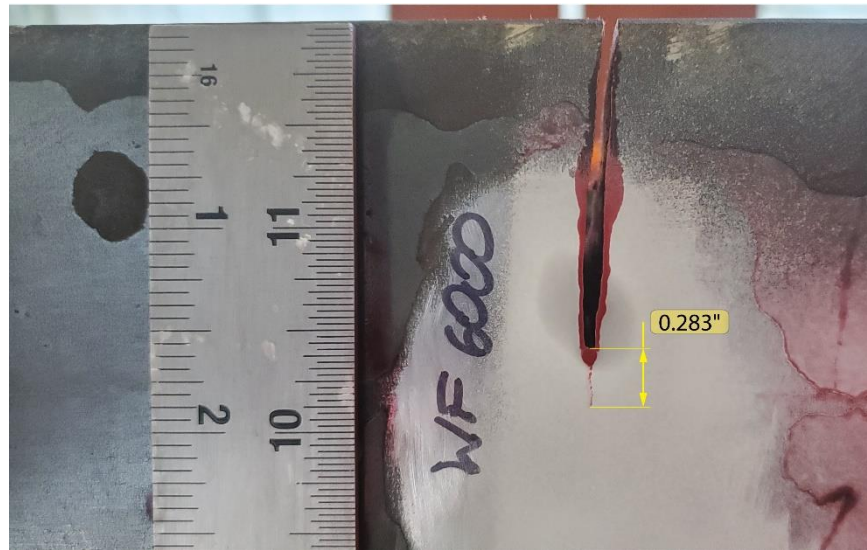


Figure B.26: Fatigue crack at the West bottom flange after 6,000 load cycles

**Table B.9: Final crack lengths (initial notch + fatigue crack) and Novak & Barsom ratio for PS2A**

Location	Notch Size	N&B Ratio
East Bottom Flange Edge	2.126 in.	2.360
East Web	4.826 in.	0.206
West Bottom Flange Edge	1.981 in.	1.794
West Web	4.529 in.	0.243

### Cooling down procedure

The same procedure that was described for PS1 was used to cool down Pilot Specimen 2A. As in PS1, thermocouples TC-0 and TC-5 were installed in the top third of the web depth on the West and East sides, respectively; TC-1 and TC-4 were located in the lower third of the web depth on the West and East sides, respectively; and TC-2 and TC-3 were installed in the bottom flange, on the West and East edges, respectively. The temperature evolution measured at each thermocouple is shown in Figure B.27. Additionally, the temperature recorded at each sensor when the loading protocol started is pointed out in the plot.

Table B.10 summarizes the temperatures recorded at each thermocouple before starting the fracture loading protocol. The corresponding estimated material toughness was calculated for each thermocouple and is indicated in Table B.10 and plotted against the estimated material toughness in Figure B.28.

The temperature evolution trends of this specimen were very similar to those observed in PS1. However, TC-5 (on the East web) recorded a temperature considerably higher than TC-0 (on the opposite web), producing a 20% increase in the estimated material toughness. The rest of the points in the cross-section where the temperature was measured were well into the lower-shelf temperature range. These differences in material toughness did not prevent the cracks from propagating during the fracture loading stage.

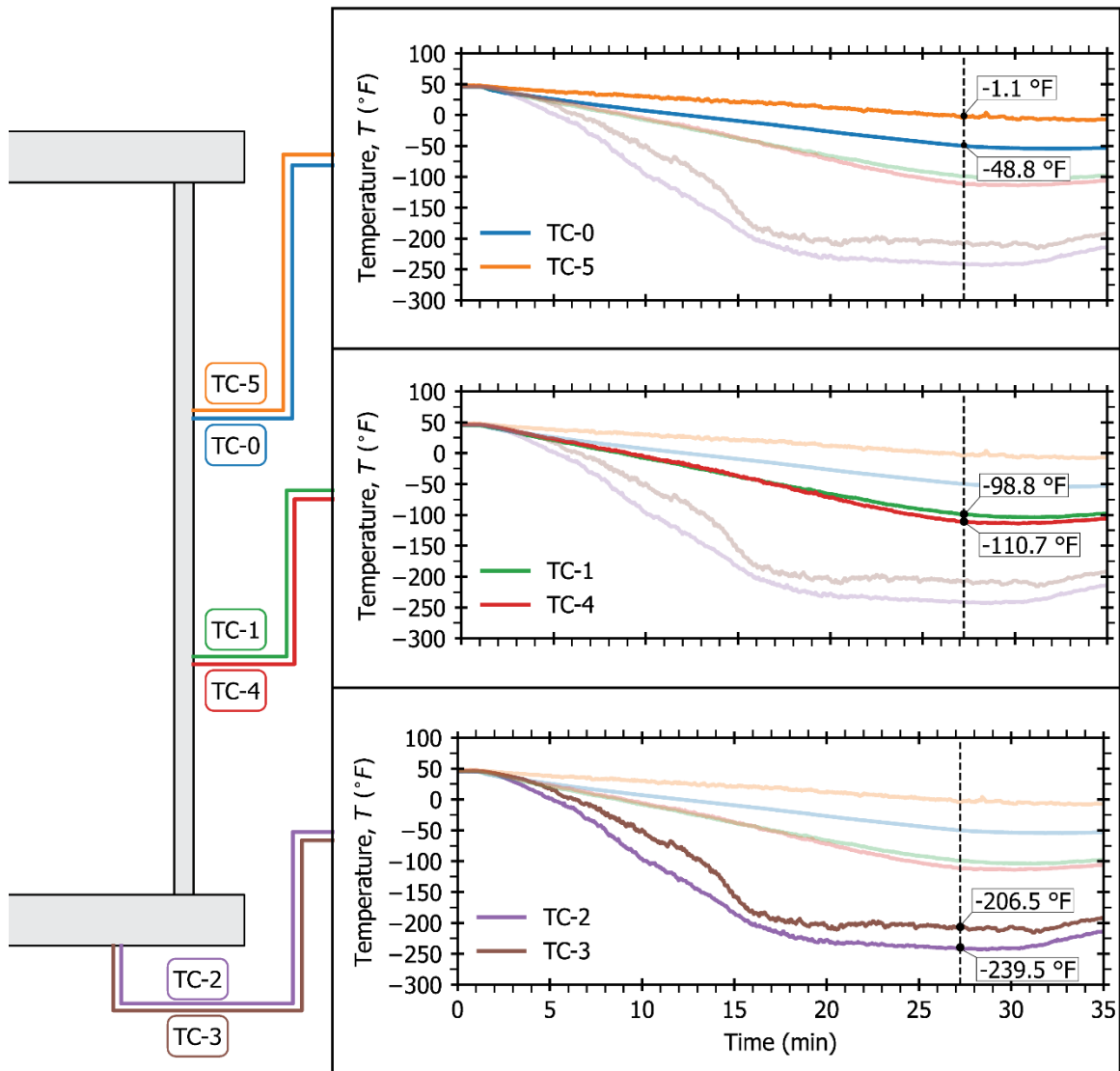
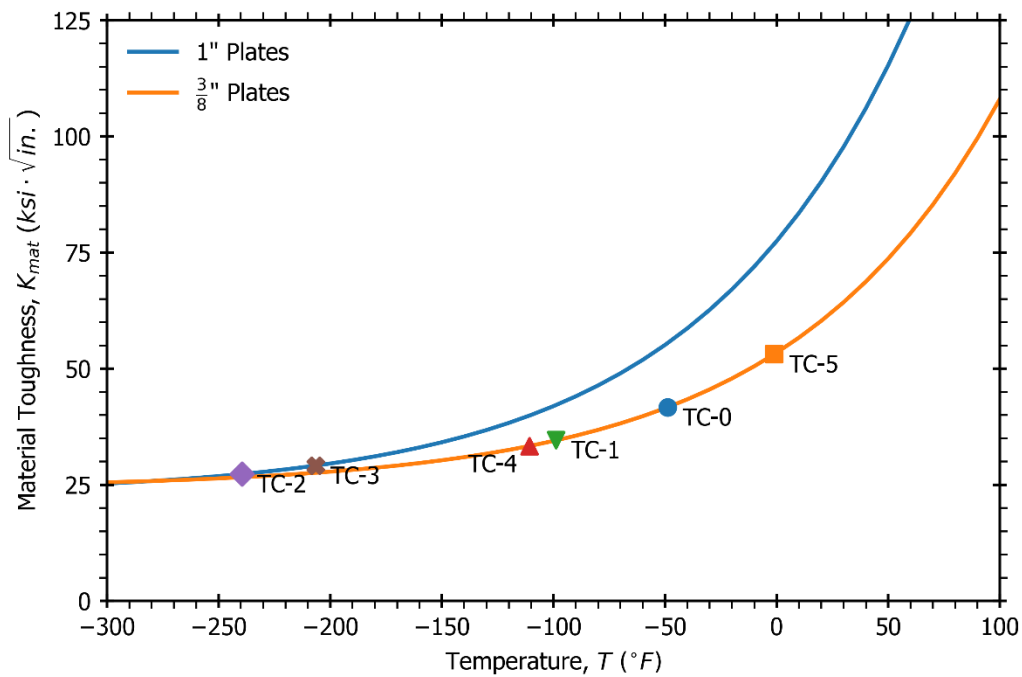


Figure B.27: Temperature evolution at different points in the cross-section. Recorded temperatures when the fracture loading protocol started are pointed out for each thermocouple.

**Table B.10: Temperatures recorded at the cross-section when fracture loading protocol started**

Thermocouple ID	Location	Temperature	Material Toughness
TC-0	West Web – Upper Third	-48.8 °F	41.7 ksi $\sqrt{\text{in.}}$
TC-1	West Web – Lower Third	-98.8 °F	34.6 ksi $\sqrt{\text{in.}}$
TC-2	West Bottom Flange Edge	-239.5 °F	27.3 ksi $\sqrt{\text{in.}}$
TC-3	East Bottom Flange Edge	-206.5 °F	29.1 ksi $\sqrt{\text{in.}}$
TC-4	East Web – Lower Third	-110.7 °F	33.3 ksi $\sqrt{\text{in.}}$
TC-5	East Web – Upper Third	-1.1 °F	53.1 ksi $\sqrt{\text{in.}}$



*Figure B.28: Temperature recorded at the different thermocouples plotted against the material toughness*

## Fracture Loading

After reaching lower shelf temperatures, the specimen was loaded to cause the unstable propagation of the cracks. Therefore, the load was first increased to 80 kips, after which the controller was set to reach 120 kips at a displacement rate of 0.67 in./sec (40 in./min). Note that the use of the displacement control mode was possible due to the addition of the linear potentiometer, as described previously.

As shown in Figure B.29, the peak load at the instant when the fracture occurred was 101.6 kips, and the corresponding deflection at that instant was 0.15 in. The specimen exhibited a linear response until the fracture occurred, as the load was well within its linear elastic range.

It must be noted that when the load reached approximately 57 kips and 80 kips, the researchers stopped the loading protocol to verify that all sensors were working correctly. Since the specimen was warming slightly, some additional deflection was observed (indicated by the horizontal portions of the plot).

After the cracks propagated, some oscillations occurred before the specimen reached its final position. Due to this dynamic effect, the maximum deflection was 0.99 in., and the final deflection after the oscillations came to a stop was 0.36 in. Figure B.30 illustrates the cracks produced on the specimen in the fracture test.

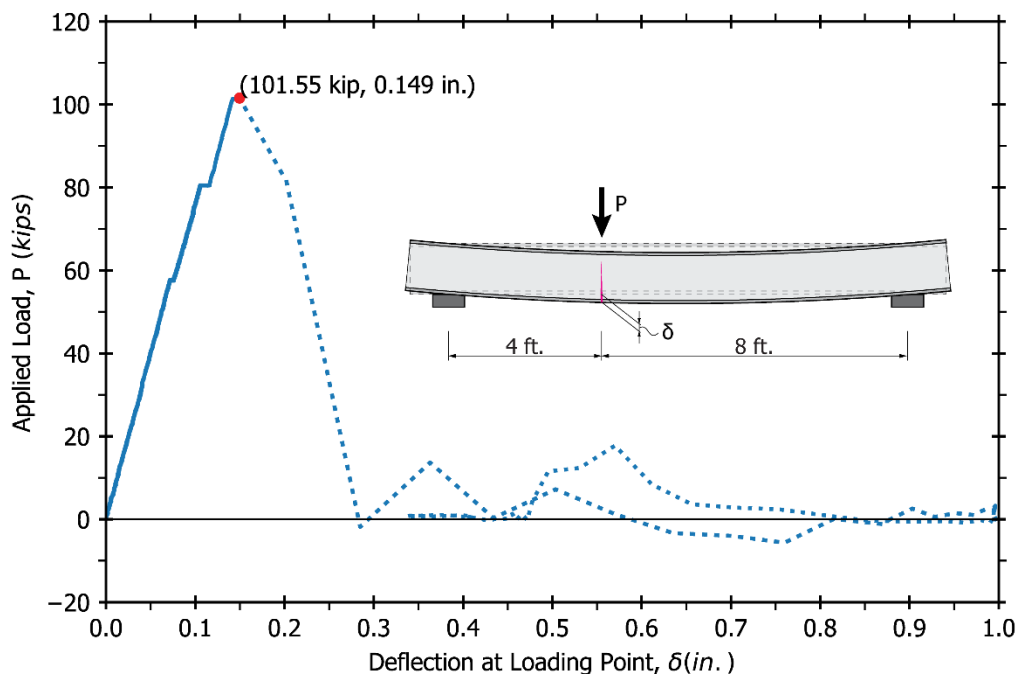


Figure B.29: Applied load versus deflection at the loading point for Pilot Specimen 2A. The dotted line indicates the post-fracture oscillation of the specimen



Figure B.30: (a) East web and (b) bottom flange cracks produced in PS2A fracture test.

### Observations from PS2A Test

Improved procedures were utilized on specimen PS2A based upon the observations from PS1:

- First, the improved tuning of the MTS controller provided a better agreement between the signal and the feedback during the cyclic loading. The addition of the linear potentiometer for the displacement feedback was successful and allowed for a precise displacement control operation of the closed-loop system.
- Moreover, the new LabView code provided reliable data collection at a sampling rate of 1,000 Hz: load, deflections, and stresses were successfully recorded in this test.
- Although no reliable load data was recorded for PS1, the peak load achieved in the fracture test of PS2A was consistent with the results of the test of PS1 and the preliminary FE results.

On the other hand, some obstacles were still found during this test:

- The linear potentiometer attached to the hydraulic ram to monitor the rod displacement fell off due to the sudden shake produced at the fracture. Consequently, the linear potentiometer extended to its full stroke, which exceeded the safety limits set on the MTS controller and stopped the HSM. Hence, the actuator stopped pushing the specimen after the fracture had occurred. In order to



avoid this problem in future tests, it was decided to attach the linear potentiometer to the ram mechanically, using a hose clamp.

- The new adhesive used to affix the Optotrak markers to the specimen was not adequate for the low temperatures and could not prevent them from falling during the cooling down procedure. Thus, the researchers looked into other products to guarantee that the markers will stay in place during the entire duration of the test.

### **Pilot Specimen 2B (PS2B)**

After conducting the first test (PS2A), Pilot Specimen 2 was spliced at the crack location and rotated to be tested again at the other third point, as shown in Figure B.31. Moreover, the specimen was flipped upside-down so that the intact flange was tested in tension.

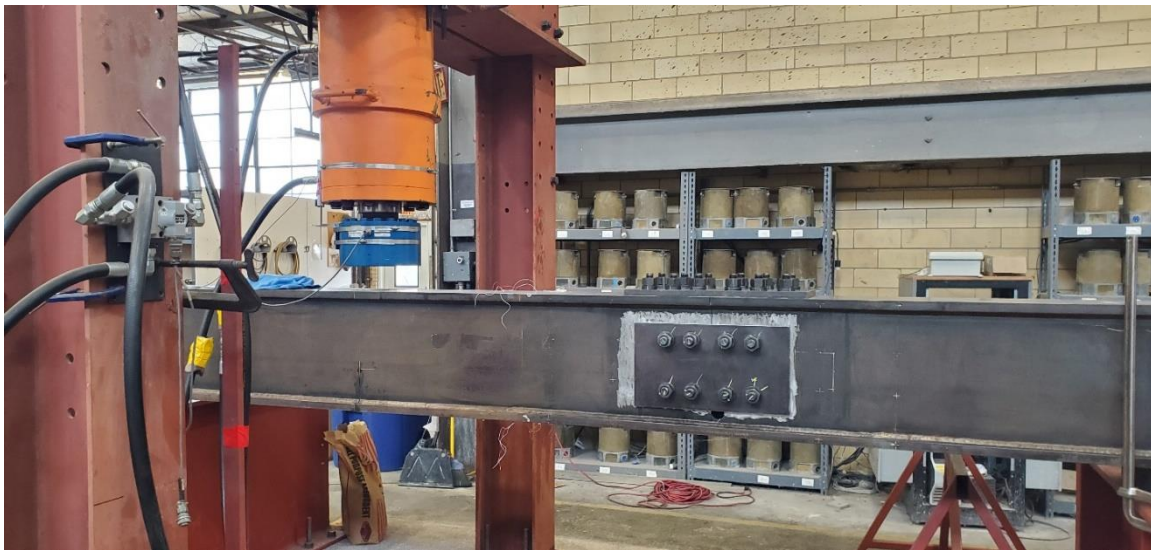


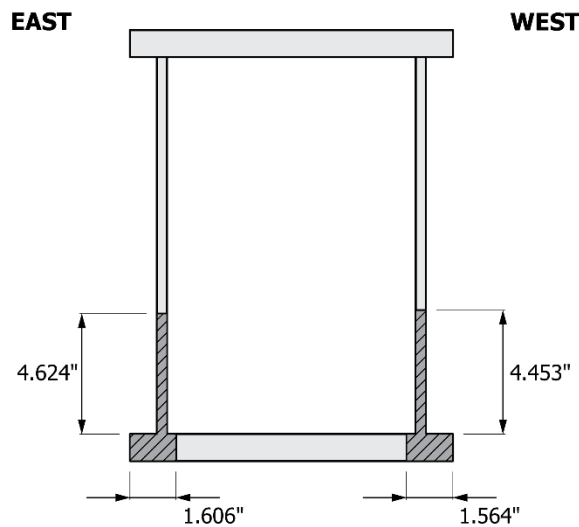
*Figure B.31: Pilot Specimen 2 after being repaired*

### **Initial Notching**

PS2B was notched using the same procedure as PS1 and PS2A at the section of maximum bending stresses. Table B.11 shows the sizes of the notches cut in this specimen, also illustrated in Figure B.32.

**Table B.11: Notch sizes for PS2B**

Location	Notch Size
East Bottom Flange Edge	1.606 in.
East Web	4.624 in.
West Bottom Flange Edge	1.564 in.
West Web	4.453 in.

*Figure B.32: PS2B Notch Sizes*

### **Crack Growth by Cyclic Loading**

As in the previous tests, PS2B was cyclically loaded between 0 and 120 kips to propagate fatigue cracks from the initial notches, stopping every 2,000 cycles to monitor and register the fatigue crack lengths using the dye penetrant method.

Figure B.33 depicts the growth of the fatigue cracks emanating from the initial notches for PS2B, which were first detected after 2,000 load cycles. As in the previous tests, fatigue cracks grew with a linear rate, higher for the bottom flange cracks where the stresses (and, hence, the stress intensity factors) were higher.

For each fatigue crack, the ratio between the fatigue crack extension and the initial notch length defined in Equation B.1 was computed and plotted in Figure B.34. The final crack lengths and their corresponding N&B ratios are shown in Table B.12. Although the fatigue

cracks located on the webs did not meet the criteria established by Equation B.1, the researchers decided to proceed with the testing because the bottom flange cracks were above the threshold, and the crack lengths were already of the same order as in the previous experiments. Figure B.35 shows a crack discovered at the West bottom flange after 12,000 load cycles.

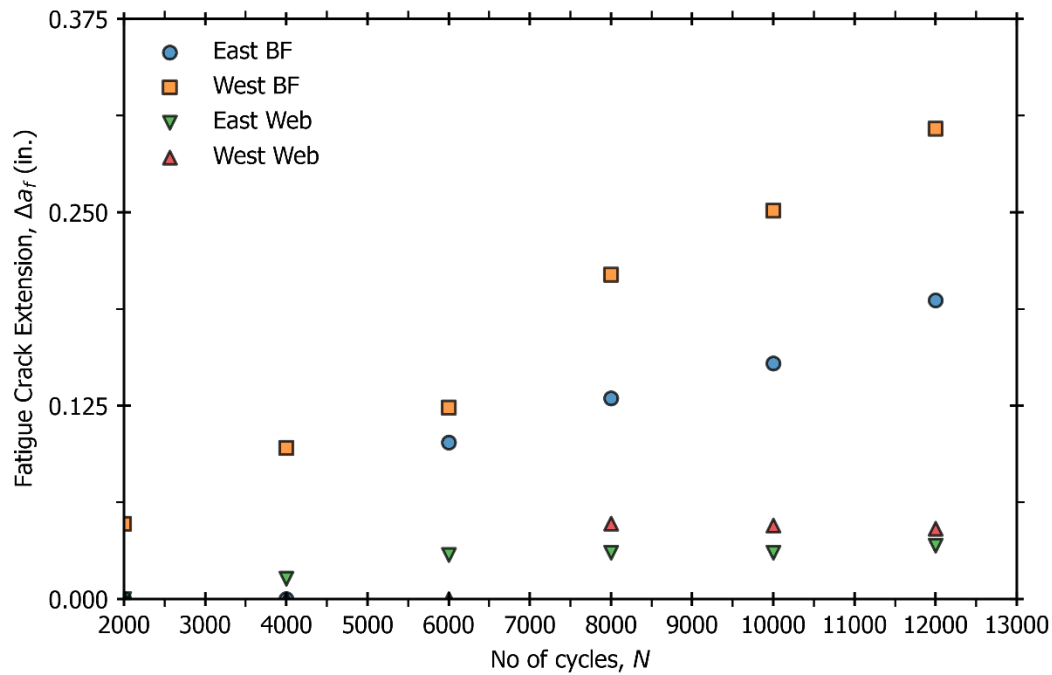


Figure B.33: PS2B Fatigue crack growth

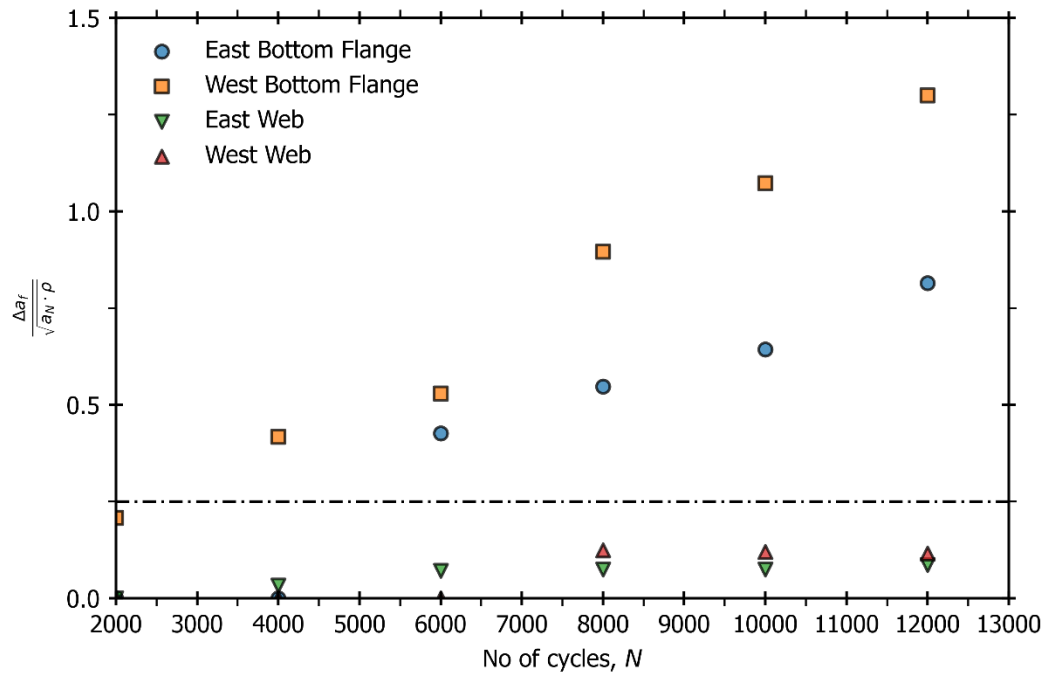


Figure B.34: Novak and Barsom Ratio for PS2B; horizontal dashed line indicates the threshold corresponding to Equation B.1

**Table B.12: Final crack lengths (initial notch + fatigue crack) and Novak & Barsom ratio for PS2B**

Location	Notch Size	N&B Ratio
East Bottom Flange Edge	1.799 in.	0.815
East Web	4.659 in.	0.086
West Bottom Flange Edge	1.868 in.	1.300
West Web	4.499 in.	0.116

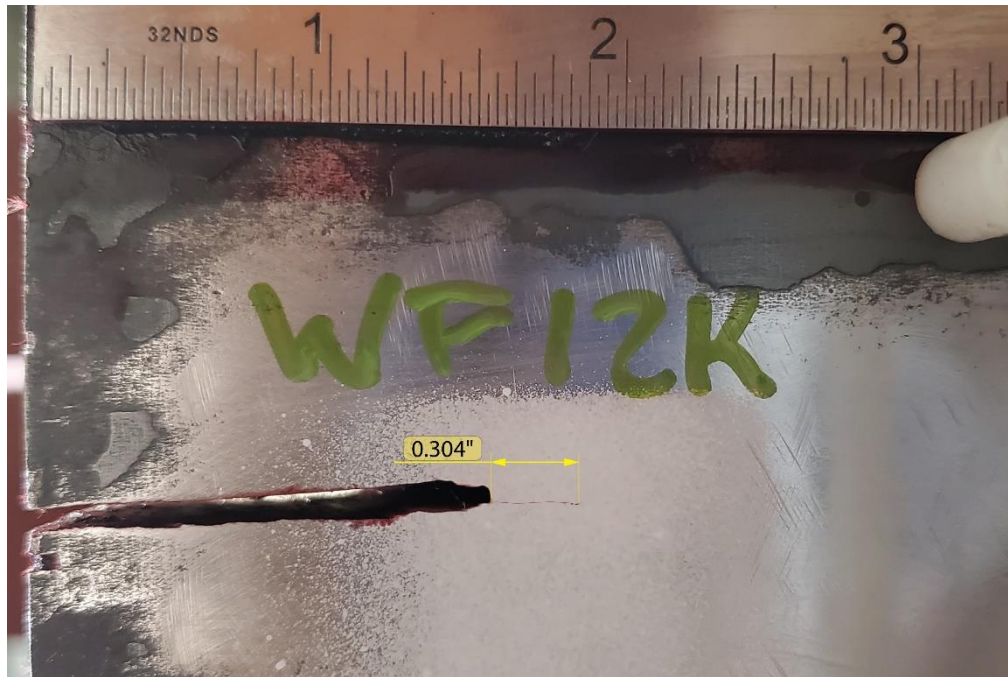


Figure B.35: Fatigue crack at the West bottom flange after 12,000 load cycles

### Cooling down procedure

Pilot Specimen 2B was cooled down following the procedure outlined previously. Thermocouples TC-0 and TC-5 were in the top third of the web depth on the West and East sides, respectively; TC-1 and TC-4 were placed in the lower third of the web depth on the West and East sides, respectively; and TC-2 and TC-3 were installed in the bottom flange, on the West and East edges, respectively. The temperature evolution measured at each thermocouple is illustrated in Figure B.36. The temperature recorded at each sensor when the loading protocol started is also pointed out in the plot. Table B.13 summarizes the temperatures recorded at each thermocouple before starting the fracture loading protocol. The corresponding estimated material toughness was calculated for each thermocouple and is shown in Table B.13 and plotted against the estimated material toughness in Figure B.37.

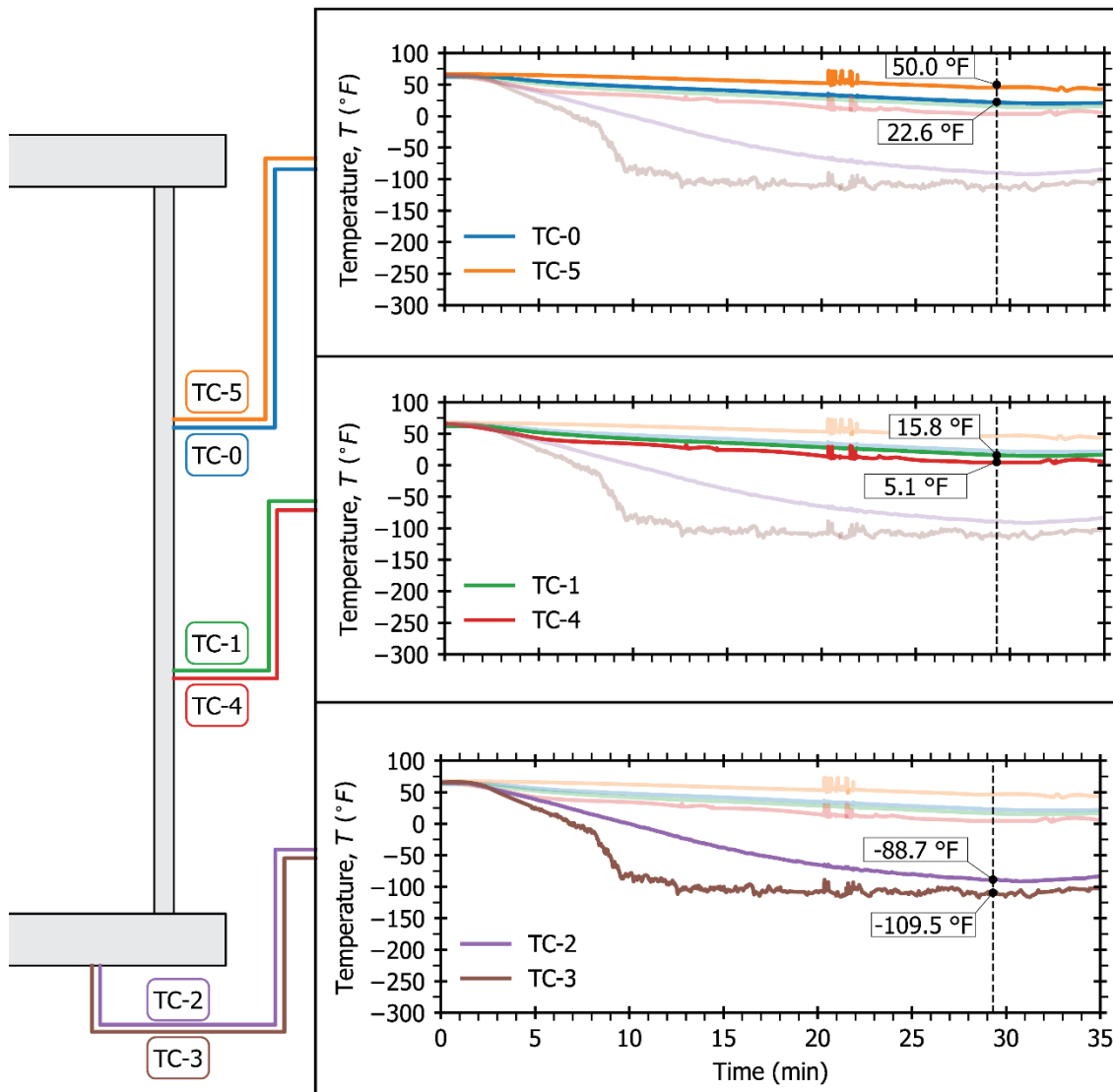
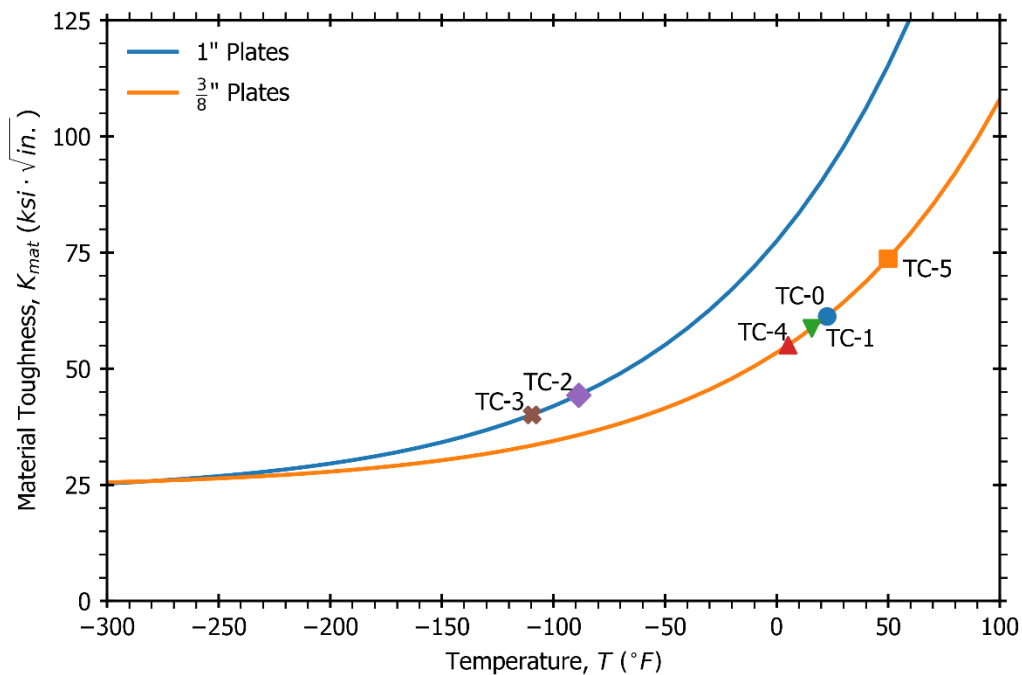


Figure B.36: Temperature evolution at different points in the cross-section of PS2B. Recorded temperatures when the fracture loading protocol started are pointed out for each thermocouple

**Table B.13: Temperatures recorded at the cross-section when fracture loading protocol started**

Thermocouple ID	Location	Temperature	Material Toughness
TC-0	West Web – Upper Third	22.6 °F	61.3 ksi $\sqrt{\text{in.}}$
TC-1	West Web – Lower Third	15.8 °F	58.7 ksi $\sqrt{\text{in.}}$
TC-2	West Bottom Flange Edge	-88.7 °F	44.3 ksi $\sqrt{\text{in.}}$
TC-3	East Bottom Flange Edge	-109.6 °F	40.1 ksi $\sqrt{\text{in.}}$
TC-4	East Web – Lower Third	5.1 °F	55.0 ksi $\sqrt{\text{in.}}$
TC-5	East Web – Upper Third	50.0 °F	73.7 ksi $\sqrt{\text{in.}}$



*Figure B.37: Temperature recorded at the different thermocouples in PS2B plotted against the material*

For this specimen, it is noteworthy that the temperatures achieved at the different measuring points on the cross-section are considerably higher than those recorded in the



two previous tests. Thus, the minimum estimated material toughness achieved at the bottom flange is only about 40.1 ksi  $\sqrt{\text{in.}}$ , approximately 47% higher than that reached on PS2A.

As shown in Figure B.37, the points corresponding to the webs are in the ascending portion of the estimated material toughness curve. The points corresponding to the bottom flange, however, are relatively close to the lower shelf region. As discussed in the next section, this slightly higher material toughness had little impact on the fracture test.

### **Fracture Loading**

After cooling with liquid Nitrogen, the specimen was loaded to produce the unstable propagation of the fatigue cracks. The load was first increased to 80 kips and, after that, the controller was set to reach 120 kips at a displacement rate of 0.67 in./sec (40 in./min).

As shown in Figure B.38, the peak load at the instant when the fracture occurred was 114.4 kips. The corresponding deflection at that instant was 0.18 in. This peak load is consistent with that of PS2A, and the increase in the peak load may be primarily attributed to the higher material toughness due to the higher temperature. The specimen exhibited a linear response until the fracture occurred, as the load was well within its linear elastic range.

When the load reached 80 kips, the researchers stopped the loading protocol for a couple of minutes to verify that all sensors were working correctly. Since the specimen was slowly warming up, some additional deflection was observed (indicated by the horizontal portion of the plot).

After the cracks propagated, some oscillations occurred before the specimen reached its final position, indicated by the tail of the plot after reaching the peak load (dotted line). The final deflection after the oscillations came to a stop was 0.42 in. The cracks present in the East web and bottom flange after the test concluded are shown in Figure B.39.

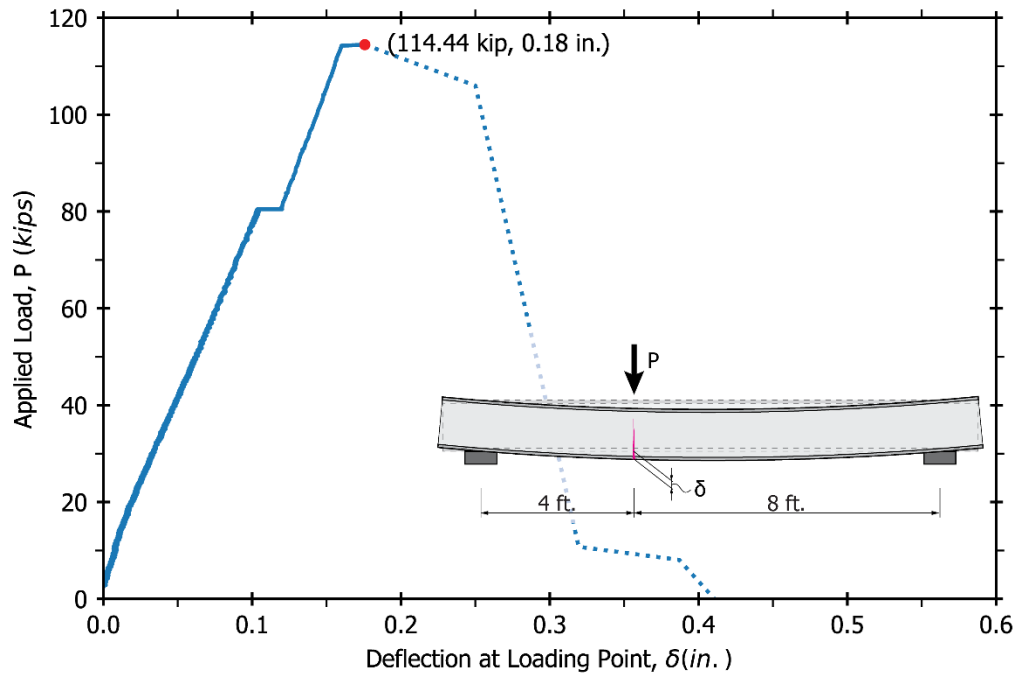


Figure B.38: Applied load versus deflection at the loading point for Pilot Specimen 2A. The dotted line indicates the post-fracture oscillation of the specimen

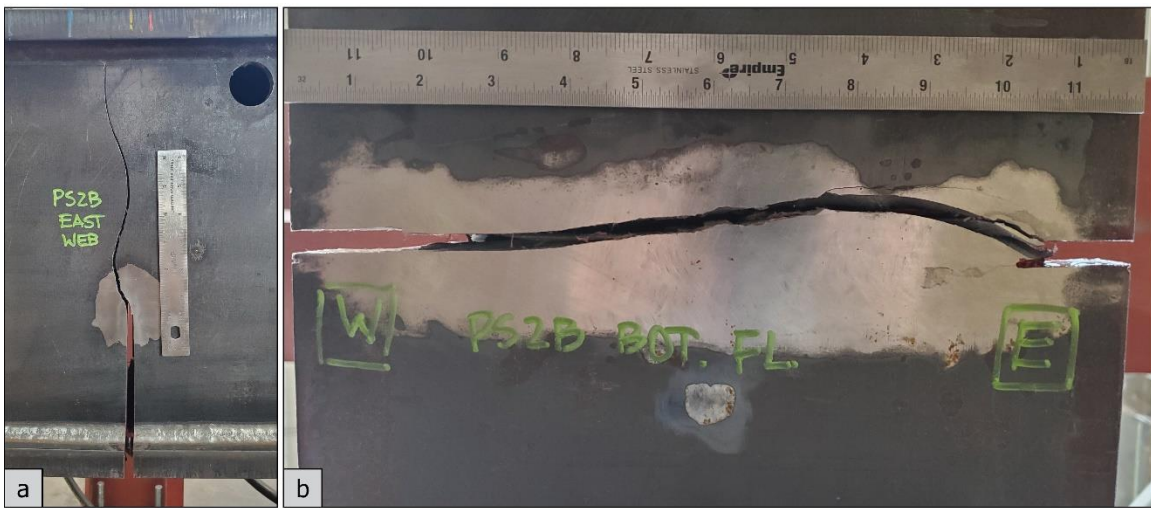


Figure B.39: (a) East web and (b) bottom flange cracks produced in PS2B fracture test.

## **Results and Observations from PS2B Test**

Overall, the test of Pilot Specimen 2B was successful and led to the following remarks:

The peak load achieved seems to be in good agreement with the previous tests. The fact that it is slightly higher than the peak load for PS2A can be attributed mainly to the higher material toughness due to the higher temperature of the material.

Despite not reaching temperatures as low as in the previous tests, the research team successfully achieved a brittle failure of the specimen, severing the bottom flange completely and with web cracks almost reaching the compression flange. This seems to indicate that as long as the bottom flange is at temperatures below -80 °F, the test can be carried out successfully.

The main drawback of this test was that it was not possible to maintain the load on the specimen and continue pushing it downwards after the fracture had occurred. The sudden loss of stiffness makes the controller shut down the HSM and, hence, the loading stops. Due to safety concerns, the Research Team believes it is reasonable to conduct the fracture test in two stages, fracturing the specimen in the first stage and continuing with the post-fracture loading on a second one.

Furthermore, some of the Optrotrak markers still showed adherence issues due to the extremely low temperatures of the steel. Therefore, alternative ways of affixing the markers to the specimens will be explored for the full-scale tests.

## **General Remarks**

Although it was not part of the original proposal, testing these pilot specimens was an extremely valuable experience for the Research Team. Some general conclusions from these experiments are:

The researchers identified difficulties with the hydraulic equipment and the data acquisition system and came up with solutions to overcome these issues. The new LabView code that was developed for these tests proved to be reliable and will be used for the full-scale tests.

Even though the flange spreader tools were not necessary to fracture the pilot specimens, the Research Team decided to purchase a toolset for the full-scale tests. It is anticipated that these will be particularly helpful for the specimens with the post-tensioning bars and the bolted bottom flange.

Using liquid Nitrogen was effective in reaching lower shelf temperatures in the steel section. Based on the pilot tests, it seems that achieving a lower-shelf temperature at the

bottom flange is of primary importance. If the cracks propagate at the bottom flange, the web cracks will do too. To verify this hypothesis, crack opening gages will be installed in the vicinity of the crack tips to measure which cracks propagate first.

Moreover, insulating the region of interest improved the procedure. Thus, the researchers will insulate the region where the cracks will be initiated using insulation boards attached to the adjacent diaphragms for the full-scale specimens.

For the full-scale tests, the Optotrak markers will be glued to a piece of aluminum angle which will be clamped to the bottom flange of the specimen. In addition, insulating material will be installed between the aluminum angle and the specimen to prevent the adhesive from freezing.

Although the initial intention of the research team was to keep the load on the specimen even during fracture (simulating a gravity load), the experience with the pilot specimens showed that this would be difficult to accomplish. Furthermore, the pilot specimens exhibited some post-fracture vibrations, which in the case of the full-scale specimens, pose a high risk of hitting and damaging the hydraulic rams. Therefore, for the sake of safety, it was decided that the full-scale specimens will be loaded to fracture and, after the oscillations stop, the post-fracture behavior will be investigated.

## Appendix C. Design Example Calculations

### Computation of the strength of the intact section<sup>1</sup>

Table C.1: Cross-section dimensions of the intact section

	Top Flange Thickness, in	$t_{tf}$	2.50
	Top Flange Width, in	$b_{tf}$	70.0
	Bottom Flange Thickness, in	$t_{bf}$	1.50
	Bottom Flange Width, in	$b_{bf}$	70.0
	Web Thickness, in	$t_w$	1.125
	Web Depth, in	$d_w$	105.0
	Flange Connection Plate Thickness, in	$t_l$	1.50
	Flange Connection Plate Width, in	$b_l$	24.0
	Clear Projecting Width, in	$b_p$	2.0
	Yield Stress, ksi	$F_y$	50.0
	Young's Modulus, ksi	$E$	29,000
	Unbraced Length, in	$L_b$	1368.0

#### 1. Computation of top flange effective width, $b_e$ , and effective sectional properties (Article 6.12.2.2.2c)

Flange width between the faces of the webs (Table 6.9.4.2.1-1)

$$b = b_{tf} - 2 \cdot b_p - 2 \cdot t_w = 63.75 \text{ in}$$

Flange Slenderness (Table 6.9.4.2.1-1)

$$\lambda_f = \frac{b}{t_{tf}} = 25.5$$

Limiting Flange Slenderness (Table 6.9.4.2.1-1)

<sup>1</sup> Unless otherwise indicated, the Articles and Tables referenced in these calculations correspond to the provisions of the AASHTO LRFD Specifications (2020).

$$\lambda_r = 1.09 \cdot \sqrt{\frac{E}{F_y}} = 26.3$$

Effective Flange width

$$\rightarrow \lambda_f < \lambda_r \therefore b_e = b_{tf} = 70.0 \text{ in}$$

**Table C.2: Effective Cross-sectional Properties**

Gross Area, in <sup>2</sup>	$A_{ge}$	588.25
Elastic Neutral Axis, in	$y_{ge}$	55.20
Plastic Neutral Axis, in	$y_{pe}$	55.06
Moment of Inertia about 33 axis, in <sup>4</sup>	$I_{33e}$	1.24 E6
Radius of Gyration about 33 axis, in	$r_{33e}$	45.94
Section Moduli about 33 axis (top), in <sup>3</sup>	$S_{33te}$	22,452
Section Moduli about 33 axis (bot), in <sup>3</sup>	$S_{33be}$	22,493
Plastic Section Mod about 33 axis, in <sup>3</sup>	$Z_{33e}$	25,190
Moment of Inertia about 22 axis, in <sup>4</sup>	$I_{22e}$	4.04 E6
Radius of Gyration about 22 axis, in	$r_{22e}$	26.22
Section Moduli about 22 axis, in <sup>3</sup>	$S_{22e}$	11,556
St. Venant Torsional Constant, in <sup>4</sup>	$J_e$	774,570

Depth of the webs in compression in the elastic range (Article 6.9.4.2.2b)

$$D_{ce} = 52.8 \text{ in}$$

Yield moment with respect to the compression flange.

- For sections in which  $S_{33be} > S_{33te}$ ,  $M_{yce} = S_{33te} \cdot F_y$
- For sections in which  $S_{33be} < S_{33te}$ ,  $M_{yce}$  is the moment at nominal first yielding of the compression flange, considering early nominal yielding in tension (Article C6.12.2.2.2c)

$$\rightarrow S_{33be} > S_{33te} \therefore M_{yce} = S_{33te} \cdot F_y = 93,552 \text{ kip} \cdot \text{ft}$$

Depth of the webs in compression in the plastic range (C6.12.2.2.2c-2)

$$D_{cep} = 52.94 \text{ in}$$

Plastic moment:

$$M_{pe} = Z_{33e} \cdot F_y = 104,959 \text{ kip} \cdot \text{ft}$$

## 2. Web Classification (Article 6.12.2.2.2c)

Limiting Slenderness for a compact web (6.12.2.2.2c-3)

$$\lambda_{pw} = 3.1 \frac{D_{ce}}{D_{cep}} \sqrt{\frac{E}{F_y}} = 74.5$$

Limiting Slenderness for a noncompact web (6.12.2.2.2c-6)

$$\lambda_{rw} = 4.6 \sqrt{\frac{E}{F_y}} = 110.8$$

Web Slenderness (6.12.2.2.2c-2)

$$\lambda_w = 2 \cdot \frac{D_{ce}}{t_w} = 93.87 \rightarrow \text{Noncompact web}$$

Web Plastification Factor for noncompact webs (6.12.2.2.2c-4, 7 & 8)

$$R_{pc} = \left[ 1 - \left( 1 - \frac{M_{yce}}{M_{pe}} \right) \cdot \left( \frac{\lambda_w - \lambda_{pw}}{\lambda_{rw} - \lambda_{pw}} \right) \right] \frac{M_{pe}}{M_{yce}} = \mathbf{1.06}$$

Web Load-Shedding Factor,  $R_b$

Ratio of two times the web area in compression to the area of the compression flange (6.10.1.10.2-8)

$$a_{wc} = \frac{2 \cdot D_{ce} \cdot t_w}{b_e \cdot t_{tf}} = 1.36$$

Limiting slenderness ratio for a noncompact web, expressed in terms of  $2D_c/t_w$ , (6.10.1.10.2-5)



$$\lambda_{rws} = 4.6 \sqrt{\frac{E}{F_y}} \leq \left(3.1 + \frac{5}{a_{wc}}\right) \sqrt{\frac{E}{F_y}} \leq 5.7 \sqrt{\frac{E}{F_y}} = 137.3$$

Web Load Shedding Factor (6.10.1.10.2)

$$\rightarrow \lambda_w < \lambda_{rws} \therefore R_b = 1.0$$

### 3. Compression Flange Classification (Article 6.12.2.2.2d)

Limiting Slenderness for a compact flange (Table 6.9.4.2.1-1)

$$\lambda_{pf} = 1.09 \cdot \sqrt{\frac{E}{F_y}} = 26.3$$

Limiting Slenderness for a noncompact flange (6.12.2.2.2c-13)

$$\lambda_{rf} = 1.56 \cdot \lambda_{pf} = 40.9$$

Compression Flange Slenderness (6.12.2.2.2c-10)

$$\lambda_f = 25.1 \rightarrow \text{Compact Flange}$$

Compression Flange Slenderness Factor for a compact flange (6.12.2.2.2c-11, 14 & 16)

$$\lambda_f < \lambda_{pf} \therefore R_f = 1.0$$

### 4. General Yielding, compression flange local buckling, and Lateral Torsional Buckling (Article 6.12.2.2.2e)

Limiting unbraced length to achieve the nominal flexural resistance  $R_f R_b R_{pc} M_{yce}$  (6.12.2.2.2e-4)

$$L_p = \frac{0.1 \cdot r_{22e} \cdot E \cdot \sqrt{J_e \cdot A_{ge}}}{M_{yce}} = 1,446 \text{ in} \approx 120.5 \text{ ft}$$

Limiting unbraced length for the calculation of the lateral torsional buckling resistance (6.12.2.2.2e-5)

$$L_r = \frac{0.6 \cdot r_{22e} \cdot E \cdot \sqrt{J_e \cdot A_{ge}}}{0.5 \cdot F_y \cdot S_{33te}} = 17,351 \text{ in} \approx 1446 \text{ ft}$$

Nominal Flexural Resistance (6.12.2.2.2e-1 & 2)

$$\rightarrow L_b < L_p \therefore M_n = R_b R_{pc} R_f \cdot M_{yce} = 98,863 \text{ kip} \cdot \text{ft}$$

Factored Flexural Resistance

$$\phi_f \cdot M_n = 1.0 \cdot 98,863 \text{ kip} \cdot \text{ft} = 98,863 \text{ kip} \cdot \text{ft}$$

## 5. Shear Strength of Interior Panels

Plastic Shear Force per web (6.10.9.3.2-3)

$$V_p = 0.58 \cdot F_y \cdot t_w \cdot d_w = 3,426 \text{ kip}$$

Transverse Diaphragm Spacing

$$d_0 = 120 \text{ in}$$

Shear buckling coefficient (6.10.9.3.2-7)

$$k = 5 + \frac{5}{\left(\frac{d_0}{d_w}\right)^2} = 8.83$$

Ratio of the shear-buckling resistance to the shear yield strength (6.10.9.3.2-4, 5 & 6)

$$1.12 \cdot \sqrt{\frac{E \cdot k}{F_y}} = 80.2$$

$$1.4 \cdot \sqrt{\frac{E \cdot k}{F_y}} = 100.2$$

$$\frac{d_w}{t_w} = 93.3 \rightarrow C = \frac{1.12}{\left(\frac{d_w}{t_w}\right)} \cdot \sqrt{\frac{E \cdot k}{F_y}} = 0.86$$

Panel proportion limit (6.10.9.3.2-1)

$$\frac{2 \cdot d_w \cdot t_w}{\left(\frac{b_{tf}}{2} t_{tf} + \frac{b_{bf}}{2} t_{bf}\right)} = 1.69 < 2.5$$

Nominal Shear Resistance of an interior web panel, per web (6.10.9.3.2-2)

$$\rightarrow V_n = V_p \cdot \left( C + \frac{0.87(1 - C)}{\sqrt{1 + \left(\frac{d_0}{d_w}\right)^2}} \right) = 3,219 \text{ kip}$$

Factored Shear Resistance for the section (2 webs):

$$\phi_v \cdot 2V_n = 1.0 \cdot 2(3,219 \text{ kip}) = 6,438 \text{ kip}$$

(\* Strength reduction factor proposed based on the results of the parametric study presented in Chapter 6)

## 6. Shear Strength of End Panels

Plastic Shear Force per web (6.10.9.3.3-2)

$$V_p = 0.58 \cdot F_y \cdot t_w \cdot d_w = 3,426 \text{ kip}$$

Transverse Diaphragm Spacing

$$d_0 = 120 \text{ in}$$

Shear buckling coefficient (6.10.9.3.2-7)

$$k = 5 + \frac{5}{\left(\frac{d_0}{d_w}\right)^2} = 8.83$$

Shear buckling coefficient (6.10.9.3.2-4, 5 & 6)

$$1.12 \cdot \sqrt{\frac{E \cdot k}{F_y}} = 80.2$$

$$1.4 \cdot \sqrt{\frac{E \cdot k}{F_y}} = 100.2$$

$$\frac{d_w}{t_w} = 93.3 \rightarrow C = \frac{1.12}{\left(\frac{d_w}{t_w}\right)} \cdot \sqrt{\frac{E \cdot k}{F_y}} = 0.86$$

Panel proportion limit (6.10.9.3.2-1)

$$\frac{2 \cdot d_w \cdot t_w}{\left(\frac{b_{tf}}{2} t_{tf} + \frac{b_{bf}}{2} t_{bf}\right)} = 1.69 < 2.5$$

Nominal Shear Resistance of an interior web panel, per web (6.10.9.3.2-2)

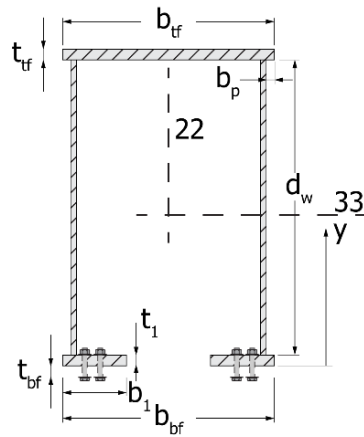
$$\rightarrow V_n = V_{cr} = V_p \cdot C = 2,942 \text{ kip (per web)}$$

Factored Shear Resistance for the section (2 webs):

$$\phi_v \cdot 2V_n = 1.0 \cdot 2(2,946 \text{ kip}) = 5,892 \text{ kip}$$

## Factored Strength of the Faulted Section with the bottom flange fractured

**Table C.3: Cross-section dimensions of the faulted section (bottom flange fractured)**



Top Flange Thickness, in	$t_{tf}$	2.50
Top Flange Width, in	$b_{tf}$	70.0
<del>Bottom Flange Thickness, in</del>	<del><math>t_{bf}</math></del>	<del>0.00</del>
<del>Bottom Flange Width, in</del>	<del><math>b_{bf}</math></del>	<del>0.00</del>
Web Thickness, in	$t_w$	1.125
Web Depth, in	$d_w$	105.0
Flange Connection Plate Thickness, in	$t_l$	1.50
Flange Connection Plate Width, in	$b_l$	24.0
Clear Projecting Width, in	$b_p$	2.0
Yield Stress, ksi	$F_y$	50.0
Young's Modulus, ksi	$E$	29,000
Unbraced Length, in	$L_b$	1368.0

### 1. Computation of top flange effective width, $b_e$ , and effective sectional properties (Article 6.12.2.2.2c)

Flange width between faces of webs (Table 6.9.4.2.1-1)

$$b = b_{tf} - 2 \cdot b_p - 2 \cdot t_w = 63.75 \text{ in}$$

Flange Slenderness (Table 6.9.4.2.1-1)

$$\lambda_f = \frac{b}{t_{tf}} = 25.5$$

Limiting Flange Slenderness (Table 6.9.4.2.1-1)

$$\lambda_r = 1.09 \cdot \sqrt{\frac{E}{F_y}} = 26.3$$

Effective Flange width

$$\rightarrow \lambda_f < \lambda_r \therefore b_e = b_{tf} = 70.0 \text{ in}$$

**Table C.4: Effective Cross-sectional Properties**

Gross Area, in <sup>2</sup>	$A_{ge}$	483.3
Elastic Neutral Axis, in	$y_{ge}$	65.5
Plastic Neutral Axis, in	$y_{pe}$	76.9
Moment of Inertia about 33 axis, in <sup>4</sup>	$I_{33e}$	8.63 E5
Radius of Gyration about 33 axis, in	$r_{33e}$	42.25
Section Moduli about 33 axis (top), in <sup>3</sup>	$S_{33te}$	19,845
Section Moduli about 33 axis (bot), in <sup>3</sup>	$S_{33be}$	13,164
Plastic Section Mod about 33 axis, in <sup>3</sup>	$Z_{33e}$	18,263
Moment of Inertia about 22 axis, in <sup>4</sup>	$I_{22e}$	3.62 E5
Radius of Gyration about 22 axis, in	$r_{22e}$	27.35
Section Moduli about 22 axis, in <sup>3</sup>	$S_{22e}$	10,332
St. Venant Torsional Constant, in <sup>4</sup>	$J_e$	387,285*
*50% of $J_e$ of the intact section		

Depth of the webs in compression in the elastic range (Article 6.9.4.2.2b)

$$D_{ce} = 28.6 \text{ in}$$

Yield moment with respect to the compression flange.

- For sections in which  $S_{33be} > S_{33te}$ ,  $M_{yce} = S_{33te} \cdot F_y$

- For sections in which  $S_{33be} < S_{33te}$ ,  $M_{yce}$  is the moment at nominal first yielding of the compression flange, considering early nominal yielding in tension (Article C6.12.2.2.2c)

$$\rightarrow S_{33be} < S_{33te} \therefore M_{yce} = 73,585 \text{ kip} \cdot \text{ft}$$

Depth of the webs in compression in the plastic range (C6.12.2.2.2c-2)

$$D_{cep} = 29.6 \text{ in}$$

Plastic moment:

$$M_{pe} = Z_{33e} \cdot F_y = 76,096 \text{ kip} \cdot \text{ft}$$

## 2. Web Classification (Article 6.12.2.2.2c)

Limiting Slenderness for a compact web (6.12.2.2.2c-3)

$$\lambda_{pw} = 3.1 \frac{D_{ce}}{D_{cep}} \sqrt{\frac{E}{F_y}} = 72.2$$

Limiting Slenderness for a noncompact web (6.12.2.2.2c-6)

$$\lambda_{rw} = 4.6 \sqrt{\frac{E}{F_y}} = 110.8$$

Web Slenderness (6.12.2.2.2c-2)

$$\lambda_w = 2 \cdot \frac{D_{ce}}{t_w} = 50.9 \rightarrow \text{Compact web}$$

Web Plastification Factor for noncompact webs (6.12.2.2.2c-4, 7 & 8)

$$\lambda_w < \lambda_{pw} \therefore R_{pc} = \frac{M_{pe}}{M_{yce}} = \mathbf{1.03}$$

*Web Load-Shedding Factor,  $R_b$*

Ratio of two times the web area in compression to the area of the compression flange (6.10.1.10.2-8)

$$a_{wc} = \frac{2 \cdot D_{ce} \cdot t_w}{b_e \cdot t_{tf}} = 0.74$$

Limiting slenderness ratio for a noncompact web, expressed in terms of  $2D_c/t_w$ ,  
(6.10.1.10.2-5)

$$\lambda_{rws} = 4.6 \sqrt{\frac{E}{F_y}} \leq \left(3.1 + \frac{5}{a_{wc}}\right) \sqrt{\frac{E}{F_y}} \leq 5.7 \sqrt{\frac{E}{F_y}} = 137.3$$

Web Load Shedding Factor (6.10.1.10.2)

$$\rightarrow \lambda_w < \lambda_{rws} \therefore R_b = 1.0$$

### 3. Compression Flange Classification (Article 6.12.2.2.2d)

Limiting Slenderness for a compact flange (Table 6.9.4.2.1-1)

$$\lambda_{pf} = 1.09 \cdot \sqrt{\frac{E}{F_y}} = 26.3$$

Limiting Slenderness for a noncompact flange (6.12.2.2.2c-13)

$$\lambda_{rf} = 1.56 \cdot \lambda_{pf} = 40.9$$

Compression Flange Slenderness (6.12.2.2.2c-10)

$$\lambda_f = 25.1 \rightarrow \text{Compact Flange}$$

Compression Flange Slenderness Factor for a compact flange (6.12.2.2.2c-11, 14 & 16)

$$\lambda_f < \lambda_{pf} \therefore R_f = 1.0$$

### 4. General Yielding, compression flange local buckling, and Lateral Torsional Buckling (Article 6.12.2.2.2e)

Limiting unbraced length to achieve the nominal flexural resistance  $R_f R_b R_{pc} M_{yce}$  (6.12.2.2.2e-4)

$$L_p = \frac{0.1 \cdot r_{22e} \cdot E \cdot \sqrt{J_e \cdot A_{ge}}}{M_{yce}} = 1,229 \text{ in} \approx 102.4 \text{ ft}$$



Limiting unbraced length for the calculation of the lateral torsional buckling resistance (6.12.2.2.2e-5)

$$L_r = \frac{0.6 \cdot r_{22e} \cdot E \cdot \sqrt{J_e \cdot A_{ge}}}{0.5 \cdot F_y \cdot S_{33te}} = 13,125 \text{ in} \approx 1094 \text{ ft}$$

Nominal Flexural Resistance (6.12.2.2.2e-1 & 2)

$$\rightarrow L_p < L_b < L_r \therefore$$

$$M_n = R_b (R_{pc} R_f \cdot M_{yce} - (R_{pc} R_f M_{yce} - 0.5 F_y S_{33te}) \alpha)$$

$$\alpha = \frac{L_b - L_p}{L_r - L_p} = 0.01$$

$$M_n = 75,690 \text{ kip} \cdot \text{ft}$$

**Factored Flexural Resistance**

$$\phi_f \cdot M_n = 1.0 \cdot (0.9^* \cdot 75,690 \text{ kip} \cdot \text{ft}) = 68,121 \text{ kip} \cdot \text{ft}$$

(\* Resistance factor proposed based on the results of the parametric study presented in Chapter 6)

## 5. Shear Strength of Interior Panels

Plastic Shear Force per web (6.10.9.3.2-3)

$$V_p = 0.58 \cdot F_y \cdot t_w \cdot d_w = 3,426 \text{ kip}$$

Transverse Diaphragm Spacing

$$d_0 = 120 \text{ in}$$

Shear buckling coefficient (6.10.9.3.2-7)

$$k = 5 + \frac{5}{\left(\frac{d_0}{d_w}\right)^2} = 8.83$$

Ratio of the shear-buckling resistance to the shear yield strength (6.10.9.3.2-4, 5 & 6)

$$1.12 \cdot \sqrt{\frac{E \cdot k}{F_y}} = 80.2$$

$$1.4 \cdot \sqrt{\frac{E \cdot k}{F_y}} = 100.2$$

$$\frac{d_w}{t_w} = 93.3 \rightarrow C = \frac{1.12}{\left(\frac{d_w}{t_w}\right)} \cdot \sqrt{\frac{E \cdot k}{F_y}} = 0.86$$

Panel proportion limit (6.10.9.3.2-1)

$$\frac{2 \cdot d_w \cdot t_w}{\left(\frac{b_{tf}}{2} t_{tf} + \frac{b_{bf}}{2} t_{bf}\right)} = 2.70 > 2.5$$

Nominal Shear Resistance of an interior web panel, per web (6.10.9.3.2-2)

$$\rightarrow V_n = V_p \cdot \left( C + \frac{0.87(1 - C)}{\sqrt{1 + \left(\frac{d_0}{d_w}\right)^2 \frac{d_0}{d_w}}} \right) = 3,100 \text{ kip}$$

Factored Shear Resistance for the section (2 webs):

$$\phi_v \cdot 2V_n = 1.0 \cdot 2(0.9^* \cdot 3,100 \text{ kip}) = 5,579 \text{ kip}$$

(\* Strength reduction factor proposed based on the results of the parametric study presented in Chapter 6)

## 6. Shear Strength of End Panels

Plastic Shear Force per web (6.10.9.3.3-2)

$$V_p = 0.58 \cdot F_y \cdot t_w \cdot d_w = 3,426 \text{ kip}$$

Transverse Diaphragm Spacing

$$d_0 = 120 \text{ in}$$

Shear buckling coefficient (6.10.9.3.2-7)

$$k = 5 + \frac{5}{\left(\frac{d_0}{d_w}\right)^2} = 8.83$$

Shear buckling coefficient (6.10.9.3.2-4, 5 & 6)

$$1.12 \cdot \sqrt{\frac{E \cdot k}{F_y}} = 80.2$$

$$1.4 \cdot \sqrt{\frac{E \cdot k}{F_y}} = 100.2$$

$$\frac{d_w}{t_w} = 93.3 \rightarrow C = \frac{1.12}{\left(\frac{d_w}{t_w}\right)} \cdot \sqrt{\frac{E \cdot k}{F_y}} = 0.86$$

Panel proportion limit (6.10.9.3.2-1)

$$\frac{2 \cdot d_w \cdot t_w}{\left(\frac{b_{tf}}{2} t_{tf} + \frac{b_{bf}}{2} t_{bf}\right)} = 1.69 < 2.5$$

Nominal Shear Resistance of an interior web panel, per web (6.10.9.3.2-2)

$$\rightarrow V_n = V_{cr} = V_p \cdot C = 2,946 \text{ kip (per web)}$$

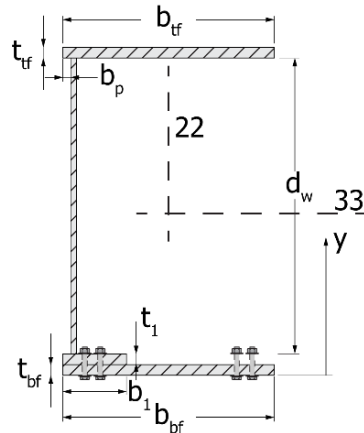
Factored Shear Resistance for the section (2 webs):

$$\phi_v \cdot 2V_n = 1.0 \cdot 2(0.9^* \cdot 2,946 \text{ kip}) = 5,302.8 \text{ kip}$$

(\* Resistance factor proposed based on the results of the parametric study presented in Chapter 6)

## Factored Strength of the Faulted Section with an entire web and flange connection plate fractured

**Table C.5: Cross-section dimensions of the faulted section (web and flange connection plate fractured)**



Top Flange Thickness, in	$t_{tf}$	2.50
Top Flange Width, in	$b_{tf}$	70.0
Bottom Flange Thickness, in	$t_{bf}$	1.50
Bottom Flange Width, in	$b_{bf}$	70.0
Web Thickness, in	$t_w$	1.125
Web Depth, in	$d_w$	105.0
Flange Connection Plate Thickness, in	$t_l$	1.50
Flange Connection Plate Width, in	$b_l$	24.0
Clear Projecting Width, in	$b_p$	2.0
Yield Stress, ksi	$F_y$	50.0
Young's Modulus, ksi	$E$	29,000
Unbraced Length, in	$L_b$	1368.0

### 1. Computation of top flange effective width, $b_e$ , and effective sectional properties (Article 6.12.2.2.2c)

Flange width between faces of webs (Table 6.9.4.2.1-1)

$$b = b_{tf} - 2 \cdot b_p - 2 \cdot t_w = 63.75 \text{ in}$$

Flange Slenderness (Table 6.9.4.2.1-1)

$$\lambda_f = \frac{b}{t_{tf}} = 25.5$$

Limiting Flange Slenderness (Table 6.9.4.2.1-1)

$$\lambda_r = 1.09 \cdot \sqrt{\frac{E}{F_y}} = 26.3$$

Effective Flange width

$$\rightarrow \lambda_f < \lambda_r \therefore b_e = b_{tf} = 70.0 \text{ in}$$

**Table C.6: Effective Cross-sectional Properties**

Gross Area, in <sup>2</sup>	$A_{ge}$	434.1
Elastic Neutral Axis, in	$y_{ge}$	59.5
Plastic Neutral Axis, in	$y_{pe}$	70.6
Moment of Inertia about 33 axis, in <sup>4</sup>	$I_{33e}$	1.02 E6
Radius of Gyration about 33 axis, in	$r_{33e}$	48.6
Section Moduli about 33 axis (top), in <sup>3</sup>	$S_{33te}$	20,083
Section Moduli about 33 axis (bot), in <sup>3</sup>	$S_{33be}$	17,208
Plastic Section Mod about 33 axis, in <sup>3</sup>	$Z_{33e}$	19,915
Moment of Inertia about 22 axis, in <sup>4</sup>	$I_{22e}$	2.09 E5
Radius of Gyration about 22 axis, in	$r_{22e}$	21.9
Section Moduli about 22 axis, in <sup>3</sup>	$S_{22e}$	4,579
St. Venant Torsional Constant, in <sup>4</sup>	$J_e$	387,285*
*50% of $J_e$ of the intact section		

Depth of the webs in compression in the elastic range (Article 6.9.4.2.2b)

$$D_{ce} = 37.3 \text{ in}$$

Yield moment with respect to the compression flange.

- For sections in which  $S_{33be} > S_{33te}$ ,  $M_{yce} = S_{33te} \cdot F_y$
- For sections in which  $S_{33be} < S_{33te}$ ,  $M_{yce}$  is the moment at nominal first yielding of the compression flange, considering early nominal yielding in tension (Article C6.12.2.2.2c)

$$\rightarrow S_{33be} < S_{33te} \therefore M_{yce} = 80,524 \text{ kip} \cdot \text{ft}$$

Depth of the webs in compression in the plastic range (C6.12.2.2.2c-2)

$$D_{cep} = 37.4 \text{ in}$$

Plastic moment:

$$M_{pe} = Z_{33e} \cdot F_y = 82,983 \text{ kip} \cdot \text{ft}$$

## 2. Web Classification (Article 6.12.2.2.2c)

Limiting Slenderness for a compact web (6.12.2.2.2c-3)

$$\lambda_{pw} = 3.1 \frac{D_{ce}}{D_{cep}} \sqrt{\frac{E}{F_y}} = 74.4$$

Limiting Slenderness for a noncompact web (6.12.2.2.2c-6)

$$\lambda_{rw} = 4.6 \sqrt{\frac{E}{F_y}} = 110.8$$

Web Slenderness (6.12.2.2.2c-2)

$$\lambda_w = 2 \cdot \frac{D_{ce}}{t_w} = 66.3 \rightarrow \text{Compact web}$$

Web Plastification Factor for noncompact webs (6.12.2.2.2c-4, 7 & 8)

$$\lambda_w < \lambda_{pw} \therefore R_{pc} = \frac{M_{pe}}{M_{yce}} = \mathbf{1.03}$$

Web Load-Shedding Factor,  $R_b$

Ratio of two times the web area in compression to the area of the compression flange (6.10.1.10.2-8)

$$a_{wc} = \frac{2 \cdot D_{ce} \cdot t_w}{b_e \cdot t_{tf}} = 0.96$$

Limiting slenderness ratio for a noncompact web, expressed in terms of  $2D_c/t_w$ , (6.10.1.10.2-5)

$$\lambda_{rws} = 4.6 \sqrt{\frac{E}{F_y}} \leq \left( 3.1 + \frac{5}{a_{wc}} \right) \sqrt{\frac{E}{F_y}} \leq 5.7 \sqrt{\frac{E}{F_y}} = 137.3$$

Web Load Shedding Factor (6.10.1.10.2)

$$\rightarrow \lambda_w < \lambda_{rws} \therefore R_b = \mathbf{1.0}$$

### 3. Compression Flange Classification (Article 6.12.2.2.2d)

Limiting Slenderness for a compact flange (Table 6.9.4.2.1-1)

$$\lambda_{pf} = 1.09 \cdot \sqrt{\frac{E}{F_y}} = 26.3$$

Limiting Slenderness for a noncompact flange (6.12.2.2.2c-13)

$$\lambda_{rf} = 1.56 \cdot \lambda_{pf} = 40.9$$

Compression Flange Slenderness (6.12.2.2.2c-10)

$$\lambda_f = 25.1 \rightarrow \text{Compact Flange}$$

Compression Flange Slenderness Factor for a compact flange (6.12.2.2.2c-11, 14 & 16)

$$\lambda_f < \lambda_{pf} \therefore R_f = 1.0$$

### 4. General Yielding, compression flange local buckling, and Lateral Torsional Buckling (Article 6.12.2.2.2e)

Limiting unbraced length to achieve the nominal flexural resistance  $R_f R_b R_{pc} M_{yce}$  (6.12.2.2.2e-4)

$$L_p = \frac{0.1 \cdot r_{22e} \cdot E \cdot \sqrt{J_e \cdot A_{ge}}}{M_{yce}} = 855 \text{ in} \approx 71.3 \text{ ft}$$

Limiting unbraced length for the calculation of the lateral torsional buckling resistance (6.12.2.2.2e-5)

$$L_r = \frac{0.6 \cdot r_{22e} \cdot E \cdot \sqrt{J_e \cdot A_{ge}}}{0.5 \cdot F_y \cdot S_{33te}} = 9,869 \text{ in} \approx 822 \text{ ft}$$

Nominal Flexural Resistance (6.12.2.2.2e-1 & 2)

$$\rightarrow L_p < L_b < L_r \therefore$$

$$M_n = R_b (R_{pc} R_f \cdot M_{yce} - (R_{pc} R_f M_{yce} - 0.5 F_y S_{33te}) \alpha)$$

$$\alpha = \frac{L_b - L_p}{L_r - L_p} = 0.06$$

$$M_n = 80,640 \text{ kip} \cdot \text{ft}$$

### Factored Flexural Resistance

$$\phi_f \cdot M_n = 1.0 \cdot (0.9 \cdot 80,640 \text{ kip} \cdot \text{ft}) = 72,576 \text{ kip} \cdot \text{ft}$$

(\* Resistance factor proposed based on the results of the parametric study presented in Chapter 6)

### 5. Shear Strength of Interior Panels

Plastic Shear Force per web (6.10.9.3.2-3)

$$V_p = 0.58 \cdot F_y \cdot t_w \cdot d_w = 3,426 \text{ kip}$$

Transverse Diaphragm Spacing

$$d_0 = 120 \text{ in}$$

Shear buckling coefficient (6.10.9.3.2-7)

$$k = 5 + \frac{5}{\left(\frac{d_0}{d_w}\right)^2} = 8.83$$

Ratio of the shear-buckling resistance to the shear yield strength (6.10.9.3.2-4, 5 & 6)

$$1.12 \cdot \sqrt{\frac{E \cdot k}{F_y}} = 80.2$$

$$1.4 \cdot \sqrt{\frac{E \cdot k}{F_y}} = 100.2$$

$$\frac{d_w}{t_w} = 93.3 \rightarrow C = \frac{1.12}{\left(\frac{d_w}{t_w}\right)} \cdot \sqrt{\frac{E \cdot k}{F_y}} = 0.86$$

Panel proportion limit (6.10.9.3.2-1)

$$\frac{2 \cdot d_w \cdot t_w}{\left(\frac{b_{tf}}{2} t_{tf} + \frac{b_{bf}}{2} t_{bf}\right)} = 1.69 < 2.5$$



Nominal Shear Resistance of an interior web panel, per web (6.10.9.3.2-2)

$$\rightarrow V_n = V_p \cdot \left( C + \frac{0.87(1 - C)}{\sqrt{1 + \left(\frac{d_0}{d_w}\right)^2}} \right) = 3,219 \text{ kip}$$

Factored Shear Resistance for the section (1 web):

$$\phi_v \cdot V_n = 1.0 \cdot (0.9 \cdot 3,219 \text{ kip}) = 2,897.1 \text{ kip}$$

(\* Resistance factor proposed based on the results of the parametric study presented in Chapter 6)

## 6. Shear Strength of End Panels

Plastic Shear Force per web (6.10.9.3.3-2)

$$V_p = 0.58 \cdot F_y \cdot t_w \cdot d_w = 3,426 \text{ kip}$$

Transverse Diaphragm Spacing

$$d_0 = 120 \text{ in}$$

Shear buckling coefficient (6.10.9.3.2-7)

$$k = 5 + \frac{5}{\left(\frac{d_0}{d_w}\right)^2} = 8.83$$

Shear buckling coefficient (6.10.9.3.2-4, 5 & 6)

$$1.12 \cdot \sqrt{\frac{E \cdot k}{F_y}} = 80.2$$

$$1.4 \cdot \sqrt{\frac{E \cdot k}{F_y}} = 100.2$$

$$\frac{d_w}{t_w} = 93.3 \rightarrow C = \frac{1.12}{\left(\frac{d_w}{t_w}\right)} \cdot \sqrt{\frac{E \cdot k}{F_y}} = 0.86$$

Panel proportion limit (6.10.9.3.2-1)

$$\frac{2 \cdot d_w \cdot t_w}{\left(\frac{b_{tf}}{2} t_{tf} + \frac{b_{bf}}{2} t_{bf}\right)} = 1.69 < 2.5$$

Nominal Shear Resistance of an interior web panel, per web (6.10.9.3.2-2)

$$\rightarrow V_n = V_{cr} = V_p \cdot C = 2,946 \text{ kip (per web)}$$

Factored Shear Resistance for the section (1 web):

$$\phi_v \cdot V_n = 1.0 \cdot (0.9^* \cdot 2,946 \text{ kip}) = 2,651 \text{ kip}$$

(\* Resistance factor proposed based on the results of the parametric study presented in Chapter 6)

## APPENDIX D

### Value of Research

#### D. Value of Research

The focus of the research outlined in this report was the investigation is on the development of details that can improve the redundancy of steel box straddle caps. The goal of the investigation as to develop details and design methodologies that lead to the removal of the “fracture critical” classification for these girders. In addition to improving the safety of these girder systems, achieving a “non fracture critical” designation can dramatically improve the performance and economy of steel box straddle caps. Table D. 1 summarizes the qualitative and economic values of the present research.

Table D. 1: The project value of research (VoR).

Benefit Area	QUAL	ECON	Both	TxDOT	State	Both
Level of Knowledge	x			x		
Management and Policy	x			x		
System Reliability		x		x		
Increased Service Life		x		x		
Reduced Administrative Costs		x		x		
Traffic and Congestion		x			x	
Reduced Construction, Operations, and Maintenance Cost		x			x	
Infrastructure Condition		x				x
Engineering Design Development/Improvement			x			x
Safety			x			x

Note:

- QUAL: qualitative.
- ECON: economic.
- State: State of Texas.

#### D.1 Qualitative Value

##### D.1.1 Level of Knowledge

The research in this project included full-scale experiments and detailed parametric finite element analyses. The fundamental understanding of the redundancy behavior of the box sections were investigated, including experiments and computational models that demonstrate the ability of two different detailing methods to improve the redundancy of the box sections. While the use of added bars (commonly used for post-tensioning concrete members) showed promise, the concept of a bolted bottom flange proved to be the most

effective method. The investigation demonstrated the benefits of refined details and further showed that straddle caps with bottom flanged bolted to flange connection plates, can provide suitable reliability such that steel box straddle caps with these details are not fracture critical elements, now commonly referred to as a non-redundant steel tension member. This redundancy can provide significant improvements in the structural behavior and the long-term maintenance on straddle box caps.

### **D.1.2 Management and Policy**

The improved redundancy of straddle caps with the bolted bottom flanges can provide significant improvements in management and policy decisions for bridges making use of these new details. The improved redundancy can allow TxDOT the ability to classify these elements as non-fracture critical and therefore the inspection requirements are dramatically reduced. An arms-length inspection of all welds is no longer required every two years. This change is therefore, a significant improvement for the management of TxDOT's maintenance resources. Because the level of inspections are significantly reduced, the amount of time for biennial inspections will be significantly reduced. There are also a number of other major benefits to TxDOT and the travelling public as outlined in subsequent sections.

## **D.2 Economic Value**

### **D.2.1 System Reliability**

The use of bolted connections between bottom flange plates and flange connection plates (welded to the box webs) provides redundancy against a structural collapse due to a brittle fracture of the primary tension element. Experimental results considered the behavior if the bottom flange plate fully fractured in a brittle manner. The cracks arrested after fracturing the bottom plate leaving the two flange connection plates, webs, and top flanges fully intact and able of resisting significant load. In design, the flange connection plates are sized to support the redundancy load, thereby providing sufficient redundancy to prevent a collapse of the girder system. Further, in the parametric finite element analyses, fracture of the flange connection plate and web on one side of the girder was evaluated and the intact portions of the girder provided sufficient redundancy to support the requisite redundancy load. The fabrication methods for the system with the bolted bottom flange consists of bolting the bottom flange to the flange connection plates and then welding the top flange, and webs, to the assembled bottom flange. Therefore, the fabrication methods for the proposed box girders are not significantly different from conventional box sections. While the drilling and assembling of the bolt holes will be more expensive compared to a fully conventional welded box girder, the long-term savings on maintenance greatly exceed any increases in costs. In addition, significant savings are realized by the travelling public in terms of potential traffic delays.

### **D.2.1 Increased Service Life**

The modified details of the steel box straddle caps provide improved resistance to fatigue issues since the box section has suitable redundancy to arrest the crack. With fewer

potential maintenance issues in the straddle cap with the bolted bottom flange, significant economic savings are realized due to reduced maintenance related to methods of arresting or repairing cracks during the service life of the straddle caps.

#### **D.2.2 Reduced Administrative Costs**

A major difficulty for TxDOT is managing and maintaining sufficient maintenance staff for inspection and repair of the bridge inventory. The non-fracture critical rating of steel box straddle caps provides a structural element that reduces the inspection and maintenance demands, thereby reducing administrative demands on the TxDOT Maintenance Division.

#### **D.2.3 Traffic and Congestion Reduction**

The inspection requirements for fracture critical elements (now classified as non-redundant steel tension members – NSTM) require arms-length inspection of all welds and tension elements. These inspections require personnel to inspect the insides and exterior welds of every box section. Such inspections require lane closures that dramatically increase traffic congestion and delays to the travelling public. The costs of lane closures in urban environments can exceed \$1000/hour, and the added delays to the travelling public reduce productivity leading to increased costs.

#### **D.2.4 Reduced Construction, Operations, and Maintenance Cost**

As noted previously, the length of time necessary for inspection of bridges with steel box straddle caps with the developed details will be significantly reduced since an arms-length inspection of all welds and tension components is not necessary. While some traffic control may still be necessary (as with any bridge inspection), the length of time will be significantly less. These reductions will lead to improved efficiency of maintenance and operations, leading to improved economy.

#### **D.2.5 Infrastructure Condition**

Straddle caps are generally utilized in congested environments and involve bridges vital to the traveling public. Improvements in redundancy and control of potential fatigue cracking will lead to improved conditions of these vital infrastructure components.

#### **D.2.6 Engineering Design Improvement**

The research conducted in this investigation provided vital data in understanding the design and behavior of steel box straddle caps with both existing details and newly proposed details. The combined experimental data provided improved understanding of the fundamental behavior and design requirements for straddle cap systems. The design methodology for the systems are outlined in the report and provides a resource for designers in understanding the behavior and basic requirements in various bridge geometries.

### **D.2.7 Safety**

The focus on this study was developing improved details through experimental and computational means. The details that were proposed and evaluated through full-scale experiments and parametric FE analysis results in improved redundancy that improves the safety of the structural system. From a design perspective, consideration is being given to a potential condition that, while low probability – has been considered. Considering and designing for such a catastrophic condition improves the safety of the travelling public. In addition, the reduced inspection requirements also significantly improve the safety of TxDOT inspection personnel due to reductions in time duration of positioning maintenance personnel in proximity of travelling public or at elevated positions on the bridges.